Terahertz Components and Systems : Metamaterials, Measurement Techniques and Applications

STEFANOVA, POLINA,STEFANOVA

STEFANOVA, POLINA,STEFANOVA (2024) *Terahertz Components and Systems : Metamaterials, Measurement Techniques and Applications* , Durham theses, Durham University. Available at Durham E-Theses Online: http://etheses.dur.ac.uk/15383/

Terahertz Components and Systems :
Metamaterials, Measurement Techniques and Applications

Polina S. Stefanova

A thesis submitted in partial fulfillment of the requirements
for the degree of Doctor of Philosophy

Department of Engineering
Durham University
United Kingdom

February 23, 2024

Abstract

THz technology has been a promising, yet problematic field in science for a long time. Up until two decades ago, the lack of fundamental components and materials operating at THz frequencies constrained its use mostly to astronomy, with very little commercial focus. Today, the field has grown remarkably, with both scientific and industrial applications pushing the development of new devices and systems to control THz radiation. Further work is necessary to overcome the region's fundamental challenges and advance the technology on par with the rest of the electromagnetic spectrum. This thesis aims to address new applications for THz spectroscopy, both in the frequency and time domain, as well as enhancement of THz device performance. A new design approach for THz resonant metamaterials is proposed that aims to improve their resonant response, irrespective of individual resonator geometries. The new approach can be applied to a wide range of already existing structures without altering the individual resonator design and relies on metamaterial cell symmetry and substrate dimensions. The design approach is used to create split-ring optical modulators, demonstrating their response is strong enough to be actuated with an LED lamp as a light source alone.

The development of a multiple-angle-of-incidence, multi-wavelength THz ellipsometry system is also presented. The utility of the system for material characterisation is demonstrated, extracting complex optical parameters of composite materials, as well as non-homogeneous, anisotropic and highly absorptive materials in the THz range, which can be otherwise problematic to characterise. The use of the ellipsometry system as an imaging tool for visualising and measuring internal material stresses is introduced.

Finally, the application of THz-TDS in conjunction with machine learning for waste oil quality control is investigated, introducing a new potential field of application for THz spectroscopy.

Acknowledgements

It would make for a very long list to acknowledge everyone who have willingly (and unwillingly) involved themselves with this work. Most of all I would like to thank Claudio, who inspired me to pursue a PhD in the first place and provided his continuous support and help throughout the years. Together with Andrew, they've been both great teachers and company.

I would also like to thank my fellow PhD victims, Andreas Klein, Rhiannon Lees and Jonathan Hammler for making me want to spend time with them, rather than do any work. Also a grateful wave to my parents, without whom I would have had to face real life much sooner. Finally, I would like to thank my support group of friends, cats and Ice the Dog, as well as a special shout out to James for his immense patience with me.

""Explain to him that we don't do things, Stibbons," said the Lecturer in Recent Runes. "We are academics"."

Terry Pratchett

Declaration of Authorship

The work in this thesis is based on research carried out at the Department of Engineering, University of Durham, England. No part of this thesis has been submitted elsewhere for any other degree or qualification, and it is the sole work of the author unless referenced to the contrary in the text.

Publications

- Stefanova, Polina & Hammler, Jonathan & Klein, Andreas & Gallant, Andrew & Balocco, Claudio. (2016). Polymer-based micro-golay cells for THz detection. 1-2. 10.1109/IRMMW-THz.2016.7758964.
- Stefanova, Polina & Klein, Andreas & Lees, Rhiannon & Gallant, Andrew & Balocco, Claudio. (2018). Optically Controlled THz Metamaterial Modulators. 1-2. 10.1109/IRMMW-THz.2018.8510223.
- Lees, Rhiannon & Stefanova, Polina & Klein, Andreas & Balocco, Claudio & Gallant, Andrew. (2018). Paper-based Optical Components for the THz Region. 1-2. 10.1109/IRMMW-THz.2018.8510036.
- Fenlon, Vanessa & Lees, Rhiannon & Stefanova, Polina & Klein, Andreas & Gallant, Andrew & Balocco, Claudio. (2018). Evolutionary Optimisation of THz components. 1-2. 10.1109/IRMMW-THz.2018.8510407.
- Klein, Andreas & Stefanova, Polina & Gallant, Andrew & Balocco, Claudio. (2018). Material Characterization with Frequency Domain THz Ellipsometry. 1-2. 10.1109/IRMMW-THz.2018.8510238.
- Klein, Andreas & Stefanova, Polina & Cooke, Michael & Balocco, Claudio & Gallant, Andrew. (2019). Whispering-Gallery Resonators for Highly Integrated Plasmonic THz Circuits. 1-2. 10.1109/IRMMW-THz.2019.8874418.
- Stefanova, Polina & Klein, Andreas & Gallant, Andrew & Balocco, Claudio. (2019). THz Spatial Modulation in the Fourier Plane. 1-1. 10.1109/IRMMW-THz.2019.8873889.

- Stefanova, Polina & Hehne, Timon & Klein, Andreas & Gallant, Andrew & Balocco, Claudio. (2020). Tensile Stress Measurements with Photoelastic Scattering at THz Frequencies. 1-2. 10.1109/IRMMW-THz46771.2020.9370726.
- Stefanova, Polina & Ji, Ruidong & Gallant, Andrew & Graham, Darren & Balocco, Claudio. (2020). Waste oil feedstock quality control using THz spectroscopy. 1-1. 10.1109/IRMMW-THz46771.2020.9370580.

Contents

List of Figures

List of Tables

List of Abbreviations

2DEG	**2 D**imentional **E**lectron **G**as
AI	**A**rtificial **I**ntelligence
ANN	**A**rtificial **N**eural **N**etwork
BWO	**B**ackward - **W**ave **O**scillator
CFL	**C**ourant - **F**riedrich - **L**ewy
CMOS	**C**omplementary **M**etal - **O**xide **S**emiconductor
CNN	**C**onvolutional **N**eural **N**etwork
CPS	**C**o**P**lanar **S**trip
CW	**C**ontinuous **W**ave
DBR	**D**istributed **B**ragg **R**eflector
DFT	**D**iscrete **F**ourier **T**ransform
DL	**D**eep **L**earning
DUT	**D**evice **U**nder **T**est
FDTD	**F**inite **D**ifference **T**ime **D**omain
FEA	**F**inite **E**lement **A**nalysis
FTIR	**F**ourier **T**ransform **I**nfra**R**ed Spectroscopy
FWHM	**F**ull **W**idth **H**alf **M**aximum
HEMT	**H**igh **E**lectron **M**obility **T**ransistor
HRFZ	**H**igh **R**esistivity **F**loat **Z**one
IF	**I**ntermediate **F**requency
IFT	**I**nverse **F**ourier **T**ransform
JSRR	**J**oint **S**plit **R**ing **R**esonator
K-K	**K**ramer - **K**ronig
LED	**L**ight **E**mmiting **D**iode
MEMS	**M**icro**E**lectro**M**echanical **S**ystems
MSE	**M**ean **S**quare **E**rror

PML	**P**erfectly **M**atched **L**ayer
ReLU	**Re**ctified **L**inear **U**nit
RF	**R**adio **F**requency
SC-PML	**S**tretched **C**oordinate **P**erfectly **M**atched **L**ayer
SOLT	**S**hort **O**pen **L**oad **T**hrough
SRR	**S**plit **R**ing **R**esonator
SSIM	**S**tructural **S**imilarity **I**ndex **M**atrix
TDS	**T**ime **D**omain **S**pectroscopy
TE	**T**ransverse **E**lectric
THz	**T**erahertz
TM	**T**ransverse **M**agnetic
UPML	**U**niaxial **P**erfectly **M**atched **L**ayer
UPML	**U**niaxial **P**erfectly **M**atched **L**ayer
VDI	**V**irginia **D**iodes
VNA	**V**ector **N**etwork **A**nalyser

Chapter 1

Introduction

The following chapter provides an introduction to the field of Terahertz (THz) technology and its various unique properties, applications and challenges. An overview of the THz spectrum and the reasons behind its lag in practical development in comparison to other frequency bands are presented. This is followed by a brief summary of the thesis structure.

1.1 The THz Spectrum

The electromagnetic spectrum from 0.1 THz (100 GHz) to 10 THz is referred to as terahertz frequencies, and it lies between the microwave and infrared bands. It is also commonly known as "the THz gap" (as shown in Figure 1.1). The name relates to the fact that unlike other parts of the electromagnetic spectrum, the exploration of THz frequencies is a relatively young field, only a few decades old. Challenges associated with the generation, detection and manipulation of THz waves have therefore left a "gap" in the technology available in this region.

The interest in THz waves started with astronomy : 98% of the total photons emitted in the history of the universe since the Big Bang lie within the THz region [1]. This makes THz spectroscopy an important tool for the diagnostics of both the physical and chemical conditions of astrophysical environments. Furthermore, THz waves were found to exhibit various unique properties, differentiating them from other spectral ranges. They have high transmission through paper, plastic and textiles, exhibit high absorption in water, do not produce harmful ionization effects on biological tissues and have correspondence to many molecular absorption lines. These properties have made THz waves a candidate for many different applications in spectroscopic material identification, communication and imaging. Due to the high transparency of common packaging materials and spectral "fingerprints" of illicit drugs and explosives in THz frequencies, there has been ongoing research in security applications for body and package screening [2]. Promising imaging applications have been explored within the biomedical field, providing a safer alternative to X-rays and better resolution than microwaves. In conjunction with THz spectroscopy, the early detection and diagnosis of cancerous tissue has been demonstrated. This is possible both through spectroscopic identification of cancerous biomarkers [3] and due to the high contrast between healthy and carcinoma tissues, which tend to have higher water content and structural differences [4]. THz communications is another large field of applications with great scientific and commercial potential. The demand for constantly increasing wireless communication bandwidth is pushing the development of next generation networks into the THz regime, promising to support over 1 Tbps data transfer. Additionally, THz communication can be used to complement bus-based chip-to-chip communication architectures by establishing high speed wireless interconnects. [5]. The last two decades have shown an immense progress in the development of THz sources, detectors and components. The THz gap is continuously closing, however many challenges remain ahead before the technology is widespread and commercially available.

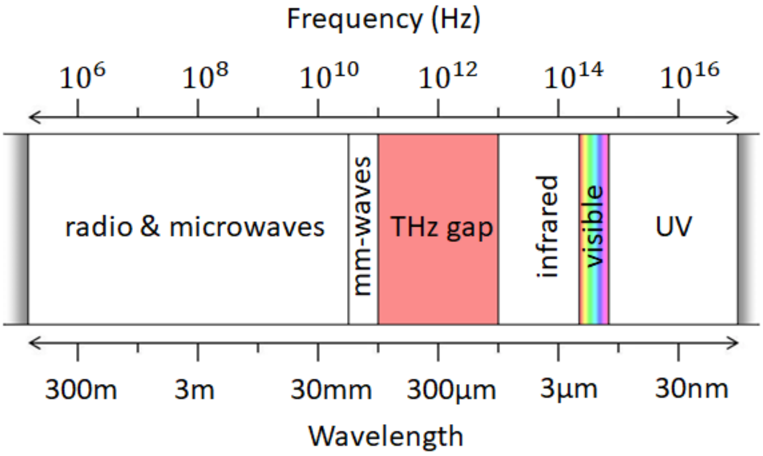

FIGURE 1.1: The THz gap within the electromagnetic spectrum

1.2 THz Challenges

THz radiation shares properties with both optical frequencies and microwaves, which give it its wide scope of applications and unique traits. However, this is also the reason why neither traditional photonics, nor electronics alone are suitable for its generation, detection and manipulation. The existence of the THz gap is rooted in the fundamental principles behind how these technologies operate.

1.2.1 Sources

The first biggest challenge to THz technology is THz wave generation. Traditional solid-state electronic sources, such as oscillators and amplifiers, are based on direct electronic oscillations or non-linearities in semiconductor devices. As such they are restricted by resistive losses, reactive parasitics and carrier transit times that prevent them from operating at frequencies higher than 100 GHz [6]. High-powered tube sources, which dominated RF generation before the expansion of solid-state devices, suffer from physical scaling problems, metallic losses, and the need for extremely high electric and magnetic fields, as well as high current densities. Nowadays, they are also very scarcely produced. Optical sources, such as diode lasers, rely on interband transitions of charge carriers. The photon energy at 1 THz (or 300 µm), however is 4.1 meV, a quanta comparable to the relaxation energy of the semiconductor crystal, and therefore too small for lasing at room temperatures [7]. Nevertheless, the last decade has seen great improvements in THz sources, utilising two general approaches - frequency upconversion from microwave sources and downconversion from optical sources. One of the most successful upconversion approaches is by chain multiplication of microwave oscillators (20-40 GHz), using GaAs Schottky diode doublers and tripplers. The technique achieves high-resolution, narrow band, continuous wave (CW) microwatt power THz radiation. Direct semiconductor oscillation with resonant tunneling diodes (RTDs) is also being used, producing powers in the microwatt range. Optical sources tend to provide higher output powers in comparison to solid-state ones. Downconversion from optical sources include direct laser to laser pumping, laser photomixing, optical mixing in non-linear crystals, direct lasing in gases, femtosecond laser pumping of photoconductive (PC) switches and quantum cascade lasers. The cornerstone of THz spectroscopy, Time Domain Spectroscopy (THz- TDS), uses the femtosecond laser approach, which produces picosecond THz pulses through illuminating a photoconducting antenna with the pump laser beam. THz-TDS sources provide high signal-to-noise ratios (SNR), a broad frequency band and good spectral resolution. THz-TDS systems, however, still produce THz output power only in the tens of microwatts. Quantum Cascade Lasers (QCLs) have grown to be one of the most promising THz sources. They have undergone rapid development since the first QCL working at THz frequencies was introduced in 2002 [8], [9]. QCLs are now able to produce output powers in the milliwatt range, but their biggest downside is that they do not operate at room temperatures and require cryogenic cooling. Advances in THz QCL research have mainly focused on improving the operating temperatures, with recent pulse lasing achieved at temperatures around 250 K [10]. Another hurdle is their limited tunability, which is also an active area of research.

1.2.2 Detectors

Detectors are perhaps the most successfully developed THz component, achieving both wide band and narrow band near quantum-limited sensing (where signals are comparable to the ambient quantum noise, arising from fluctuations of the number of photons hitting the detector). Individual photon counters are hindered by the low photon energies in comparison to shorter wavelengths, as well as the large focal spots at THz (an Airy disk of hundreds of micrometers). The low photon energy results in the detected signals being dominated by thermal noise, forcing sensors to be cryogenically cooled or apply long integration times. In comparison to microwave detectors, THz also lacks available electronic elements, such as amplifiers, low-loss transmission media and lumped resistors, capacitors and inductors [7]. Broadly, THz detectors can be categorised in three groups, based on their principle of operation. These are in no way absolute, as there are many overlapping technologies. The first are thermally actuated sensors, where the THz radiation is absorbed leading to a change in temperature which is detected. In essence these are very sensitive thermometers. Example detectors include Golay cells, microbolometers, thermocouples and thermopiles. The second group can generally be described as "electronic" detectors, where the THz radiation induces charge motion or band transitions. These include graphene Field Effect Transistors (FETs), surface plasmons, surface plasmon polaritons, Schottky diodes, tunneling junction backward diodes, quantum dot and quantum well structures. The final group of detectors is based on the interaction of THz radiation with ultra-short optical pulses, a sensing technique relevant for THz-TDS systems. These include electro-optical sampling, air biased coherent detection and photoconductive receivers [11].

1.2.3 Auxillary Components and THz Materials

The challenges for THz technology are not isolated only to detectors and sources, but also to auxillary components, such as waveguides, amplifiers, modulators, absorbers and various other optics. Furthermore, these components suffer from a lack of availability of suitable materials that they can be fabricated from. The most investigated material in THz applications is High Resistivity Float Zone Silicon (HRFZ-Si). Besides synthetic diamond, high resistivity silicon is the only isotropic crystalline material suitable for transmission of the extremely wide range from NIR (1.2 µm) to MM (1000 µm) waves and more [12]. It is cheaper to grow and machine, in comparison to diamonds, and can be fabricated in relatively large dimensions, necessary for THz components. To get an appreciation of the disadvantage of materials transmitting at THz, one just needs to look at the attenuation of HRFZ-Si at THz frequencies - it is more than two orders of magnitude higher than in the infrared [13]–[15]. Many other materials, such as polymers also exhibit higher absorption at THz, leading to higher losses in the devices fabricated from them. These challenges have pushed efforts into the development and use of artificial materials, such as graphene and metamaterial structures for the construction of many THz components. In the following chapters metamaterial structures in the context of THz modulators will be investigated and ways for enhancing their performance proposed, which can be implemented in various metamaterial applications.

1.3 Introduction to Metamaterials

Metamaterials are composite materials that are purposefully engineered to exhibit properties not found in nature. They enable exotic phenomena, such as negative refractive index, invisibility and cloaking [16]. The metamaterial properties are derived from their physical structure and not their chemistry. A typical metamaterial consists of a replicating pattern, called a "cell". When the cell's geometry is small, compared to the wavelength of the incident radiation (around $\lambda/10$), the material is homogeneous from the perspective of the incident wave. Consequently, the metamaterial behaves like a real material in the sense that for large wavelengths it can be characterised by effective constitutive parameters – an effective permittivity ε, and permeability μ. The cells of the metamaterial in this case are analogous to the atoms in a normal material. Resonant metamaterials are patterned materials, where the repeated pattern is usually made out of metal. The metallic parts, when exposed to electromagnetic radiation store electromagnetic energy and exhibit a resonant behaviour. Resonant metamaterials are highly susceptible to changes in the substrate, which would increase the modulation depth under illumination at the resonating frequencies. An inherent downside to any resonating structure is that the response is very narrow band. The higher the Q-factor of the resonator, the more underdamped and "fine tuned" the system is, leading to greater changes in transmission as the conductivity of the substrate changes, but also to a narrower band response. Therefore the modulation depth and bandwidth of the resonating structures are inversely proportional.

1.4 Thesis Structure

The objective of the following thesis is focused in three main directions :
- A new approach to THz metamaterial design, which focuses on tailoring substrate thickness along with metamaterial cell symmetry to create photonic crystal slabs in conjunction with traditional individual metallic resonators. The combination of the two can be tuned to create constructive interference between resonance modes, achieving a strong resonant response with a high quality factor and a strong field

confinement. The design approach can be applied to a variety of existing metamaterial structures and devices to enhance their performance.
- The development and utilisation of a THz ellipsometer, capable of measuring both amplitude and phase information under multiple angles of incidence and a spectrum of frequencies. The ellipsometer is then used to characterise the optical parameters of unknown materials, as well as an imaging tool for mapping the internal stresses in materials transparent to THz radiation.
- The exploration of THz time-domain spectroscopy as a solution for quality control of waste oil in the waste oil refining industry and it's capability of creating a benchmark for hazardous waste acceptance and rejection criteria.

Chapter 2 presents the measurement methods and techniques used for the purpose of this research. Two main instruments are introduced - a THz - TDS system and a frequency domain Vector Network Analyser (VNA) THz system. This is followed by post-processing algorithms, numerical calculation methods and fabrication.
Chapter 3 demonstrates the design and testing of semiconductor metamaterials for THz optical amplitude and phase modulators. A new design approach, treating the metamaterials as photonic crystal slabs, is investigated for the increase of modulation depth and the fabricated devices are tested as spatial modulators.
In Chapter 4 several THz metrology methods are discussed. The development of a THz ellipsometry system is presented, as well as an evaluation of the method by characterising a number of materials, including insitu measurements and anisotropic materials. Results are compared to literature values of other measurement techniques. Consequently, a grazing angle measurement technique is introduced for thin film thickness measurements, as well as photoelasticity at THz. The photoelastic constants of Si at THz frequencies are extracted and used to image the internal stresses and strains in a Si wafer.
Chapter 5 explores THz-TDS as a quality control method for waste oil re-refining. A convolutional neural network was trained on obtained data and tested to determine waste oil quality based on THz spectral data.

Chapter 2

Methods

The following chapter introduces the instrumentation, fabrication techniques and computational methods used in the presented research.

2.1 THz Vector Network Analyser

Before the use of a Vector Network Analyser (VNA) in THz measurements is discussed, a brief introduction to multiport networks and the scattering parameters is necessary. A linear radio frequency (RF) network can be described as a "black box", characterised only by the relations between the incident and transmitted and reflected waves on its ports (the inputs and outputs). The scattering parameters, or S-parameters, describe these relations for any number of ports. In the case of a two-port network, as seen in Figure 2.1, S_{11} is reflection at port 1, S_{21} the transmission at port 2 (forward gain), S_{22} the reflection at port 2 and S_{12} the transmission at port 1 (reverse gain).

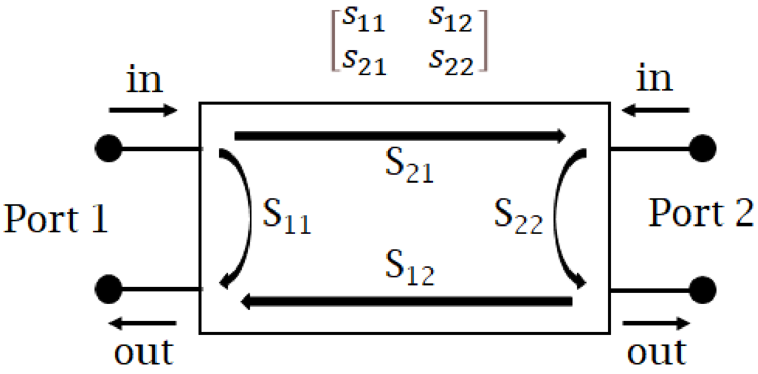

FIGURE 2.1: S-parameters of a 2-port linear network

VNAs are used to accurately measure the complex scattering parameters of various devices and systems. They are a key instrument in the microwave and millimetre wave fields and provide high accuracy by employing high quality signal sources and receivers, as well as sophisticated calibration techniques that eliminate systematic errors and noise [17]. The THz VNA system used for the purposes of this research, is a combination of an Agilent N5224A network analyser [18] and two full-band WR-1.0 Virginia Diodes (VDI) multipliers [19], which extend the original N5224A frequency band of 10 MHz - 43.5 GHz to 0.75 - 1.1 THz.

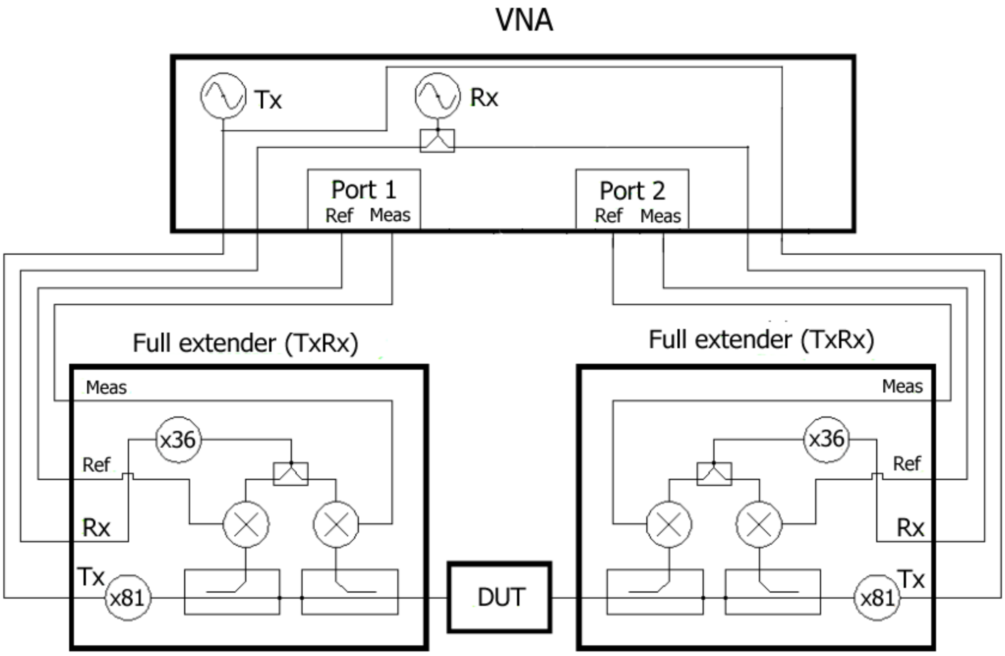

FIGURE 2.2: Four-port VNA connected to two full TxRx extender heads (WR-1.0 Virginia diodes). The "Tx" and "Rx" are the two local VNA oscillators, "Ref" is the reference signal and "Meas" is the measured signal.

The four-port VNA is connected with the WR-1.0 extender heads, resulting in a 2-port THz system, which is able to measure all four S-parameters of a device under test (DUT) without re-arranging the system. The frequency extension is achieved through a series of Schottky diode frequency doublers and tripplers, as shown in the diagram in Figure 2.2. The performance parameters of the WR-1.0 extender heads provided by the manufacturers and the comparable performance achieved in practical experiments in our labs is shown below in Table 2.1. The dynamic range for free space was measured by first placing the TxRx heads together as closely as possible without them touching and normalising. One module was then terminated with a short and the S21 and S12 measurements averaged over 10 sweeps for all frequencies was taken as the dynamic range. The magnitude and phase stability measured was averaged over the entire frequency band for continuous sweeps lasting for 1 minute. The decreased performance in dynamic range and stability in the experimental setup is expected, as a free-space measurement is intrinsically noisier - the dynamic range was measured by the manufacturer using a waveguide coupling. The dynamic range typically also decreases towards the two ends of the spectrum. Stability was measured after the equipment has warmed up (approximately 1h), however the environment wasn't temperature or humidity controlled, which introduces additional noise.

Parameter	VDI Specification	Free-space lab measurement
Standard Frequency Coverage (GHz)	750 -1000	750-1100
Dynamic Range (bandwidth = 10 Hz, dB, typical)	65	51
Dynamic Range (bandwidth = 10 Hz, dB, minimum)	45	39
Magnitude Stability (±dB)	0.5	1.18
Phase Stability (±°)	6	14.48
Test Port Power(dBm typ. power)	-30	-30
Directivity (dB)	30	Not measured

TABLE 2.1: VDI WR-1.0 frequency extender heads factory [19] and experimental specifications

Calibration of the system is advantageous in comparison to other THz measurement systems, as it uses readily available S-parameter callibration kits. Short, open, load and through (SOLT) waveguide standards were used in order to account for systematic errors between the VNA ports and the extender heads' waveguide flanges. The callibration plane is behind the horn antennas used on the WR-1.0, therefore the VNA measurements are not fully callibrated, as they do not account for system errors introduced between the waveguides and horn antennas. The VNA measurement technique is in many ways complimentary to the most popularly used THz-TDS system and provides both advantages and disadvantages. Unlike time-domain systems, THz VNA spectroscopy provides measurements in the frequency domain directly. It provides fast scanning times, which are beneficial in measuring time-dependent processes, such as the in-situ measurements in Chapter 4. It is compact and mobile in comparison to the TDS, and full S-parameters in both transmission and reflection can be easily measured without change in setup. Whereas TDS systems are broadband (ours working between 0.5 - 5 THz) with higher output power (several microwatts), the VNA is very narrowband (0.75-1.1 THz) and has relatively low output power at THz (fractions of microwatts, around 0.3 μW). Their respective bands make the TDS suitable for coarser broadband measurements with resolutions up to around 0.5 GHz, and the VNA for finer measurements with resolutions of several kHz.

2.2 Terahertz Time Domain Spectroscopy

THz-TDS has been the dominant technology in the field for THz characterisation. The main principle behind the technique is to measure a short THz pulse (usually in the order of picoseconds), as a function of time. A Fourier transform of the time trace can then be applied to obtain the spectral information. There are various ways of generating and detecting pulses in THz-TDS systems, however this thesis will concentrate on the methods used at the Durham University THz lab. These are photoconductive switching for generation and electro-optical sampling for detection.

2.2.1 Photoconductive Antennas (PCAs)

Photoconductive antennas are optically actuated switches, which radiate when a laser pulse is shone onto them. They consist of a semiconductor substrate with electrically biased metal pads, as shown in Figure 2.3. When a laser pulse with photon energy above the semiconductor bandgap is shone on the antenna gap, a transient current is generated, due to the increase in conductivity through photoexcitation. When the laser pulse duration is sub-picosecond, the energy radiated by the PCA is in THz frequencies. PCAs can also be used "in reverse", as THz detectors. When the antenna contacts are unbiased, the laser pulse produces charge carriers, which are then accelerated by the incident THz radiation, producing a current. This transient current can then be detected electronically.

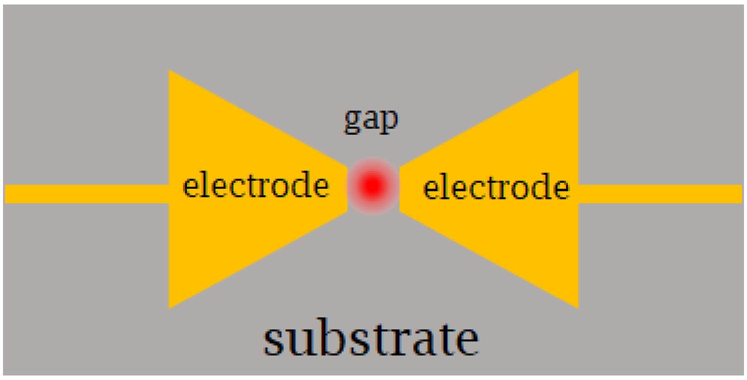

FIGURE 2.3: Bow-tie photoconductive antenna geometry. A pump laser beam, indicated in red, is focused on the antenna gap.

The PCA's radiation output frequency and bandwidth depend on the pulse duration of the photocurrent. This is determined by both the duration of the laser pulse and the charge carrier lifetime in the semiconductor. Since the photocurrent pulse duration is larger than that of the laser pulse generating it, femtosecond laser pulses are necessary for the generation of picosecond THz pulses. The charge carrier generation and recombination times need to be within the picosecond range as well, which is achieved in direct bandgap semiconductors. The traditionally used direct semiconductor is GaAs, with a bandgap energy of 1.39 eV, which is exceeded by laser wavelengths shorter than ~ 892 nm. Therefore the use of Ti:Sapphire lasers is required for GaAs PCAs.

Antenna geometry can vary, influencing the shape of the emitted spectrum and the polarisation [20]. Our antennas made in-house were a standard bow-tie design, as shown in Figure 2.3, with Au/Ti contacts, patterned using photolithography. This design aims to confine the electric field in the gap. The emitted electric field E_{THz} of the PCA is typically proportional to the change in photocurrent, given by

$$E_{THz} \propto \frac{dj}{dt} \tag{2.1}$$

, where j is the current density and t is the time. To further expand this, the current density itself is proportional to the charge carrier concentration n_e and the relative velocity between electrons and holes v_e, giving

$$\frac{dj}{dt} \propto ev_e \frac{dn_e}{\delta t} + en_e \frac{dv_e}{dt} \tag{2.2}$$

where e is the charge of an electron. The change in carrier concentration is a function of the laser pulse power and the first term in equation 2.2 dominates the output field. The change in drift velocity has a smaller contribution and is related to the bias voltage applied at the antenna contacts.

2.2.2 Electro-Optical Sampling

Detection via electro-optical sampling is a technique, where a crystal's birefringence is changed due to THz radiation and the change in polarisation of an optical beam going through the crystal is detected. This approach offers better results in our experimental setup to PCA detection, as our antennas are produced in small batch sizes, which leads to changes in their characteristics between batches. This is mostly due to differences in the resistivity of GaAs substrates used between batches, as well as changes to the design geometry as a result of manufacturing tolerances. This has led to large differences in bias voltage to generate a set amplitude of the THz signal between different PCAs. In comparison, electro-optical sampling offers a larger bandwidth, flatter frequency response and a larger surface area, which accommodates for beam drift. Changes in refractive index as a linear function of an applied optical field is observed in noncentrosymmetric crystals and is called the Pockels effect [21]. ZnTe is the usual crystal of choice due to its high signal to noise ratios [22]. The full detection setup is shown in Figure 2.4. The probe beam is linearly polarised as it first passes through the ZnTe crystal. It then passes through a quarter wave plate, which changes the linear polarisation to circular, with equal amounts in the horizontal and vertical components. A Wollaston prism then splits the two polarisations into two different paths, which are detected by two balanced photodiodes. When there is no THz radiation present, the ZnTe crystal keeps the polarisation of the beam linear and the beam is split equally between the two photodiodes, producing a zero differential current. When THz radiation falls on the crystal, the beam becomes elliptically polarised, and the change between polarisation components gives rise to a differential photocurrent, which is then read out by an lock-in amplifier.

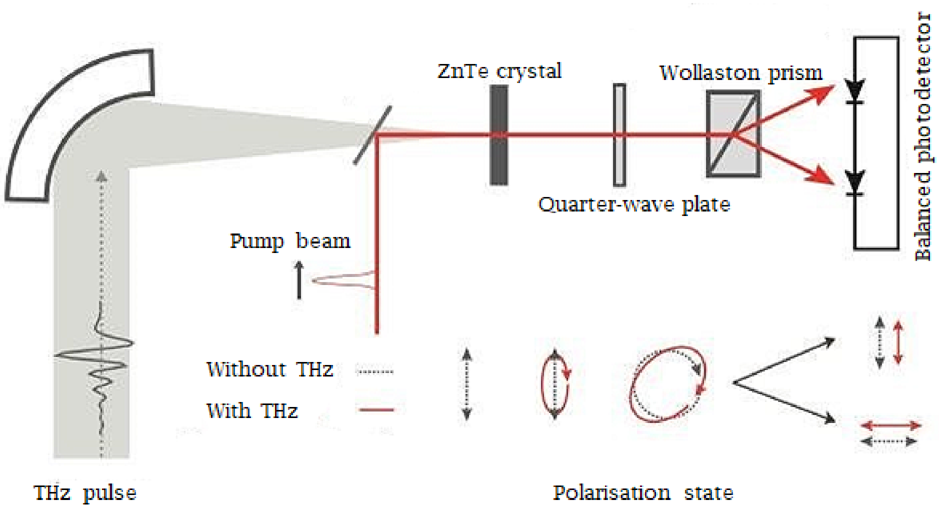

FIGURE 2.4: Schematic representation of electro-optical sampling in THz-TDS [23]

2.2.3 System Configuration

Having gone over the THz generation and detection, the complete TDS system can now be presented. A schematic representation is shown in Figure 2.5. The mode-locked Ti:Sapphire femtosecond laser beam is first split in two by a 90/10 beam splitter. 90 % of the power is directed towards the THz generation path and 10% towards the optical reference path. This is done as the photodiodes detecting the optical beam are quite sensitive and maximum optical power is needed for the generation of the THz pulse. The probe beam then goes through an optical delay line with two mirrors. By changing the mirror positions, the delay line delays the time at which the pulse reaches the detectors. The delay line length is 15 cm, giving a maximum delay path of 30 cm or 1 ns delay in time. The line provides micrometer precision on the mirror position, resulting in picosecond temporal resolution (1 ps = 300 µm change in path length). The probe beam is then directed at the ZnTe crystal and passes through the rest of the electro-optical sampling.

The second path after the beam splitter goes through an APE scanDelay 50 shaker. The shaker is also a type of delay line, with a much smaller scan range of ± 3.75 mm, which "shakes" periodically. In our typical setup a deflection of 600 µm with a frequency of 1 Hz is used. Shaker readouts are used for the daily alignment of the system, as it provides very quick and coarse visualisations of the main THz pulse. This way the system can be aligned for maximum power output. For full spectroscopic scans, the shaker is turned off.

The following component on the beam path is a chopper wheel, which provides a reference frequency for the lock-in amplifier at the detection stage. The beam is then focused onto the PCA's gap and the THz radiaiton is generated. Samples under investigation are placed in a purged box filled with N_2, in order to avoid water vapour absorption from the environment. Samples can be placed between sets of parabolic mirrors - mirrors 1 and 2 or 3 and 4 for a collimated THz beam, or between mirrors 2 and 3 for a focused beam. The THz pulse is then directed towards the ZnTe crystal for detection.

When the path lengths of the optical probe beam and the THz pulse are the same, the THz and optical pulses coincide in time. As the optical pulse is orders of magnitude shorter than the THz pulse, by delaying the probe pulse in time via the delay line, the THz pulse can be sampled. The refractive index change in the ZnTe crystal is linear with the amplitude of the THz electric field, so each sample of the THz pulse is recorded as an amplitude point via the photodetectors and lock-in amplifier.

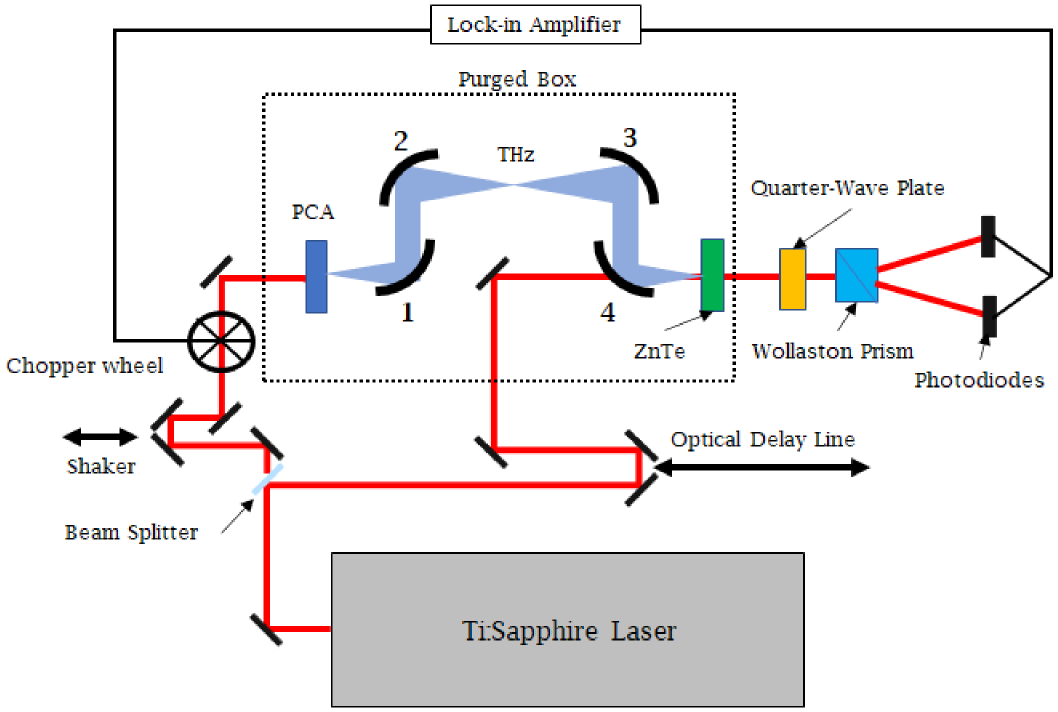

FIGURE 2.5: Schematic representation of the THz-TDS setup used

2.3 Numerical Methods

Simulations are often necessary in order to predict the behaviour of electrodynamic systems and devices under investigation. They aid the understanding of new phenomena, device design and optimisation. The methods employed in computational electrodynamics can broadly be separated in two categories - analytical and numerical. They both have advantages and disadvantages and are to be employed depending on the circumstances. Analytical methods are more suitable for simpler systems, with a high degree of symmetry, such as 1-dimensional dielectric stacks. They can provide exact solutions and quick computing times, but are limited by the complexity of the problems, such as complicated geometries. Numerical methods, and most notably the Finite-Difference Time Domain (FDTD) method, has become a standard in modelling electrodynamics. It is a flexible method, which can be employed in a wide range of applications, providing approximate solutions to the associated differential equation. It can be used with complex 3D geometries, but may require long computation times and caution must be taken when verifying boundary conditions and convergence [24]. Here an in-house built FDTD engine is presented, as well as an analytical dielectric stack computing method with effective refractive index extraction from S-parameter data. These tools are then compared to the commercial FDTD software Lumerical.

2.3.1 FDTD Simulations

While the Lumerical FDTD package is a powerful computational tool, it is beneficial to have a baseline comparison to check if a particular response or model is correct. For highly resonant responses with many spectral features, one can easily be misled by simulation results. A simplified FDTD engine was implemented in MATLAB, in order to run quick simulations that require less computing power. This way simulation parameters such as mesh size, simulation times and volumes and boundary conditions could be optimised, as well as quick conversion tests performed before a more complex (usually 3D) simulation is ran in Lumerical. The MATLAB FDTD was also used to compare between the final results from the two engines.

The Yee Method

FDTD modelling is a type of finite element numerical analysis, where the device under investigation is divided into small volumes, or cells, and the discrete time-dependent Maxwell equations are solved for each cell. By obtaining the impulse response of the device, the frequency response can be calculated, through applying the Discrete Fourier Transform (DFT). The FDTD method is sometimes called Yee's method, named after mathematician Kane S. Yee, corresponding to the specific Yee grid that is used to define the electromagnetic field components (E_x, E_y, E_z, H_x, H_y, H_z) in space for every cell [25]. Analytically, the field is defined for each point in space, however, as the FDTD algorithm deals with finite volumes, a specific point in each cell must be chosen, where the electric and magnetic field components are defined. As opposed to the intuitive collocated grid cell shown in Figure 2.6a , where the field components coincide in one point in space, in this case the origin of the cell, the Yee grid cell introduces a staggered placement. In Figure 2.6b, it can be seen that the electric and magnetic field components in the 3D Yee cell are offset, with the E-components staggered along the axis of the cell and the H-components along the faces.

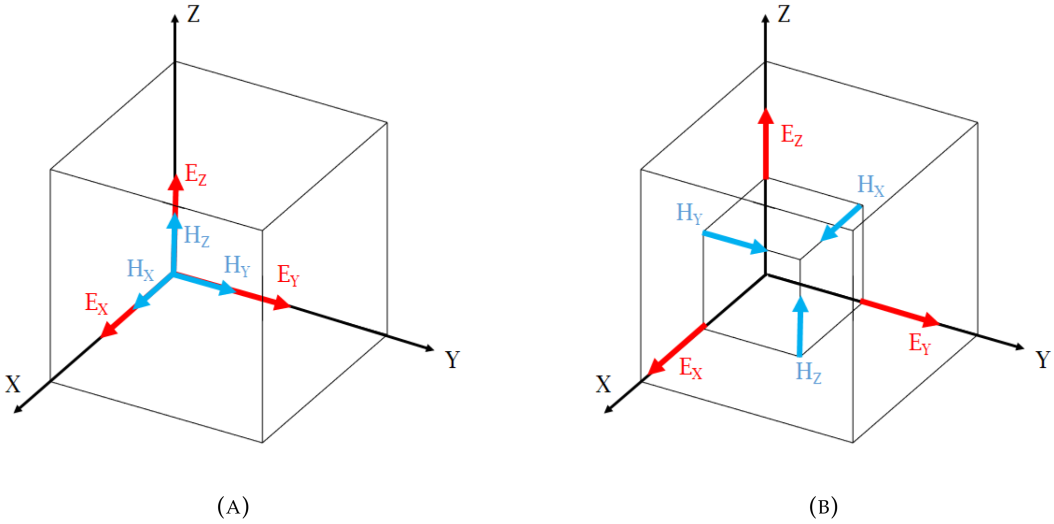

(A) (B)

FIGURE 2.6: The positions of the electromagnetic field components in cells from a a) collocated grid cell and b) Yee grid cell

This achieves several goals that help simplify the FDTD algorithm. Firstly, Yee cells are divergence free, that is $\nabla(\epsilon\vec{E}) = 0$ and $\nabla(\mu\vec{H}) = 0$. This can be seen from solving for the discrete divergence of the D field in the cell

$$\nabla D = \frac{(\epsilon_0 E_x(0) - \epsilon_{\Delta x} E_x(\Delta x))\Delta y \Delta z}{\Delta x \Delta y \Delta z} + \frac{(\epsilon_0 E_y(0) - \epsilon_{\Delta y} E_y(\Delta y))\Delta x \Delta z}{\Delta x \Delta y \Delta z} + \frac{(\epsilon_0 E_z(0) - \epsilon_{\Delta z} E_z(\Delta z))\Delta x \Delta y}{\Delta x \Delta y \Delta z}$$

Assuming there are no charges in the volume of the cell, $\epsilon_0 E_k(0) = \epsilon_{\Delta k} E_k(\Delta k)$ and $\nabla D = 0$. The divergence free condition of the H-field follows directly from Maxwell's equations and lack of single magnetic charges. As a material change can occur through a cell, each field component is assigned their own permitivity ϵ. The Yee cell configuration naturally satisfies the boundary conditions between two media, as shown in Figure 2.7, where the subscript "T" denotes the transverse component of the fields in relation to the boundary and "N" the normal component. k_T is the transverse component of the wavevector.

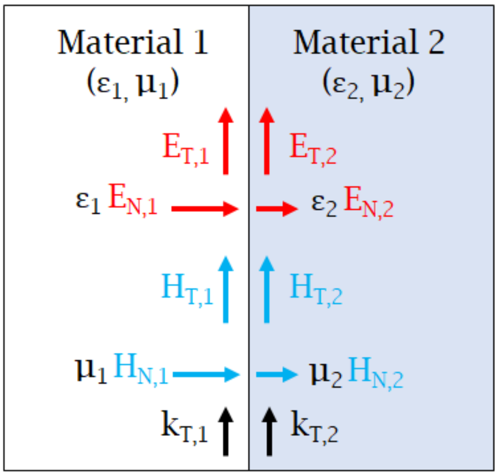

FIGURE 2.7: The Yee grid arrangement satisfying the physical boundary conditions

Finally, the staggered locations of the electric and magnetic fields provide an elegant geometric representation of the curl equations, as shown in Figure 2.8. This greatly simplifies their calculation.

The Update Equations

The FDTD algorithm uses discrete approximations of Maxwell's equations in a leapfrog type manner, where the coupled E and H fields for each point in the simulated space are computed and updated for each time step. The differential forms of

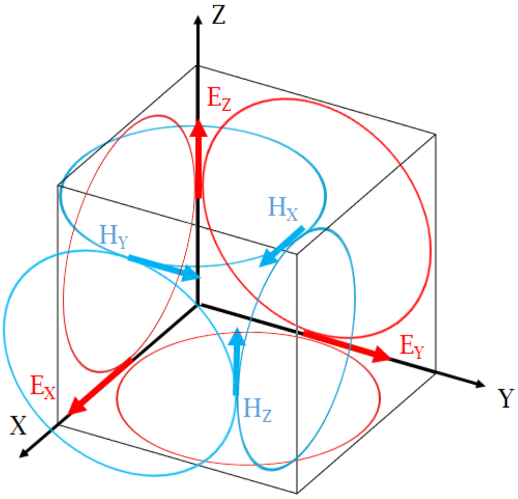

FIGURE 2.8: Intuitive representation of the curl equations on a Yee grid

Maxwell's equations are given by

$$\nabla.\boldsymbol{D} = \rho \tag{2.3}$$

$$\nabla.\boldsymbol{B} = 0 \tag{2.4}$$

$$\nabla \times \boldsymbol{E} = -\frac{\partial \boldsymbol{B}}{\partial t} \tag{2.5}$$

$$\nabla \times H = \boldsymbol{J} + \frac{\partial \boldsymbol{D}}{\partial t} \tag{2.6}$$

, where $\boldsymbol{D} = \epsilon \boldsymbol{E}$ and $\boldsymbol{B} = \mu \boldsymbol{H}$ for a linear, isotropic dielectric material. Since the Yee cell naturally satisfies the conditions of a divergenless field, the FDTD algorithm needs to only compute the bottom two curl equations. As there are no charges in the cell, the current density $\boldsymbol{J}$ will also be zero and the curl of the magnetic field strength is given by $\nabla \times H = \frac{\partial \boldsymbol{D}}{\partial t}$. The simulated space can be divided by a 3D mesh where the number of the cell in the x, y and z directions are indexed by i, j and k, respectively, as shown in Figure 2.9.

The time step is denoted by n, with n+1, n+2 etc. showing future time steps and n-1, n-2 etc. past time steps. The curl equations can be expanded into triplets (one

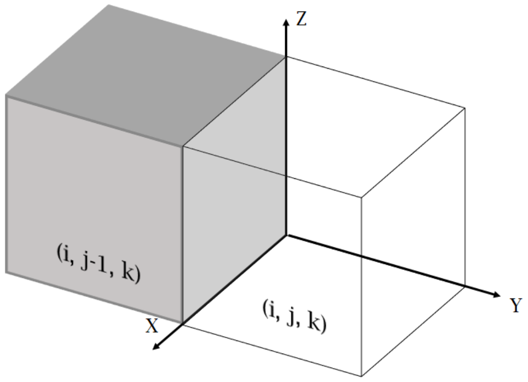

FIGURE 2.9: Index positions of the Yee cells used in the discrete update equations

partial differential equation for each dimension) and subsequently made discrete as follows

$$\nabla \times \boldsymbol{E} = -\frac{\partial \boldsymbol{B}}{\partial t}$$

$$\Downarrow$$

$$\frac{\partial E_x(t)}{\partial z} - \frac{\partial E_z(t)}{\partial x} = -\frac{\partial B_y(t)}{\partial t} \tag{2.7}$$

$$\frac{\partial E_y(t)}{\partial x} - \frac{\partial E_x(t)}{\partial y} = -\frac{\partial B_z(t)}{\partial t} \tag{2.8}$$

$$\frac{\partial E_z(t)}{\partial y} - \frac{\partial E_y(t)}{\partial z} = -\frac{\partial B_x(t)}{\partial t} \tag{2.9}$$

$$\Downarrow$$

$$\frac{E_x|^n_{i,j,k+1} - E_x|^n_{i,j,k}}{\Delta z} - \frac{E_z|^n_{i+1,j,k} - E_z|^n_{i,j,k}}{\Delta x} = B_y|^n_{i,j,k} - B_y|^{n+1}_{i,j,k} \tag{2.10}$$

$$\frac{E_y|^n_{i+1,j,k} - E_y|^n_{i,j,k}}{\Delta x} - \frac{E_x|^n_{i,j+1,k} - E_x|^n_{i,j,k}}{\Delta y} = B_z|^n_{i,j,k} - B_z|^{n+1}_{i,j,k} \tag{2.11}$$

$$\frac{E_z|^n_{i,j+1,k} - E_z|^n_{i,j,k}}{\Delta y} - \frac{E_y|^n_{i,j,k+1} - E_y|^n_{i,j,k}}{\Delta z} = B_x|^n_{i,j,k} - B_x|^{n+1}_{i,j,k} \tag{2.12}$$

Similarly for the magnetic field

$$\nabla \times \boldsymbol{H} = \frac{\partial \boldsymbol{D}}{\partial t}$$

$$\Downarrow$$

$$\frac{\partial H_x(t)}{\partial z} - \frac{\partial H_z(t)}{\partial x} = \frac{\partial D_y(t)}{\partial t} \tag{2.13}$$

$$\frac{\partial H_y(t)}{\partial x} - \frac{\partial H_x(t)}{\partial y} = \frac{\partial D_z(t)}{\partial t} \tag{2.14}$$

$$\frac{\partial H_z(t)}{\partial y} - \frac{\partial H_y(t)}{\partial z} = \frac{\partial D_x(t)}{\partial t} \tag{2.15}$$

$$\Downarrow$$

$$\frac{H_x|_{i,j,k}^{n+1} - H_x|_{i,j,k-1}^{n+1}}{\Delta z} - \frac{H_z|_{i,j,k}^{n+1} - H_z|_{i-1,j,k}^{n+1}}{\Delta x} = D_y|_{i,j,k}^{n+1} - D_y|_{i,j,k}^{n} \tag{2.16}$$

$$\frac{H_y|_{i,j,k}^{n+1} - H_y|_{i-1,j,k}^{n+1}}{\Delta x} - \frac{H_x|_{i,j,k}^{n+1} - H_x|_{i,j-1,k}^{n+1}}{\Delta y} = D_z|_{i,j,k}^{n+1} - D_z|_{i,j,k}^{n} \tag{2.17}$$

$$\frac{H_z|_{i,j,k}^{n+1} - H_z|_{i,j-1,k}^{n+1}}{\Delta y} - \frac{H_y|_{i,j,k}^{n+1} - H_y|_{i,j,k-1}^{n+1}}{\Delta z} = D_x|_{i,j,k}^{n+1} - D_x|_{i,j,k}^{n} \tag{2.18}$$

Equations 2.10 to 2.18 are called the update equations for the FDTD algorithm and they show how the fields in a cell are updated for each time step. In the general in-house FDTD engine implemented, the source used was a Gaussian pulse.

The source was injected using the total field - scatter field method (TFSF), where the volume after the source injection plane has the total field (including the source) and the volume behind the source only takes into account the scattered waves, excluding the source field.

It is worth noting that a correction factor needs to be included for the electric and magnetic fields in the two cells adjacent to the source injection plane, so the the cell in the total field volume contains only total field terms and the cell in the scattered field contains only scattered field terms. This is done by subtracting the source term

Device composition	N
Low-contrast dielectrics	1-20
High-contrast dielectrics	20-30
Most metallic structures	40-60
Plasmonic devices	100-200

TABLE 2.2: Empirical values for N for different simulated materials

in the scattered field cell and adding it in the total field cell.

Stability and Convergence

Two important aspects for achieving correct results through numerical analysis are stability and convergence. Numerical stability in the context of differential equations refers to the solution errors being bounded. A numerically unstable simulation would amplify the solution errors beyond a bounded region [26]. Convergence is the measure of a simulation reaching (or converging) to the true result. It is not possible to remove all sources of numerical error, but rather determine an acceptable level of error required from the simulation. The correct grid resolution in both time and space is crucial for achieving both stability and convergence. The maximum time step is determined by the Courant- Friedrich-Lewy (CFL) condition, ensuring that the speed of a physical wave cannot travel faster than the numerical speed of the wave. This was implemented in our FDTD engine by setting the time step Δt as

$$\Delta t < \frac{n_0}{c_0}\sqrt{\frac{1}{\Delta x}^2 + \frac{1}{\Delta y}^2 + \frac{1}{\Delta z}^2}$$

, where n_0 is the smallest refractive index in the simulation, and $\Delta x, \Delta y$ and Δz are the smallest grid steps in their respective dimensions.

The maximum grid resolution takes into account both the smallest wavelength and the smallest feature that will need to be resolved, and takes the minimum of the two, $\Delta u = \min\left[\frac{\lambda_{min}}{N}, \frac{d_{min}}{M}\right]$. Experimentally it was determined that the following values achieve good results and could be used as a starting point for simulating different materials and devices 2.2.

The value of M is also determined experimentally, depending on the problem, but 5-10 is a good starting point.

Boundary conditions

The most common type of boundary condition necessary for the implementation of 1D FDTD is a perfectly absorbing boundary condition. This prevents reflections off the boundaries of the grid and is equivalent to waves going off to infinity after reaching the end of the simulation volume.

For a 1D FDTD simulation, in our engine that was implemented by setting the time step Δt, such that the waves at both boundaries travel a single cell in exactly two time steps, or

$$\Delta t = \frac{n_b \Delta z}{c_0}$$

, where n_b is the refractive index at both boundaries. The fields at the boundary cells are then the same as the fields in the previous cell two time steps ago. This definition of the time step also satisfies the Courant stability.

For a 2D or a 3D simulation, the absorbing boundary condition implemented was a perfectly matched layer (PML). This was achieved using the uniaxial PML method (UPML) , which although a bit outdated in respect to the stretched-coordinate PML method (SC-PML), offers similar performance and is simpler and quicker to implement. The boundary material was defined as a doubly-diagonally anisotropic lossy material, such that the impedance of it remains the same as that of the simulation volume, in order to prevent reflections off the boundaries. The permitivity and permeability in the frequency domain of the boundary material becomes

$$[\epsilon_b] = [\epsilon_r][s] \tag{2.19}$$

$$[\mu_b] = [\mu_r][s] \tag{2.20}$$

, where $[s]$ is the impedance transformation matrix of the PML, defined as

$$[s] = \begin{bmatrix} \frac{s_y s_z}{s_x} & 0 & 0 \\ 0 & \frac{s_x s_z}{s_y} & 0 \\ 0 & 0 & \frac{s_x s_y}{s_z} \end{bmatrix} \tag{2.21}$$

The real part of the refractive index of the boundary material was set as 1 and the conductivity σ (the introduced loss) was chosen to follow a cubic dependency along the thickness L of the boundary (a harsh cut-off in conductivity between the environment and boundary materials would lead to reflections). For any Cartesian coordinate $u = x, y, z$

$$s_u(u) = 1 + \frac{\sigma_u(u)}{jw\epsilon_0} \tag{2.22}$$

$$\sigma_u(u) = \frac{\epsilon_0}{2\Delta t}\left(\frac{u}{L_u}\right)^3 \tag{2.23}$$

The introduction of the UPML is in the frequency domain and the FDTD equations are in the time-domain, therefore they need to be updated to include the UPML and inverse fourier transformed into the final update equations.
A periodic boundary condition option was also implemented in the FDTD engine, in order to simulate periodic structures. The field values outside the grid in a given direction are just taken as the field values already calculated from the opposite end of the grid, so the effects on the total field are as if the simulated cell is being infinitely repeated.

Reducing Sources of Error

Errors from Windowing

An FDTD simulation cannot be run for an infinite amount of steps, therefore a finite time window is applied, leading to some of the spectral information to be lost due to "blurring". According to the Nyquist-Shannon sampling theorem [27], the maximum frequency resolution (Δf) we can achieve is proportional to the number of time steps in the simulation, and for devices with sharp resonances, this has to be accounted for. The number of time steps N_{steps} has to be chosen so that

$$N_{steps} \geq \frac{1}{\Delta t \Delta f} \tag{2.24}$$

Staircasing Effect

For uniform square meshes, as the one used in our FDTD engine, device geometries would more often than not, not snap perfectly to the grid cells (this can be achieved with very fine meshes, but this is computationally cumbersome). Rounding to the closest integer number of cells can lead to large errors. Better results and faster convergence times can be achieved through dielectric smoothing of the device materials. This can be simply implemented by taking a weighted average of the refractive index on the partially filled edge cells, as shown in Figure 2.10. There are more complicated and involved types of dielectric smoothing, which achieve better results by introducing anisotropy in the device materials. This introduces non-trivial changes to the update equations, especially for complicated device shapes and was out of the scope of this light-weighted FDTD engine. Grid dispersion errors arise from the fact that the wavenumber of waves propagating along the grid does not linearly depend on their frequency, they travel at different numerical speeds. This is generally combated either by reducing the grid resolution, or by employing higher-order approximations for the discrete differential equations. [28]

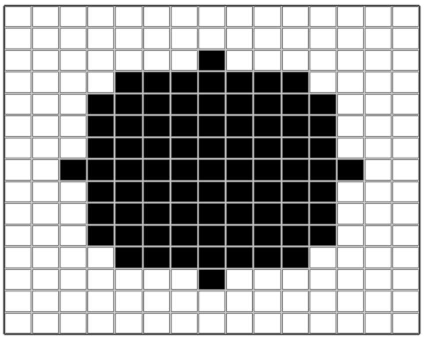

(A) A circular dielectric material on a 2D grid without smoothing

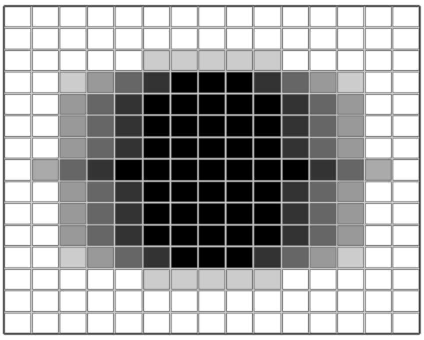

(B) A circular dielectric material on a 2D grid with Laplacian smoothing applied

FIGURE 2.10: Visual representation of dielectric smoothing on a circular geometry

2.3.2 Explicit Computations

The FDTD approach is well-suited to a diverse range of problems, however there are certain drawbacks. It can be computationally intensive and require long calculation times and substantial memory, in order to simulate large simulation volumes. Furthermore, caution should be taken in order to reduce the error as a result of numerical approximations to a desired amount (e.g. less than the expected measurement error) and that the simulation setup doesn't lead to erroneous artifacts. It is good practice, where reasonably possible, to verify results with an explicit, or analytical model as a complimentary approach to FDTD. Such models generally take very little computation time, but are less flexible in terms of problem definition and can usually be applied to more simple, symmetric geometries. Here we present the development of a dielectric stack transmission and reflection model, which can quickly solve the ideal transmission and reflection spectra for any N-layered stratified media.

Transmission and Reflection Coefficients of Stratified Media

Single layer coefficients

Firstly, the propagation of electromagnetic waves through a "sandwich" of three media with complex refractive indexes will be introduced. The refractive indexes are denoted n_1, n_2 and n_3, and the middle material thickness d, as shown in Figure 2.11. The source is a linearly polarized plane wave, incident on the first boundary with an angle of incidence θ_i. The angle of the transmitted wave into medium 2 is θ_t, and the angle of the transmitted wave into medium 3 is $\theta_t 1$. The angles of reflection are equal to the angles of incidence $\theta_i = \theta_r$, and the angles of transmission follow Snell's law, as follows:

$$n_1 \sin(\theta_i) = n_2 \sin(\theta_t) \tag{2.25}$$

The amplitude transmission and reflection coefficients of the electric field from medium A to medium B are defined as T_{AB} ,R_{AB} at $z = 0$ and T_{ABd} , R_{ABd} at $z = d$. The subscripts s and p would are used to denote S and P polarisation respectively.

From the Fresnel equations for the amplitude coefficients, for the S polarization of the electric field, the following equations can be written:

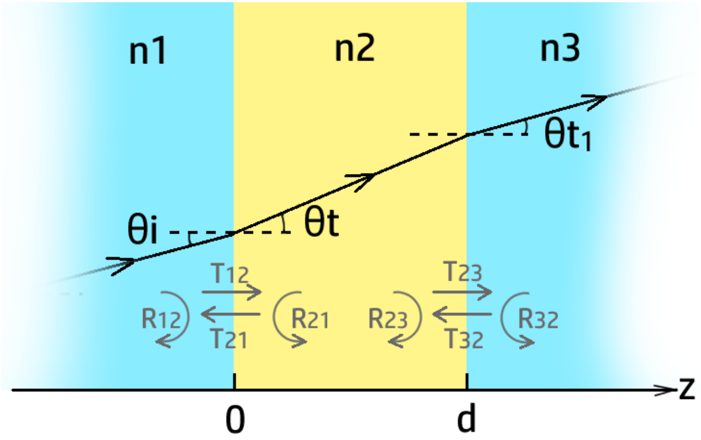

FIGURE 2.11: Illustrated wave propagation through a "sandwich" of three media.

At $z = 0$

$$R_{12s} = \frac{n_1\cos(\theta_i) - n_2\cos(\theta_t)}{n_1\cos(\theta_i) + n_2\cos(\theta_t)} \tag{2.26}$$

$$R_{21s} = -R_{12s} \tag{2.27}$$

$$T_{12s} = \frac{2n_1\cos(\theta_i)}{n_1\cos(\theta_i) + n_2\cos(\theta_t)} \tag{2.28}$$

$$T_{21s} = \frac{2n_2\cos(\theta_t)}{n_1\cos(\theta_i) + n_2\cos(\theta_t)} \tag{2.29}$$

$$R_{12p} = \frac{n_2\cos(\theta_i) - n_1\cos(\theta_t)}{n_2\cos(\theta_i) + n_1\cos(\theta_t)} \tag{2.30}$$

$$R_{21p} = -R_{12p} \tag{2.31}$$

$$T_{12p} = \frac{2n_1\cos(\theta_i)}{n_2\cos(\theta_i) + n_1\cos(\theta_t)} \tag{2.32}$$

$$T_{21p} = \frac{2n_2\cos(\theta_t)}{n_2\cos(\theta_i) + n_1\cos(\theta_t)} \tag{2.33}$$

At $z = d$ the Fresnel equations are modified to accommodate for the change of phase, as the wave has traveled through a finite medium. This will be simplified to the case of normal incidence on the boundary, where the expressions for P and S polarisation are identical. Due to continuity at the second boundary at $z = d$ for two dielectric media, for the electric and magnetic fields in each medium, it can be written respectively

$$\boldsymbol{E}_2(d) = \boldsymbol{E}_3(d) \tag{2.34}$$

and

$$\boldsymbol{H}_2(d) = \boldsymbol{H}_3(d) \tag{2.35}$$

From Maxwell's equations the relationship between the amplitudes of the electric and magnetic field is

$$E = \frac{-\boldsymbol{k} \times \mu H}{n}, \tag{2.36}$$

where n is the refractive index of the medium and $\boldsymbol{k}$ is the directional vector of the wave propagation. Assuming that the media of interest are non-magnetic and μ is 1, as well as that the electric field in a medium is the sum of an incident forward wave and a reflected backward wave, the field in media 2 and 3 can be represented as

$$\boldsymbol{E}_2 = E_i e^{-j\beta_2 z} + E_r e^{j\beta_2 z} \tag{2.37}$$

$$\boldsymbol{E}_3 = E_t e^{-j\beta_3 z} \tag{2.38}$$

And similarly for the magnetic field, substituting with equation 2.36

$$\boldsymbol{H}_2 = n_2 E_i e^{-j\beta_2 z} - n_2 E_r e^{j\beta_2 z} \tag{2.39}$$

$$\boldsymbol{H}_3 = n_3 E_t e^{-j\beta_3 z}, \tag{2.40}$$

where β_2 and β_3 are the propagation constants in medium 2 and 3 respectively. Substituting these expressions in equations 2.34 and 2.35, with $z = d$ gives

$$E_i e^{-j\beta_2 d} + E_r e^{j\beta_2 d} = E_t e^{-j\beta_3 d} \tag{2.41}$$

$$n_2 E_i e^{-j\beta_2 d} - n_2 E_r e^{j\beta_2 d} = n_3 E_t e^{-j\beta_3 d} \tag{2.42}$$

After re-arrangement, the expressions for the amplitude transmission and reflection coefficients at $z = d$, defined by $T = E_t/E_i$ and $R = E_r/E_i$ become

$$T = \frac{2n_2}{n_2 + n_3} e^{-j(\beta_2 - \beta_3)d} \tag{2.43}$$

$$R = \frac{n_2 - n_3}{n_2 + n_3} e^{-j2\beta_2 d} \tag{2.44}$$

Expressions 2.43 and 2.44 can be interpreted as the phase retardation that the wave experiences as it bounces between the boundaries of the material. The transmitted wave goes through the material only once, whereas the reflected wave bounces and travels through the thickness of the material twice.

For an oblique incidence of θ_i, the spatial distribution of the phase for both P and S polarisations is represented by

$$e^{-j\beta_1 (x \sin(\theta_i) + z \cos\theta_i)} \tag{2.45}$$

valid for every x. Substituting 2.45 in equations 2.43 and 2.44 gives

$$T_{23s} = \frac{2n_2 \cos(\theta_t)}{n_2 \cos(\theta_t) + n_3 \cos(\theta_{t1})} e^{-j(\beta_2 \cos(\theta_i) - \beta_3 \cos(\theta_t))d} \tag{2.46}$$

$$R_{23s} = \frac{n_2 \cos(\theta_t) - n_3 \cos(\theta_{t1})}{n_2 \cos(\theta_t) + n_3 \cos(\theta_{t1})} e^{-j2\beta_2 d \cos(\theta_i)} \tag{2.47}$$

$$T_{23p} = \frac{2n_2 \cos(\theta_t)}{n_3 \cos(\theta_t) + n_2 \cos(\theta_{t1})} e^{-j(\beta_2 \cos(\theta_i) - \beta_3 \cos(\theta_t))d} \tag{2.48}$$

$$R_{23p} = \frac{n_3 \cos(\theta_t) - n_2 \cos(\theta_{t1})}{n_3 \cos(\theta_t) + n_2 \cos(\theta_{t1})} e^{-j2\beta_2 d \cos(\theta_i)} \tag{2.49}$$

This leads to an expression for the complete amplitude reflection and transmission coefficients of the system of all 3 media, taking into account infinite bouncing between the two boundaries at $z = 0$ and $z = d$. For every bounce between the boundaries, the phase of the wave will retard by $e^{-j2\beta_2 d\cos(\theta_i)}$. The total transmission is therefore

$$T = T_{12}T_{23} + T_{12}R_{23}R_{21}T_{23} + T_{12}{R_{23}}^2{R_{21}}^2T_{23} + T_{12}{R_{23}}^3{R_{21}}^3T_{23} + ... \tag{2.50}$$
$$= \frac{T_{12}T_{23}}{1 - R_{23}R_{21}},$$

and the total reflection

$$R = R_{12} + T_{12}R_{23}T_{21} + T_{12}R_{23}R_{21}R_{23}T_{21} + ... \tag{2.51}$$
$$= R_{12} + \frac{T_{12}R_{23}T_{21}}{1 - R_{23}R_{21}} = \frac{R_{12} + R_{23}}{1 - R_{23}R_{21}}.$$

N-layer Coefficients

The expressions derived so far for multiple layers of dielectric slabs of finite thickness need to be expanded, starting with a stratified medium of two finite thickness slabs between two semi-infinite materials as shown in Figure 2.12a. This can be broken down as the interaction between two single slabs as represented in Figure 2.12b. The expression for a single slab has already been derived, however applying it directly in this case will lead to counting every transition between the two slabs twice - once as part of the expression for the first slab and once as part of the second. Therefore, an adjusted expression for each individual slab will be used, which represents a wave path originating in the slab in question and exiting it, either as a transmitted wave in the positive z-direction, or as a reflected wave in the negative z-direction. This is illustrated in Figure 2.12c. Defining $t_{i(i+1)}$ as the transmission coefficient of the interface between media "i" and media "i+1", including the phase delay from media "i", $e^{-j\beta_i d_i}$. Here d_i is the thickness of the media. Similarly $r_{i(i+1)}$ is the reflection coefficient of the same interface, which includes the phase delay $e^{-2j\beta_i d_i}$. $t^0_{i(i+1)}$ and $r^0_{i(i+1)}$ are defined as the transmission and reflection between the same interface but with no phase delay. For instance, following equations 2.46-2.49, the expressions for the interface between media 1 and media 2 become

$$t^0_{12} = \frac{2n_2}{n_1 + n_2} \tag{2.52}$$

$$t_{12} = \frac{2n_2}{n_1 + n_2} e^{-j\beta_2 d_2} \tag{2.53}$$

$$r^0_{12} = \frac{n_1 - n_2}{n_1 + n_2} \tag{2.54}$$

$$r_{12} = \frac{n_1 - n_2}{n_1 + n_2} e^{-2j\beta_2 d_2} \tag{2.55}$$

The adjusted expressions for a single finite slab of dielectric in a stratified media with refractive indexes n(i), n(i+1) and n(i+2) respectively, would be:

$$T_i = \frac{t_{(i+1)(i+2)}}{1 - 1 - r^0_{(i+1)i} r_{(i+1)(i+2)}} \tag{2.56}$$

$$R_i = \frac{r_{(i+1)(i+2)} t^0_{(i+1)i}}{1 - r^0_{(i+1)i} r_{(i+1)(i+2)}} \tag{2.57}$$

Since there are reflected waves that interact with the dielectric slab, propagating in the negative z-direction, the same expressions are needed for the reverse medium order n(i+2), n(i+1), n(i), as shown in Figure 2.12d. These are

$$T^{rev}_i = \frac{t_{(i+1)i}}{1 - r_{(i+1)i} r^0_{(i+1)(i+2)}} \tag{2.58}$$

$$R^{rev}_i = \frac{r_{(i+1)i} t^0_{(i+1)(i+2)}}{1 - r_{(i+1)i} r^0_{(i+1)(i+2)}} \tag{2.59}$$

In T_i and R_i the index "i" represents the number of the finite dielectric slab excluding the two semi-infinite media. The expression for the total transmission and reflection amplitude coefficients for a system of two finite slabs then becomes

$$T_{TOT} = \frac{t^0_{12} T_1 T_2}{1 - R^{rev}_1 R_2} \tag{2.60}$$

$$R_{TOT} = r^0_{12} + t^0_{12} R_1 + \frac{t^0_{12} T_1 T^{rev}_1 R_2}{1 - R^{rev}_1 R_2} \tag{2.61}$$

$$T_{TOT}^{rev} = \frac{t_{43}^{0} T_1^{rev} T_2^{rev}}{1 - R_1^{rev} R_2} \tag{2.62}$$

$$R_{TOT}^{rev} = r_{43}^{0} + t_{43}^{0} R_2^{rev} + \frac{t_{43}^{0} T_2^{rev} T_2 R_1^{rev}}{1 - R_1^{rev} R_2} \tag{2.63}$$

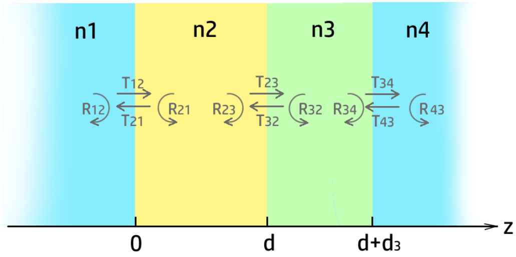

(A) Stratified media of two finite dielectric slabs

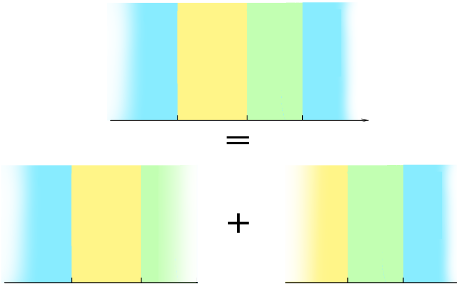

(B) Stratified media of two finite dielectric slabs represented as a function of two single slab systems

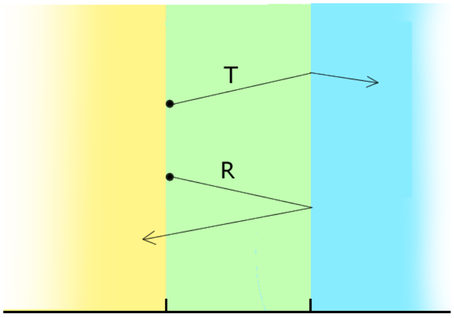

(C) The transmitted and reflected wave paths represented in the adjusted equations for a single dielectric slab

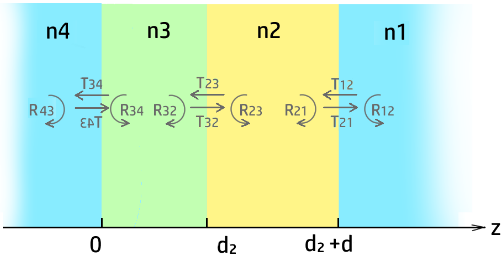

(D) Reverse wave propagation diagram

FIGURE 2.12: Diagrams of systems of dielectric slabs and their respective wave paths.

The analytical expression of any N-layered dielectric system can now be recursively found by using the algorithm, shown in Figure 2.13.

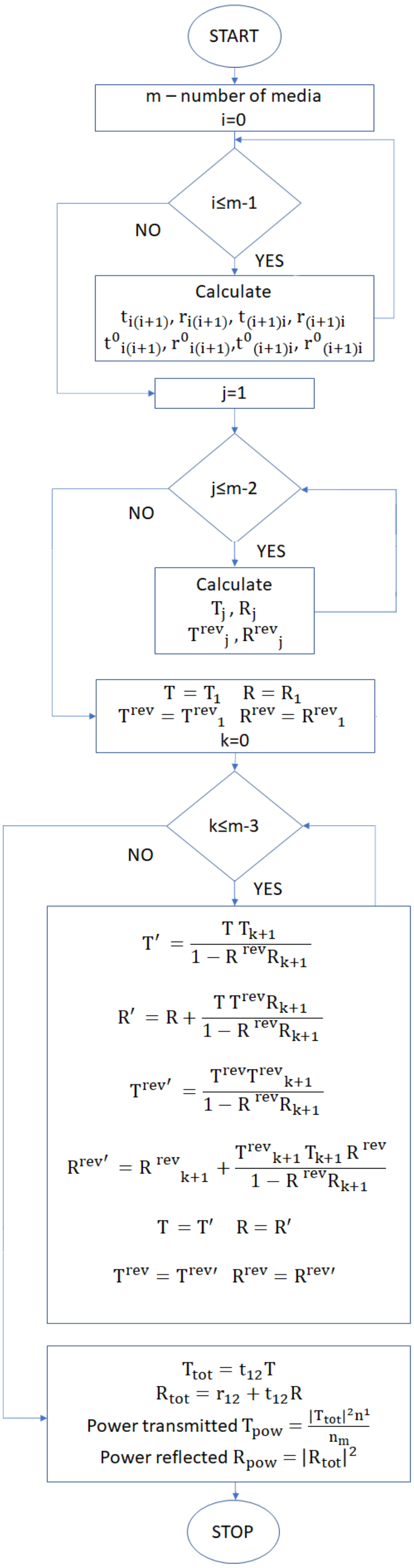

FIGURE 2.13: Algorithm for calculating the power transmission and reflection coefficients T_{pow} and R_{pow} in a system of m stratified dielectric media.

The analytical model presented so far assumes linear, isotropic dielectric media in a single dimension. In order for it to compute more realistic THz devices, introducing losses and dispersion, the dielectric response of each material is included, according to the Lorentz model [29]. This can also be used to model metals, as the Drude model is a special case of the Lorentz model. The complex refractive index of any media as a function of frequency is then given in the form

$$n(w)^2 = 1 + \frac{w_p^2}{w^2 + i\gamma w + w_o^2} \tag{2.64}$$

Here w_p is the plasma frequency, w_o is the natural frequency and γ is the dissipation constant at the natural frequency of the material. For metals, this can be simplified to

$$n(w)^2 = 1 + \frac{w_p^2}{w^2} \tag{2.65}$$

Fully anisotropic materials can be also computed by specifying the nine values of the second order refractive index tensor, given by

$$\begin{bmatrix} n_{xx} & n_{xy} & n_{xz} \\ n_{yx} & n_{yy} & n_{yz} \\ n_{zx} & n_{zy} & n_{zz} \end{bmatrix}$$

Using equation 2.64 to model resonant materials, these can be incorporated in the analytical solutions for the transmission and reflection in stratified media. The real and imaginary parts of the permitivity of a lorentzian material with a resonant frequency of 0.8 THz are plotted in Figure 2.14.

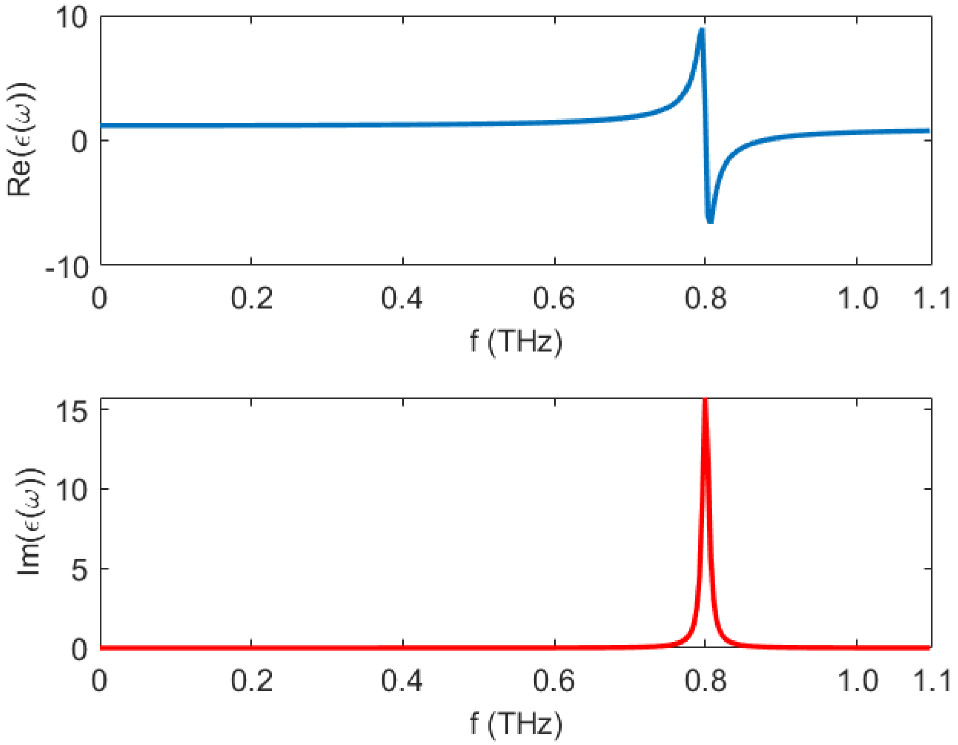

FIGURE 2.14: Real and imaginary parts of a lorentzian material with a resonant frequency at 0.8 THz

When using the stratified model both the refractive index and the thickness of the layer need to be defined. The effective thickness chosen for a resonant material layer has an effect on its transmission and reflection response. As shown in Figure 2.15, if the layer is too optically thin, the resonance Q-factor is reduced. When the layer is chosen to be too thick, broadening of the response, as well as ripple artifacts appear. This effect must be considered for accurate modeling.

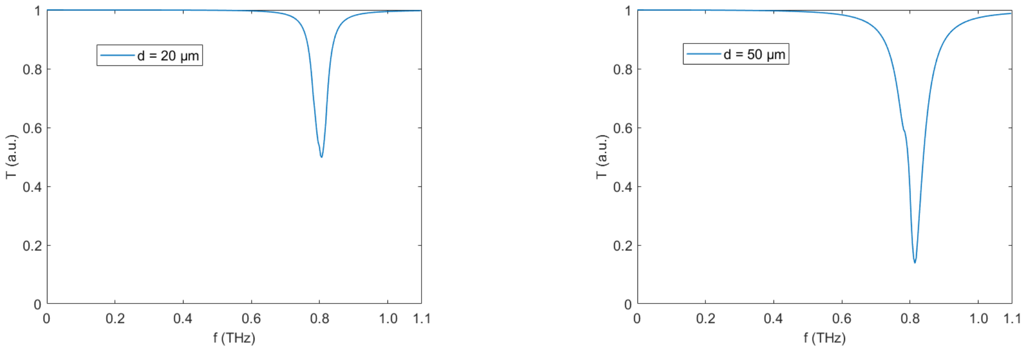

(A) d = 20 μm (B) d = 50 μm

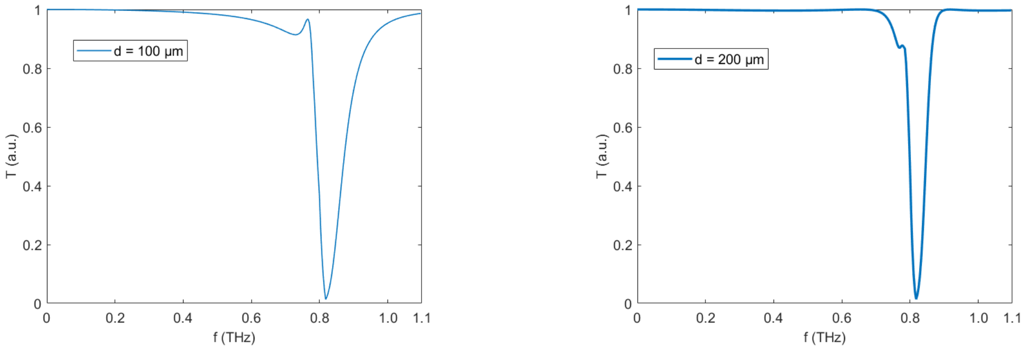

(C) d = 100 μm (D) d = 200 μm

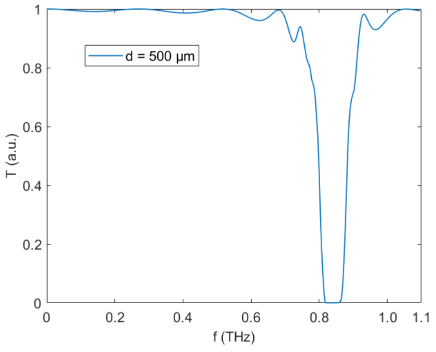

(E) d = 500 μm

FIGURE 2.15: Change in transmission of lorentzian medium with varying effective optical thickness

Extraction of Effective Material Parameters

Any linear, isotropic, homogeneous material can be represented for the purposes of macroscopic electrodynamic computations, by its effective parameters e_{eff} and μ_{eff}, which are respectively the effective permittivity and effective permeability of the bulk material. Both of these parameters are represented by continuous functions of frequency [30]–[33]. Often, it is necessary to solve the inverse problem, where the S-parameters (the transmission and reflection spectra) of a slab of material are given, and we would like to extract the effective permeability and permittivity. These are related to the effective complex refractive index n_{eff} and impedance z_{eff} of the material as follows:

$$n_{eff} = \sqrt{\epsilon\mu} \tag{2.66}$$

$$z_{eff} = \sqrt{\frac{\mu}{\epsilon}} \tag{2.67}$$

Rewriting equations 2.50 and 2.51 in terms of n_{eff} and z_{eff} gives

$$T = \frac{(1 - (\frac{z_{eff}-1}{z_{eff}+1})^2)e^{-jn_{eff}kd}}{1 - (\frac{z_{eff}-1}{z_{eff}+1})^2 e^{-j2n_{eff}kd}} \tag{2.68}$$

$$R = \frac{(\frac{z_{eff}-1}{z_{eff}+1})(1 - e^{-j2n_{eff}kd})}{1 - (\frac{z_{eff}-1}{z_{eff}+1})^2 e^{-j2n_{eff}kd}}, \tag{2.69}$$

where k is the free-space wavenumber. Rewriting one more time gives the expressions for the effective refractive index and wave impedance as functions of T and R:

$$z_{eff} = \pm\sqrt{\frac{(1+R)^2 - T^2}{(1-R)^2 - T^2}} \tag{2.70}$$

$$n_{eff} = \frac{-j}{kd} ln \left(\frac{R}{1 - T(\frac{z_{eff}-1}{z_{eff}+1})} \right) \tag{2.71}$$

The imaginary part of the complex wave impedance and the real part of the complex refractive index for passive materials has to be a positive value [34], which determines the sign of the solution of 2.70. The explicit expressions for the real (n′) and imaginary part (n") are then given by:

$$n' = \frac{1}{kd} im \left(ln \left(\frac{R}{1 - T\left(\frac{z-1}{z+1}\right)} \right) \right) + \frac{2m\pi}{kd} \tag{2.72}$$

and

$$n'' = \frac{-1}{kd} Re \left(ln \left(\frac{R}{1 - T\left(\frac{z-1}{z+1}\right)} \right) \right), \tag{2.73}$$

where m is the branch index of the multivaried logarithmic function [30], [31], [34]. For optically thin slabs of material, m can be set to 0. For large values of d however, the uncertainty of the choice of m can lead to ambiguity in the effective refractive index expressions. Several methods have been proposed to overcome this problem. The real and imaginary parts of the complex refractive index are not independent and are related by the Kramer-Kronig (K-K) relationship [35]. This can be used to extract the correct values for m, such as in methods proposed by the authors in [31]. In practice there is a limitation to the correct extraction of the effective refractive index parameters through these methods, due to the necessary truncations in the upper frequency limits when computing K-K integrals and a saturation of the method that occurs at a maximum kd value of about 3.17. Therefore, the method for computing m was chosen in favour of a data driven discontinuity detection algorithm proposed in [34]. Since e_{eff} and μ_{eff} have to be continuous as functions of frequency, the algorithm selects the correct solution branch by preserving the continuity of n'. For the discrete real part of the refractive index $n'(f_i)$ as a function of the discrete frequency points f_i, the break points $D(f_i)$ in the refractive index function are given by

$$D(f_i) = \frac{n'(f_i) - n'(f_{i-1})}{f_i - f_{i-1}} \tag{2.74}$$

The value of m is then determined by the condition

$$m_i = \begin{cases} Round\left[(n'(f_{i-1}) - n'(f_i))\frac{kd}{2\pi}\right] & \text{for } |D(f_i)| = |q(f_i)| \\ 0 & \text{otherwise,} \end{cases} \tag{2.75}$$

where $m_0 = 0$ is the low frequency branching number and $i = 1, 2, 3...N$, N being the number of discrete frequency points in the data. The branching value $q(f_i)$ is given by

$$q(f_i) = \frac{2n'(f_{i-1})}{f_i - f_{i-1}} \tag{2.76}$$

and the final value of the branching index m is given by the summation of branching at all points

$$m = \sum_{i=0}^{N-1} m_i \tag{2.77}$$

Since most real-life spectroscopy measurements do not start at a frequency of

0, the lowest frequency branching number m_0 has to be chosen with caution. To demonstrate, the above algorithm is tested to extract the refractive index from the computed S-parameters for a single uniform slab of thickness 100 μm and the refractive index of Si, 3.42. Firstly the algorithm [1] is run with data, which is generated for a frequency spectrum from 0 - 1.1 THz and then on truncated data with a spectrum from 0.28 - 0.9 THz. As seen in Figure 2.16, in the first case the algorithm converges on the correct refractive index, however it shows big errors when given truncated data.

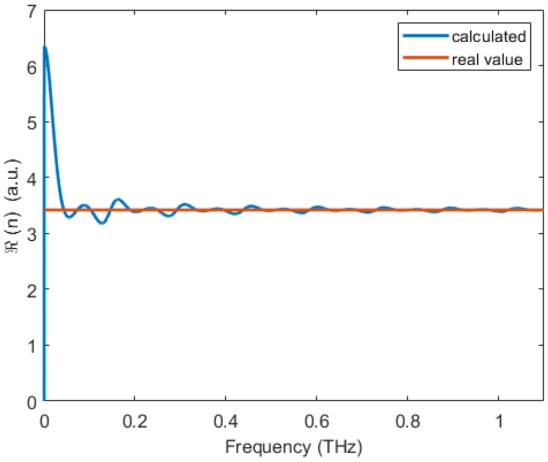

(A) Extracted real part of the refractive index for input data with frequency spectrum starting from 0

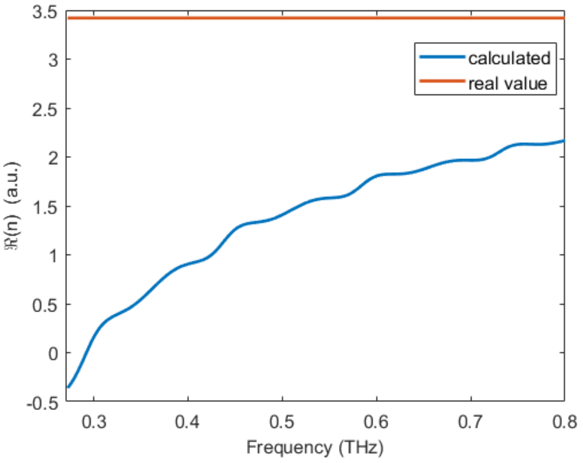

(B) Extracted real part of the refractive index for input data with truncated frequency spectrum

FIGURE 2.16: Comparison of results obtained from effective optical parameters extraction algorithm with generated data when using full spectrum and truncated spectrum.

---

[1] This approach is later used to extract the complex optical parameters in metamaterials in Chapter 4

Comparison between Computation Methods

Next, results obtained by the different computational electrodynamics methods previously presented will be compared by simulating the same device. A Distributed Bragg Reflector (DBR), also known as a Bragg mirror, is a commonly used reflector in waveguides. It is a periodic structure of alternating dielectric slabs of material with a different refractive index. The periodic variation of the refractive index causes multiple reflections on the interfaces of the device, which can be designed to interfere constructively to create a frequency stop band, thus acting as a high reflecting mirror. This is achieved when the optical path of each dielectric layer nd (where n is the refractive index and d is the thickness of that layer) is a quarter of the stop band center wavelength in vacuum, or $nd = \lambda/4$. An inexpensive and easy to manufacture THz Bragg mirror centered at 0.25 THz can designed by alternating layers of polymer (such as PLA, ABS, PDMS etc.) with air gaps between them, as shown in Figure 2.17. The refractive index of the polymer in the THz range is assumed to be 1.5, which is a close approximation to most common polymers in this frequency band. The thickness of the slabs d is 200μm and the spacing between them d_1 is 300μm. The stop band reflection increases with the increase in the number of pairs of layers N. Here this is set to $N = 20$.

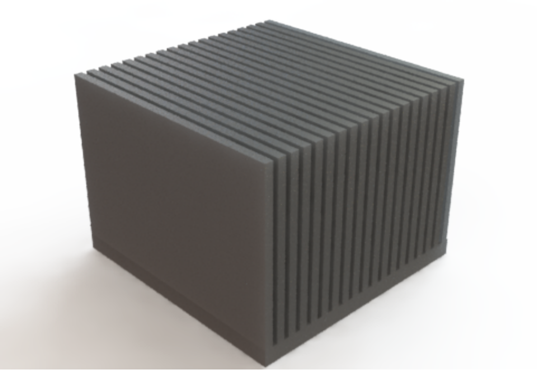

(A) Isometric view

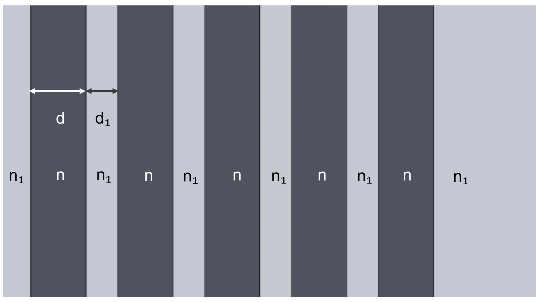

(B) THz Bragg reflector dimensions and material parameters

FIGURE 2.17: 3-D printable THz Bragg reflector

The structure in Figure 2.17 is simulated using four methods - the in-house FDTD engine described earlier, the commercial FDTD software Lumerical using both a full-wave and a proprietary stack function, and the explicit method discussed in 2.18a. All three computations are run with the same frequency resolution of 800 frequency points over the band 0 - 1.1 THz.

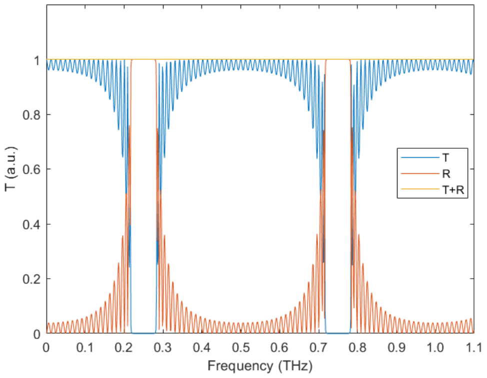

(A) Explicit method

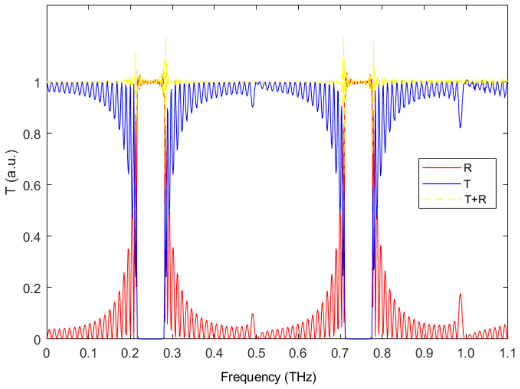

(B) 1-D Matlab FDTD

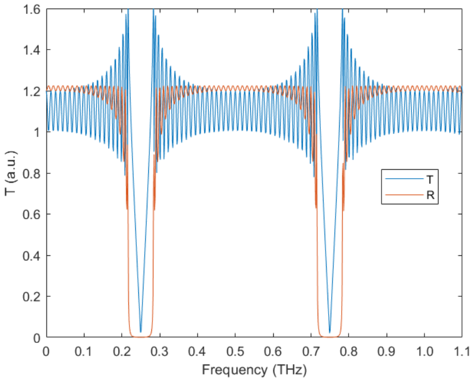

(C) Lumerical STACK

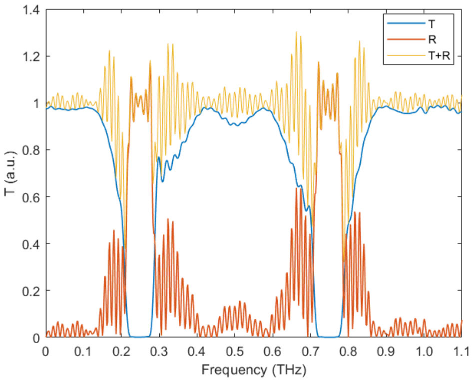

(D) Lumerical FDTD

FIGURE 2.18: Transmission and reflection spectra calculated with different numerical methods for a THz Bragg reflector

It can be seen in Figure 2.18, that all methods predict stop bands of zero transmission between 0.2 - 0.3 THz and 0.7-0.8 THz on average, with a variation of 0.1 % . The explicit method (Figure 2.18a) exhibits 100% convergence, as the reflected and transmitted power in all frequencies add to 1. The Lumerical model used in Figure 2.18c was the "STACK" optical solver, which provides a quick solution to dielectric stack problems using the analytic transfer matrix method [36]. It shows a correct envelope for the transmission spectra, but exhibits poor convergence, with both transmission and reflection coefficients reaching values above 1. Both FDTD simulations shown in Figure 2.18b and 2.18d used simulation times of over 50000 fs, ensuring there is close to no energy left in the system and stability is achieved. The in-house FDTD used a uniform mesh, whereas the Lumerical simulation used a non-uniform autogenerated mesh. Both simulations used PML boundary conditions. The convergence of the Lumerical simulation is a worse than the in-house FDTD engine, both exhibiting uncertainty around the sharp edges of the stop bands. Increasing the mesh resolution would mitigate these effects, while also increasing the cost of computing time. The differences between the two results could also originate from the definition of the plane wave sources illuminating the Bragg mirror. The BFAST plane wave source was used in the Lumerical simulation, which is known to be more numerically unstable. Commercial FDTD solvers, such as Lumerical are powerful tools and offer many different options for simulating a wide range of devices. However, caution should be exercised when analyzing the results of more complicated systems and verification through a more simplified FDTD solver, such as the one presented earlier, as well as analytical computation where possible, should be implemented.

2.3.3 Fabrication Methods

Several fabrication techniques were used to prepare samples for the purpose of the presented research. For the fabrication of metamaterials, grid polarisers and thin films, photolithography was used. Laser cutting, 3D printing and casting methods were utilised for bulk polymer samples.

Photolithography

Photolithography is a standard microfabrication method, which transfers images from a photomask onto thin films. This is achieved through a photosensitive layer, called photoresist. There are two types of photoresist - positive and negative, which determines whether the shadowed, or transparent pattern of the mask is transferred. A typical lift-off process using positive photoresist for the microfabrication of metallic features is shown in Figure 2.19. During the exposure stage, the photoresist is illuminated by UV light. For positive photoresists, the UV-illuminated get dissolved by the chemical treatment in the development stage, whereas for negative photoresists, the illuminated areas become cross-linked, so they are not affected by the developer. A lift-off process was favoured for the fabrication of small metallic features, as it was found to achieve better results with fewer defects. The main negative photoresist used in this thesis was SU-8 2000 series [37], which is an epoxy based resist. It is suitable for both thin (10 µm) and thick (100 µm) layer depositions. The positive photoresist used was Microposit S1813 [38], designed for layer thicknesses of up to 1.5 µm. The recipes used for spin coating, baking, exposure rates, post exposure bake and development can be seen in A and A in the Appendix.

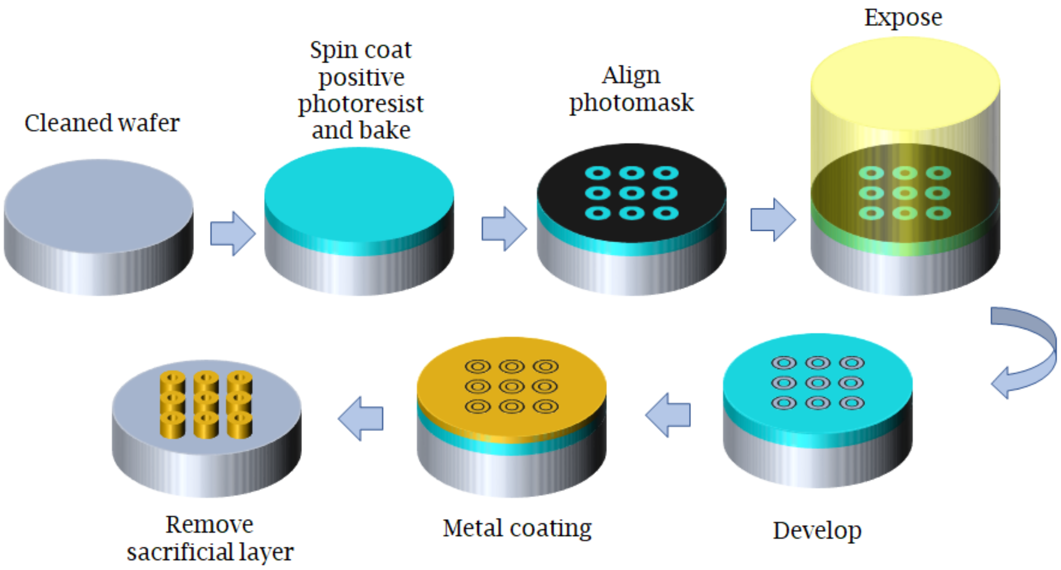

FIGURE 2.19: Photolithography lift-off process for fabrication of metallic features

Metal coating

In order to produce metal features and layers onto our samples two metal deposition techniques were used interchangeably - sputtering and thermal evaporation. For gold depositions, a 10 nm layer of Cr was used to improve adhesion to the substrate. All metal layer depositions were above 100 nm, in order to overcome skin-depth at THz frequencies. Skin depth is inversely proportional to the square root of frequency and at 1 THz falls below 100 nm for metals such as gold, silver, aluminium and copper.

Laser cutting

A laser cutter was used for the fabrication of polymer samples for material characterisation, as well as transmission windows and acrylic holders. The laser cutter used was 50-watt HPC LS6840 PRO, consisting of a water-cooled CO_2 gas tube. The cutting head position can be programmed in x, y and z with a positioning precision of < 0.01 mm and minimum feature size of 150 μm. The minimum feature size realised in practice depends on both the cutting material and the material thickness. Higher aspect ratios result in larger feature sizes. For polymers, heat dissipation poses an issue at small feature sizes, the smallest cuts we were able to achieve in HDPE without melting defects being around 500 μm.

3D printing and casting

3D printing is an additive manufacturing method, where typically a liquid polymer is hardened layer by layer either by cooling or photopolymerisation (fused powder 3D printing is also available, but was not a technique implemented in this research). Extruder type 3D printers, also known as Fused Deposition Modelling (FDM) printers, commonly use ABS and PLA as their filament material. Stereolithography (SLA) printers use various light-reactive resins, polymerised using laser diodes. SLA printers are generally able to achieve smaller feature sizes and better surface finish than FDMs, but they are more costly to operate and cannot print large surface areas. The relatively large feature sizes of THz components make additive manufacturing a viable prototyping technique. The problem arises once again, with material properties at THz. SLA resins were found to exhibit quite high absorption at THz frequencies, with attenuation coefficients at 0.8 THz measured to be between 13.47 - 20.915 cm^{-1} [39]. The refractive index at THz is similar for post photoresins, in the range between 1.5 - 1.7. This makes them unsuitable for bulk THz components, but still advantageous for thin, planar components, such as diffraction gratings. An example of 3D printed phase plates, designed for THz frequencies using extruded PLA is shown in Figure 2.20.

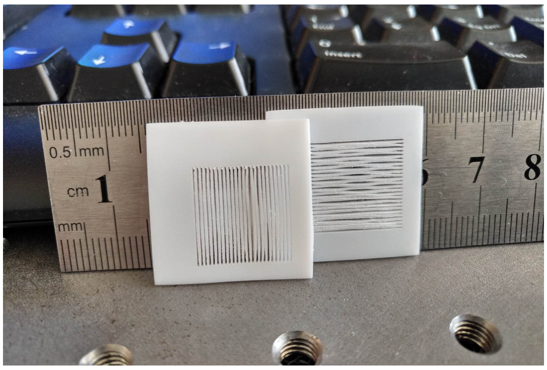

FIGURE 2.20: PLA phase plates, printed using FDM 3D printer with 0.2 mm nozzle size.

2.3.4 Summary

The "Methods" chapter presented two measurement instruments, which were used in THz experiments - a THz-TDS system and a THz-VNA system. The two measurement techniques are complimentary to each other. THz-TDS provides wide band measurements up to 5 THz and THz power in the microwatt range. On the other hand, the THz-VNA system measurements are narrow band between 0.75 - 1.1 THz, with a THz power sub 1 microwatt, but they support high resolutions of several kilohertz, compactness and flexibility for different measurement arrangements (e.g. switching between transmission and reflection measurements without changes to the setup).

Several computational methods for electromagnetics were discussed. Firstly, an overview of an FDTD engine implementation in Matlab was introduced, with some key design points, such as the Yee method, stability and convergence considerations and boundary conditions. An explicit computation for the transmission and reflection coefficients in stratified media was also presented. Explicit computations, where practical, have an advantage over numerical methods in terms of speed and accuracy. The implemented FDTD engine and explicit stratified media model were compared to the commercial software Lumerical in a Bragg mirror example, and have proven to serve as good benchmarks for simulation validation. It is often necessary to perform the opposite operation and extract unknown material optical parameters from scattering matrix data. Therefore, a numerical algorithm used to perform this was also discussed. Finally, there is an overview of the microfabrication methods and materials used.

Chapter 3

THz Modulators

3.1 Background on Modulators, Optical Modulators and THz Metamaterials

3.1.1 The Need for THz Modulators

Modulation is a key part of many signal processing systems, most notably in communications. Through modulation, the range of the transmitted signals, information density and the speed of communication is increased. The importance of modulation stretches beyond just the field of communications, as it's underlying principles of wave manipulation are frequently applied in detection, sensing, imaging, security and more. This applies just as well in the context of THz technology, where efficient, high-speed modulators are paramount for the advancement of THz communication networks, leading to great interest in the research of materials, methods and devices for THz modulation. State of the art materials include metamaterial structures, photonic crystals, phase change materials, high electron mobility transistors (HEMTs), and graphene [40]. Modulators encode information by controlling the amplitude, phase, polarisation, beam form, direction or a combination of these parameters of the carrier wave. In THz amplitude and phase modulators, both parameters usually change simultaneously and a change in amplitude leads to a change in phase and vise versa. This is due to most THz modulators' underlying mechanism for wave manipulation being the change of the complex refractive index of the modulator's bulk material. THz modulators can be classified based on the physical quantity they control - amplitude, phase etc. or based on their technique or actuation method they utilise - optical, electronic, thermal, mechanical, magnetic and others [41],[42].

The key figures of merit for the performance of the modulators are the modulation depth, modulation frequency and operating frequency or bandwidth. Modulation depth is most often defined as $\frac{A_{on}-A_{off}}{A_{off}}$, where A is the controlled quantity. Modulation frequency is the rate at which the modulator is being driven between its "on" and "off" state, and the bandwidth are the frequencies where the modulator can be operated at. Between the years 2006-2022, the THz community has seen an exponential growth in the research of THz modulators. As shown in Figure 3.1 the number of publications from the Web of Science with keywords "THz", "metamaterial" and "modulator" increased from 10 in 2006 to reaching an all time high of 220 in 2020 [43].

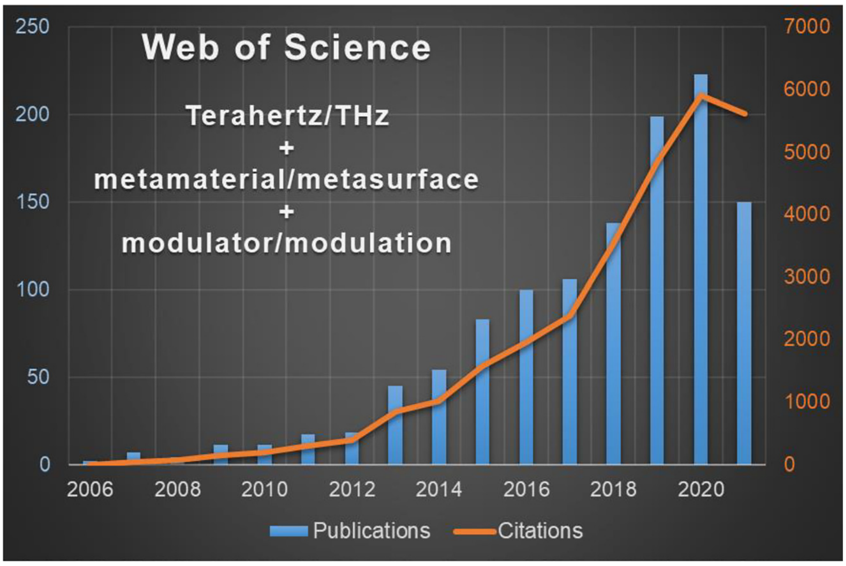

FIGURE 3.1: Review on THz modulator research between the years 2006-2022. Figure from [43]

Figure 3.2 reviews the performance of the current state of the art THz modulators developed between the years 2006 - 2022. The modulators are grouped into four sets based on their driving method - optical, electrical, thermal and microelectromechanical systems (MEMS), and a separate set representing devices based on graphene, as there is a great volume of work focusing on this technique.

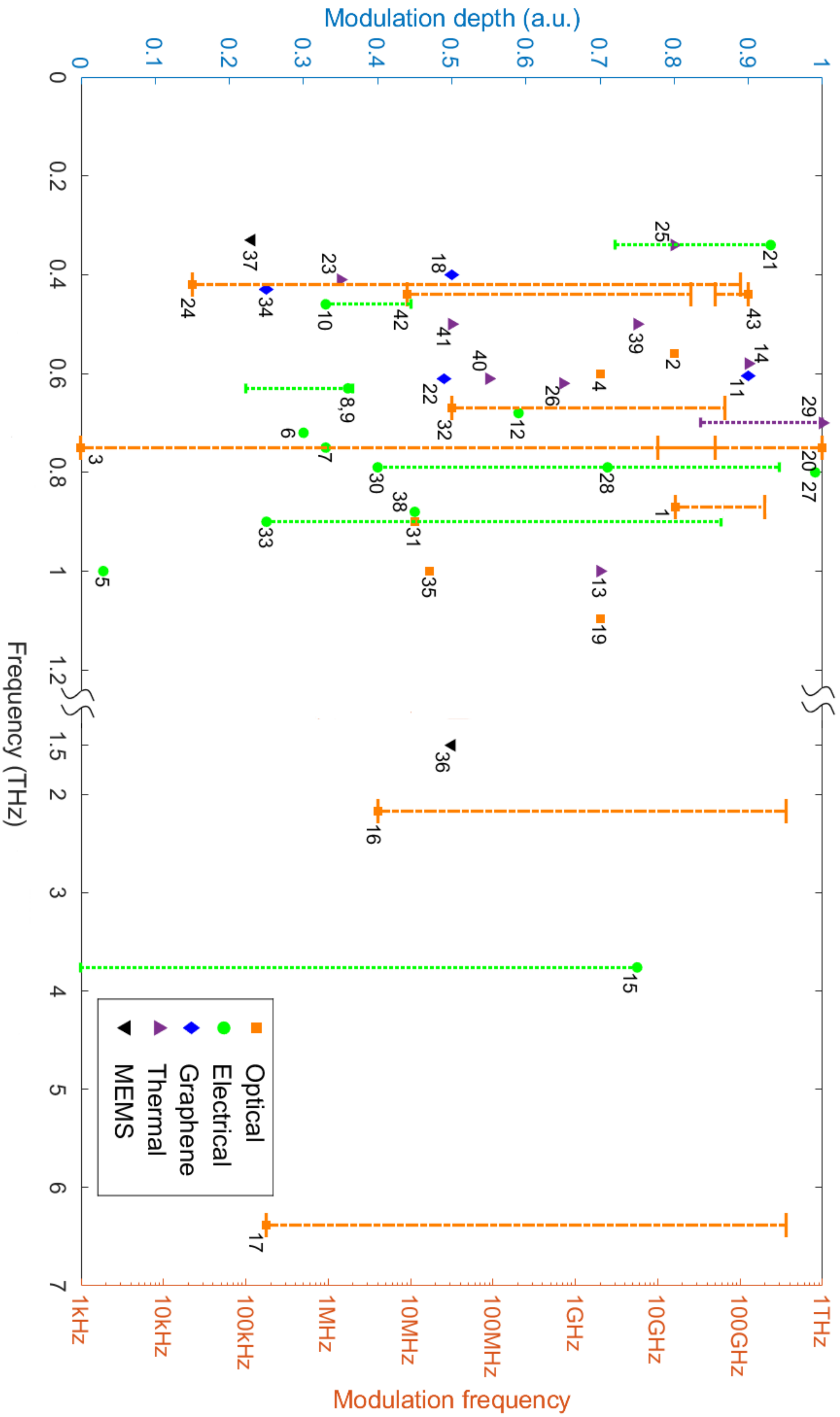

FIGURE 3.2: Review on THz modulator research between the years 2006-2022. Table of the works included and their corresponding data points can be seen in Table A.1

The x-axis shows the operating central frequency of the modulators and the left y-axis shows the measured modulation depth at that frequency. For research, where the modulation speed (frequency) has been measured, the corresponding data point is connected to a dotted/ dashed line, the end of which (denoted as a horizontal dash) marks the modulation frequency on the right hand y-axis. The majority of work on THz modulators has been done in the operating frequencies between 0.2 and 1 THz, with only a few in the region between 1.5 - 7 THz. Data points 18,23,24,34,42 and 43 all have been measured to operate at approximately 0.4 THz, but have been shifted along the x-axis on the graph for visual clarity. Some works have also presented an indicative modulation speed in terms of a relaxation time of the charge carriers in their materials, which here have been re-calculated in terms of frequency in vacuum in order to present data uniformly.
Over the past decade optical modulators have shown the best results in terms of modulation speed. The research conducted by Hendry et. al [44] in 2007 (data point 1) achieved an unprecedented switching speed for a THz switch at the time, with a transmission recovery time (time taken for the transmission to decay sufficiently after photo excitation) of 2 picoseconds. This was achieved by optically pumping a golden square hole array on silicon. The modulation depth of the transmitted signal was measured to be a maximum of 80%. The trade-offs of these results was that the fast switching speeds were achieved at a temperature of 20 K, where the recovery time of Si carriers is reduced. At room temperature, as Si is an indirect band gap semiconductor, recombination and trapping times would increase the recovery time to the microsecond scale. Furthermore, even though a modulation depth of 80% is quite high, the overall transmission of the modulator was only around 2%. Over the next years both transmission and modulation depth in THz modulators have experienced a great improvement in the modulation depth and transmission with the introduction of metamaterials - some optical modulators have since reached modulation depths close to 1, as seen in the works shown by Singh et. al [45] (data point 20), while keeping transmission at around 50%. The trade-off between speed, modulation depth, and bandwidth however remains, with the highest speed reached in this review being 358 GHz with a maximum modulation depth of 0.4, as presented by Tasolamprou et. al [46] (data point 16) for a THz absorber comprising of a

graphene sheet on a SU-8 substrate. On average, the majority of optical modulators exhibit a modulation depth below 60% and switching frequencies in the GHz range. Another important downside of optical modulators is the source of actuation itself. Almost exclusively, all optical modulators are actuated by a high-power pumping beam, with an average pulse laser fluence of 200 μJ/cm^2 (equivalent to about 160 mW for CW radiation) [44]–[49]. This sets optical modulators as much bulkier and energy consuming than their electronic counterparts, making them harder to integrate.

THz electronic modulators operate using a similar principle to optical THz modulators, but instead of photo-doping carriers in semiconductors, the carrier concentration can be controlled electrically. A popular approach is the application of the high electron mobility transistor (HEMT) architecture. HEMTs are field effect transistors, which make use of a two-dimensional electron gas (2DEG) at the heterojunction between a highly doped semiconductor donor (usually AlGaAs) and an undoped semiconductor (GaAs). The carriers are then concentrated in the quantum well at the interface [42]. This approach has been demonstrated by Kleine-Ostmann et.al [50] (data point 5) and Padilla et. al [51] (data point 10), achieving a modulation depth of 3% and 33% respectively. The latter was also successfully modulated at 10 MHz. Other architectures include combinations of metamaterials and liquid crystals [52] (data point 15), metamaterial arrays on semiconductor substrates employing Schottky contacts [53]–[56] (data points 6,7,8,9 respectively), phase-transition materials, such as vanadium dioxide (VO_2) [57] (data point 27), and metamaterials on 2D perovskite [58] (data point 43).

Architectures based on graphene are another big branch of electrically driven THz modulators, raising a big interest in the field. Graphene can exhibit extremely high carrier mobility of up to 20000 cm^{2}V^{-1}s^{-1} for both holes and electrons (by comparison low doped GaAs has a maximum electron mobility of 9400 cm^{2}V^{-1}s^{-1} [59]), and can have large carrier concentration swings when an external electric field is applied [42]. Electrically controlled THz modulators tend to exhibit higher modulation depths but lower modulation speed in comparison to optically actuated modulators. The biggest advantage however, is their potential for integration with existing CMOS technology. Thermal and MEMS-based THz modulators are less common in the field. Thermal modulators have the capacity to exhibit modulation depths close to 1 [60], but are limited by the time it takes for the sample to heat and cool, which is much longer than optical and electronic switching times. MEMS architectures on the other hand are complex and expensive to manufacture.

3.1.2 Optical THz modulators

As previously discussed in section 3.1.1, optically controlled THz modulators generally make use of photoconductivity in semiconductors. Illuminating a semiconductor with photon energy above the semiconductor band gap leads to the generation of carriers, also known as photogenerated carriers. The rise of conductivity of the semiconductor therefore changes its effective refractive index and the medium becomes more reflective and less transmissive at THz frequencies. As the optical pumping is most often done with ultrafast lasers, which can reach fs pulse durations, the limiting factor of the modulation speed of optical THz modulation becomes the photogenerated carriers' lifetime. For indirect band-gap semiconductors, such as silicon, the majority carrier lifetime can range between 1ms to a few hundred ns, depending on doping concentration [61]. Direct semiconductors, such as GaAs exhibit shorter lifetimes, which can reach sub-picosecond values [62]. Commonly, the semiconductor bulk materials used are HRFZ-Si, high-resistance GaAs and Si on sapphire. At high energies the pump laser can also increase modulation speed, by dynamically modifying the plasma frequency of the localized surface plasmon, rather than changing the conductivity of the substrate [40]. However, a high power laser is not a sustainable solution for making THz modulators for wide applications. Reducing the power required to actuate the modulators, as well as dependence of the quality of the light source (such as coherence, angle of incidence, spectral purity) can make a THz optical modulator easier to integrate. Rather than with a pulse or CW laser, a HRFZ-Si wafer was illuminated by a white light LED array. The Cree XLamp CXB3070 LED 4000K [63] (as seen in Figure 3.4) was used, which had a large viewing angle of 110 ° and a spectral distribution as shown in Figure 3.3. The power received at the sample at the highest relative spectral power wavelength, 450 nm, was measured to be 200 mW. As the LED array was switched on and off, the transmission through the sample in the region between 0.75 -1.1 THz was measured using a VNA. Figure

3.5 shows the averaged transmission when the light was in the "off" and "on" state, where the shaded area is the standard deviation. The equipment produced too much noise in the two extreme ends of the measured spectrum, therefore the results at 0.75 and 1.1THz are ignored. The maximum modulation depth measured was -0.55 dB, or 11.9 % and an average modulation over the spectrum of -0.25 dB, or 5.6 %. By comparison the modulation change in a bare high-resistance Si wafer when illuminated by a 808 nm CW laser in the work done by Qi-Ye Wen et. al [64] for 200 mW laser power can be extrapolated to be on average 15% over the 0.2-1 THz region.

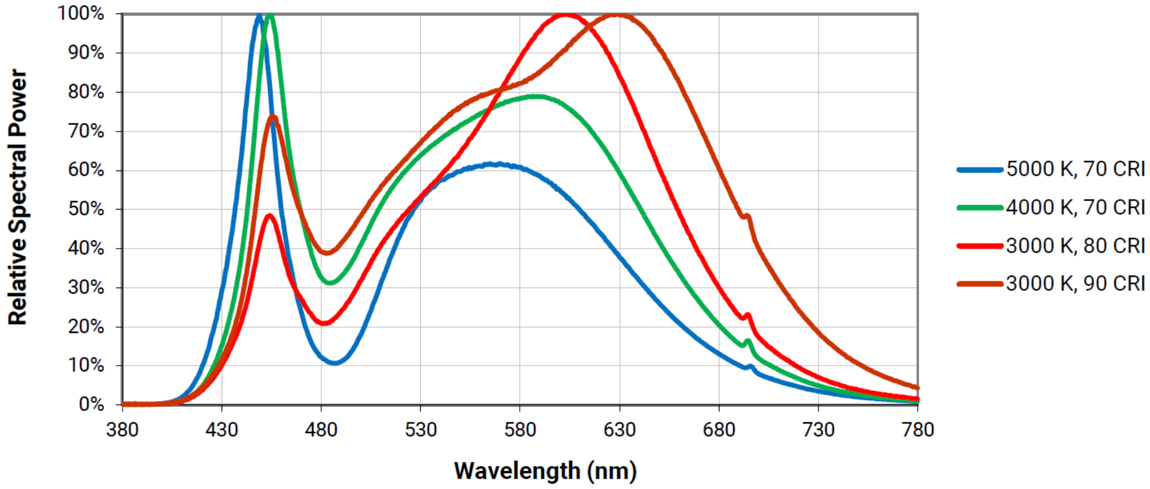

FIGURE 3.3: Output spectrum of CXB3070 LED 4000K, according to the manufacturer [63]

FIGURE 3.4: Photo of the CXB3070 LED array [63]

In order to increase the modulation depth achieved through photo illumination, resonating metal structures, also known as metamaterials are often incorporated. For the LED-actuated modulators to perform on par with laser-actuated ones, the metamaterial structures would need to be at least 3 times more sensitive to changes in the bulk material carrier density.

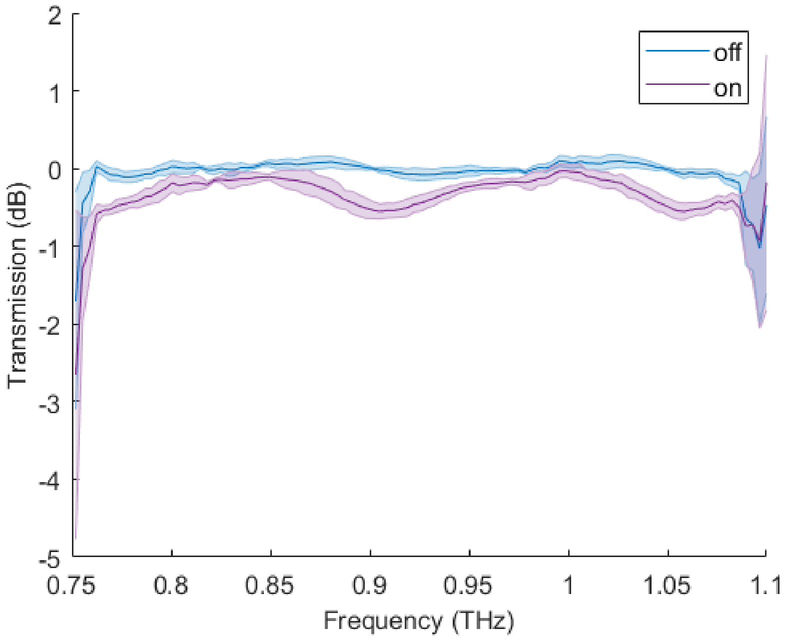

FIGURE 3.5: Changes in transmission after consecutive illumination of a HRFZ-Si sample with LED array

3.2 Metamaterials

3.2.1 The Split Ring Resonator

Perhaps the most famous resonant metamaterial is the Split-Ring Resonator (SRR), the geometry of which is shown in Figure 3.6 a). It was first introduced by Pendry et al. in 1999 [65]. The topology was the first metamaterial to exhibit a negative permeability and was the starting point of the SRR metamaterial field, from which numerous other geometries exhibiting exotic properties have been designed. As shown in Figure 3.6, the SRR cell may consist of two metallic concentric circles with slits on opposite sides. When a time-varying electromagnetic field is directed at the rings along the z-axis, an electromotive force around the rings is generated, that in turn, induces currents in the rings. The slit on each ring prevents the currents from circulating along the individual rings, so that the slits force the current to flow from one ring to the other through the concentric inner-ring slot, taking the form of a displacement current (Figure 3.6 b) [66].

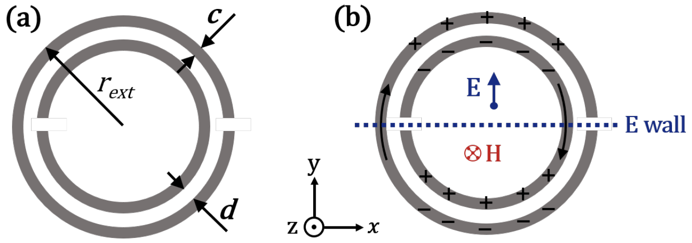

FIGURE 3.6: a) Split ring resonator geometry b) Fundamental resonance: orientation of the polarisation fields, sketch of the charge distribution and boundary condition at the symmetry plane [66]

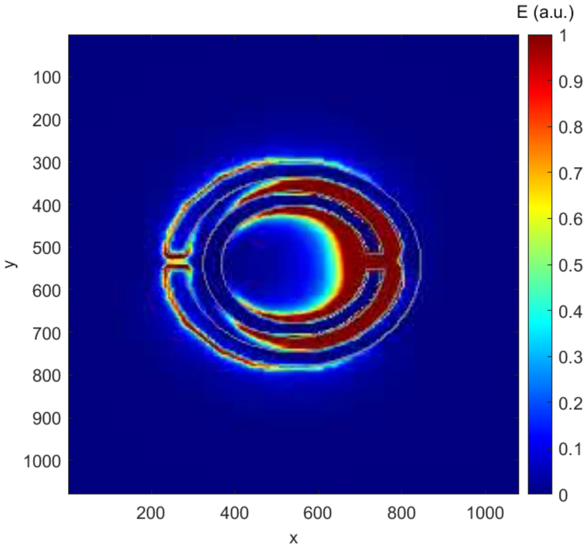

(A) t

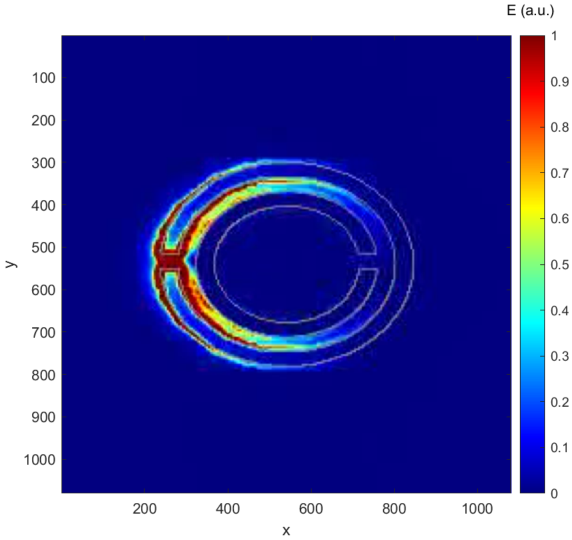

(B) t+T/2

FIGURE 3.7: Simulated electric field intensity at fundamental resonance showing the oscillation along the circumference of the split rings at times t and $t + T/2$. 2D simulation in Lumerical FDTD with periodic boundary conditions for a single resonator cell.

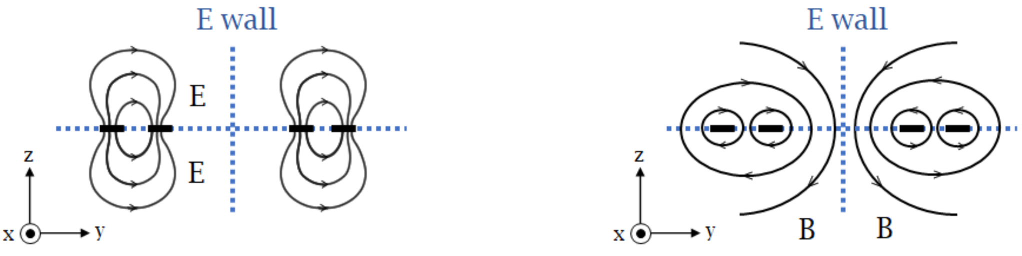

(A) (B)

FIGURE 3.8: a) Side view of the electric field lines at fundamental resonance expected from theory b) Side view of the magnetic field lines at fundamental resonance expected from theory. [66].

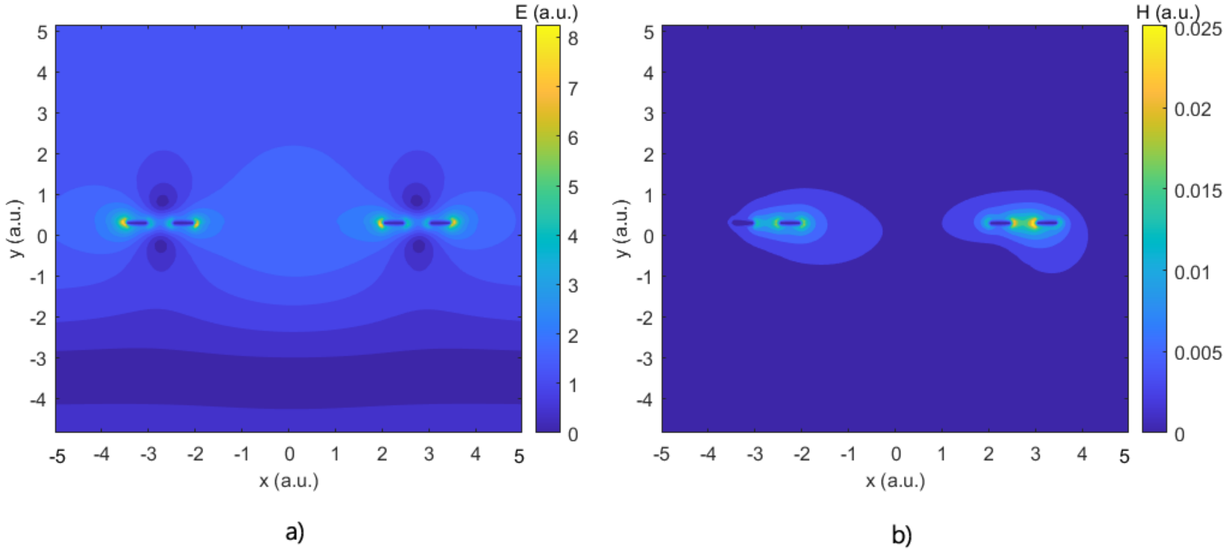

FIGURE 3.9: a) FDTD Simulated side view of the electric field lines b) FDTD simulated side view of the magnetic field lines

As shown on Figure 3.6 b) and in Figure 3.8, the xz-plane of symmetry acts as a virtual electric wall - the electric field passing through is symmetrical and perpendicular to the plane of the wall. The current loops induce a magnetic dipole moment along the z-axis and an additional electric dipole moment is generated orthogonally to the plane of symmetry, in the yz-plane.

By symmetry, the charges generated on the rings are mirror images of each other and two parallel electric dipoles are generated on each half. This means that a time-varying electric field is also able to excite the SRRs, inducing a charge density in the form of an electric dipole that causes currents to flow. Since there are both magnetic and electric dipoles present in the SRRs, they suffer from cross-polarisation effects.

Although SRRs show simultaneous electromagnetic response in resonance, the magnetic field is found to be the dominant excitation mechanism [66]. Simulations were made using the approach given in section 3.3. Figure 3.7 shows the FDTD-simulated oscillation of the electric field between the two rings in response to the rotation of the displacement current along the ring circumference. This oscillatory mode is found to be the strongest, but there are also other high-order modes present. Figure 3.9 shows the simulated side view of the electric and magnetic field in the SRR. The simulation assumed an infinite substrate, where PML boundary conditions were applied to the boundaries normal to the injected source pulse (z-axis) and periodic boundary conditions were set in the plane of the split-ring features (x- and y-axis). The position of the injected source and simulated space can be seen in Figures **??**. The results agree well with the theory in Figure 3.8, however it was found that the field distribution at the fundamental resonance is not symmetric between the inner and outer ring. The symmetric condition shown in Figure 3.9 a) is actually met above fundamental resonance. This is most likely be due to errors associated with the approximating nature of the FDTD method. Staircasing errors due to the circular geometry are also present and could be reduced by using finer mesh sizes. Resonance, as expected is achieved when the field is most strongly confined in the inner ring gap.

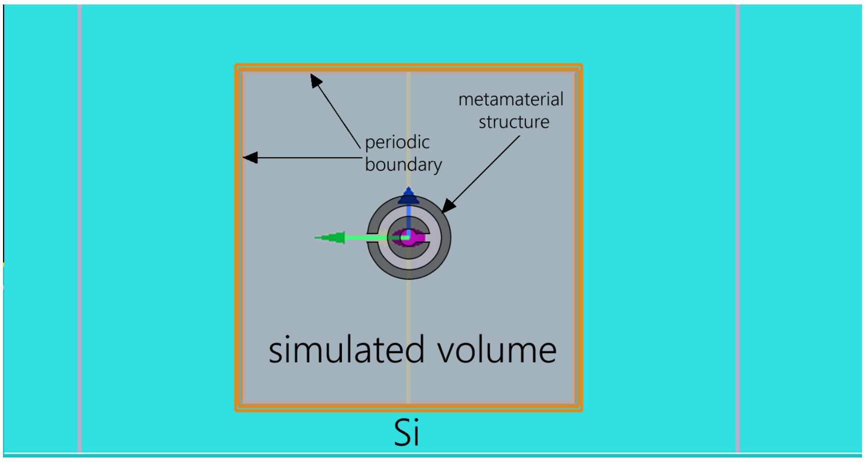

(A) XY-view

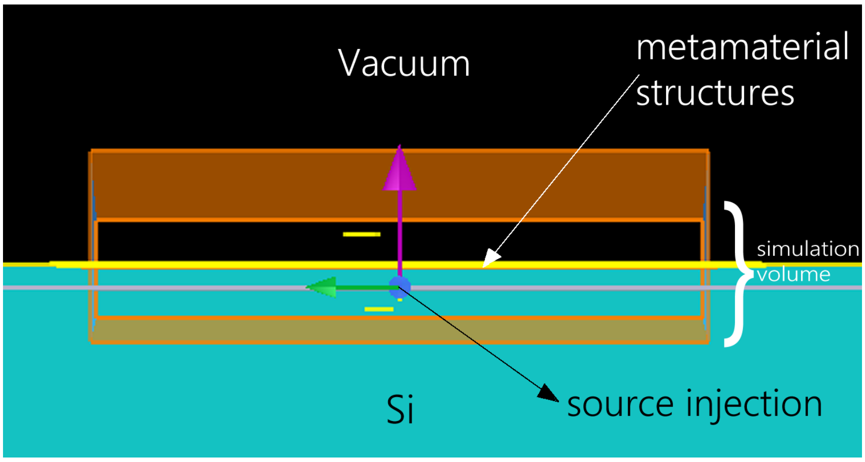

(B) XZ-view

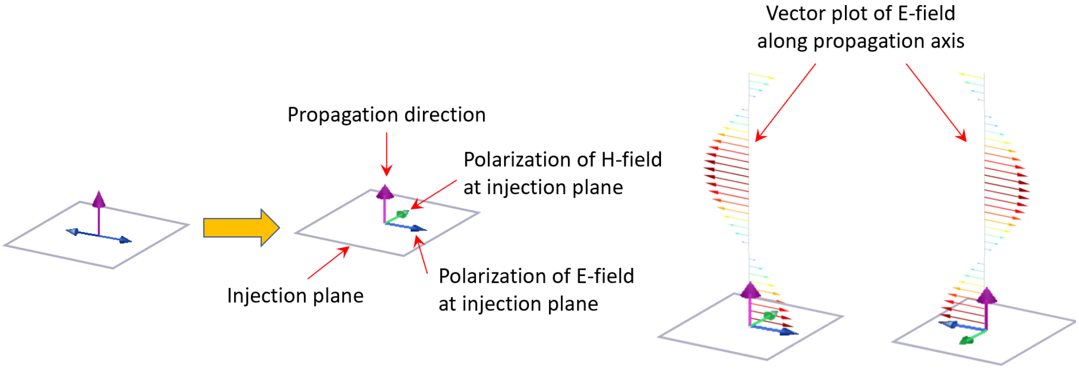

(C) Lumerical source injection notation

FIGURE 3.10: a) XY-view of SRR FDTD simulation volume, showing the periodic boundary conditions, b) XZ-view of SRR FDTD simulation volume, showing the source position and a semi-infinite substrate [67]

3.2.2 Conductively Coupled Resonator

Another geometry chosen for the investigation of optical THz modulators based on SRRs was a conductively coupled supercell, consisting of two square split rings, connected by a microstrip line, as introduced by Morandotti et. al., [68] as seen in Figure 3.11. The microstrip forces a conductive coupling regime between the two individual SRRs, which is much stronger than the conventional inductive or capacitive coupling between rings. When the composite structure is excited with the electric field perpendicular to the gaps of the SRRs, a new high Q-factor resonance is expected to be excited in addition to the fundamental resonance of the individual SRRs. At the frequency of this resonance, the induced currents in each SRR resemble that of the fundamental resonance of the individual SRR but the currents oscillate out of phase, leading to the formation of the high Q-factor mode. This geometry was chosen in order to investigate the effect of different excitation mechanisms and high Q-factors with respect to the optical modulation depth. The current distributions in individual SRRs and the joint SRR (JSSR) supercell are shown in Figure 3.12 [68].

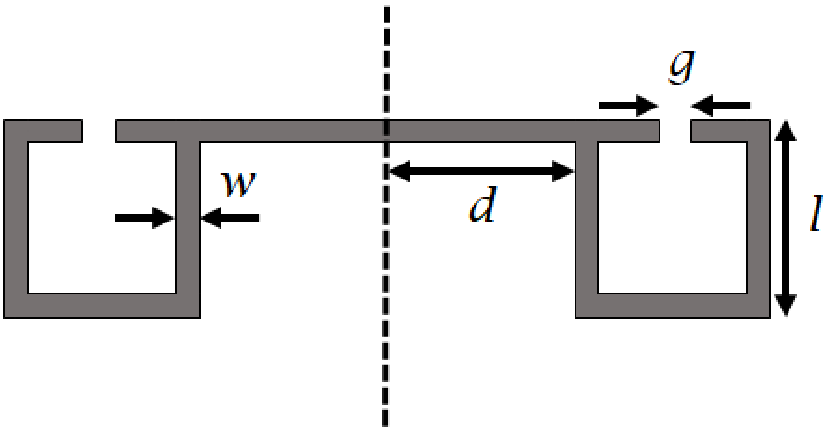

FIGURE 3.11: JSRR cell geometry [68]

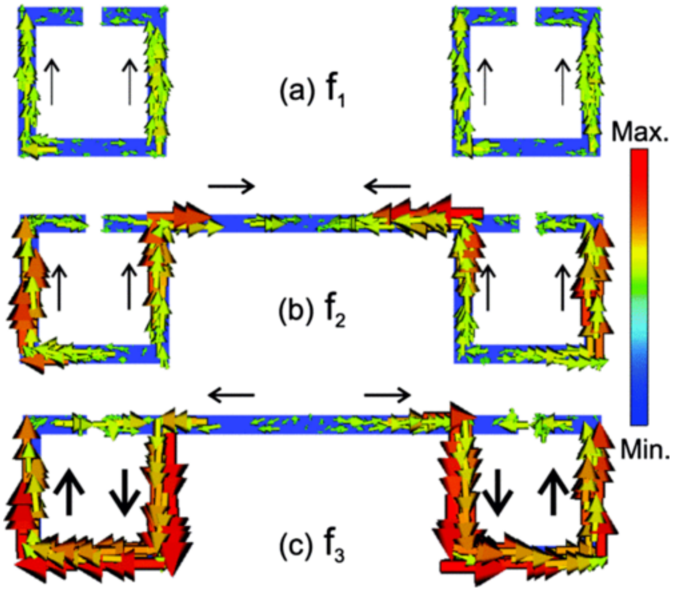

FIGURE 3.12: Current distribution at the a) fundamental resonance of individual SRRs, b) fundamental resonance of JSRRs and c) JSRR additional high-Q resonance mode [68]

3.3 Design and Simulation

The Lumerical FDTD solver was used to design the dimensions of both SRR and JSRR geometries on Si, so that their resonance falls within the measurement range of our VNA. Similar results were obtained using the in-house FDTD engine in 2D, with shifts in the predicted resonance peaks of up to 5 MHz with spectral resolution of 1.25 MHz set on both simulations. The metal patterns were simulated as an ideal conductor, and the silicon subtrate was simply represented by a dielectric with a constant refractive index of 3.42 over the simulated spectrum. The dispersion of Si for THz frequencies is quite small - a change of the real part of the refractive index of approximately 1.5^{-4} for frequencies between 0.5 - 4.5 THz [69]. Therefore a constant refractive index is a good approximation. For an expected resonance of 0.811 THz for the SRRs and 0.785 THz for the JSRRs, the structures' respective dimensions are shown in Table 3.1.

SRR	µm	JSRR	µm
r_{ext}	13	g	3
c_{outer}	3	d	3
d	3	w	3
c_{inner}	5	l	24

TABLE 3.1: SRR and JSRR structure dimensions

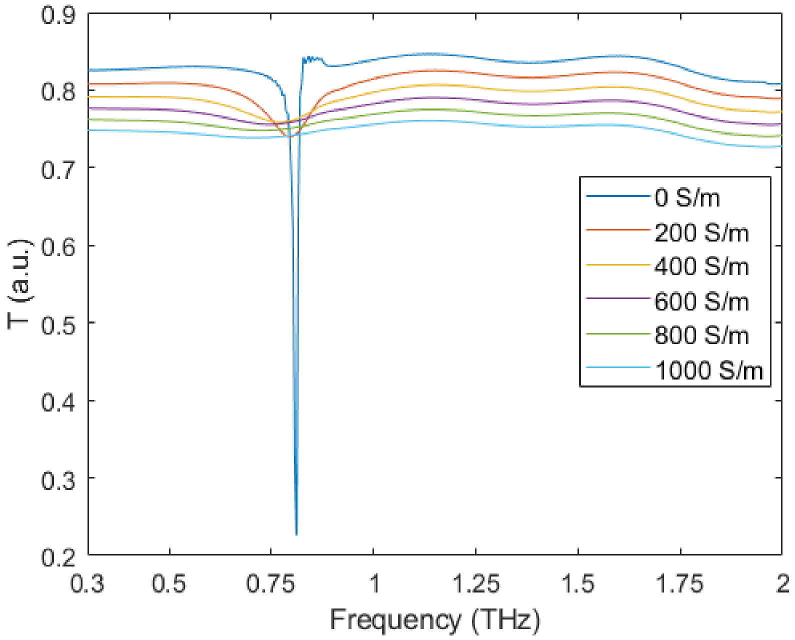

FIGURE 3.13: Simulated transmission of SRR structures on Si with increasing surface conductivity

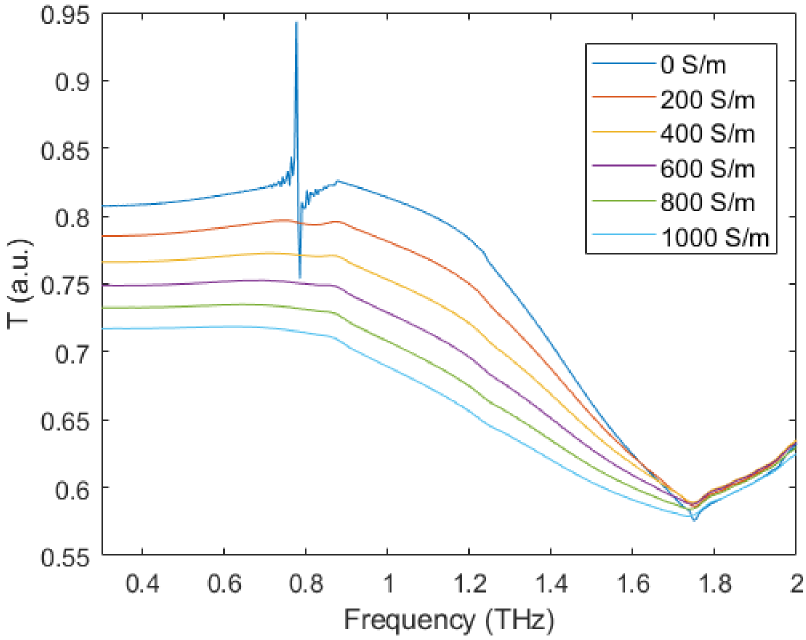

FIGURE 3.14: Simulated transmission of JSRR structures on Si with increasing surface conductivity

The fundamental resonance of the SRR can also be verified analytically, using the LC circuit model shown in Figure 3.15 [70]. The resonant frequency of the SRR is given by $f_0 = \frac{1}{2\pi\sqrt{C_{srr}L_{srr}}}$, where C_{srr} and L_{srr} are the total capacitance and inductance of the structure. The capacitance between two concentric rings is given by $C_0 = 2\pi r_0 C_{pul}$, where C_{pul} is the per unit length capacitance and r_0 is the averaged radius of the rings. The total capacitance of the SRR is equivalent to two half-ring concentric ring capacitances ($C_0/2$) in series, or $C_0/4$. The series inductance can be approximated by a single ring inductor with the same width d of the original rings, and a radius which is the average of the two rings (r_0).

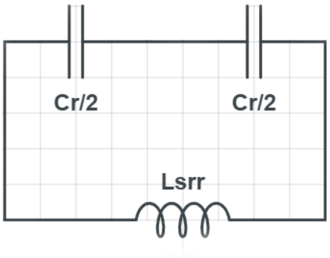

FIGURE 3.15: Equivalent circuit diagram of SRR

According to the analytical model suggested by [70], for the dimensions given in Table 3.1 (assuming equal ring thickness of 3 μm for both rings), the resonance of the SRR would be 0.878 THz, which is higher than the expected resonance from FDTD simulations. This is in part because of the assumption of a thinner inner circle. The simulated transmission response of both the SRRs and JSRRs can be seen in figures 3.13 and 3.14. By incorporating a thin 1μm layer of dielectric with variable conductivity under the metal patterns, the change in transmission response due to an increase in photogenerated carriers can be seen. The metamaterial responses seen in figures 3.13 and 3.14 are calculated assuming to reflections from a substrate with finite thickness. This is the usual response seen from THz-TDS systems as well, where secondary reflections of the main THz pulse are apodized in post-processing and secondary reflections are generally ignored. In order to achieve an infinite substrate in FDTD simulation, (and hence no reflections) the source wave was injected within the substrate domain, as shown in Figure 3.10. The planar boundaries around the metamaterial cells were set as periodic and the boundaries in the z-axis are PML. The region of periodic boundaries defines the size of the metamaterial cell. Since the real-life testing of the metamaterials was to be done in the frequency domain using the THz VNA system, reflections from the substrate slab cannot be ignored. Furthermore, in any real application, they will also persist. For the same SRR geometry in Table 3.1, the metamaterial response was calculated with the addition of Fabry-Pérot reflections from a finite substrate. The substrate thickness was set to 325 μm and the source wave was injected from outside the volume of the device. For varying cell sizes, the response is shown in Figure 3.16. The position of the oscillator's resonating frequency remains at 0.811 THz and the Fabry-Pérots are determined by the refractive index and thickness of the substrate, which also remain the same. However, it can be seen that some sharp and spectrally dense resonances occur from a set frequency and continue for all higher frequencies. It can be seen that the wavelength for which these resonances begin in vacuum is the same as the characteristic dimension of the metamaterial cell. The correlation between the two for the traces in Figure 3.16 is plotted in Figure 3.17. To further explore this phenomena, both the infinite and finite substrate responses of the metamaterial geometries showed in Figure 3.18 were calculated and displayed in figures 3.19 - 3.21.

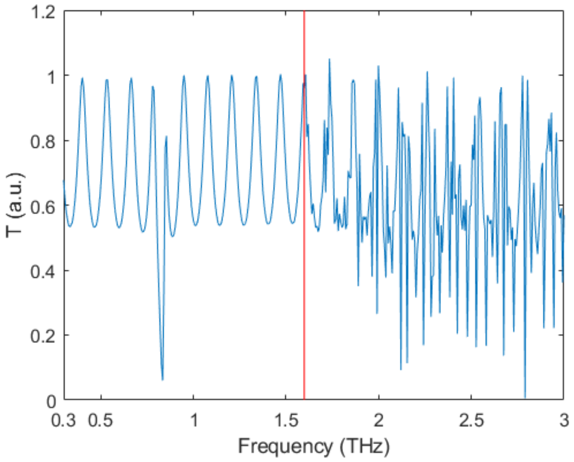

(A) 55μm cell

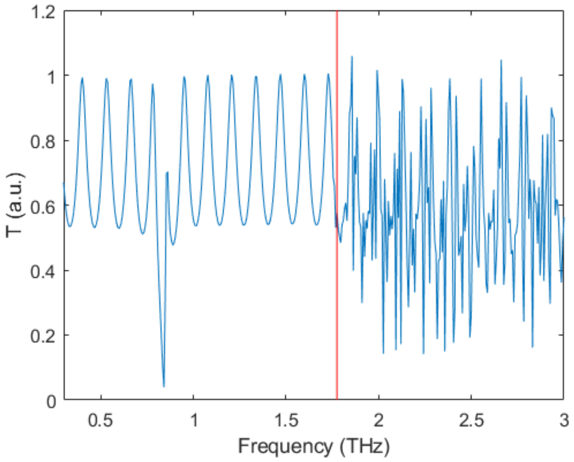

(B) 50μm cell

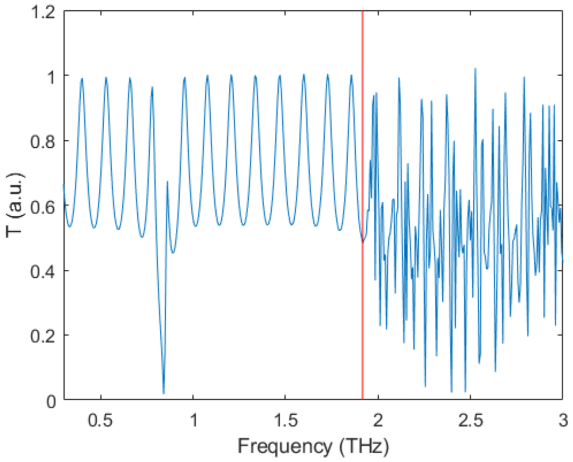

(C) 45μm cell

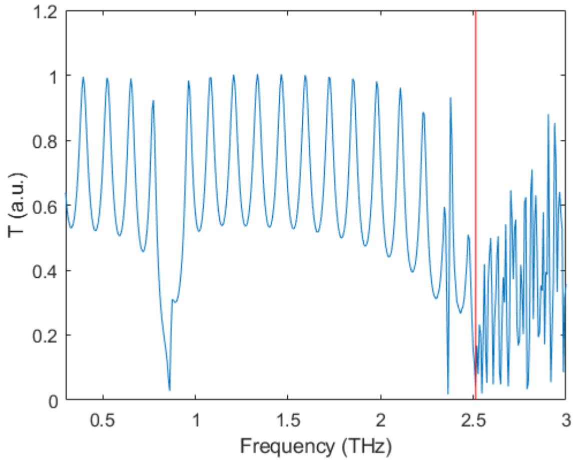

(D) 35μm cell

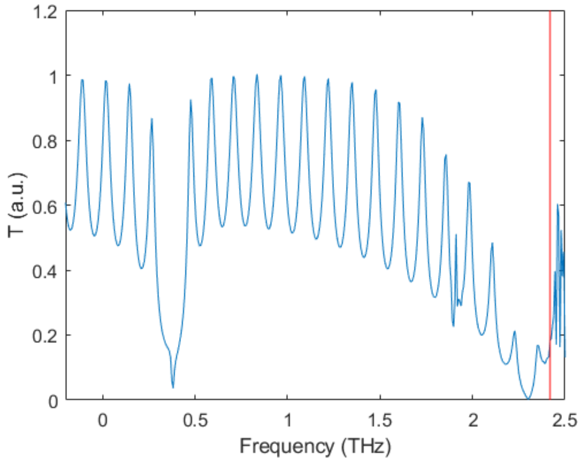

(E) 30μm cell

FIGURE 3.16: Simulated transmission spectra for SRR with resonance frequency of 0.811 THz with varying cell dimensions

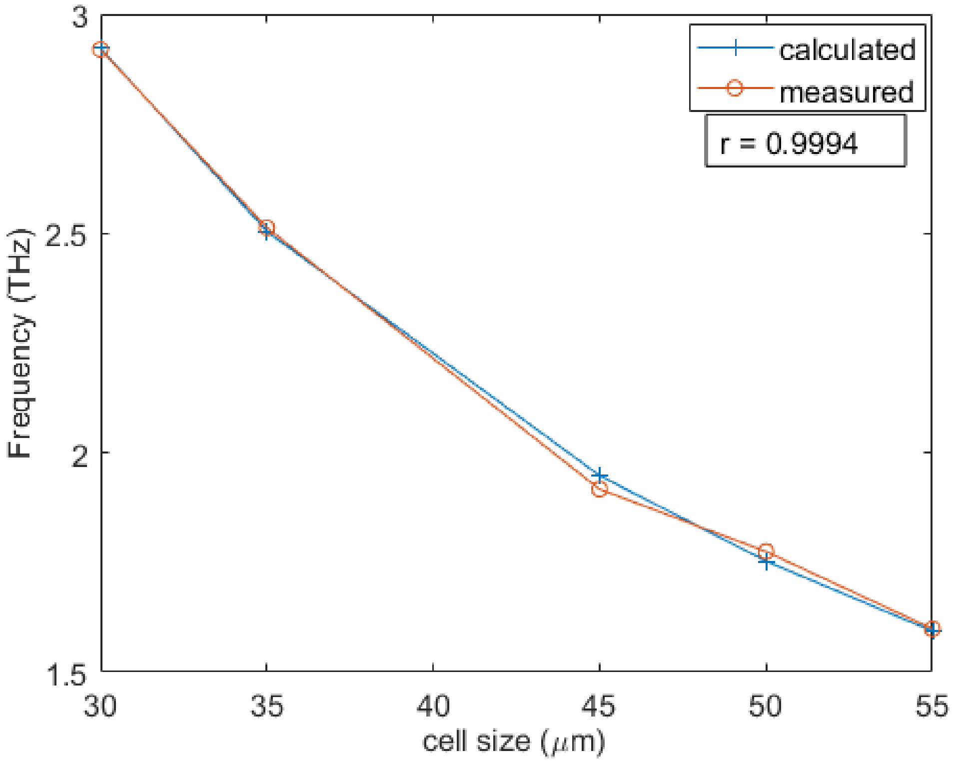

FIGURE 3.17: Correlation between the sharp resonances starting frequency and cell size

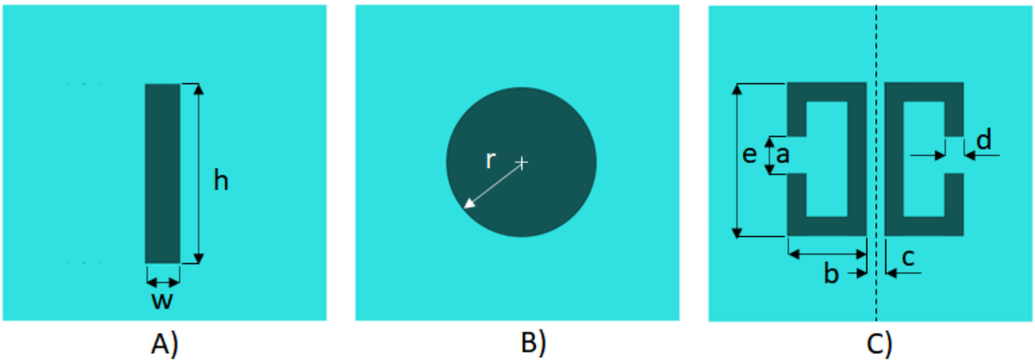

A)
B)
C)

FIGURE 3.18: Metamaterial geometries

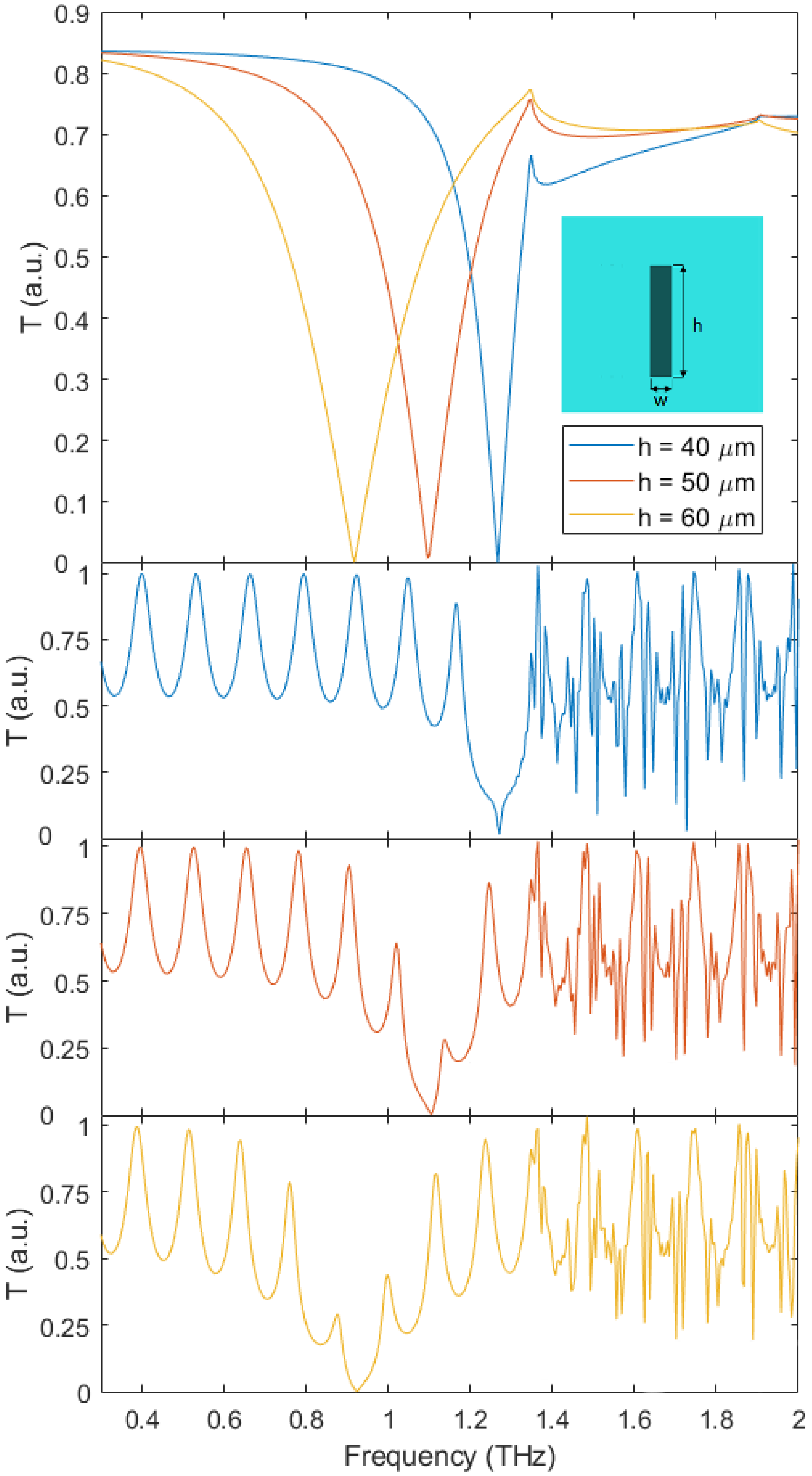

FIGURE 3.19: Simulated transmission spectra of rectangular strip metamaterial of varying lengths on 325 μm Si substrate

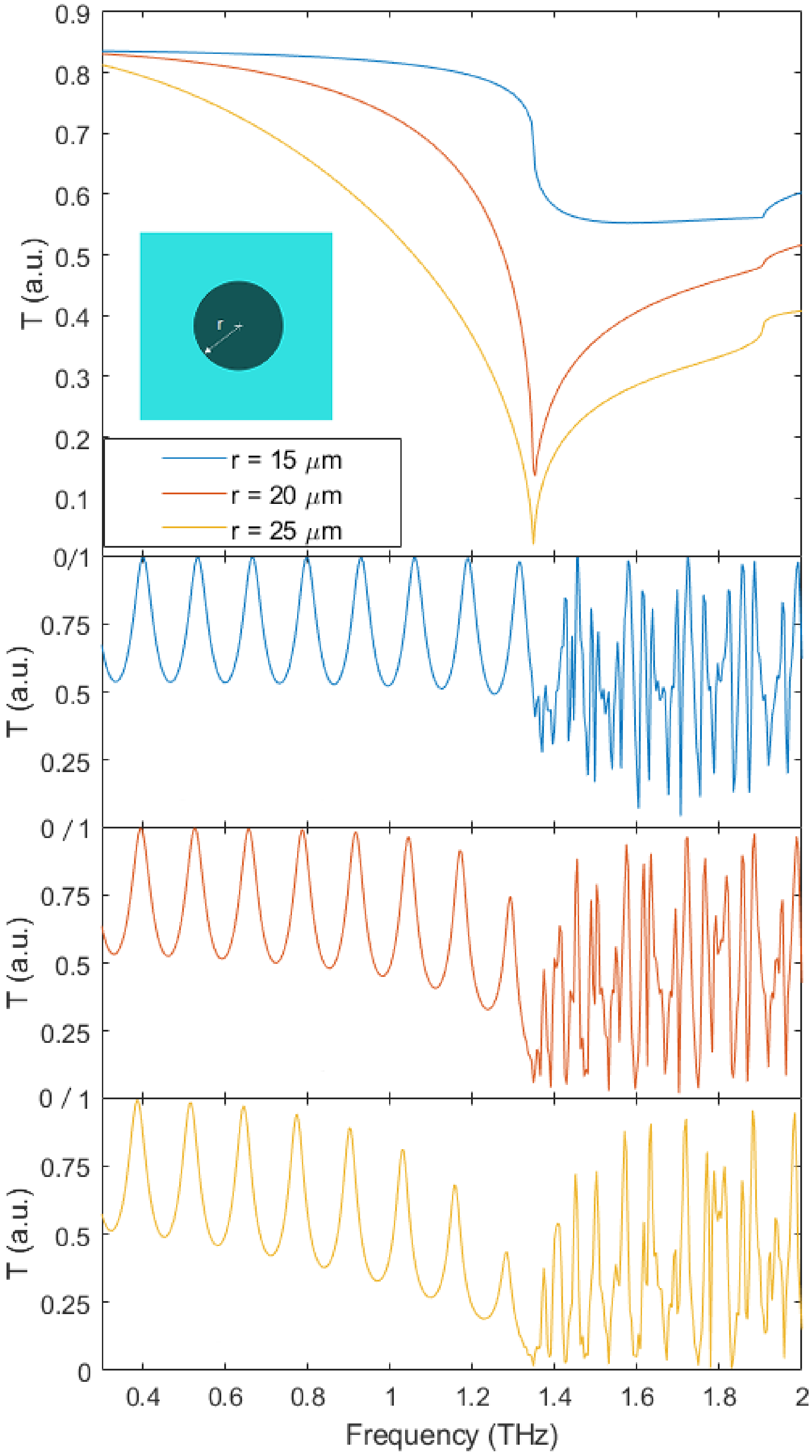

FIGURE 3.20: Simulated transmission spectra of circle metamaterial of varying radius on 325 µm Si substrate

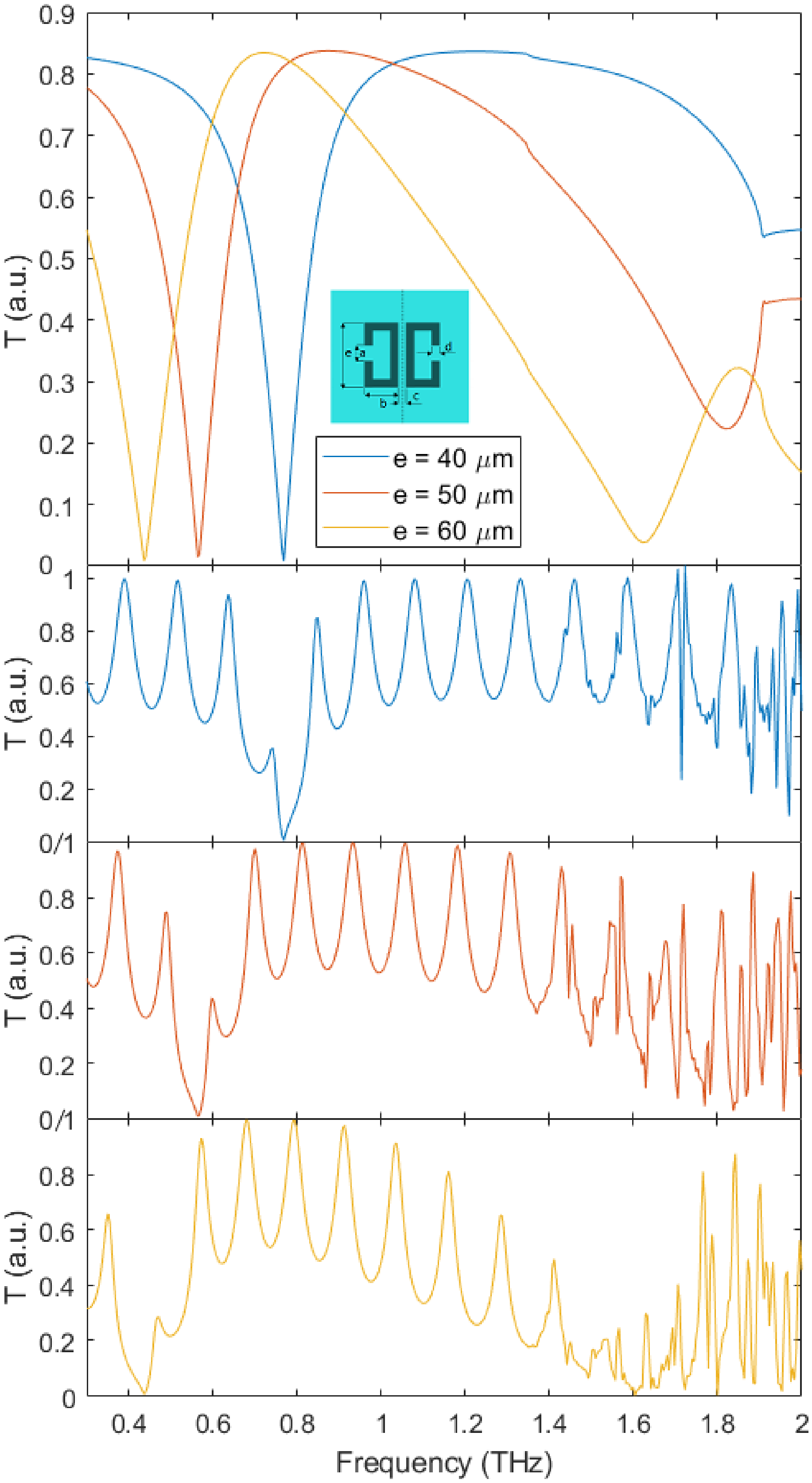

FIGURE 3.21: Simulated transmission spectra of metamaterial of varying radius on 325 µm Si substrate

All spectra shown in figures 3.19 - 3.21 has been calculated with a cell size of 65 μm, which produces a resonant feature at the expected frequency of 1.348 THz (the inverse of the cell size). The frequency of this feature is invariant of the geometry of the resonator and hence of the resonator frequency. This suggests that even though the effect is a result from interaction between resonators from adjacent cells, it is not from hybridisation of resonating modes, which generally leads to shifting and generation of new eigenmodes as a function of the eigenmodes of the original resonators. As the effect is dependent on the cell periodicity, or the meta-atom size, it can be concluded that it is a diffraction effect. By treating the metamaterial as a photonic 2D-crystal it can be shown that the sharp resonances exhibited at wavelengths shorter than the meta-atom size are in fact photonic crystal guided resonances, which are excited from the Fabry-Pérot reflections of the substrate.

Photonic crystals are structures with periodically repeating regions of high and low refractive index, which mimics the lattice structure of naturally occurring crystals. The constructive and destructive interference of waves between the lattice interfaces leads to the creation of modes - where certain wavelengths can propagate through the crystal, and band gaps - where certain wavelengths are forbidden to propagate through the crystal. This gives rise to multiple optical phenomena, such as low-loss waveguiding, perfect reflectors and absorbers, cavity resonators, inhibition of spontaneous emission and others [71]. Photonic crystals support in-plane guided modes, where the energy is confined within the crystal slab and does not couple to external resonances. However they also support guided resonances, which can be coupled to external sources and can be used to achieve high transmissions or reflections. These properties have been employed in the design of novel photonic-crystal based diodes, lasers and directional output couplers [72]. The present study aimed to exploit the complex and narrow shapes of the guided resonances to improve the performance of the optical split-rings modulator by increasing the quality factor of the resonant modes and hence increase the modulator's sensitivity.

Photonic crystals can be realised in one, two and three dimensions, depending on the number of dimensions the crystal experiences periodicity in, as shown in Figure 3.22. In the case of the examined metamaterial, it is periodic in both the x and y-direction, hence it acts as a 2D photonic crystal.

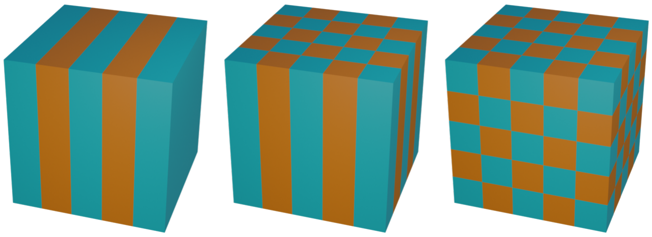

FIGURE 3.22: Photonic crystal structure showing periodic areas of low and high refractive index in a) 1D, b) 2D and c) 3D

The resonances present in the transmission (and by extension the reflection) spectrum of the metamaterial as shown in figure 3.19 - 3.21 are not symmetric Lorentzian shapes, but display an assymetrical dispersion, typical of Fano resonances. This is most visible when the thickness of the substrate is decreased and fewer resonances are excited in the calculated band, as demonstrated in Figure 3.23. The numerically calculated transmission spectrum shown is for a metallic circle of radius r=13 µm, periodicity of a=65 µm and a Si substrate thickness of t=32 µm.

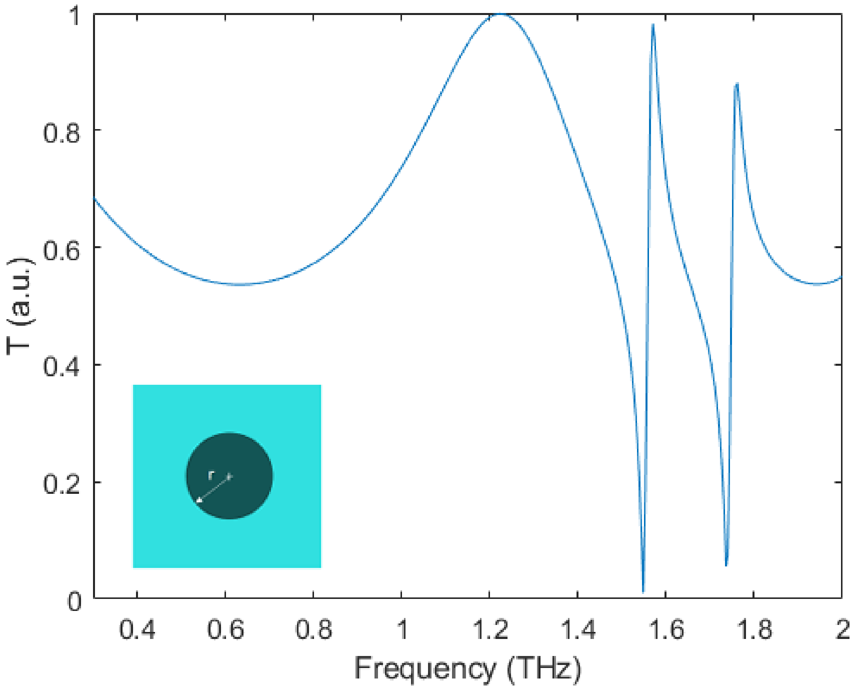

FIGURE 3.23: Numerically calculated transmission spectra of metamaterial with structure radius r=13 µm, periodicity of a=65 µm and a Si substrate thickness of t=32 µm

There are two distinct resonances that can be seen in Figure 3.23, corresponding to 1.548 THz and 1.736 THz. The resonance shape matches that of a Fano resonance, which is typically observed when there is an interference between two weakly coupled resonators, and only one of them is being driven. This type of behaviour is often exhibited in quantum systems, where a discrete quantum state interferes with a continuum of states, and is manifested in the absorption spectrum σ(E), with the shape described by the Fano formula [73]

$$\sigma(E) = 4\sin^2\delta\frac{(q+\Omega)^2}{1+\Omega^2}, \tag{3.1}$$

where E is the energy, δ is the phase shift of the continuum, $q = \cot\delta$ is the Fano parameter and $\Omega = 2(E - E_0)/\Gamma$, where Γ and E_0 are the resonance width and energy. For the normalised frequency Ω, the shape of the Fano response changes with varying the Fano parameter, as shown in Figure 3.24. The phase shift δ is periodic in π, and in the extreme cases when $\delta \rightarrow n\pi$ (where n is an integer), equivalent to $q \rightarrow +\infty$ and $q \rightarrow -\infty$, the resonance becomes a Lorentz shape. When q = 0, as seen in Figure 3.24, the shape is Quasi-Lorenzian.

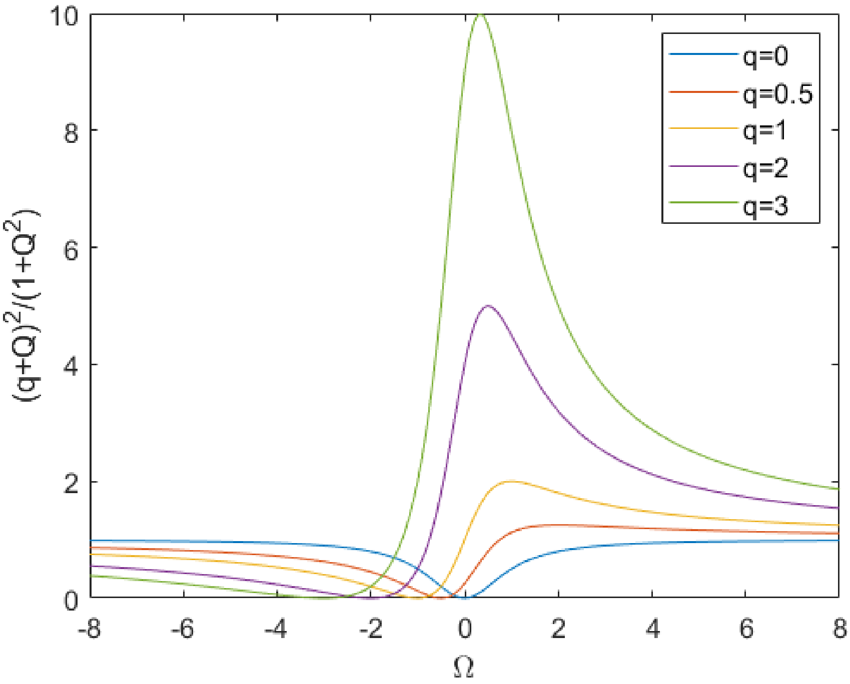

FIGURE 3.24: Fano resonance dispersion with varying Fano parameter q

By fitting the resonance shapes in Figure 3.23 to the Fano equation, it can be seen that the resonances indeed fit the Fano shape with a $q = 1.5$ for the resonance at 1.548 THz and $q = 1.2$ for the resonance at 1.736 THz, as shown in Figure 3.25.

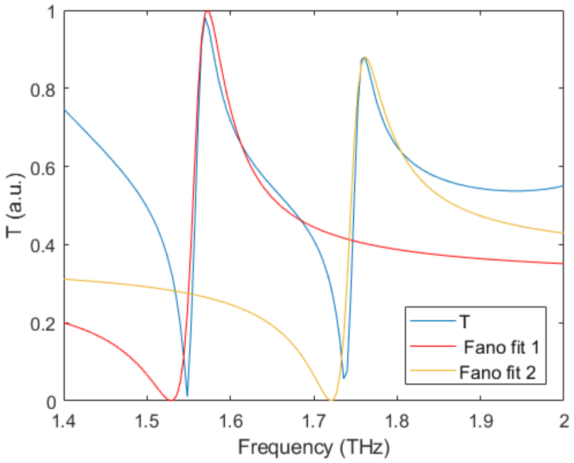

FIGURE 3.25: Fitting of Fano shapes to the resonances in metamaterial transmission as seen in Figure 3.23

It can be shown that the Fano resonances in the transmission spectra are indeed generated by the excitation of the guided resonances of the photonic crystal. By analysing the transmitted fields in the time domain, two distinct transmission pathways can be observed - an initial pulse, which is the direct excitation from the source, and a slowly decaying tail, which is due to the guided resonances Figure 3.26. By apodising the tail from $t = 8$ ps and applying the Fast Fourier Transform (FFT), the frequencies of the guided resonances from Figure 3.23 can also be seen in Figure 3.27, which now have the expected Lorenzian shape.

The transmission spectrum as a function of the crystal guided resonances has been analytically developed by Fan and Joannopoulos [74], and for each mode frequency w_0, the transmission and reflection amplitude coefficients are given by

$$t = t_d + f\frac{\gamma}{i(w - w_0) + \gamma} \tag{3.2}$$

$$r = r_d \pm f\frac{\gamma}{i(w - w_0) + \gamma} \tag{3.3}$$

.

Here t_d and r_d are the transmission and reflection coefficients of the background,

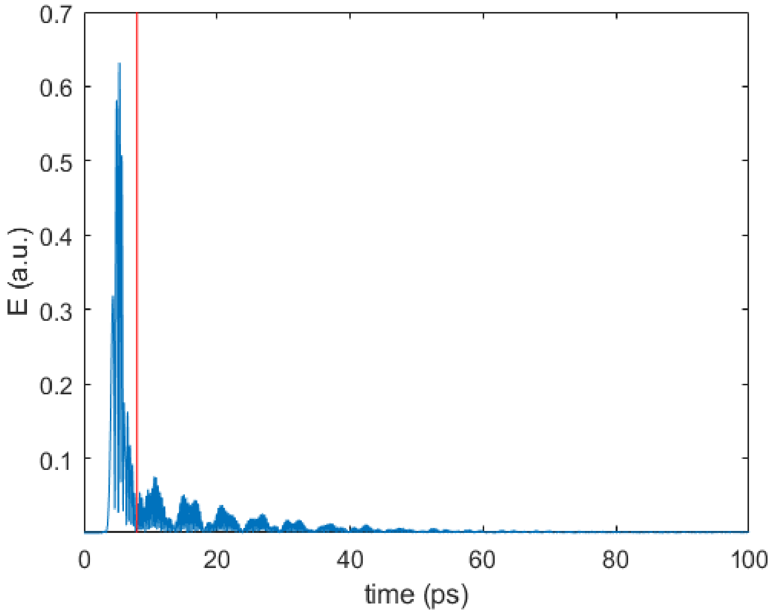

FIGURE 3.26: Metamaterial transmission as seen in Figure 3.23 in the time domain

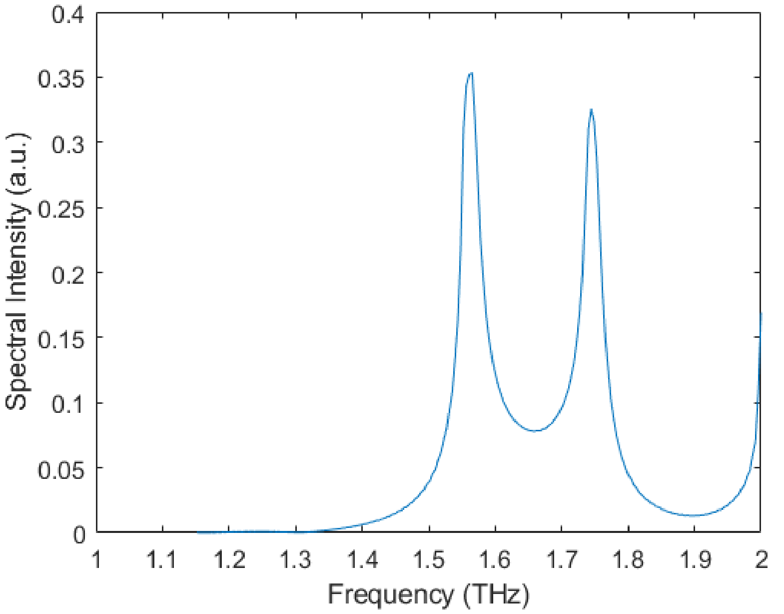

FIGURE 3.27: Fourier transform of the time domain signal shown in Figure 3.26 from 8-100 ps

which is represented by the Fabry-Pérot reflections from the substrate with an averaged effective refractive index. The parameter f is the complex amplitude of the resonance and w_0 and γ are the center frequency and width of the Lorentzian resonance.

3.3.1 Improving Split-Ring Metamaterial Resonance

So far it was shown that there are two mechanisms that contribute to the resonances in the split-ring based metamaterial transmission spectrum - the resonance of the split-rings themselves and the photonic crystal resonances excited by the Fabry-Pérot reflections in the substrate. There are three ways to design for the increase in intensity of these two oscillatory mechanisms. One is by matching a guided resonance to the split-rings resonance, therefore coupling more energy into the desired frequency. In this case the photonic crystal mode aids the split-ring mode. Alternatively, the photonic crystal can be designed, such that the split-ring resonance matches with a photonic crystal band gap. The band gap doesn't permit waves within the band within to be guided into the substrate, therefore they can efficiently radiate outside the metamaterial slab. This approach has been previously used to design highly efficient LEDs. Finally, the split-ring resonance can be used to change the substrate effective refractive index in a way that aids a higher-order photonic guided resonance. In this case the frequency band of interest is set by the photonic crystal and the split-ring structure has a supporting role. The metamaterial is most susceptible to changes in the substrate's refractive index when as an oscillator it is as underdamped as possible. The best way to quantify this is by comparing the resonator's Q-factor in the transmission (reflection) spectrum, defined as $Q = f_0/\Delta f$, where f_0 is the center frequency and Δf is the bandwidth of the resonance, defined at the full-width half-maximum (FWHM). The other useful parameter that contributes to the modulator performance is the amplitude of the resonance, which is proportional to the square root of the energy coupled to that resonance.

Effect of Substrate Thickness

In order to tune the transmission spectrum of the 2D photonic crystal, there are three features that can be varied - the effective optical thickness of the substrate, which is a function of its refractive index and physical thickness in the direction of wave propagation, the size and shape of the metallic structures in the crystal lattice and the lattice itself, again by changing its shape and size. Keeping the unit cell square with a periodicity of a=65 µm, for the circle features shown in Figure 3.23, with increasing substrate thickness the density of excited resonances also increases, as seen in Figure 3.29. Their density seems to saturate, but this convergence can be both due to limitations in the numerical calculation resolution and resonances that are close together merging into a single wider peak. The Q-factors of the resonances are calculated to be in the range between 50-210, with higher substrate thicknesses more likely to produce sharper resonances, but also lower resonant amplitudes as the energy is distributed between more modes (Figure 3.28).

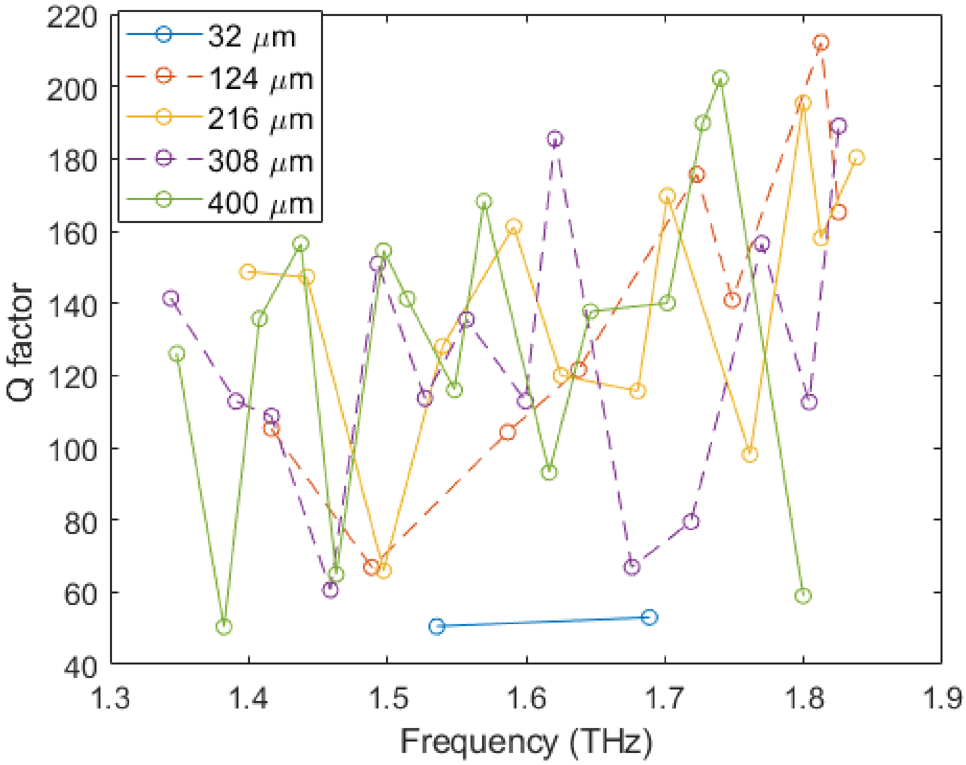

FIGURE 3.28: Resonance frequencies and their corresponding Q-factors with increasing substrate thickness

When computing the modes of the photonic crystal in 2D only, all modes are restricted to the lattice plane and therefore all modes behave as guided modes - they do not radiate outside the lattice plane. This is equivalent to the substrate and background material being infinite and retaining the crystal lattice symmetry throughout the z-axis. The introduction of a wave vector in the vertical direction produces a continuum of states, shown in the shaded gray area in Figure 3.30. This area is commonly referred to as the "light line" or "light cone", and is a continuous region indicating all possible frequencies of the bulk background. All modes within the gray area are resonance modes that are of interest in and can couple to the outside environment, while the modes below the light cone remain as the guided modes of the crystal and only propagate in the slab [75]. The area outside of the slab is referred to as the background. When the background of the metamaterial is uniform, the light cone boundary is given by the wave vector divided by the refractive index. This is what was observed for the metamaterial slab in Figure 3.16 - the background photonic crystal guided resonances were above the threshold frequency $f_t = c/an$, where a is the lattice constant and n is the refractive index of the substrate. For a periodic background condition, the boundary of the light cones is the lowest band in the bandstructure computed by the 2D equivalent [75].

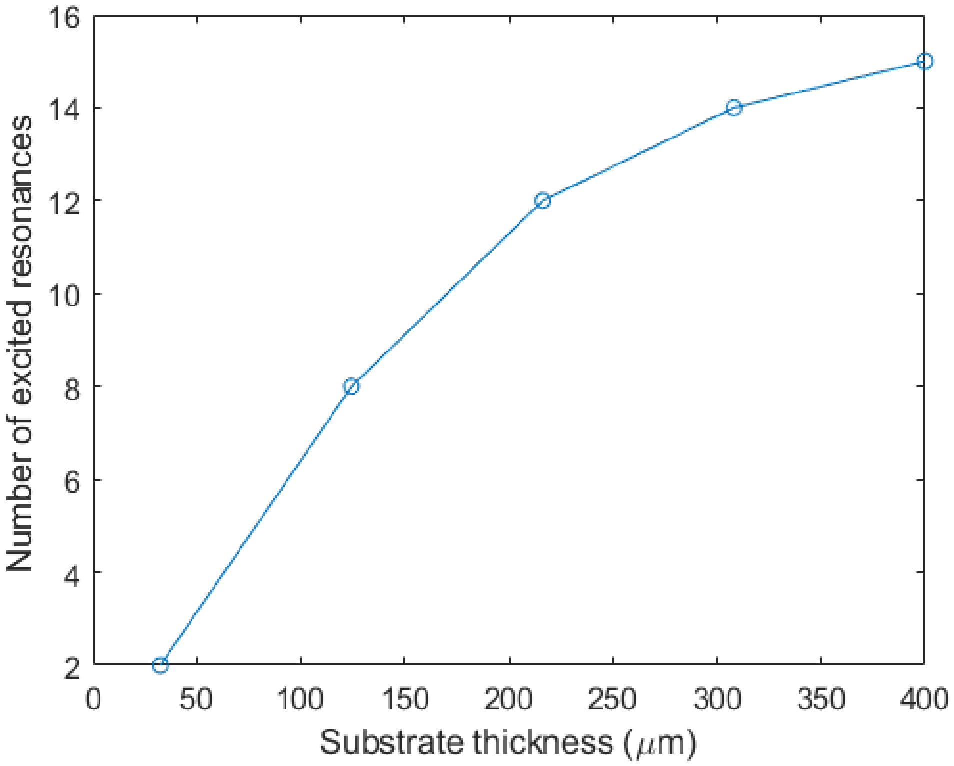

FIGURE 3.29: Increasing number of excited resonances in the 0.3 -2 THz range with increasing substrate thickness

Tuning 2D Photonic Crystal Modes

To find out the guided modes of a photonic crystal slab, its bandstructure was numerically computed using Lumerical FDTD. The split ring can easily be approximated to circles, as it was shown not to affect the location of the crystal's guided modes significantly. For a square lattice the first irreducible Brillouin zone is Γ-X-M-Γ, as shown in Figure 3.30. In order to calculate the band diagram of a photonic crystal using FDTD, a common method is to excite all possible modes in the system by using randomly placed broadband dipole sources. Where modes exist, the fields will continue indefinitely, whereas all other frequencies will destructively interfere and disappear. Therefore randomly placed and polarised dipole sources were injected into the metamaterial surface and the time domain fields were recorded at different wave vector points in the Brillouin zone using Lumerical FDTD. By taking the FFT of the time domain fields and recording the modes which persist in the plane of the metamaterial, the guided modes were extracted. For a finite slab thickness of the photonic crystal, periodic boundary conditions can be still used in the z-axis, while ensuring that the simulation boundary is far enough from the substrate. When there is sufficient background between the periodicity of the substrate, the guided modes are not affected noticeably. (The guided resonances, however are, so this type of calculation should not be used to determine their positions. The FDTD transmission analysis showed previously is more suitable for finding the exact positions of the guided resonances.)

To demonstrate coupling of the split-ring resonance to a guided resonance of the photonic crystal, the following structure was designed. The photonic crystal shown in Figure 3.23, showed a strong guided resonance at 1.518 THz and the location of that resonance has showed low susceptibility towards changes in the size of the metal disks, as long as the rotational symmetry is conserved. To match that resonance, the split-rings were resized appropriately, as shown by the individual split-rings in the unit cell in Figure 3.31. As the size of the split-rings is quite small in comparison to the crystal lattice 65 µm, and this decreases the interaction between adjacent cells, instead of one split-ring, the unit cell was designed with a 3 x 3 array of split-rings, as shown in Figure 3.31. This way any split-ring geometry can be matched to any lattice size, as long as the individual split-ring is smaller than the lattice constant. The polarisation of the E-field is perpendicular to the split-ring gap line, to ensure the strongest split-rings response. The transmission spectra of the split-rings on an infinite substrate has been calculated with a cell size of 14 µm , matching the separation of the split-ring array. There is a clear improvement in

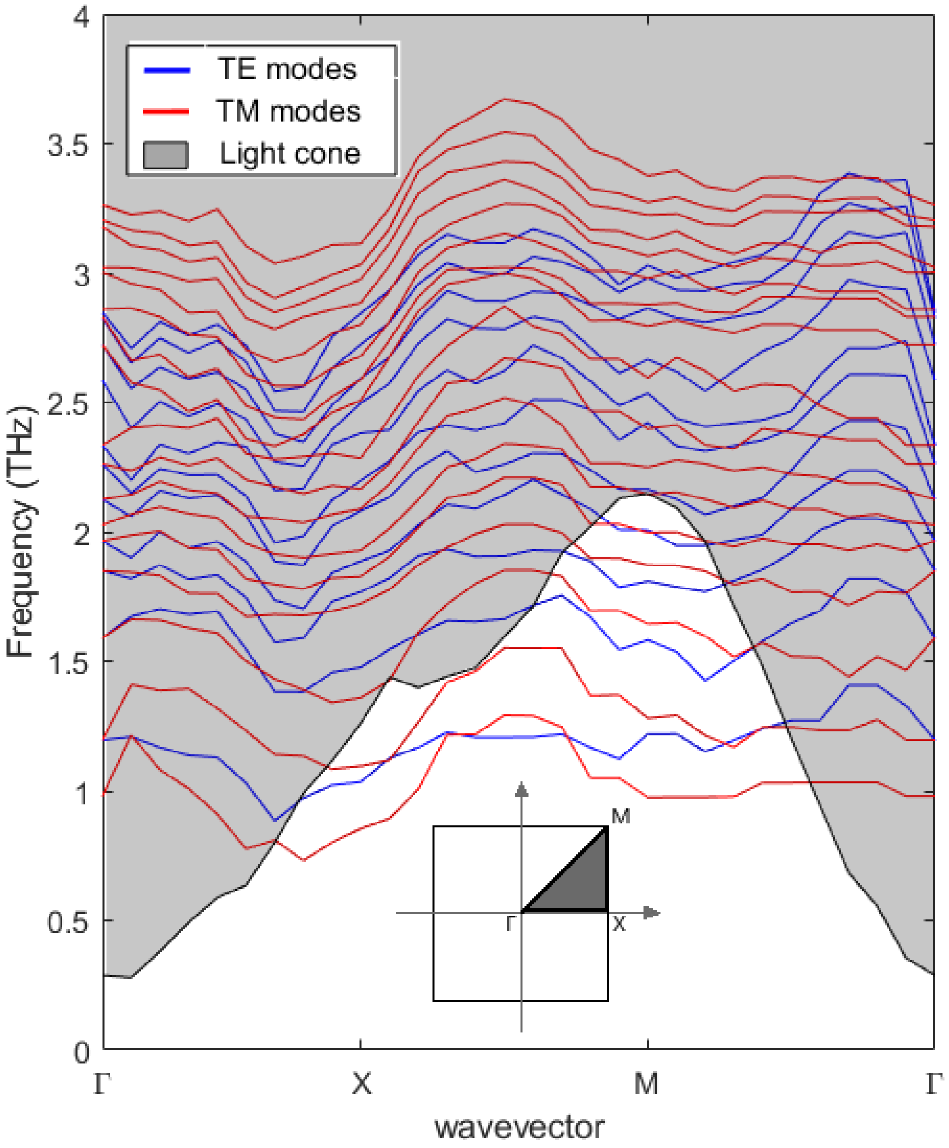

FIGURE 3.30: Band diagram of the metamaterial described in Figure 3.23

the Q-factor of the matched resonance in comparison to just the split-ring resonance. The former being Q = 93.98 with an amplitude of A = 0.91, and the latter having Q = 28.48 and A = 0.56, giving a more than three-fold improvement in the Q-factor and a 91 % change in transmission at resonance.

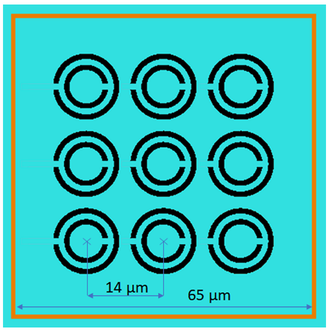

FIGURE 3.31: Unit cell geometry

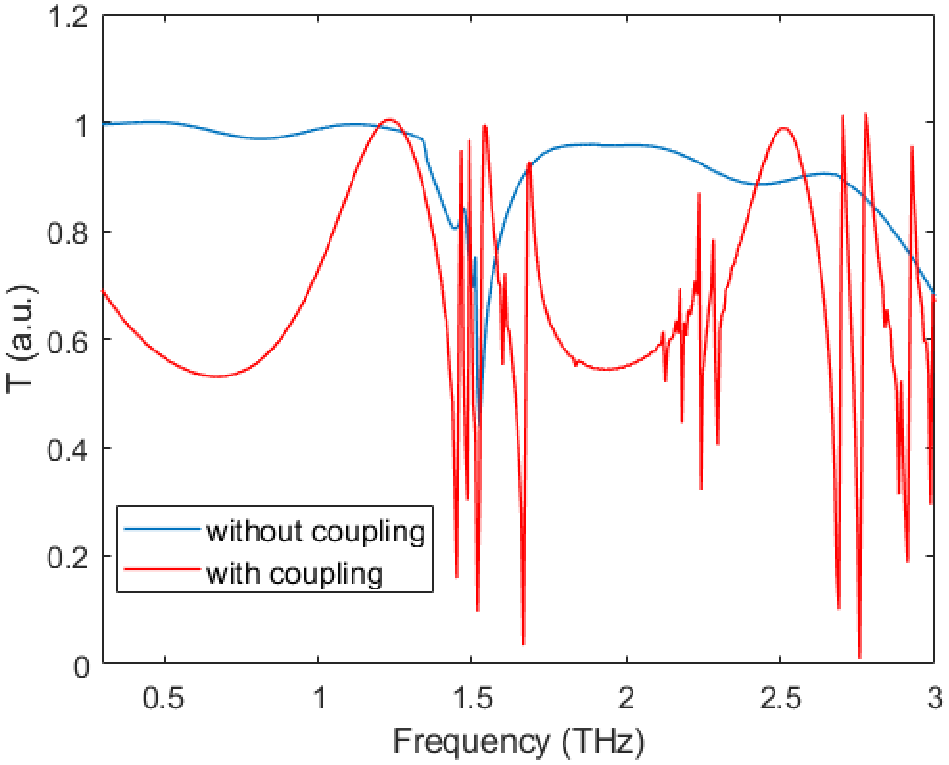

FIGURE 3.32: FDTD simulated transmission spectra of the structures from Figure 3.31

To confirm the theory presented so far and demonstrate lower resonance enhancement of the guided resonances, the method was tested experimentally.

3.4 Experimental Results

The SRR and JSRR metamerial geometry introduced earlier was resized and simulated using Lumerical FDTD, so they have a resonant frequency within the 0.75-1.1

THz band, coinciding with our VNA. The transmission response of the metamaterials without the effects of a finite slab with increasing surface conductivity is shown in Figure 3.34. The most effective coupling to the slab resonant modes is expected to be at 0.83 THz for the SRR structures and 0.95 THz for the JSRR structures, where the gradient of the transmission is the highest (in the 0.75 - 1.1 THz region). The Fano resonance at 0.4 THz of the JSRR seen in Figure 3.34b was calculated to have a transmission above 1. This is a numerical error produced by the FDTD boundary conditions, as the response is too resonant to decay fully. Convergence testing proved that this does not affect the rest of the transmission response in a significant way, but achieves shorter simulation times. The JSRR structures were designed such that the Fano resonance was not included in the measurement bandwidth, as the minimum feature size of the structure became too small to be reliably fabricated using the available microlithography methods. The structure dimensions can be seen in Table 3.2.

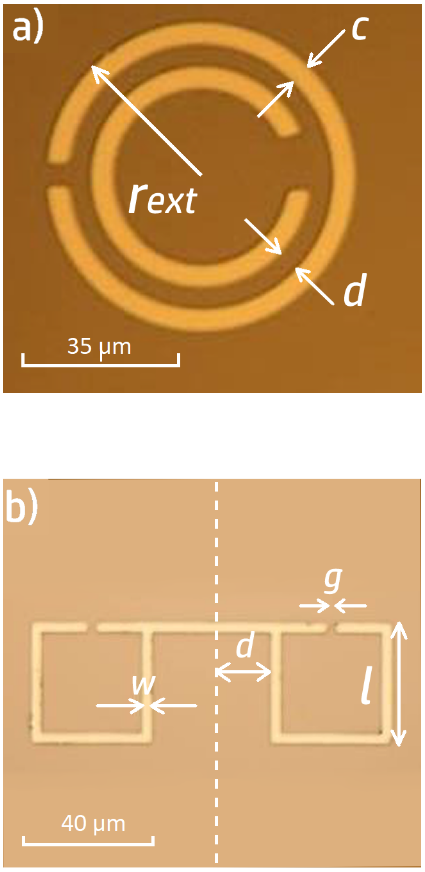

FIGURE 3.33: Microscope photograph of the fabricated SRR (a) and JSRR (b) cells on silicon

TABLE 3.2: Table of the dimensions of the SRR and JSRR features respectively, corresponding to the notation shown in Figure 1.

SRR	μm	JSRR	μm
cell x-dimension	105	cell x-dimension	180
cell y-dimension	105	cell y-dimension	70
c	5	d	20
r_{ext}	35	g	3
d	5	w	3
		l	40

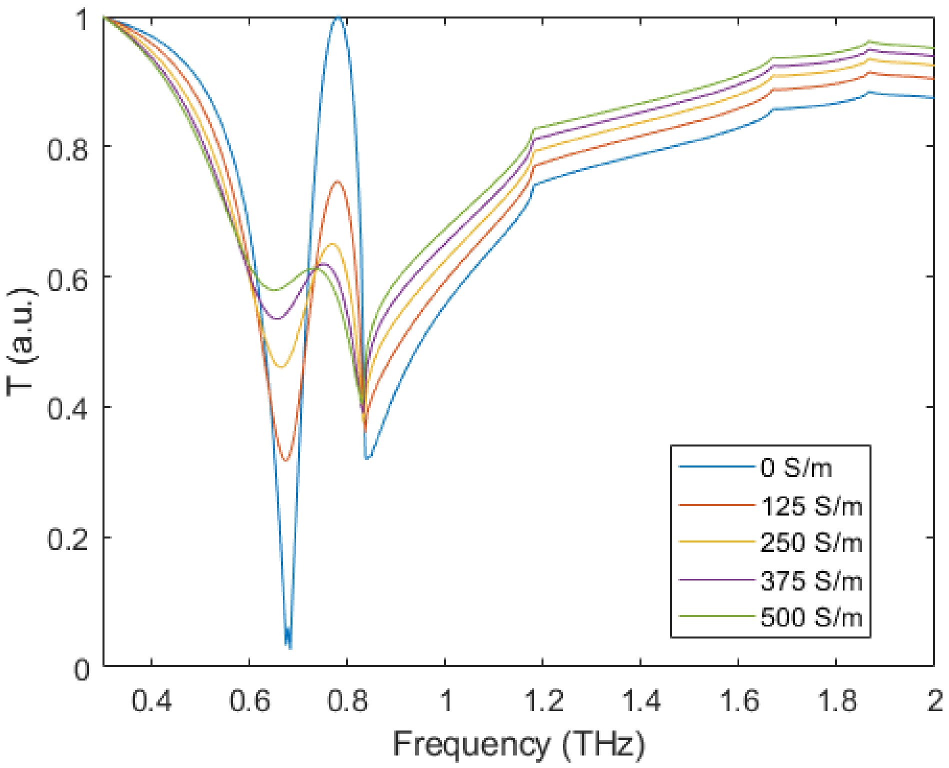

(A) SRR structures

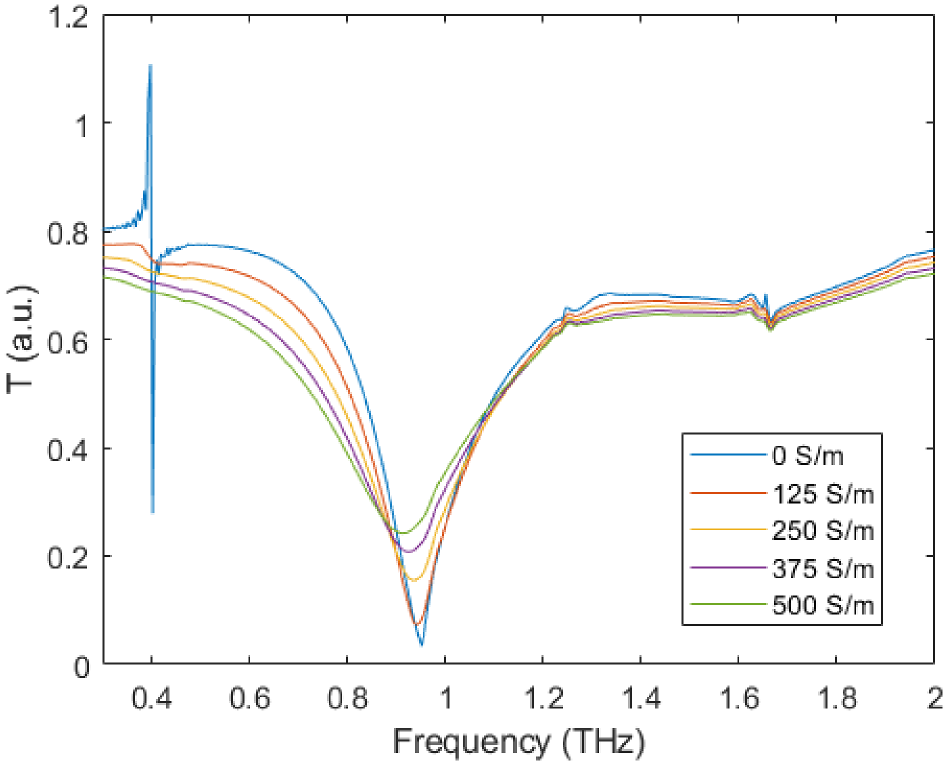

(B) JSRR structures

FIGURE 3.34: Computed transmission spectrum using apodised time-domain signal to remove substrate reflections

The modulators were microfabricated on a 2-inch, 325 µm thick HRFZ silicon wafer, using standard photolithographic techniques. A 200 nm aluminum layer was thermally evaporated on to the substrate and etched to create the metamaterial structures. The measurement equipment used was the 4-port Keysight N5224A VNA, equipped with VDI WR1.0 THz frequency extender heads. A set of 1-inch gold coated parabolic mirrors was also used, as the active area of the modulators was a 1x1 inch square, centered on the silicon wafer. The measurements were set up so that the THz radiation is normal to the resonant features. The THz beam was polarized perpendicular to the line connecting the split ring gaps, which is expected to give the highest resonance response [66]. The source used for the optical modulation was the 170 W CW white light photodiode array introduced earlier in the chapter. The optical radiation was incident at an angle on the surface of the metamaterial, as seen in Figure 3.35, in order not to obstruct the THz signal. The angle of incidence was of small significance in comparison to the distance between the light source and the sample, as the source beam was extremely divergent. The comparison between the computed transmission for finite slab thickness and the measured transmission of the metamaterial modulators with no optical illumination is shown in Figure 3.36. Good agreement is shown between the predicted and the measured response, with an R value of 0.73 for the SRR structures and 0.805 for the JSRR structures respectively. The effects of the guided resonances of the substrate slab are clearly present,

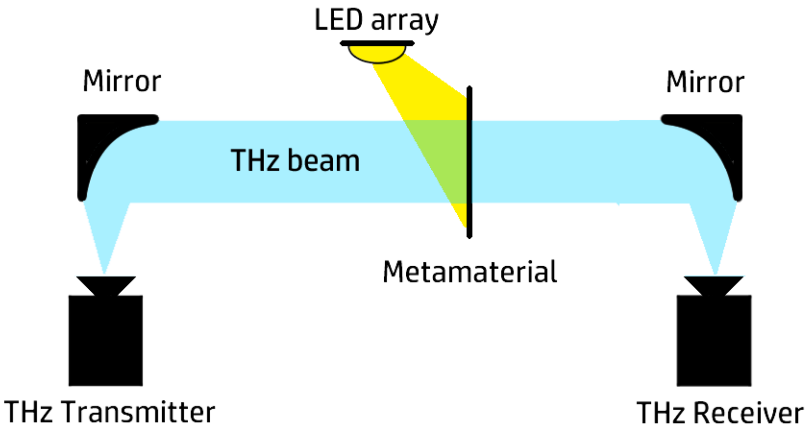

FIGURE 3.35: Diagram of the measurement set up.

as the transmission response is very different from the infinite substrate response shown in Figure 3.34 and SRR responses obtained through THz-TDS measurements in literature [76], where the time-domain signal is apodised to remove secondary reflections.

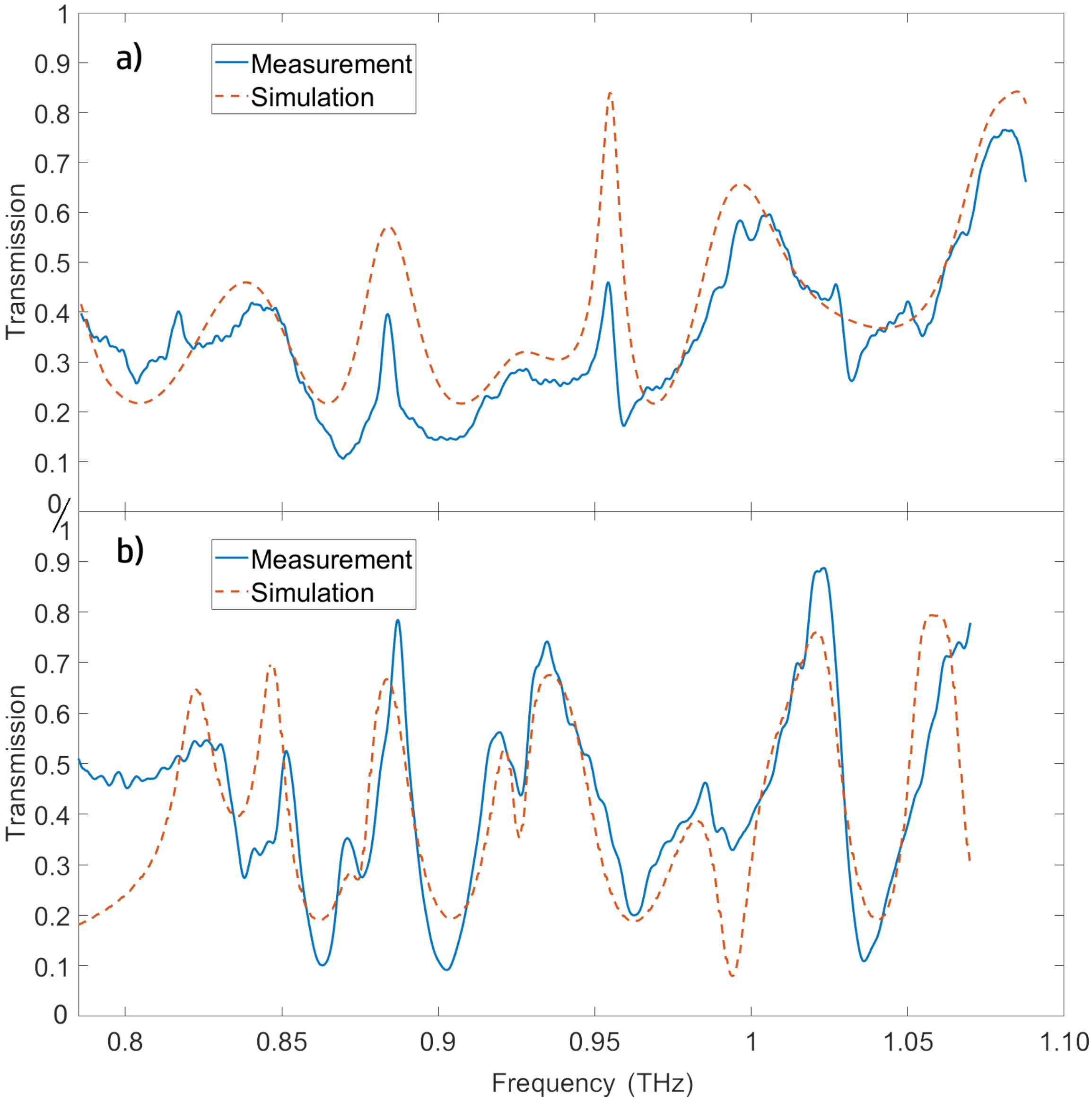

FIGURE 3.36: Measured and simulated transmission spectra of: a) JSRR features and b) SRR features, under no illumination.

The optical modulation response of the metamaterials was subsequently investigated. To account for any thermal effects on the metamaterial conductivity, the transmission was continuously recorded in time. The photodiode source was also switched on and off with pauses in between to allow cooling of the sample. The modulators was under illumination between 20-100s, switched-off between 100-160s and then switched on again for another 100s. This can be seen in the results shown in Figure 3.37. The average illumination power density was measured to be 200 mW/cm^2. Under illumination, the transmission peaks exhibited significant amplitude and phase modulation depth. An amplitude modulation depth of 80% was achieved for the SRR structures at the transmission peaks as shown in Figure 3.37 a). This also corresponded to a phase shift of over 100° (Figure 3.37 b)) at the same frequencies, most pronounced at 0.87 THz, 0.895 THz and 1.03 THz. The overall transmission also remained quite high, averaging at 70% for the resonant peaks under no optical illumination. Similar results were observed with the JSRR metamaterial, albeit not as strong as in the SRR features. The two maximum amplitude modulation depths of the JSRR cells were found to be 56% and 36%, at 0.88 THz and 0.95 THz respectively, which correspond to the maximum phase differences of -131° and 111° at the same frequencies. The maximum amplitude and phase modulations also correspond to the sharpest peaks in the transmission plot for the JSRR metamaterial and 0.88 THz and 0.95 THz. These results compare well to performance of other state of the art THz metamaterial modulators presented in Figure 3.1, while employing a low-power, non-coherent, broadband optical source. Modulation enhancement through photonic crystal slab coupling can also be employed to any existing resonant structure design with very little modifications.

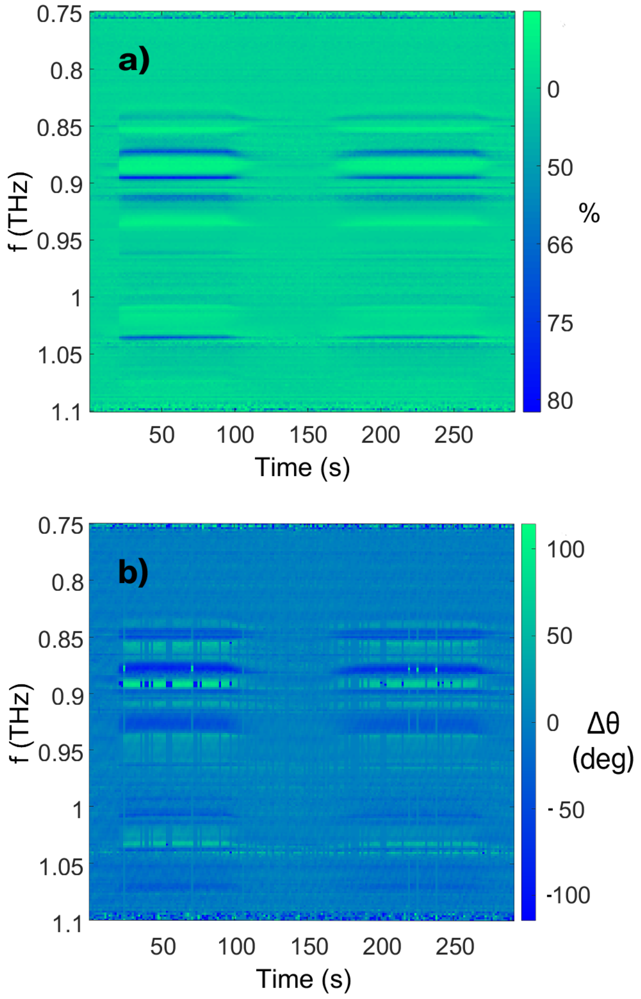

FIGURE 3.37: a): Amplitude modulation in time of SRR features, with illumination switched on between 20-100 seconds and 160-260 seconds. b): Phase difference in time of SRR feautures, with illumination switched on between 20-100 seconds and 160-260 seconds.

3.5 Spatial Optical Modulators

The SRR-based optical modulators were subsequently tested as spatial THz modulators. Spatial modulation finds application in beam forming and steering, compressive sensing, THz image spectroscopy and increasing the performance of amplitude and phase modulation in high speed THz communication [52]. Previously presented techniques for the implementation of THz spatial light modulators (SLMs) include electrically reconfigurable metamaterials, addressable phase changing materials, optically controlled photo-active semiconductors, micromirror arrays and microfluidic droplet arrays [77]. Here a retrospective approach to THz spatial modulation is presented, by using the well known in Fourier optics 4F system. This method has been historically used for real-time image processing in filtering applications, such as edge detection. Here it is used to directly apply a modulation function to the Fourier transform of the original spatial signal in order to achieve beam forming and steering.

The 4F system consists of a set of two identical thin lenses, two focal lengths (F) apart from each other. The image plane, which is one focal distance in front of the first lens, is then reconstructed one focal distance after the second lens, and the plane between the two lenses gives the Fourier transform of the image plane. The measurement system used was a 2F system, as shown in Figure 3.38. A 4F system is a 2F system, symmetrical about the Fourier plane. By applying a spatially modulated signal to the image plane through optically illuminating the metamaterials previously presented, the Fourier transform of that signal can be reconstructed at the Fourier plane. The generated THz signal in Figure 3.38 can be approximated to a point source, coming from the VDI extender head horn antenna. The THz beam is then collimated to a plane wave using parabolic mirrors. The image in the Fourier plane is then reconstructed by scanning with a single pixel detector over the surface area of the thin lenses. The detector is again a VDI extender head, mounted on an XYZ linear stage, which can achieve a spatial resolution of 0.5 mm.

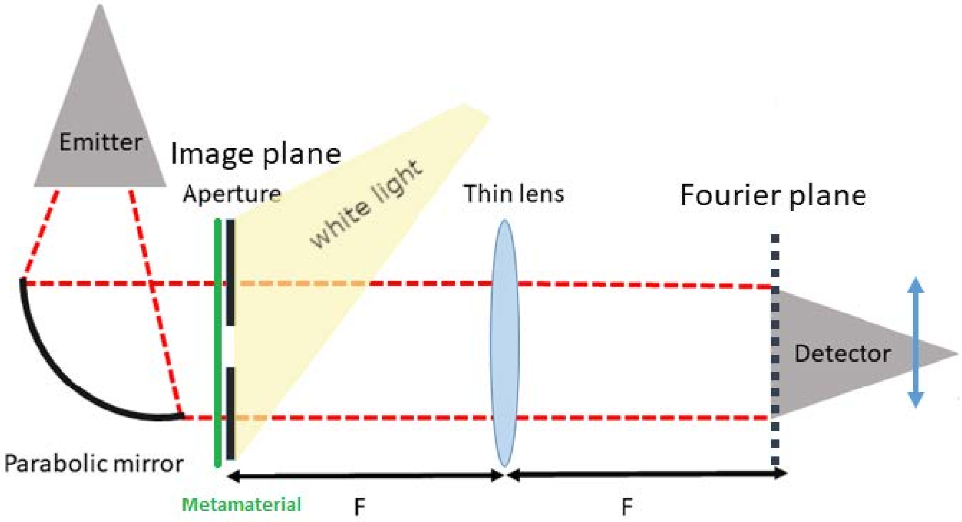

FIGURE 3.38: Concept diagram of the 4F measurement setup

Several apertures (masks) were tested in the image plane and the image was modulated using the SRR metamaterial modulator actuated using the Cree LED array. The scans were done at 0.895 THz, corresponding to the highest modulation depth and a transmission of 80 % under no illumination. A square, rectangle and a circle aperture was tested, with dimensions as shown in Figure 3.39. The aperture sizes had to be less than 1 x 1 inch, in order for the beam size to not exceed the metamaterial active region.

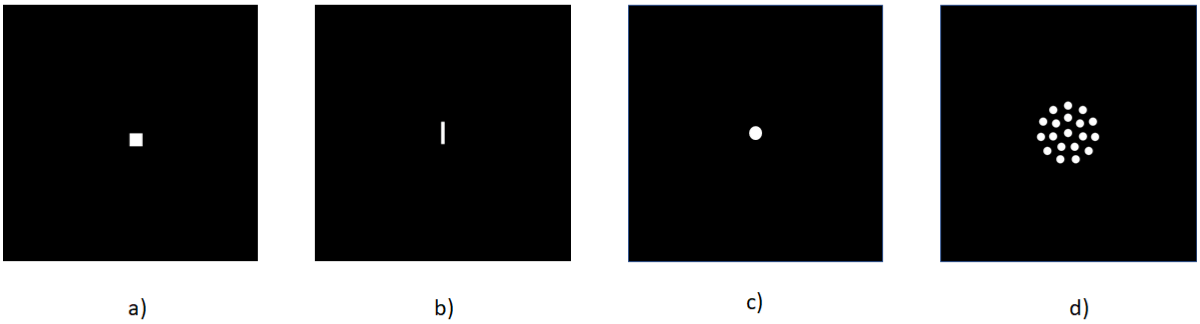

FIGURE 3.39: Aperture masks for spatial Fourier transform a) 1 cm x 1 cm square aperture, b) 1.8 cm x 0.3 cm rectangle aperture, c) 1 cm - diameter circle aperture, d) cluster of circles with 0.6 cm diameter each

The corresponding normalised modulated to unmodulated spatially recorded image at the Fourier plane is plotted in Figures 3.40, 3.41 and 3.42, next to the numerically computed 2D Fourier transform of the apertures. A window function was applied to the calculated transform, in order to filter high frequency components, which cannot be resolved due to the effective size of the detector and the noise in the system. Features in the order of 5-10 mm can be seen to be better defined than smaller ones, with Figure 3.40, showing some definition in gaps of 2 mm and above. The vertical features expected for the rectangular aperture (b) were in the order of less than 0.5 mm, hence below the maximum resolution of the detector. A relatively good contrast in the features for the circular aperture (c) can be observed.

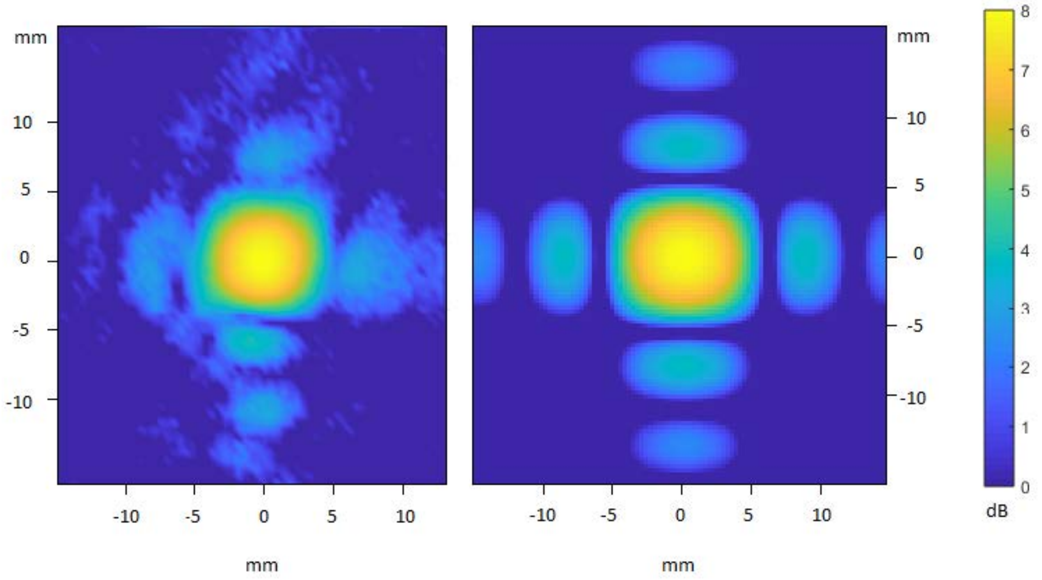

FIGURE 3.40: Comparison between the measured Fourier transform of the masked metamaterials (left) and the corresponding calculated transform (right) for the square aperture in Figure 3.39 a)

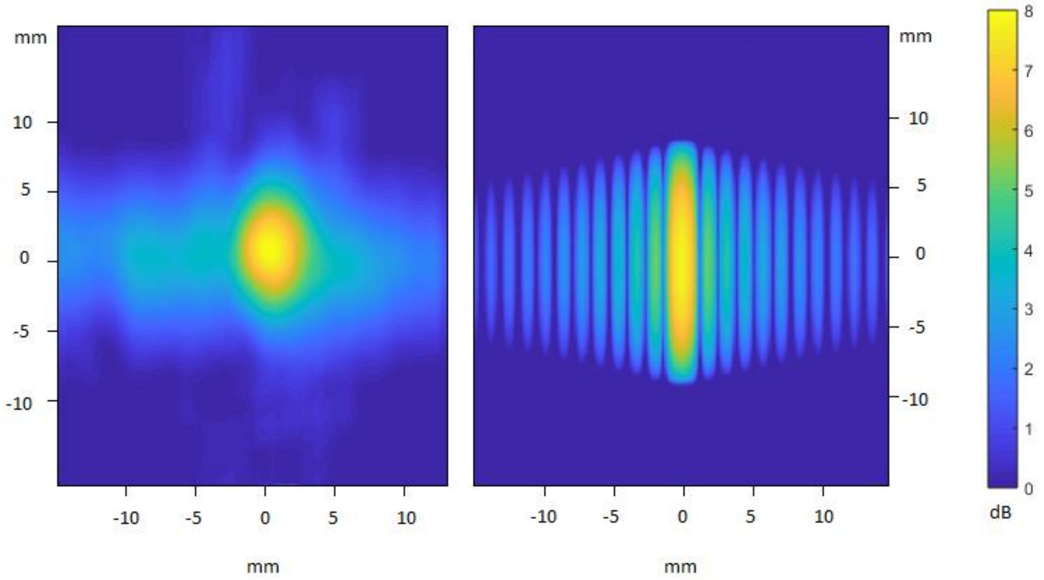

FIGURE 3.41: Comparison between the measured Fourier transform of the masked metamaterials (left) and the corresponding calculated transform (right) for the rectangle aperture in Figure 3.39 b)

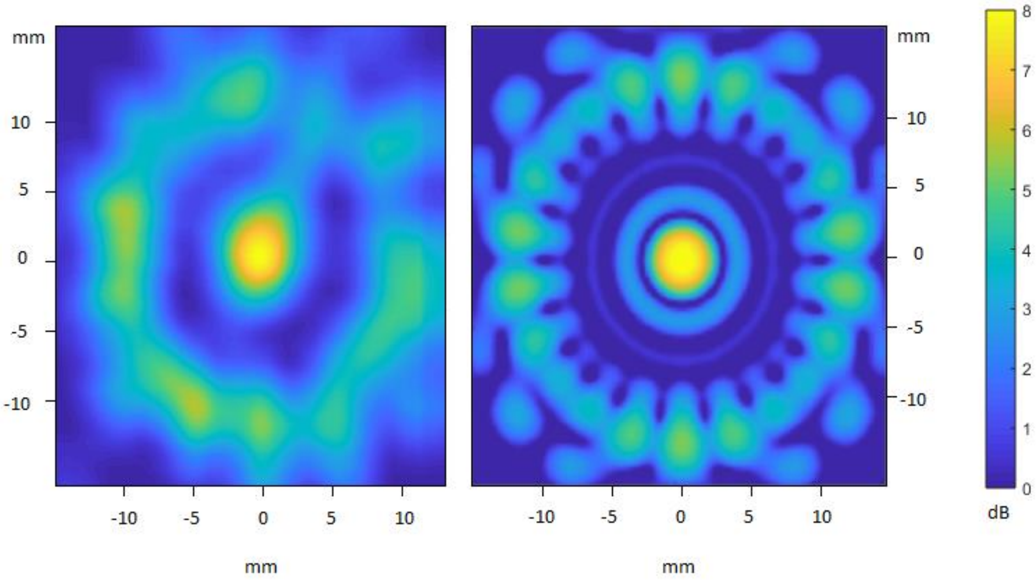

FIGURE 3.42: Comparison between the measured Fourier transform of the masked metamaterials (left) and the corresponding calculated transform (right) for the circle aperture in Figure 3.39 c)

As the Fourier transform of mask d) is quite complicated, which makes feature recognition cumbersome, the Inverse Fourier Transform (IFT) of the measured modulated signal was computed and compared to the original mask, shown in Figure 3.43. The center circle matches to the highest field intensity in the image, although the circular shape is not well defined. The bottom circles exhibit a better fit than those at the top, suggesting that there is misalignment in the beam during the single-pixel scanning. Given the low power of the THz source and the low pixel resolution of the system, the metamaterial modulators demonstrate spatial contrast between the examined features which is promising for further applications.

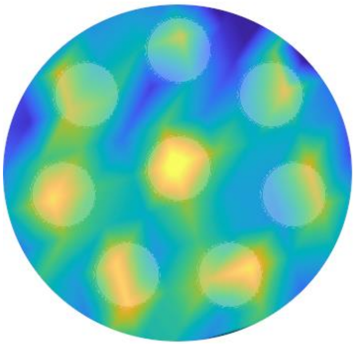

FIGURE 3.43: IFT of recorded image compared to the image mask

3.6 Summary

A new approach towards metamaterial design for THz optical modulators is presented. Actuating metallic resonators on a semiconductor substrate with visible light, is known to achieve amplitude and phase modulation in THz frequencies. Photonic crystal resonant modes from the substrate slab were found to be excited by the metamaterial lattice. By tuning the symmetry and size of the metamaterial unit cell to the substrate thickness and resonant frequency of the individual resonators, an enhanced resonant response is achieved. The design is tested with both standard split ring metamaterial geometry and conductively coupled square split rings on HRFZ-Si substrate. A maximum amplitude modulation depth on 80 % and phase modulation of 131 ° is achieved by optically switching the metamaterial with a white light, incoherent LED array. The approach can be easily adopted in various metamaterial applications to increase their performance. Rather than a single modulation frequency, the design allows for multiple simultaneous frequencies of operation, depending on the tuning. The application of the metamaterial as a spatial modulator is also demonstrated.

Chapter 4

THz Metrology

4.1 THz Ellipsometry

4.1.1 Introduction

The following chapter discusses the development of an angle-resolved measurement method in THz frequencies for thickness measurements and material characterisation. The method enables the use of a 4-port VNA with THz range extender heads as a fully automated THz ellipsometer. As opposed to polarisation measurement techniques in the infrared and optical frequencies, where the polarisation state is analysed using wave plates or phase modulators to extract complex data, most THz measurement instruments measure phase data directly, making ellipsometry a suitable candidate for material characterisation [78]–[82]. TDS-based methods provide a large frequency bandwidth, but suffer from inflexibility when it comes to measuring different angles of incidence. CW-sources such as the VNA on the other hand, can provide the flexibility for a fine sweep of incident angles, as well as high resolution in the phase information. The presented system is capable of 200° rotation around the optical axis with 0.25° resolution, as well as direct measurement of the complex S and P-polarisation reflection parameters. As the phase information is directly measured, the system is simplified to using only linear polarisers in the beam path. Subsequently, the data extraction is also simplified and layer models using Fresnel equations can be applied without going through the traditional Mueller-Jones formalism [83]. The physical background behind the ellipsometry technique is first discussed, followed by characterisation of the measurement system and the data extraction and analysis algorithms. The characterisation of different materials is then discussed, including materials with low refractive index and high absorption in the THz range, as well as composite materials. In-situ measurements of the changing thickness of a Si wafer etched in KOH is presented, followed by measurements of an optically anisotropic metamaterial.

4.1.2 Ellipsometry Background

Ellipsometry is traditionally a technique used for the characterisation of the optical parameters of thin dielectric films. The changes in polarisation of light after its interaction with a material, such as after reflection, transmission, absorption or scattering, can be used to extract material parameters. Properties like film thickness, dielectric constant, surface roughness, doping concentration, crystallinity and others all have an effect on the change in polarisation [84]–[86]. The name "ellipsometry" derives from the fact, that most light that undergoes interaction with a material becomes elliptically polarised - the transverse and parallel component of the polarisation are non-zero, non-equal and not in phase. In the general case, any known polarisation initial and end state is sufficient to describe the system. The change in polarisation is defined by the complex ratio ρ between two linear polarisation states - an "S" polarisation, where the electric field oscillates perpendicular to the plane of incidence, and a "P" polarisation, parallel to the plane of incidence (Figure 4.1). The ratio is represented by an amplitude component Ψ and a phase difference Δ, as shown in Equation 4.1.

$$\rho = \frac{r_p}{r_s} = \tan \Psi e^{i\Delta} \tag{4.1}$$

In order to insure the maximum difference between r_s and r_p, ellipsometry measurements are taken at incident angles around the Brewster angle. For an interface between two materials with different indexes of refraction, the Brewster angle is given by

$$\theta_B = \arctan(\Re(n_2)/\Re(n_1)) \tag{4.2}$$

where n_1 is the refractive index of the medium of incidence and n_2 is the index of the second medium. It is the angle at which r_p is at its minimum. For non-absorptive materials r_p can reach zero, meaning that P-polarised light is fully transmitted at this angle.

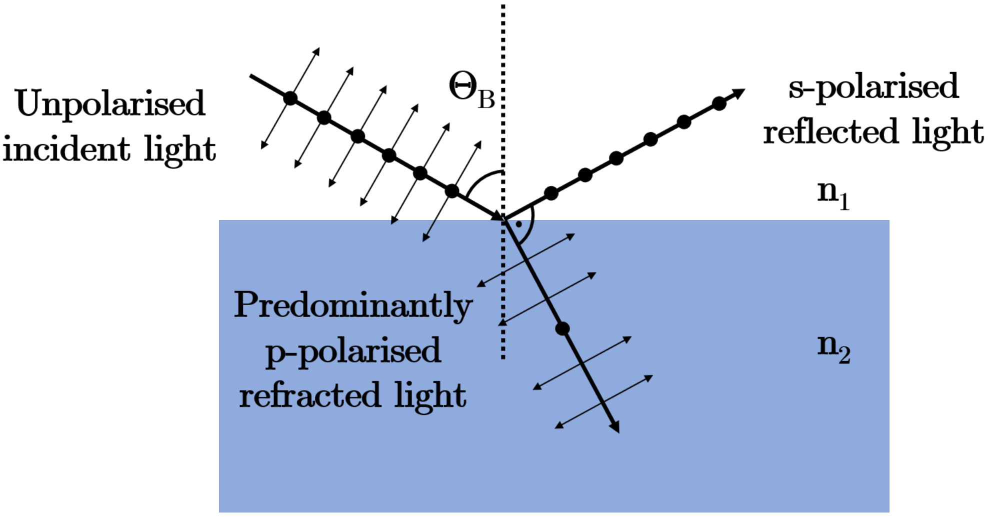

FIGURE 4.1: Brewster angle

As the change in polarisation is essentially a phase difference, ellipsometry is not a diffraction-limited measurement technique and can reach sub-wavelength resolution. It is also an indirect technique, as the optical material parameters cannot be directly extracted from the measurement data, but always have to be compared to a model, as shown in the diagram in Figure 4.10. This means that in order for right model to be applied, the structure under investigation must be known. For optically isotropic and homogeneous structures, the simplest case, known as standard ellipsometry can be applied. This assumption is valid for amorphous materials and crystalline materials with a cubic crystal structure. Anisotropic materials, such as composite metamaterials, however can introduce depolarisation, where S-polarised light can be converted to P-polarised and vise-versa and more general models must be applied [87]–[89]. The model must also account for stacked structures, where a single-layer approximation of the target is no longer valid. Ellipsometry setups can also be divided into single-frequency and spectroscopic. Single-frequency ellipsometry measurements tend to use high-powered sources, such as lasers, which provide a higher signal to noise ratio than spectrosopic measurements, but they also only provide the response of the system for only a single frequency, which is not sufficient for the application of generalised anisotropic models .

4.1.3 Angle-Resolved Measurement Setup

In order to automate the measurement of a sweep of incident angles, a proprietary stage for the VNA extender heads was developed. The stage, as shown in Figure 4.2 has two aluminium plates, which are attached to the optical table by the red screw. They can then freely pivot around that point, with the use of bearings that reduce the friction as they move on the table. A 15-cm motorised linear stage with an extender plate was attached to both plates via connecting arms, which pushed the plates simultaneously and determined the angle θ between them. The plates have slots, so that the THz extender heads can be mounted on them. This already provided a rough alignment of the system and the two angular plates could be fixed and screwed parallel to each other, providing a simple transmission setup. Once the system was finely aligned, with the sample placed on a rotating stage in the pivoting point of the plates, the angular setup could automatically switch between normal transmission and reflection at a desired angle, while maintaining its alignment.

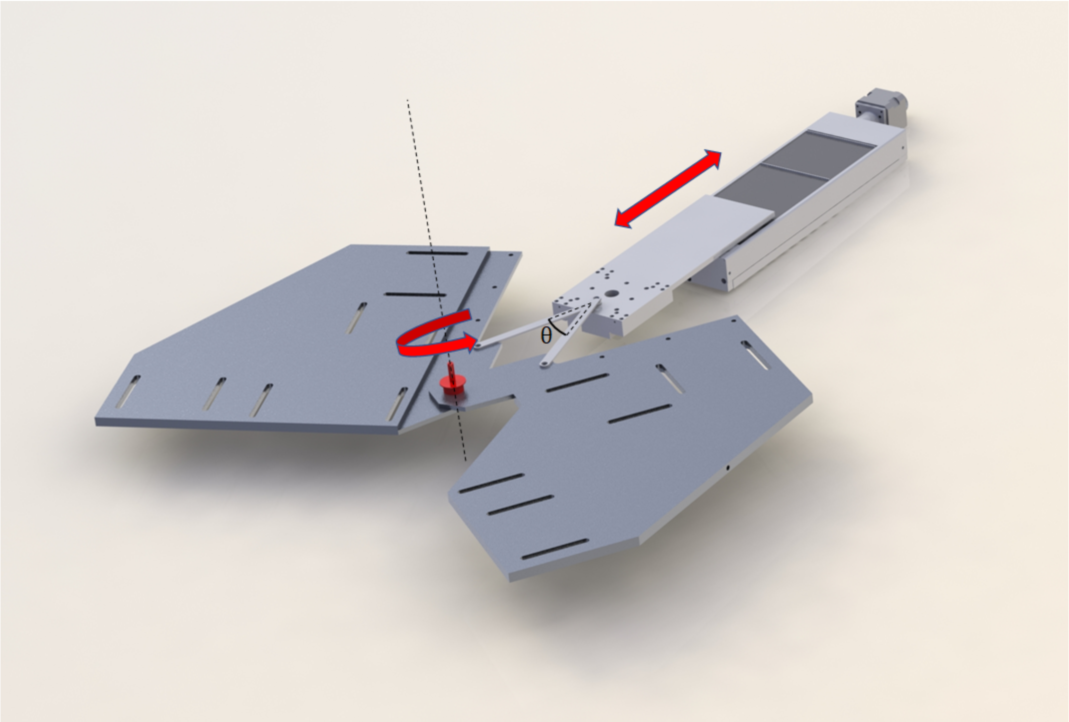

FIGURE 4.2: Ellipsometry angular setup

As the linear stage only had a limited range, the connecting arms could be moved to different positions, in order to achieve larger angles. The arms' attachment points on both the angular plates and the linear stage extender plate are specified with their corresponding angle ranges in Figure 4.3. It should be noted that even though the plates could freely rotate in a range between 0-200°, a larger force is required to push on them for values of θ above 51°. This is something our motor could not handle, but it is entirely possible with a more powerful one. Angular sweeps in reflection were fully automated in a MATLAB GUI, where the the input parameters were the angle range, number of angle sweep points and the VNA measurement settings, such as the frequency range, number of frequency points, IF frequency and averaging. The results were then mapped in real time, showing 2D image plots of the magnitude and phase of the signal vs angle and frequency. A scan at a single angle took several seconds, depending on the VNA scan settings.

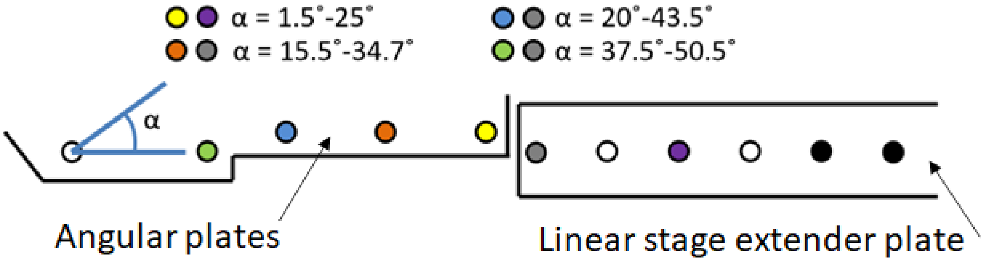

FIGURE 4.3: Diagram of connecting arms attachment points as seen in GUI for angle range selection

Improving the Polarisation Sensitivity of the Setup

For ellipsometry measurements it is necessary to switch between measuring S and P polarisation while also ensuring there is no cross-polarisation. The transmitting VNA head was placed on a 45° mounting bracket, so that the incident radiation is linearly polarised with equal components in the S and P polarisation, removing the need to reposition the transmitter. The receiver was mounted on a motorised stage, which could rotate it between 0° and 90° with respect to the plane of incidence, therefore switching between measuring the transverse or parallel polarisation. The VDI extender heads used diagonal horn antennas, which although polarisation sensitive, radiate approximately 10% of their total power into the cross-polarisation mode [90]. The measured difference in transmission between the transmitter and receiver directed at the same angle and with 90° offset only amounted to a spectral average of -3dB. The polarisation sensitivity was therefore insufficient for the intended purpose and polarisers needed to be added in the beam path - one aligned at 45° at the transmitter and one rotating with the receiver head. The optical instrument setup is shown in Figure 4.4.

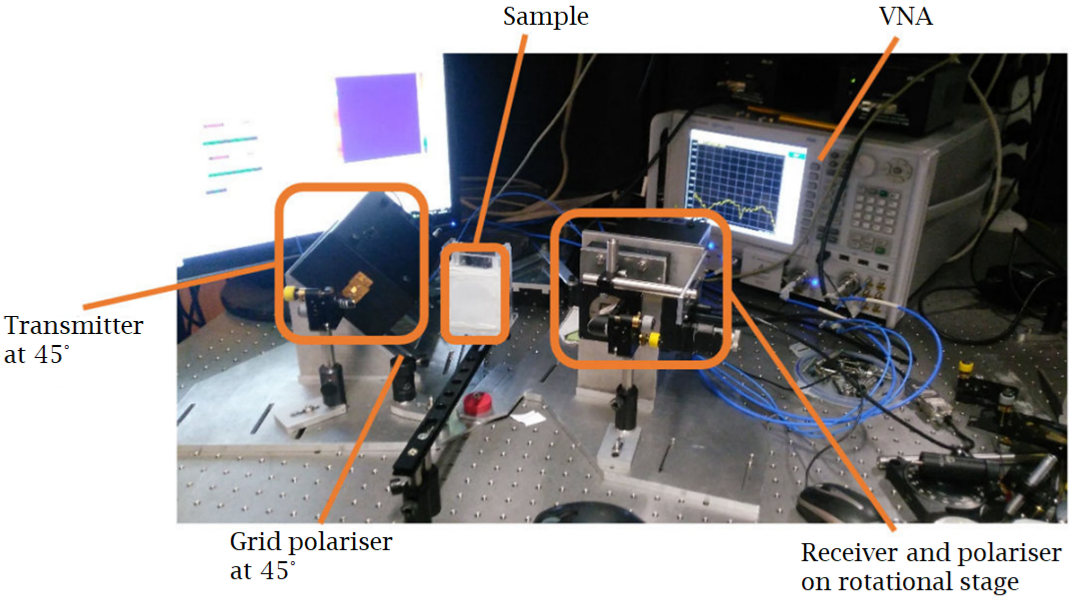

FIGURE 4.4: Photo of the ellipsometry setup [91]

The polarisers used were wire grid polarisers, fabricated in-house. Wire-grid polarisers as the name suggests, comprise of an array of thin (5-50 µm) parallel conducting wires and is commonly used at mm and sub-mm wavelengths. When the incident electric field is polarised perpendicular to the length of the wires, and the wires are thin compared to the wavelength, the grid becomes essentially transparent and the radiation passes through. When the electric field is oscillating parallel to the grid, the free electrons in the wire start oscillating along its length, re-radiating a wave. The re-radiated wave in the forward direction cancels out the original transmitted wave and the re-radiated wave in the backwards direction appears as a reflected wave [92]. For a wire grid with a wire thickness of 15 µm and varying spacing between the wires, the TM and TE polarisation transmission was numerically calculated using the Lumerical FDTD engine. The thickness of the wires was chosen close to the minimum resolution achievable when using a low-cost acetate mask for the photolithography process of microfabricating the wire grid, which is 10 µm. As shown in Figure 4.5, for the frequency band of interest - from 0.7 to 1.1 THz, the best trade-off between the isolation of the TE mode and transmission of the TM mode is achieved with a wire separation of 15 µm. This geometry is also in good agreement with microfabrication constraints. To fabricate the polariser, a 10 µm polyimide film was spun on a glass wafer. A 150 nm gold film was deposited using thermal evaporation and the wire-grid patter was transferred using photolithography and wet etched. The polyimide film was then peeled off the wafer to be free standing.

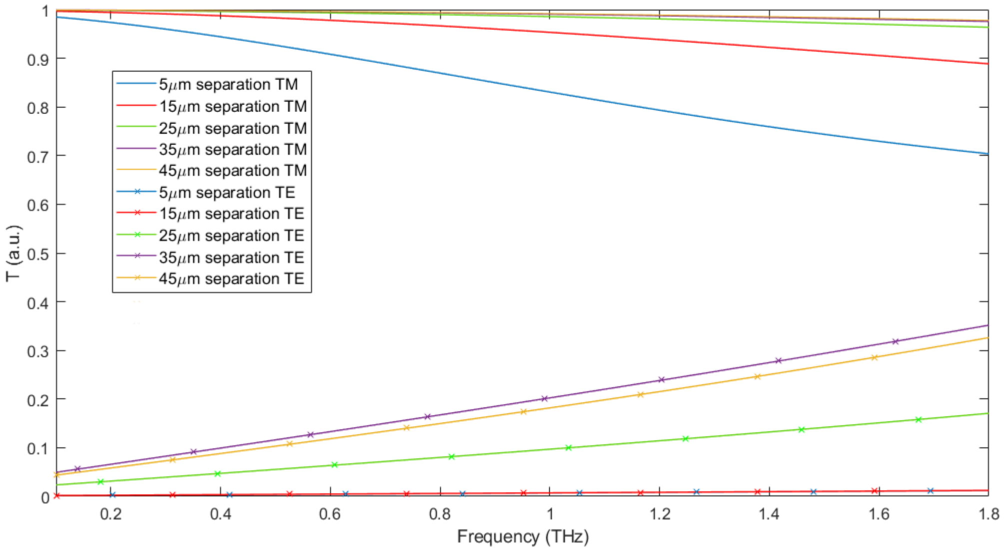

FIGURE 4.5: Simulated transmission for wire grid polariser with varying separation distance between the conducting wires

The performance of the wire grid polarisers was experimentally tested by placing one polariser in line with the transmitter and rotating a second one along with the receiver in a simple transmission setup. As seen in Figure 4.6, the transmission spectral average when the two polarisers are in line with each other is just above 90% and drops down to close to zero (corresponding to an attenuation of -33 dB) at 90°. The difference between the ideal cosine relationship of the transmission magnitude and the measured transmission with changing angle is mostly due to the polariser's frequency dependent response. For the ellipsometry setup only the 0° and 90° configurations are needed, where the polarisers are showing a very good polarisation isolation.

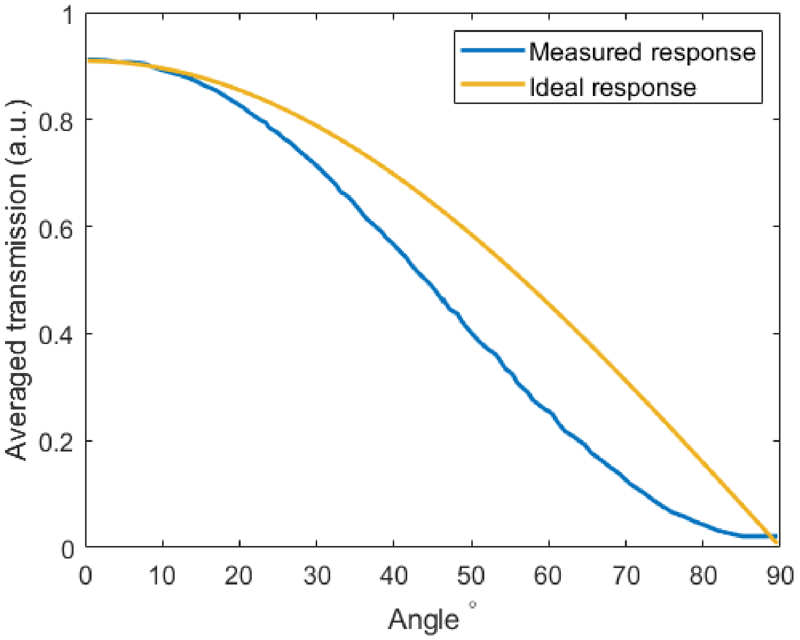

FIGURE 4.6: Averaged spectral transmission of a 2-polariser setup vs change in polarisation angle.The ideal relationship accounts for an initial 10% attenuation in the transmitted signal at 0°.

Phase Information Reliability

Phase information is traditionally not recorded in ellipsometry setups. As they originate in the optical and IR region, where the wavelengths are considerably shorter, a nm-precision calibration of the sample placement and reference is needed to obtain a reliable phase reference. Measurement instruments in these regions also rarely measures phase directly, which warrants the use of additional equipment, such as autocorrelators. As waveplates can be used to directly extract Stoke's polarisation parameters at these frequencies, this remains the preferred method applied. At THz frequencies the necessity for precision in reference and sample placement is greatly reduced down to the order of tens of micrometers, which is easily achievable using manual calibration. To test this a sample metallic mirror was repeatedly placed in the ellipsometry setup and the phase information was recorded. Each time the mirror was taken off the sample holder, rotated 90° and placed back into the holder. The variance in the recorded phase measurements is shown in Figure 4.7, demonstrating a maximum confidence interval of 10°, or about 3% of the phase. As the system moves on the optical table to change the angle on incidence, a beam drift is expected from mechanical displacements and misalignment. The phase varies with around 40° over a change of 15° in angle, which corresponds to a beam drift of 40 µm, showing that the system remains in good alignment. The beam drift errors can be normalised for in post-processing with the use of a reference mirror scan. Additional sources of phase error are due to the VNA's phase stability. It was measured to be approximately ± 6°, which corresponds to a precision of ± 5 µm. The advantage of the here presented THz ellipsometry system over traditionally used TDS and backward-wave oscillator (BWO) THz ellipsometry systems is that measurements provide higher information density, thus aiding the extraction of optical parameters. Time-domain systems usually only measure at a single fixed angle of incidence, as the beam shape is angle dependent. The frequency-domain measurements presented provide a sweep of angles, as well as higher spectral resolution, but for a lower bandwidth than in a TDS. More complex BWO - based THz ellipsometry systems, much like in the optical range, rely on waveplates and do not provide phase information.

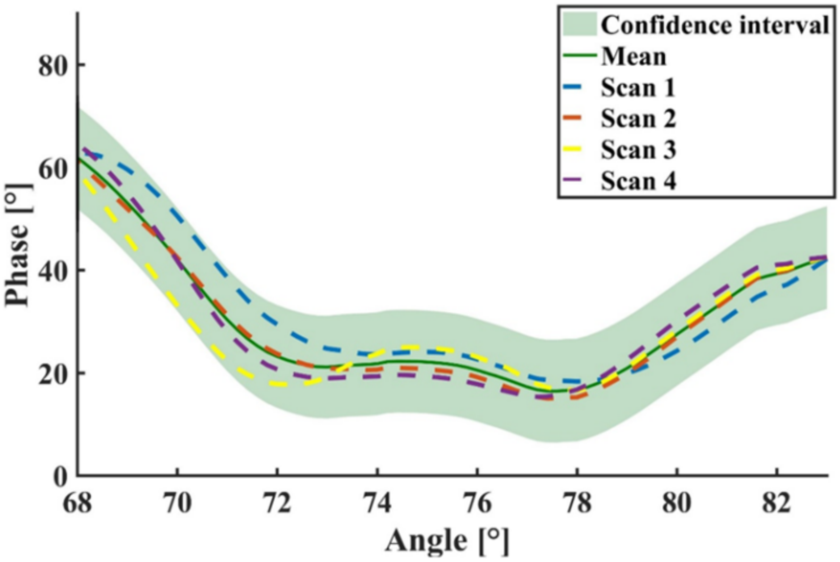

FIGURE 4.7: Phase stability over incident angles [93]

4.1.4 Extraction of Optical Properties

The extraction of optical parameters is achieved through error minimisation between the measured data and a fitted model. For the single-layer homogeneous materials later examined, the explicit expression for stratified media from Chapter 2 was applied. It was extended to accommodate oblique angles of incidence. The measurement method presented produces 3D data - the complex reflection of the electric field over angle and frequency. Fitting complex 3D data can be computationally expensive and non-trivial. For instance, measurement data for certain angles can be more corrupted than in others, but there is no clear way to distinguish between the two, leading to propagation of errors when there is sufficient information for a truer fit. A simple and powerful way to fit the complex 3D data was found to be using an image processing based approach. The data is represented as a picture, where the angle and frequency give the position of a pixel and the normalised intensity is the opacity of the pixel in grayscale. This way it is possible to apply a comparison algorithm, which calculates the similarity between the theoretical image obtained from the model and the measured image. The structural similarity index (SSIM) method was employed, which works quite differently than a simple mean-squared error (MSE) minimisation. A popular method in the field of image and video processing, the SSIM determined the perceived quality of an image with respect to a reference. For a given pixel, it measures the inter-dependence of surrounding pixels, which leads to the recognition of similar structures present in the reference and measured image [94]. This is advantageous for the fitting of our data, as the whole image is compared as a whole, rather than line-by-line, thus minimising the effect of faulty line scans.

(a) MSE = 0, SSIM = 1 (b) MSE = 200, SSIM = 0.99 (c) MSE = 200, SSIM = 0.99

(d) MSE = 200, SSIM =0.68 (e) MSE = 198, SSIM = 0.65 (f) MSE = 200, SSIM = 0.72

FIGURE 4.8: Comparison between SME and SSIM algorithms with respect to noisy images [95]

Figure 4.8 shows the output of the MSE and SSIM methods respectively, when presented with an image with different noise distributions applied to it, all giving an MSE of around 200. The SSIM output is limited between in the range [0 - 1], where 1 shows a perfect match and 0 represents no similarity. It can be seen that for strong structural similarity the SSMI value is between 0.6-1, while the MSE is unaffected. The fitting algorithm is shown in Figure 4.10. The complex S and P polarisation measurements are split to create four input images - a magnitude and a phase image for each polarisation. A search space and step size is selected for the complex refractive index and thickness of the sample, after which the theoretical images are calculated, followed by their similarity to the measurements. Both the layer thickness and the effective refractive index are fitted. The procedure is then repeated until the maximum similarity index is achieved. The sample thickness and its complex refractive index uniquely alter the shape of the image features, so both can be extracted independently. As seen in Figure 4.9a, the effective optical thickness of the sample determines the position in frequency of the Fabry-Pérot peaks, whereas the real part of the refractive index determines the width and depth of the peaks. In the ellipsometry image this translates as broader features with less contrast. The imaginary part of the refractive index creates a tapering in the Fabry-Pérot horizontal lines, which can be observed materials with higher absorption in Figure 4.9b. As the fitting results for S and P polarisations are ultimately going to be different, hence a weighted average for the final complex refractive index is taken, favouring a higher SSIM result, as shown in the following equation 4.3:

$$n = \frac{n_s SSIM_s + n_p SSIM_p}{SSIM_s + SSIM_p} \tag{4.3}$$

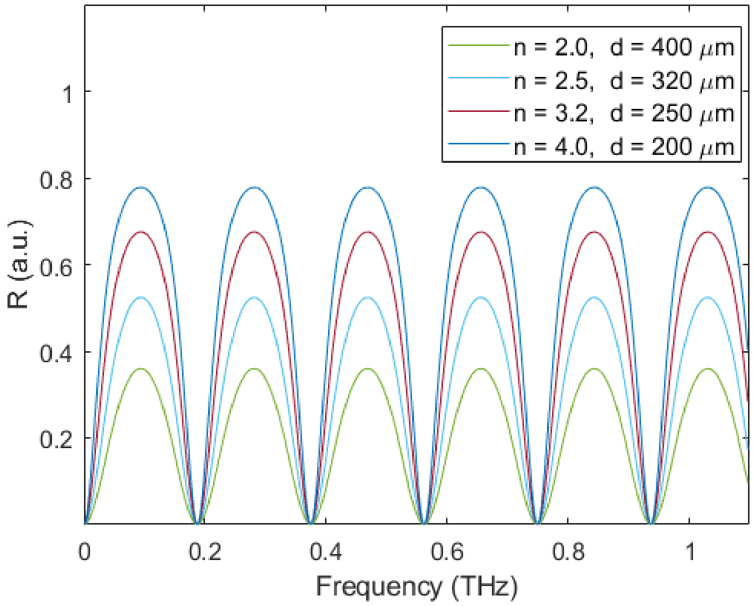

(A) Change in Fabry-Pérot resonance peaks width and depth with increase in the real part of the refractive index of the target layer in air

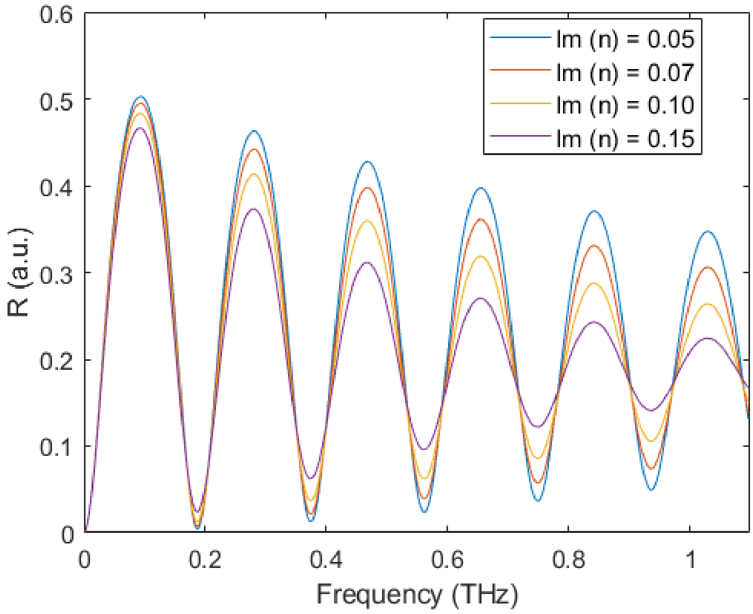

(B) Change in Fabry-Pérot resonance peaks width and depth with increase in the imaginary part of the refractive index of the target layer in air

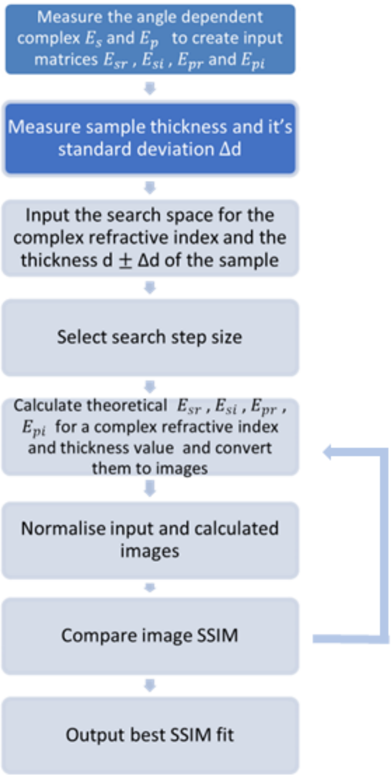

FIGURE 4.10: Flow chart of the ellipsometry fitting algorithm. E_{sr} and E_{si} correspond to the reflected magnitude and phase of the S-polarisation, and E_{pr} and E_{pi} to the P-polarisation respectively.

The ellipsometry setup and data extraction method was first verified by measuring a 500 ± 25 µm thick HRFZ-Si wafer. The wafer thickness was first measured with a micrometer. As seen in Figure 4.11, there are two distinct features that aid the structure based data fitting - the Fabry Pérot reflections, which manifest in horizontal lines in both the P and S polarisation, and the Brewster angle, which is the vertical line in the P-polarisation image. The higher the refractive index, the sharper these features appear. Low refractive index contrast, as well as higher absorbance leads to blurrying of the image. The SSIM calculated for the S- polarisation is 0.85 and the SSIM for the P- polarisation is 0.78, giving a weighted extracted refractive index of 3.416 - 0.0041i and an effective thickness of 512 µm. This is in excellent agreement with the thickness measurements of the wafer obtained with a micrometer, as well as literature values for the refractive index, as shown in Table 4.1. The attenuation coefficient at THz frequencies is most of the time not measured in literature, as the absorption of HRFZ-Si is very low and often cannot be detected by the measurement equipment.

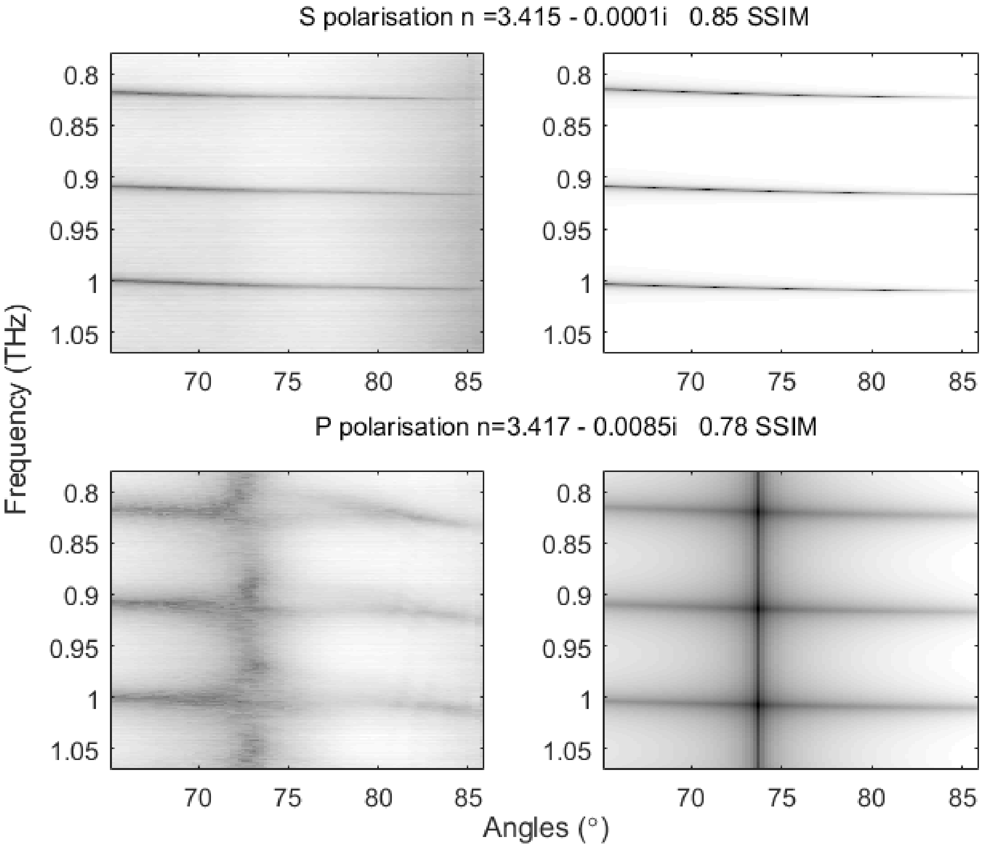

FIGURE 4.11: HRFZ-Si: Measured magnitude of the S-polarisation (top left), fitted magnitude of the S-polarisation (top right), measured magnitude of the P-polarisation (bottom left) and fitted magnitude of the P-polarisation (bottom right).

	$\Re(n)$ Refractive index	α Attenuation coefficient cm^{-1}
Measured	3.416 ± 0.001	0.0015 ± 0.0016
[96]	3.4175	~ 0.01
[97]	3.414	N/A
	3.412	N/A
	3.411	N/A
	3.406	N/A
	3.405	N/A
[98]	3.425	N/A
[99]	3.42	N/A

TABLE 4.1: Comparison between measured and literature values for the real part of the refractive index and the attenuation coefficient of HRFZ-Si at 1 THz

To demonstrate the fitting algorithm's resilience against angle sweep noise, in Figure 4.12 a noisy scan of another Si wafer is shown. For sweep angles between 77-80 ° , the scan is entirely corrupted. As expected the SSIM index is lower than in the low-noise scan, amounting to 0.71 for S-polarisation and 0.65 for P-polarisation. This still provides a weighted refractive index of 3.42 - 0.01i in very good agreement with literature values and previous measurements.

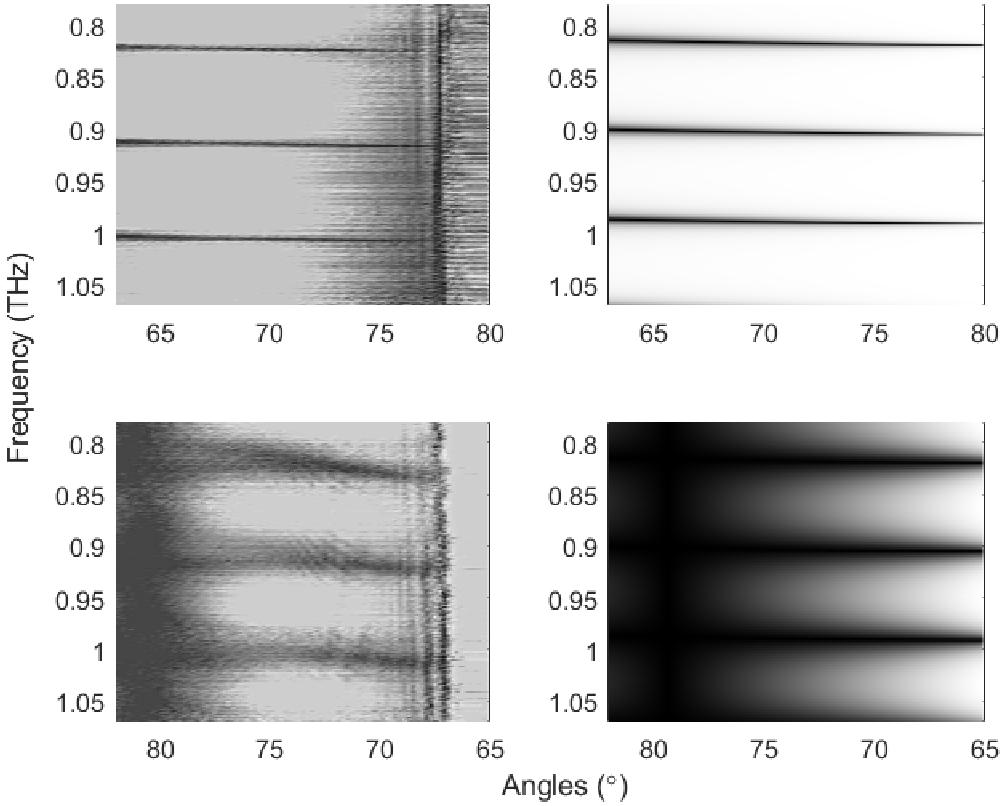

FIGURE 4.12: HRFZ Si: Measured magnitude of the S-polarisation (top left), fitted magnitude of the S-polarisation (top right), measured magnitude of the P-polarisation (bottom left) and fitted magnitude of the P-polarisation (bottom right)

4.1.5 Material Characterisation

Ellipsometry Measurement of Low Refractive Index Material - HDPE

High density polyethylene, or HDPE is a common material for THz component production. It provides high transmission while being low cost and easy to process. It is often used in the production of thick lenses, windows and polarisers. At THz frequencies its refractive index does not change with temperature, which makes it applicable to cryogenic systems [100]. The refractive index of HDPE is significantly lower than HRFZ Si at THz frequencies, with a higher attenuation coefficient. This gives a much lower signal strength in reflection, and hence a noisier ellipsometry measurement, as can be seen in Figure 4.13, where a 1mm thick HDPE sample was investigated. The measured incidence angles were also adjusted, so they can include the lower Brewster angle.

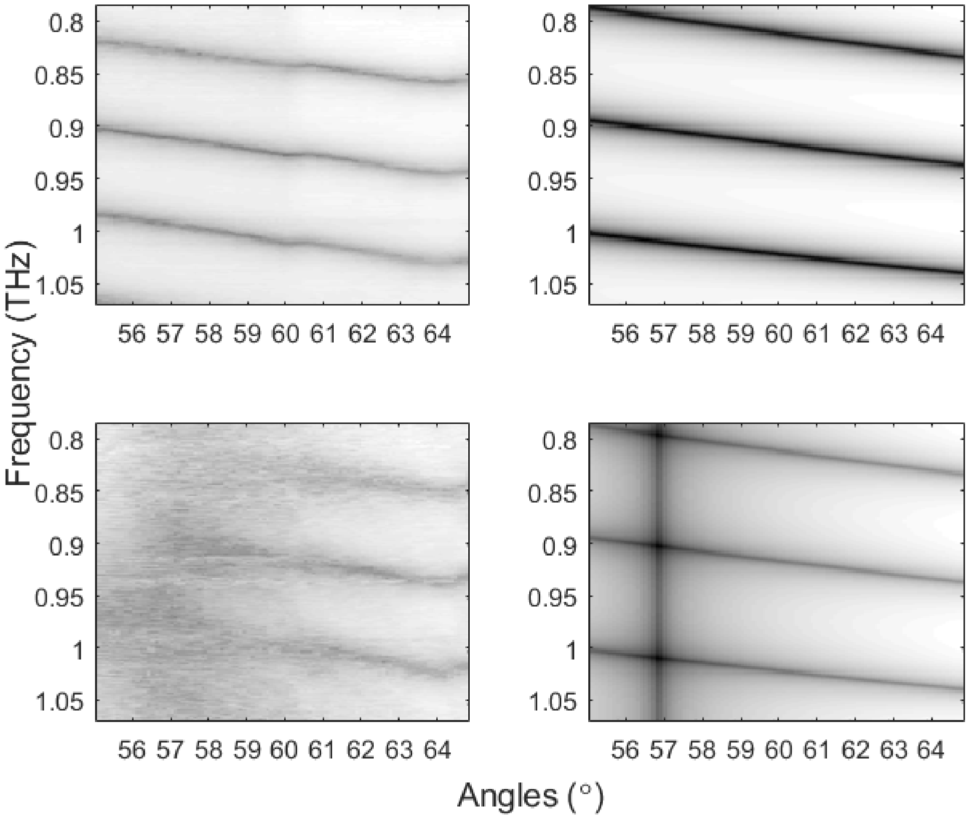

FIGURE 4.13: HDPE: Measured magnitude of the S-polarisation (top left), fitted magnitude of the S-polarisation (top right), measured magnitude of the P-polarisation (bottom left) and fitted magnitude of the P-polarisation (bottom right)

Due to the lower signal quality, the position of the Brewster angle in the P-polarisation measurement is blurred out and the spectral distance between the Fabry-Pérot resonances between the measurement and fitted model doesn't fully match. This can be potentially be also caused due to buckling in the HDPE sample. The SSIM index was calculated to be 0.63 for P- polarisation and 0.68 for S- polarisation, which although lower than the HRFZ-Si measurements, still shows a significant similarity between the measurements and fitted model. The extracted optical parameters are shown in Table 4.2. The variation within literature values for the refractive index is 3%, whereas the deviation between the measured refractive index and literature is less than 4%, which shows excellent agreement. The variance within the literature values for the attenuation coefficient is much higher, notably due to obvious outliers such as [101]. Nevertheless, the measured coefficient agrees with the majority of literature values.

	$\Re(n)$ Refractive index	α Attenuation coefficient cm^{-1}
Measured	1.538 ± 0.004	0.69 ± 0.40
[102]	1.53	0.38
[101]	1.59	13
[103]	1.526	0.15
[104]	1.54	2.2
[97]	1.545	~ 0.1
	1.53	~ 0.1
	1.5	~ 0.1
	1.48	0.2 ± 0.2

TABLE 4.2: Comparison between measured and literature values for the real part of the refractive index and the attenuation coefficient of HDPE at 1 THz

Ellipsometry Measurement of High Absorption Material - Tufnol

In order to demonstrate the ellipsometry method's performance on a high absorption material, a sample of Tufnol 1P13 was measured. Tufnol is a composite material made from cotton fabric and phenolic resin with an expected low refractive index and high attenuation coefficient. Using single layer transmission measurements, the refractive index of tufnol was measured to be 1.6 ±0.3 and the attenuation coefficient at 1THz to be 12 ±2 cm^{-1}. It should be noted that due to the high attenuation value, the transmission signal strength is low, making the measurement not very reliable. The high absorption is also evident from the ellipsometry measurements shown in Figure 4.14. The contrast in both the S- and P- polarisation images is significantly reduced with respect to previously measured materials. The Brewster angle, while still somewhat visible, is also noisy and blurry due to the low refractive index. Despite this, the SSIM index for the ellipsometry measurement fit is 0.69 for P- polarisation and 0.77 for S- polarisation, which is higher than the results obtained for HDPE. The extracted optical parameters for Tufnol are a refractive index of $n = 1.87 \pm 0.02$ and an attenuation coefficient of $\alpha = 14.7 \pm 0.8$ cm^{-1}. The uncertainty in the ellipsometry measurements is significantly lower than the transmission ones, showing the advantages of a reflection measurement of high absorption materials. Nevertheless, the results from both measurements are in good agreement.

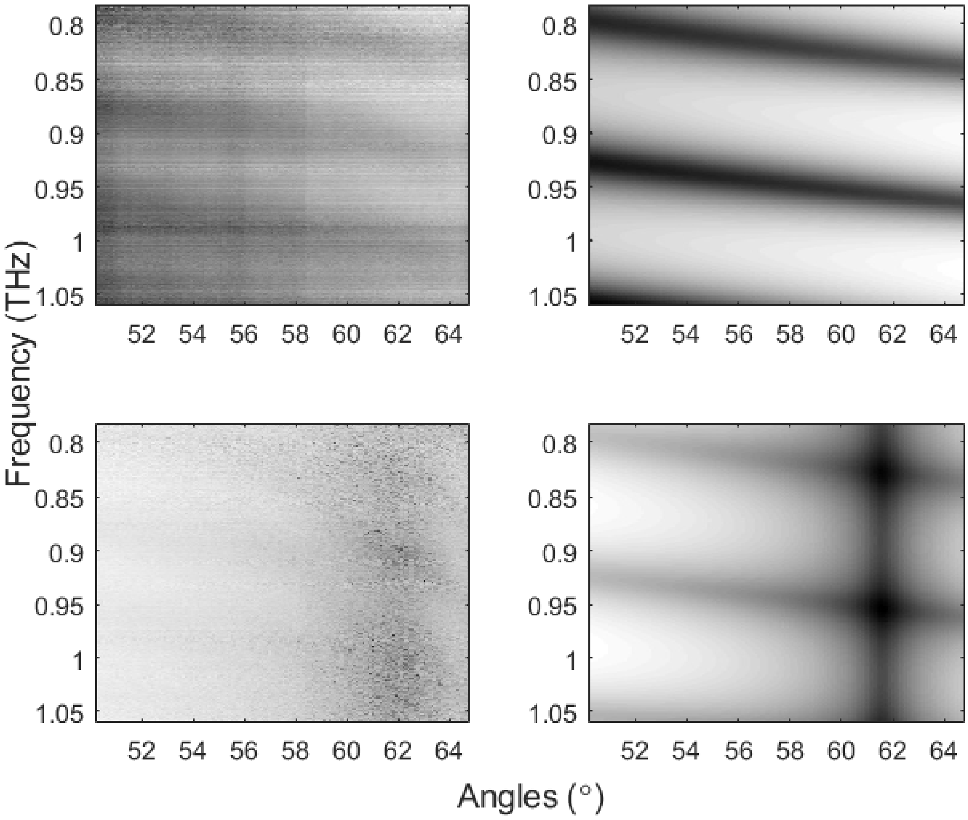

FIGURE 4.14: Tufnol: Measured magnitude of the S-polarisation (top left), fitted magnitude of the S-polarisation (top right), measured magnitude of the P-polarisation (bottom left) and fitted magnitude of the P-polarisation (bottom right)

Ellipsometry Measurement of a Featureless Composite Material - PDMS Loaded with TiO_2

The SSIM fitting method depends on the existence of discernible features - the Brewster angle and the Fabry-Pérot resonances. To test its effectiveness on materials that do not exhibit such features a composite material sample was made. Polydimethylsiloxane (PDMS) was mixed with 3.2 wt% TiO_2 nanoparticles. The sample was cast with a 5 mm thickness. The casting process creates a significant surface roughness. The top side of the sample showed a surface roughness with a standard deviation of 100 µm when measured using Dektak 3 stylus profilometer. The bottom of the sample showed a much lower deviation of nearly 4 µm, therefore this was the side used in the ellipsometry measurements. Similarly to the Tufnol sample, reference optical constants were obtained using a transmission measurement. The refractive index was measured to be n = 1.57 ± 0.09 and the attenuation constant at 1 THz α = 17 ± 2 cm^{-1}. As seen in Figure 4.15, there are no distinct features apart from the Brewster angle. The S- polarisation image only shows a gradient. Nevertheless, the SSIM index for the P- polarisation was calculated to be 0.69 and 0.73 for the S- polarisation, which is on par with previous results. The extracted optical parameters were n = 1.57 ± 0.05 and α = 16.9 ± 1.9 cm^{-1}, in very good agreement with the transmission reference.

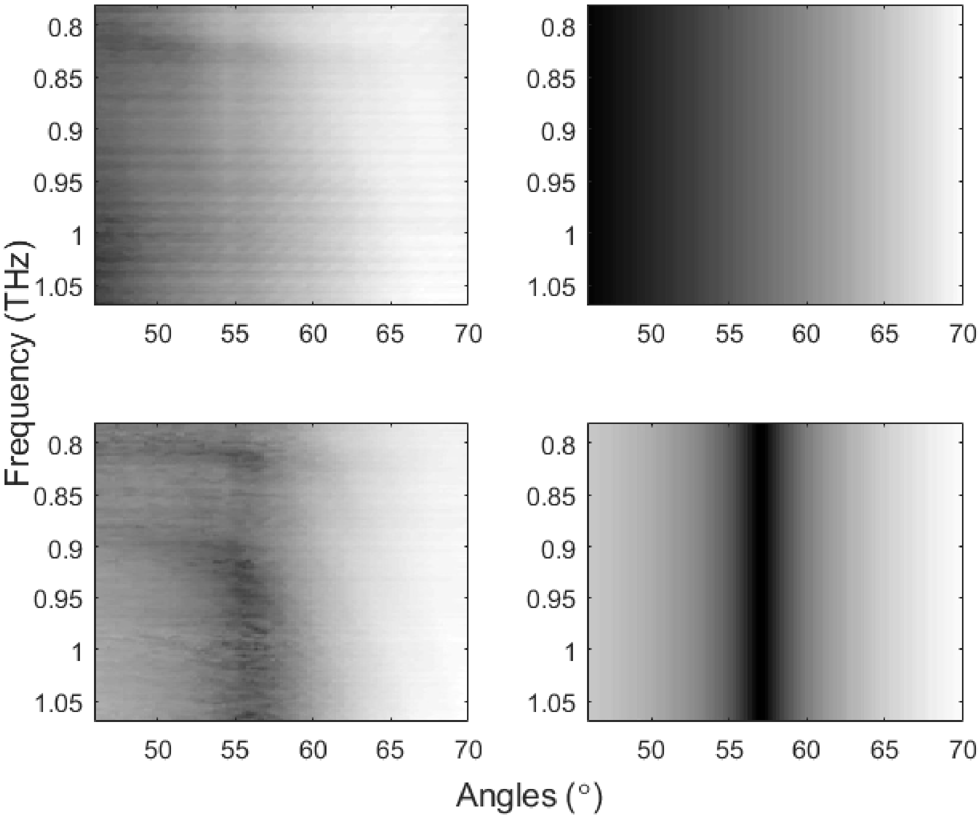

FIGURE 4.15: PDMS loaded with TiO2: Measured magnitude of the S-polarisation (top left), fitted magnitude of the S-polarisation (top right), measured magnitude of the P-polarisation (bottom left) and fitted magnitude of the P-polarisation (bottom right)

In Situ Measurements

The advantage of contactless material characterisation methods is perhaps most evident in the ability to measure in real time as the target is undergoing a process, also known as in situ measurements. To demonstrate this with the THz ellisometry setup, the continuous etching of a HRFZ-Si wafer in KOH was recorded and the decrease in wafer thickness was extracted as a function of time. Firstly, a new sample mount was constructed. It consisted of an acrylic box with a 1mm thick, 2-inch diameter PTFE window. The HRFZ-Si wafer was glued to the back of the window and the box was filled with 35% aqueous solution of KOH. This way the wafer was etched from the back and the KOH didn't interfere with the THz beam. The setup diagram can be seen in Figure 4.16. A reference wafer thickness was obtained in two ways - a micrometer measurement before and after the etching, as well as an estimated thickness from etch rate tables, as a function of continuously recorded temperature of the solution.

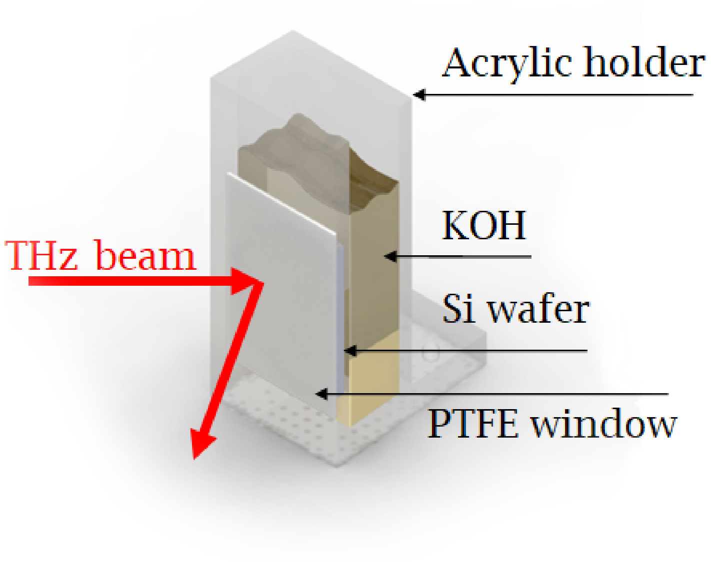

FIGURE 4.16: Conceptual diagram of the in situ measurement sample holder

In previous ellipsometry measurements scan times varied between 0.5 - 2 hours, depending on the IF bandwidth and averaging settings. As we were trying to achieve micrometer precision, for etch rates in the order of 5 µm/h, the scan times needed to be reduced to just a few minutes. This required the angle span to be reduced to 5° with 1° resolution and the frequency resolution to 1 GHz. This achieved an initial scan time of around 8 minutes. As the KOH solution cools down, the etch rate also reduces, hence the scan time was adjusted during the measurement to minimise noise. The extracted wafer thickness as a function of time is presented in Figure 4.17. The discontinuity in the temperature derived thickness arises from a top-up of hot KOH solution. The ellipsometry results follow the etch rate trend up until the very last measurement. There is however excellent agreement between the ellipsometry final estimate and the micrometer measurement of the etched wafer.

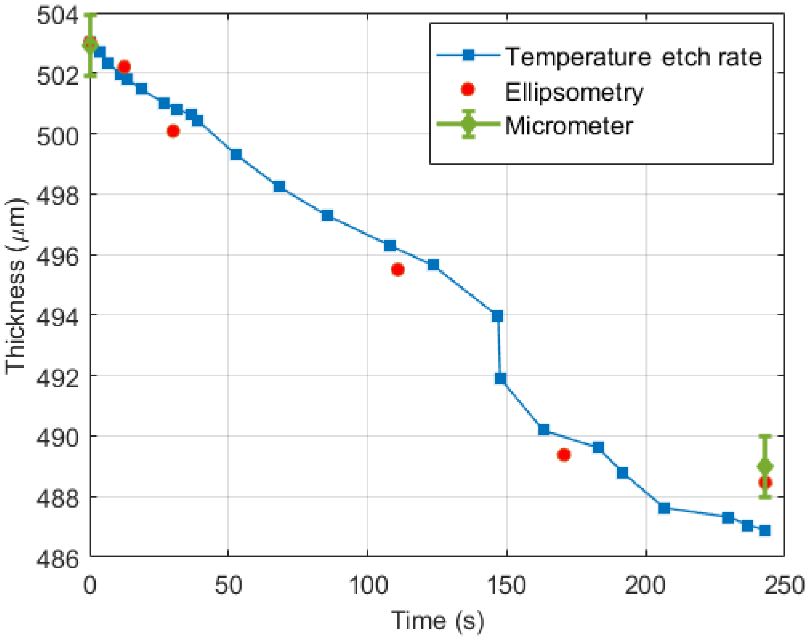

FIGURE 4.17: Comparison between thickness measurement results computed from etch rate tables (blue), insitu THz ellipsometry (red) and micrometer measurements (green)

Ellipsometry Measurements of a Resonant Metamaterial

The THz ellipsometry system was subsequently used for angle - dependent characterisation of the resonant split-ring metamaterial introduced in Chapter 3, Figure 3.33 a). Unlike the materials investigated so far, the assumption of optical isotropy no longer holds. Firstly, due to the resonant nature of the metamaterial, the effective bulk refractive index varies significantly with frequency within the measured bandwidth, therefore it cannot be approximated to be constant. Secondly, as metamaterials derive their optical properties from structural symmetries, they often experience birefringence - their refractive index changes depending on the polarisation and the angle of the incident radiation. The ellipsometry fitting model is ill-suited for the task of extracting an effective complex refractive index that changes as a function of frequency, angle and polarisation, as the search space becomes too large. Instead, a direct effective parameter extraction approach was used, based on the numerical model shown in Chapter 2. The ellipsometry setup provides only measurements in reflection, but in order to calculate the effective permitivity and permeability of the medium, the model requires both the complex reflection and transmission coefficients. This is a common downside to ellipsometry measurements, but is circumvented by using the transmission coefficients calculated from FDTD simulations. Another peculiarity of the direct extraction model is that in order to choose the correct branch for the value of the effective wave vector, calculations should start at 0 Hz. This is done in order to preserve continuity in the permittivity and permeability as a function of frequency and is shown in Figure 2.16 (Chapter 2). As the measurements are only in the range between 0.75-1.1 THz, the missing data from 0-0.75 THz was approximated to the ideal response of bulk HRFZ-Si. This ensures that the 0^{th} order refractive index is that of the substrate, rather than 0. The real and imaginary parts of the effective permittivity and permeability for TE and TM polarisations are shown in Figure 4.19 and the corresponding index of refraction in Figure 4.18. It can be seen that the magnetic response is much stronger than the electric for the TE polarisation and somewhat similar to it in the TM polarisation. This agrees with the expected response of a split-ring resonator, having a stronger magnetic excitation. The cross-symmetry between $\epsilon(\mu)_{TE}$ and $\mu(\epsilon)_{TM}$ can also be clearly seen. The effective refractive index fluctuates around 3.42, in agreement with the expected refractive index of the substrate. A negative index of refraction is exhibited for TE polarisation at angles around 72° and around 73°, 80° and above 85° for TM polarisation (Figure 4.18).

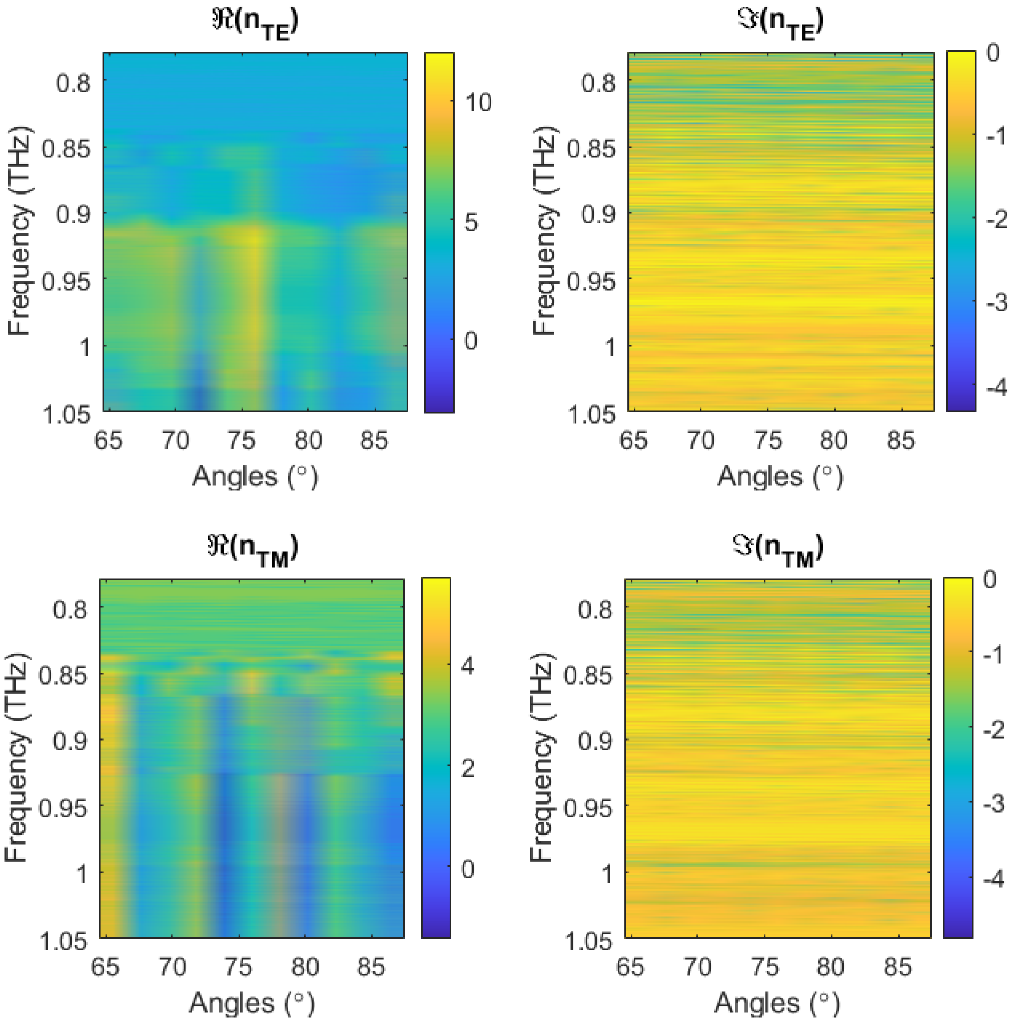

FIGURE 4.18: Metamaterial complex refractive index as a function of incidence angle in TE and TM polarisation

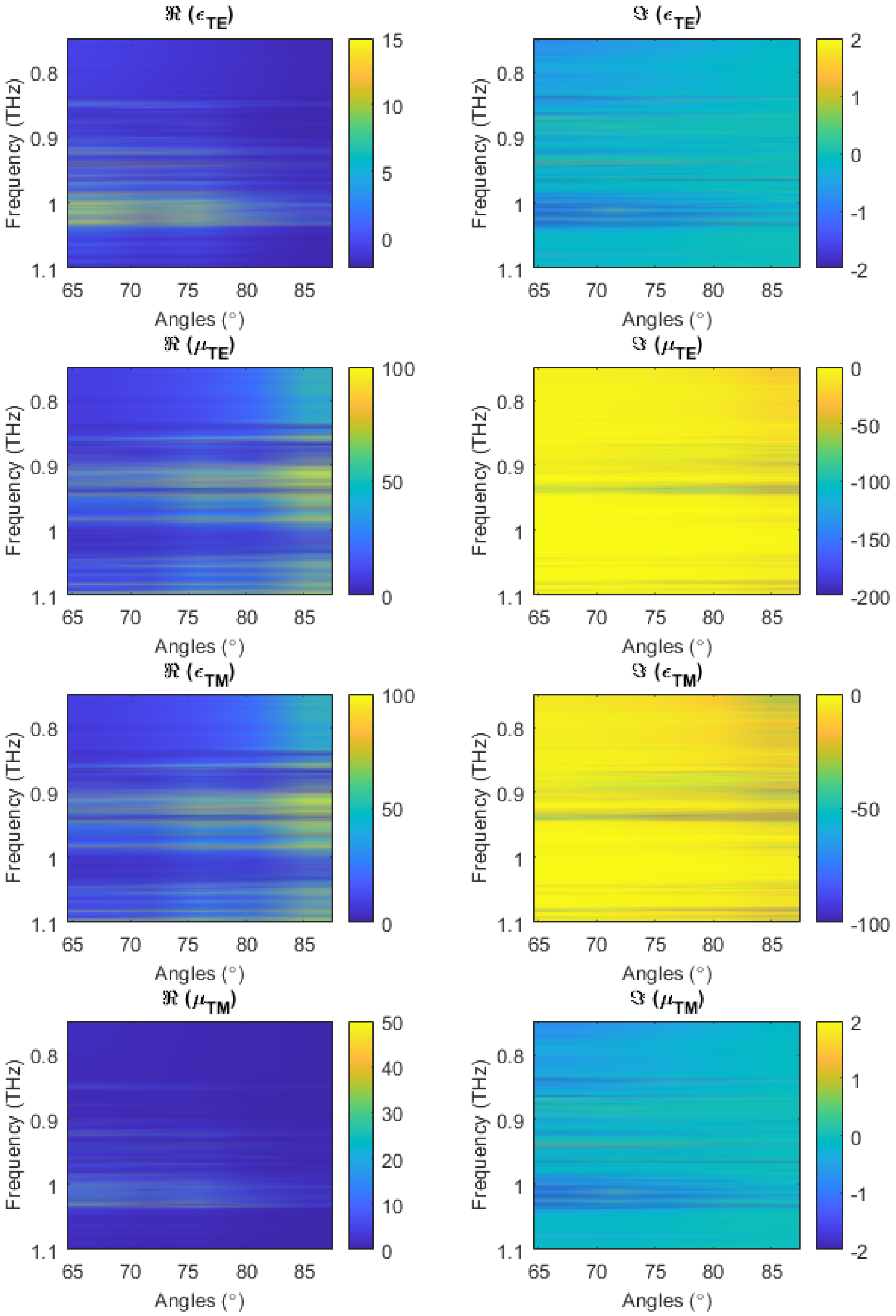

FIGURE 4.19: Metamaterial complex permittivity and permeability as a function of incidence angle in TE and TM polarisation

4.2 THz Grazing Angle Spectroscopy for Sub-μm Thickness Measurements

4.2.1 Introduction

Grazing-angle spectroscopy is a well-established technique at infrared wavelengths with sufficient sensitivity to detect monolayers [105]. Reflection measurements at high grazing angles (around 80°) greatly improve the signal-to-noise ratio in comparison to transmission measurements through thin films. Commonly used infrared instruments are often broadband, making it possible to choose an absorbance peak corresponding to the species on the surface, from which the thickness can also be extracted. As the VNA-based THz spectroscopy system is comparably narrow-band (0.75-1.1 THz), it is expected that most substances and thin films will not exhibit a clear feature within this range, and absorbance measurements would be unreliable. For thin films of low refractive index, Fabry-Pérot resonances are also too broadband for the measurement range and cannot be used to extract the thickness of the film. In order to create detectable spectral features, which are sensitive to the sample thickness, a modification to the grazing angle spectroscopic measurement was adopted.

4.2.2 Theory

By mixing the grazing angle signal with a direct transmission signal, spectral features corresponding to the phase difference due to the two different path lengths are created. A diagram of this setup is shown in Figure 4.20. The THz radiation emitted by a VDI THz extender horn antenna is collimated by a parabolic mirror. The beam is split up and a portion is redirected at a grazing angle towards a second mirror, where the sample film under investigation is deposited. A third mirror redirects the beam so it is parallel to the directly transmitted beam again and both are focused on the receiving horn antenna.

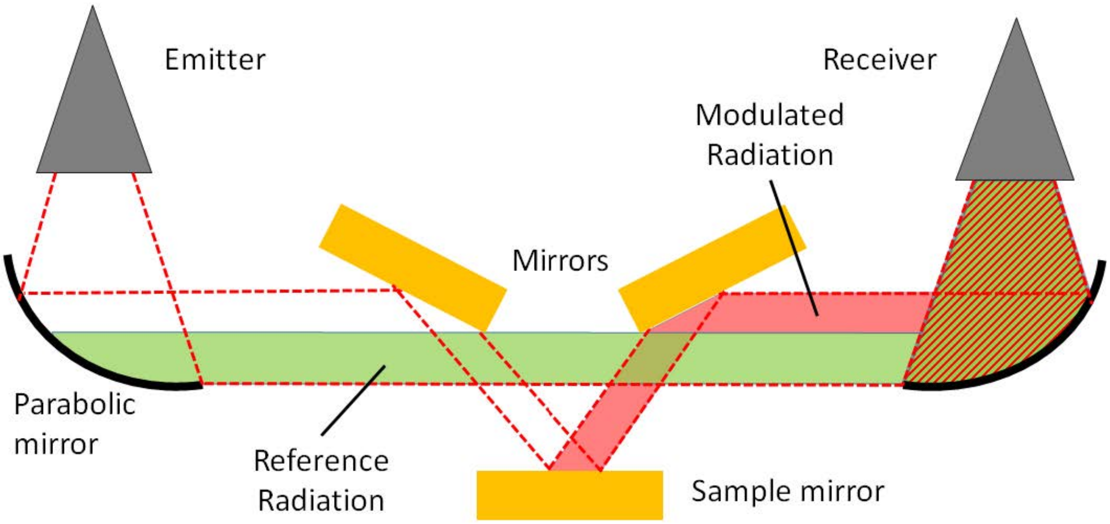

FIGURE 4.20: Schematic of the grazing-angle measurement setup.

Assuming that the transmitted beam power is split in a ratio $1 : a$, $1/(a+1)$ is the direct transmission (green path in Figure 4.20) and $a/(a+1)$ is the delayed ray (red path in Figure 4.20). The direct transmission will also serve as a reference signal, with zero phase delay. For a difference in path lengths d and wave vector k, the phase delay in the mirror path is given by e^{-jkd}. The transmission amplitude coefficient at the receiver is then given by

$$t = (1 + ae^{-jkd})/(1+a) \tag{4.4}$$

The coefficient a can be adjusted by moving the position of the parabolic mirrors. Data fitting showed that it is usually close to an even split, or $a = 1$.

4.2.3 Measurement Setup

The measurements were taken with the VNA and VDI WR1.0 frequency extenders introduced earlier in the chapter, under S and P polarisation, using wire grid polarisers. The mirror setup was constructed on a custom mount, as shown in Figure 4.21. The mirrors were fabricated on 2 x 2 x 0.5 cm glass substrates, coated with 10 nm of Cr and 100 nm Au, to improve adhesion using thermal evaporation. The mirrors were then slotted in the holes provided in the mount. The grazing angle was set to 16° and the distance between the sample mirror and the two other mirrors could be adjusted with screws, effectively changing the ratio between the direct signal power and the reflected signal power. A good trade-off between speed and noise reduction in measurements was achieved with a spectral resolution of the VNA set to 0.2 GHz. This corresponded to a thickness resolution of 20 nm at a refractive index of 1 (and proportionally higher for a higher refractive index). With longer scans and increased averaging, higher resolutions can also be achieved.

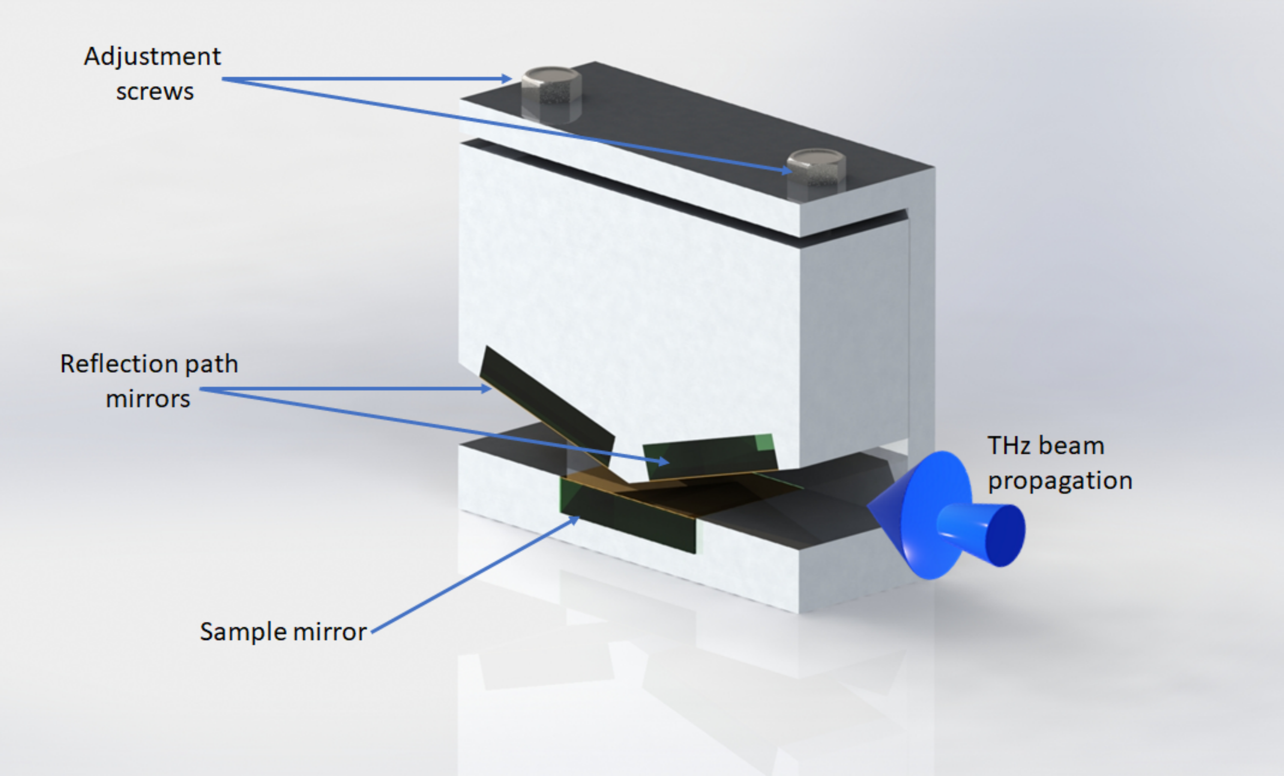

FIGURE 4.21: Grazing angle mirror mount

4.2.4 Experimental Results

To test the grazing angle system's ability to resolve film thickness, SU-8 was used as the material under investigation. SU-8 has well known properties at THz frequencies and can produce uniform films in a wide range of thicknesses from nm to hundreds of µm [106]. A clean sample mirror was first measured that served as a reference. The sample mirror was then replaced with identical mirrors with films of various thicknesses of SU-8 deposited on top. Figure 4.22 shows an example of the measured and fitted reference measurements, as well as measurements on two film samples in P polarisation. The calculated sample thicknesses were 15.2 µm and 21.5 µm respectively. The correlation factors of the fits were calculated to be 0.95 for the reference signal, 0.89 for the thinner sample and 0.95 for the thicker sample, showing a good fit to the experimental data. The refractive index of SU-8 was taken from literature values to be 1.658 [106].

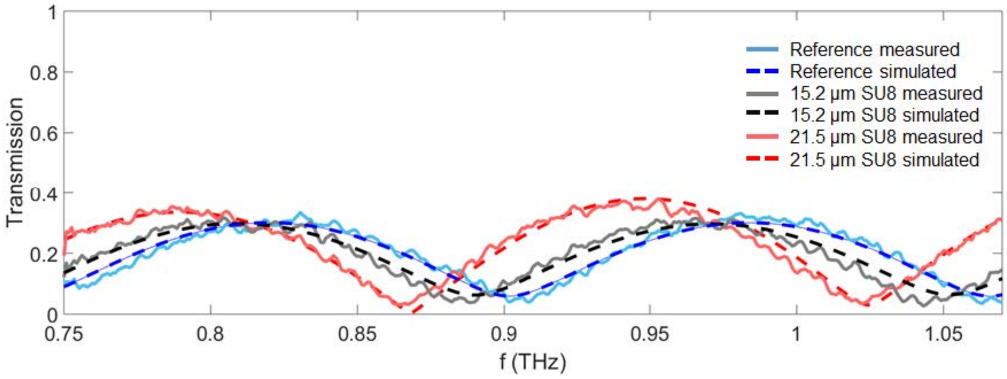

FIGURE 4.22: Measured (solid) and fitted (dashed) transmission coefficient at receiver at P polarisation. A clear frequency shift from the reference trace (blue) to the SU-8 layer trace (black) can be observed, as well as the shift's increase with layer thickness (red trace).

Table 4.3 compares the results from thickness measurements performed using the THz grazing angle setup and using a stylus profilometer (DEKTAK 3). The uncertainty in the non-contact testing is introduced through the difference in results obtained from S- and P- polarisation, as P-polarisation reflection measurements have a lower SNR than S-polarisation. The variance in results obtained from the profilometer is quite large, even though the repeated measurements were taken in the same position on the sample. This is expected to be mostly due to the stylus bending the surface of the SU-8 even at the lowest contact force of 1mg and unevenness in the surface. The grazing angle measurements are still in good agreement with the profilometer measurements, showing much smaller average variance of only 0.25 % and nm precision. The spectral resolution of the measurements had to be increased for Sample 5 in respect to the thicker samples to 0.1 GHz.

	Grazing angle measurement (μm)	Profilometer measurement (μm)
Sample 1	52.4 ± 0.2	50 ± 4.1
Sample 2	21.5 ± 0.05	20.1 ± 2.5
Sample 3	15.2 ± 0.05	14.3 ± 1.6
Sample 4	10.1	11 ± 1.7
Sample 5	3.4 ± 0.01	5.1 ± 1.9

TABLE 4.3: Comparison between thickness measurement results obtained with THz grazing angle spectroscopy and Dektak 3 Stylus Profilometer on SU-8 samples

4.3 Photoelasticisty in the THz Spectrum

4.3.1 Introduction to Photoelasticity

Photoelasticity is an experimental method, that describes the changes in the optical properties of a material as a result of mechanical stresses and strains. Typically used at optical and infrared frequencies [107], the method is yet unexplored at THz frequencies. All dielectric materials exhibit photoelastic behavior, leading to photoelastic analysis being the standard method in non-destructive stress analysis, especially before the introduction of numerical methods. Recently, the technique of digital photoelasticity has gained popularity in solving various engineering and science problems. In digital photoelasticity, the fringe patterns that are created on a stressed surface are captured as a digital image. The patterns contain the whole field stress information in terms of the difference in principal stresses and their orientation, and the image can be quantitatively evaluated [108]. Photoelasticity finds application in numerous fields - dentistry and biomedical research (such as evaluating loads on implants [109]–[111]), rapid prototyping [112], in conjunction with FEA and 3D printing for the analysis of complex structures [113], in the analysis of mechanical parts (such as seals, bearings, gears and joints), as well as quality control in glasses and plastics manufacturing [114]. As many materials are transparent to THz radiation, this method has great potential for non-destructive testing.

The photoelastic method relies on birefringence, which is the ability of materials to split an incident electromagnetic wave into two refracted waves instead of one.

The mechanical stresses on the material dictate the different coefficients of refraction and polarisation states that the two refracted waves experience. Their differences can be measured by a polariscope, and hence the mechanical stresses can be deduced [114]. Here the photoelastic scattering at THz frequencies on a silicon wafer under stress was explored. Silicon offers high transmission, but only allows for comparably small strain values due to its monocrystallinity. First, the photoelasticity for different strain values was measured at different crystal orientations and the photoelastic tensor for Si at THz was extracted. While the photoelastic tensor of silicon at optical frequencies has been known for a long time , literature values differ with up to 3 orders of magnitude [115], [116] and the values extracted at THz can contribute to the debate. Consequently, a 2D map of the silicon strain and stresses was measured and evaluated, accessing low-power THz ellipsometry as a digital photoelasticity measurement method.

4.3.2 Measurement Setup and Preliminary Results

The measurements were conducted with the THz VNA Ellipsometry setup introduced earlier, but set for transmission measurements at normal incidence. Consecutive measurements were taken with the THz source linearly polarized in the horizontal (x-axis or S-polarisation), vertical (y-axis or P-polarisation) and at 45° (S and P polarisation). For each polarisation state of the transmitter, the receiver was also polarised respectively, making the following transmitter - receiver polarisation pairs: [S-S], [P-P], [SP - S, P, SP]. Polarisation selectivity was achieved with two wire grid polarisers, as introduced in the ellipsometry setup. The polarisers rotated along with the VNAX extension heads on automated rotating stages, ensuring consistency in alignment between the different polarisation measurements. Normal strain was applied individually along the [110], [110] and [100] crystal axis of n-type, 2-inch <100> Si wafers (Figure 4.23). The wafer thickness was 300±25 µm. Strain was applied by gluing the sides of the Si wafer to a linear stage using epoxy and the strain was measured using a foil strain gauge [117], adhered to the silicon wafer. The epoxy was cured at 60°C for 1 hour, followed by 80°C for 2 hours. The strain was measured using a 2-wire bridge circuit, implemented through a Strainsert HW1-D strain indicator transducer. A photo of the measurement setup at 45° polarisation is shown in

Figure 4.24.

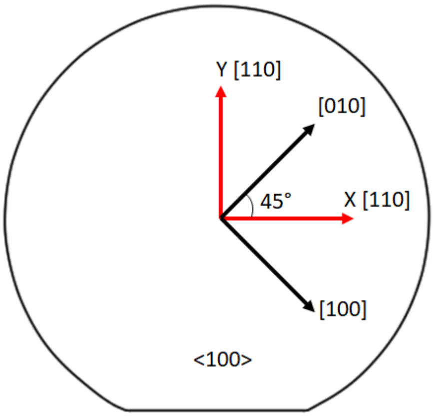

FIGURE 4.23: <100> Si wafer crystallographic axis and coordinate system

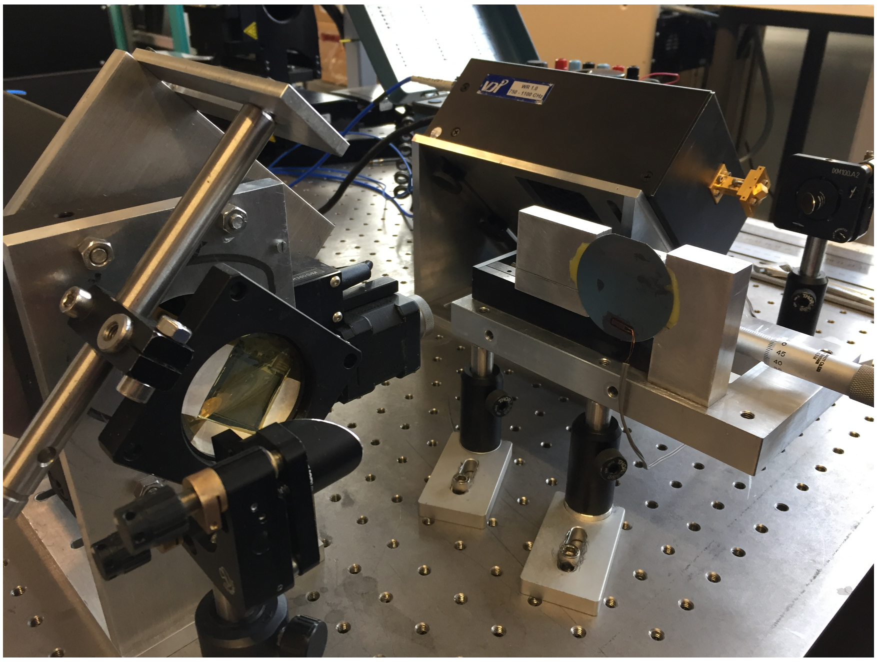

FIGURE 4.24: Measurement setup at 45° polarisation

Preliminary measurements were conducted in order to determine if the applied strain produces measurable results. The comparison between P- and S-polarisation for a silicon wafer strained along the [110] crystal axis can be seen in Figure 4.25. The incident radiation was polarised at 45°. The divergence between the two polarisations shows the transformation of the linear polarised radiation towards elliptical polarisation, associated with rotation towards the axis of the S-polarisation. The effect on the polarisation for strain applied along the [100] axis was measured to be approximately 10 times larger than for the [110] axis. This suggests that the development of artificial birefringence in monocrystalline silicon under the application of mechanical stress is significant enough to measure using low power THz radiation.

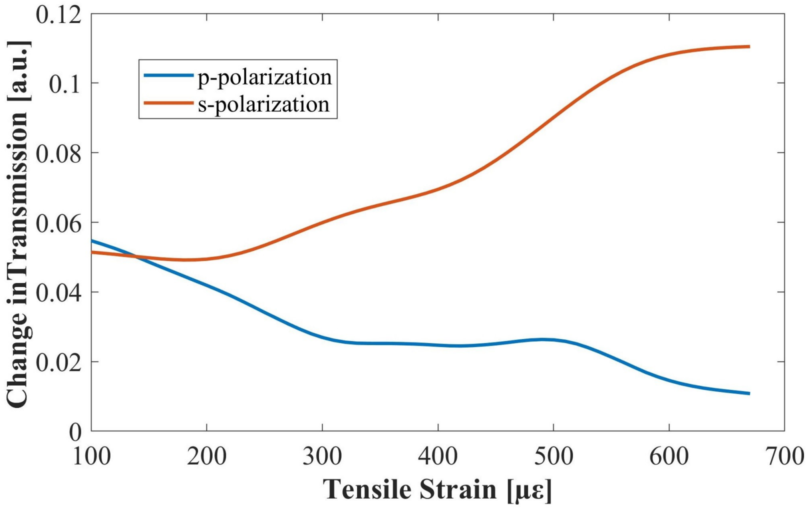

FIGURE 4.25: Relative change in transmission for P- and S- polarisation with increasing strain along the [110] crystal axis

4.3.3 Pockels Phenomenological Theory

The relationship between the changes in refractive index and stress/strain on a material is described by Pockels Phenomenological theory [21]. For an isotropic material the artificial birefringence produced is directly proportional to the applied stress within the limits of Hooke's law. Due to its diamond-lattice structure, monocrystalline silicon is governed by an anisotropic (direction dependent) stress-optic law. In order to simplify the relationship between the indices of refraction and stress, the material properties are described by an ellipsoid, in literature typically called an indicatrix. Radiation is assumed to fall into the origin of the ellipsoid. The plane perpendicular to the plane of incidence then intersects the ellipsoid, generating an ellipse. The two half axis of that ellipse correspond to the two polarisation indices of refraction n_p and n_s, as shown in Figure 4.26. The X, Y, and Z Cartesian axes are chosen to coincide with the crystallographic axes of the material, as previously shown in Figure 4.23 and can be referred to as indices (x, y, z) = (1, 2, 3). Several assumptions need to be considered:

(1) The solid under investigation is homogeneously deformed and the effect of deformation is only to alter the optical parameters of the indicatrix.

(2) When the strain is within elastic limits, the change in optical parameters can be expressed as a homogeneous linear function of all nine stress components.

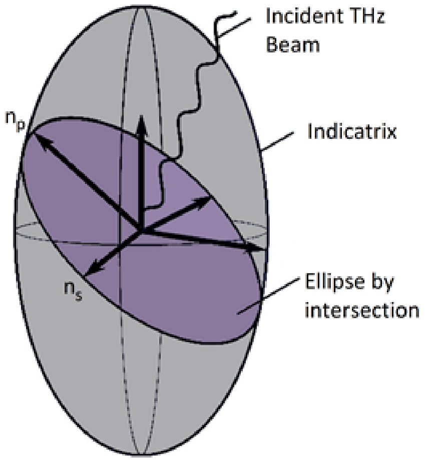

FIGURE 4.26: Graphical representation of the stress-optical ellipsoid, indicatrix [118]

In its most general form the equation describing the indicatrix is as follows:

$$B_{ij}x_ix_j = 1 \text{ for i, j= } (1, 2, 3) \tag{4.5}$$

where B_{ij} is a 3x3 symmetric tensor, called the impermeability tensor (B_{ij} can also be referred to as polarisation constants). Pockels assumes that the changes in B_{ij} are linear functions of all nine stress or strain components σ_{kl} (ϵ_{kl}), therefore the difference between the impermeability tensor between the stressed and unstressed material ΔB_ij is given by:

$$\Delta B_{ij} = -q_{ijkl}\sigma_{kl} \tag{4.6}$$

$$\Delta B_{ij} = p_{ijkl}\epsilon_{kl} \tag{4.7}$$

The q_{ijkl} are called stress-optical coefficients and p_{ijkl} are the strain-optical components. The negative sign in equation 4.6 denotes an extensional stress, as the one applied in our experiments. The impermeability tensor is ultimately a tensor representation of the change in refractive index between the stressed and unstressed material, therefore it can also be expressed by

$$\Delta B_{ij} = 1/{n_{ij}}^2 - 1/{n_{ij}}^{o2} \text{ for i, j= } (1, 2, 3) \tag{4.8}$$

To put this in the context of our Si measurements, for an anisotropic medium the electric flux density D is related to the E-field by

$$D_i = \sum_j \varepsilon_{ij} E_j \tag{4.9}$$

, where j = (1, 2, 3) and ε is the permittivity of the material.
Expanding this gives

$$D_x = \varepsilon_{xx} E_x + \varepsilon_{xy} E_y + \varepsilon_{xz} E_z \tag{4.10}$$

$$D_y = \varepsilon_{yx} E_x + \varepsilon_{yy} E_y + \varepsilon_{yz} E_z \tag{4.11}$$

$$D_z = \varepsilon_{zx} E_x + \varepsilon_{zy} E_y + \varepsilon_{zz} E_z \tag{4.12}$$

In our measurement setup, five measurements were taken for each strain on the wafer, with the transmitter-receiver combinations [S-S], [P-P] and [SP - S, P, SP]. This set E_z = 0 and E_y = 0 in S- polarisation and E_z = 0 and E_x = 0 in P- polarisation. Therefore for each strain value that was measured :

$$D_x = \varepsilon_{xx} E_x \tag{4.13}$$

$$D_y = \varepsilon_{yy} E_y \tag{4.14}$$

$$D'_x = \varepsilon_{xx} E_x + \varepsilon_{xy} E_y \tag{4.15}$$

$$D'_y = \varepsilon_{yx} E_x + \varepsilon_{yy} E_y \tag{4.16}$$

The final [SP -SP] measurement is for validation purposes only, as it does not provide any independent information. The refractive indexes n_{11},n_{12}, n_{21} and n_{22}, corresponding to the permittivity values can therefore be extracted and the impermeability tensor elements calculated. Due to symmetry, $n_{12} = n_{21}$. Expanding equation 4.8 with the strain tensor given by :

$$\epsilon = \begin{bmatrix} \epsilon_{xx} & \epsilon_{xy} & \epsilon_{xz} \\ \epsilon_{yx} & \epsilon_{yy} & \epsilon_{yz} \\ \epsilon_{zx} & \epsilon_{zy} & \epsilon_{zz} \end{bmatrix} \tag{4.17}$$

and using single suffix Voigt notation :

$$\begin{bmatrix} xx & xy & xz \\ yx & yy & yz \\ zx & zy & zz \end{bmatrix} = \begin{bmatrix} 1 & 6 & 5 \\ 6 & 2 & 4 \\ 5 & 4 & 3 \end{bmatrix} \tag{4.18}$$

for the most anisotropic crystal, the polarisation constants are given by :

$$B_1 - B_1^o = p_{11}\epsilon_1 + p_{12}\epsilon_2 + p_{13}\epsilon_3 + p_{14}\epsilon_4 + p_{15}\epsilon_5 + p_{16}\epsilon_6 \tag{4.19}$$

$$B_2 - B_2^o = p_{21}\epsilon_1 + p_{22}\epsilon_2 + p_{23}\epsilon_3 + p_{24}\epsilon_4 + p_{25}\epsilon_5 + p_{26}\epsilon_6 \tag{4.20}$$

$$B_3 - B_3^o = p_{31}\epsilon_1 + p_{32}\epsilon_2 + p_{33}\epsilon_3 + p_{34}\epsilon_4 + p_{35}\epsilon_5 + p_{36}\epsilon_6 \tag{4.21}$$

$$B_4 - B_4^o = p_{41}\epsilon_1 + p_{42}\epsilon_2 + p_{43}\epsilon_3 + p_{44}\epsilon_4 + p_{45}\epsilon_5 + p_{46}\epsilon_6 \tag{4.22}$$

$$B_5 - B_5^o = p_{51}\epsilon_1 + p_{52}\epsilon_2 + p_{53}\epsilon_3 + p_{54}\epsilon_4 + p_{55}\epsilon_5 + p_{56}\epsilon_6 \tag{4.23}$$

$$B_6 - B_6^o = p_{61}\epsilon_1 + p_{62}\epsilon_2 + p_{63}\epsilon_3 + p_{64}\epsilon_4 + p_{65}\epsilon_5 + p_{66}\epsilon_6 \tag{4.24}$$

For a thin wafer, the problem can be simplified to only looking at planar strains, so that the strain tensor becomes :

$$\epsilon = \begin{bmatrix} \epsilon_1 & \epsilon_6 & 0 \\ \epsilon_6 & \epsilon_2 & 0 \\ 0 & 0 & 0 \end{bmatrix} \tag{4.25}$$

Symmetry simplifications can also be applied, as monocrystaline silicon is a cubic crystal, therefore the photoelastic coefficients are reduced to :

$$\begin{bmatrix} p_{11} & p_{12} & p_{12} & 0 & 0 & 0 \\ p_{12} & p_{11} & p_{12} & 0 & 0 & 0 \\ p_{12} & p_{12} & p_{11} & 0 & 0 & 0 \\ 0 & 0 & 0 & p_{44} & 0 & 0 \\ 0 & 0 & 0 & 0 & p_{44} & 0 \\ 0 & 0 & 0 & 0 & 0 & p_{44} \end{bmatrix}$$

Finally, the measurements can be simplified to three equations for the strain-optical coefficients :

$$B_1 - B_1^o = p_{11}\epsilon_1 + p_{12}\epsilon_2 \tag{4.26}$$

$$B_2 - B_2^o = p_{12}\epsilon_1 + p_{11}\epsilon_2 \tag{4.27}$$

$$B_6 - B_6^o = p_{44}\epsilon_6 \tag{4.28}$$

And similarly for for the stress-optical coefficients :

$$B_1 - B_1^o = q_{11}\sigma_1 + q_{12}\sigma_2 \tag{4.29}$$

$$B_2 - B_2^o = q_{12}\sigma_1 + q_{11}\sigma_2 \tag{4.30}$$

$$B_6 - B_6^o = q_{44}\sigma_6 \tag{4.31}$$

4.3.4 Finite Element Analysis (FEA)

The strain applied on the Si wafer was measured only in one direction, depending on the orientation of the strain gauge. From Pockels theory, however it can be seen that at least three planar strains/stresses are needed to be known to fully describe the system. In order to achieve this, the Si wafer under strain was simulated using FEA and the strains ϵ_2, ϵ_6, and stresses σ_1, σ_2, and σ_3 extracted. Silicon was set as an orthotropic material, with a stiffness matrix (which gives the linear relationship between the stresses and strains) as given by the matrix in A.1, in the Appendix [119]–[121]. The simulation was set in 3D, with symmetry simplifications along the x-axis, as shown in Figure 4.27. The model was fixed with a roller fixture in the yz-plane going through the origin. This allowed the solid to slide, but not detach from the center plane. Strain was applied analogous to the real setup, along the x-axis and applied to the glued surface of the wafer (approximated by the square on the right side of the wafer). The stress and strain values extracted were the calculated average from all mesh element values in a 1/2-inch diameter circle centered at the origin of the wafer, as the radiation on the transmitter side of the experiments was collimated using a 1/2-inch gold mirror.

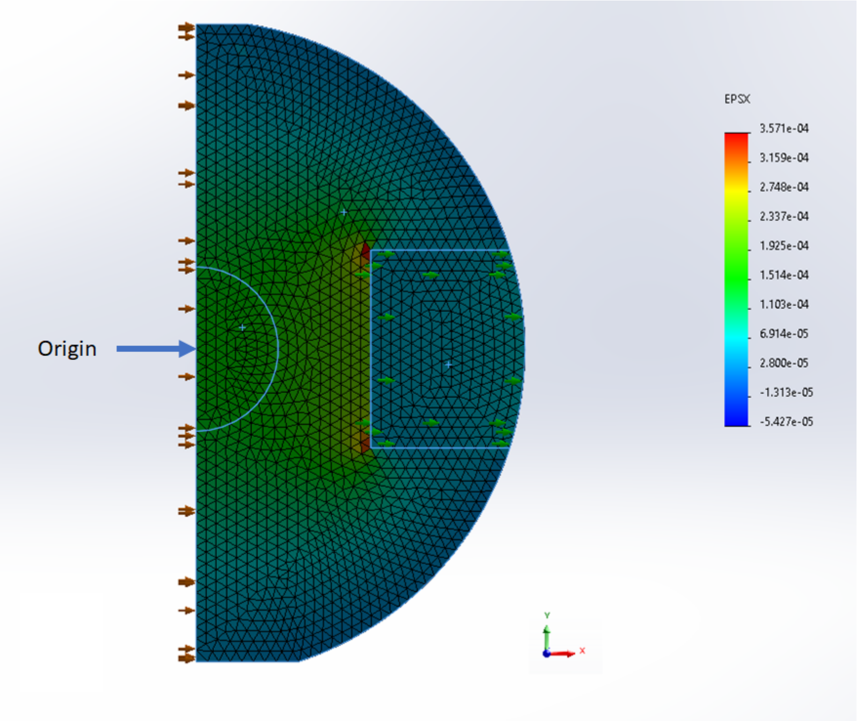

FIGURE 4.27: FEA Si wafer model with calculated ϵ_x plot

4.3.5 Extracting the Stress-Optical and Strain-Optical Parameters

For each applied strain and polarisation, the transmission spectra from 0.75 - 1.1 THz was recorded. This allowed for the refractive index to be extracted with the methods introduced in Chapter 2, by fitting the Fabry-Pérot resonances. The averaged regression coefficient of the fits was 0.98, showing a good confidence in the calculated refractive index. This allowed for the impermeability matrix ΔB to be calculated, using the relation in equation 4.8.

Applying the linear relations from 4.26-4.31, the stress-optical and strain optical coefficients averaged over several tested Si wafers were extracted. A significant difference between wafers was observed - some failed around 450 µm and others reached strain values of 680 µm before shattering. Therefore, calculations were done for strain up to 400 µm, in order to approximate the region of elastic deformation. The results, averaged over all samples, are shown in Table 4.4. Literature values for the stress-optical coefficients were found to differ by 2 orders of magnitude (Table 4.5). The extracted stress-optical coefficients at 0.75 - 1.1 THz fit within this range, with a much closer match towards the results obtained by Stoehr et. al in 2020 [115] and Kang et al [122] in 2021, the latter obtained in a similar frequency band. The models employed in [116] and [115] assumed Si to be isotropic, which requires only two independent stress components and sets

$$q_{44} = \frac{q_{11} - q_{12}}{2} \tag{4.32}$$

In our experiments it was possible to calculate q_{44} and p_{44} independently. While the two principle strain values ϵ_x and ϵ_y are in the order of hundreds of $\mu\epsilon$, ϵ_{xy} is around 3 orders of magnitude lower. The small values of ϵ_{xy} require a very fine precision in the measurement of the refractive index, therefore for the extraction of the p_{44} and q_{44}, the strain was applied in the [100] crystalographic axis. This way the ϵ_{xy} applied was up to 340 $\mu\epsilon$. The extracted p_{44} and q_{44} showed much larger deviations from their means in comparison to the other extracted parameters. This is an expected result, as the overall stresses applied to the wafers were much greater, potentially driving some away from their elastic regimes and amplifying the differences between wafers.

	a_{11}	a_{12}	a_{44}
q $[Pa^{-1}]$	-16.933e-13 ± 18.397e-14	7.2068e-13 ± 11.222e-14	18.075e-13 ± 66.8e-14
p	0.3506 ± 0.0425	0.1686 ± 0.0247	0.2685 ± 0.0991

TABLE 4.4: Photoelastic coefficients of <100> Si at 0.75 - 1.1 THz

	q_{11} $[Pa^{-1}]$	q_{12} $[Pa^{-1}]$	q_{44} $[Pa^{-1}]$
This work	-16.933e-13 ± 18.397e-14	7.2068e-13 ± 11.222e-14	18.075e-13 ± 66.8e-14
Kang et al. [122]	5.2e-13	-8.4e-13	9.8e-13
Biegelsen et al. [116]	-9.4e-11	1.7e-11	-11.1e-11
Stoehr et al. [115]	NA	NA	14.4e-13

TABLE 4.5: Comparison between measured and literature values for the photoelastic coefficients of <100> Si

4.3.6 Planar Stress and Strain Distribution Mapping

After extracting the stress- and strain-optical coefficients for Si at THz frequencies, they were used to do the process in reverse - for a <100> Si wafer under stress, the changes in THz transmission were used to map the stress and strain distributions on the wafer surface. To achieve this, the wafer was fully illuminated by the collimated THz source using a 2-inch parabolic mirror, while the receiver was placed closely at the back of the wafer on a linear XYZ-stage and moved in 0.5 mm increments in x and y to map out the transmission at every point. A reference unstressed map was also measured in order to calculate the impermeability tensor at each point. Like before, both S, P and SP polarisations were measured. The strain was applied in the y-direction (the [110] crystalographic axis). A strain gauge measurement in the y-direction established that the averaged y-strain should be in the order of 140 $\mu\epsilon$. The measured stress and strain distributions can be seen in Figure 4.28. Due to spatial restrictions on the optical table, only part of the wafer was scanned. The scanning extended over the left edge of the wafer, as clearly visible by the circular outline in each plot. In the area of maximum strain on the wafer (Figure 4.28, middle), it can be seen that the majority of strain in the y-direction is centered at 150 $\mu\epsilon$, which is in excellent agreement with the strain gauge measurements. All stress and strain values are also within a range matching what was previously observed in experiments under increasingly applied strain. There is also a good match between the stress/ strain distributions obtained through FEA and the ones measured. Figure 4.29 shows the FEA distribution of ϵ_y. A complete set of all the FEA results can be seen in figures A.2and A.3 in the Appendix. The FEA method assumed a homogeneous material, hence the lack of any distinct features. The measured stress/strain distributions, however clearly show internal defects present in the wafer due to the applied forces.

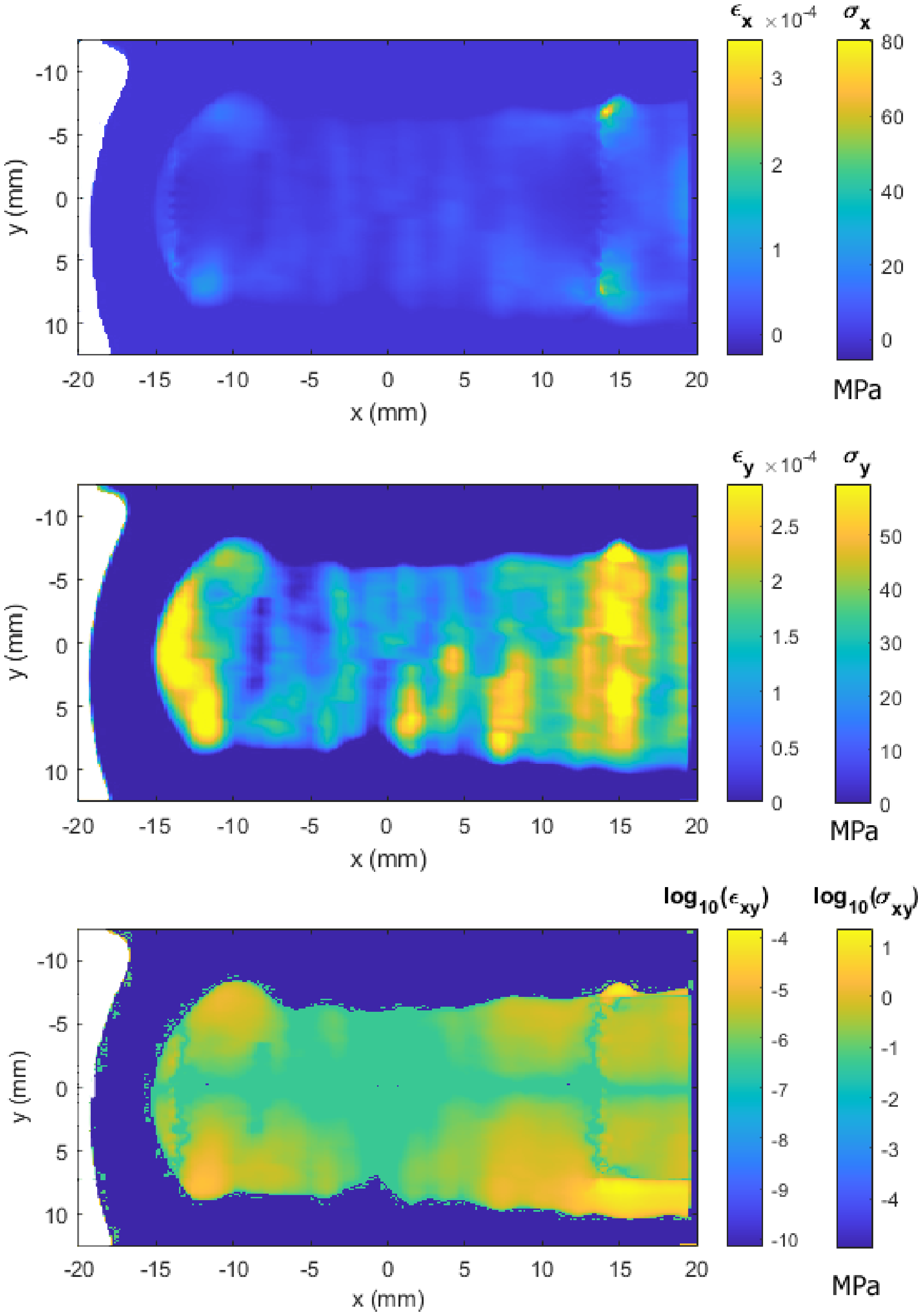

FIGURE 4.28: Measured stress and strain distributions in Si wafer under y-directional strain.

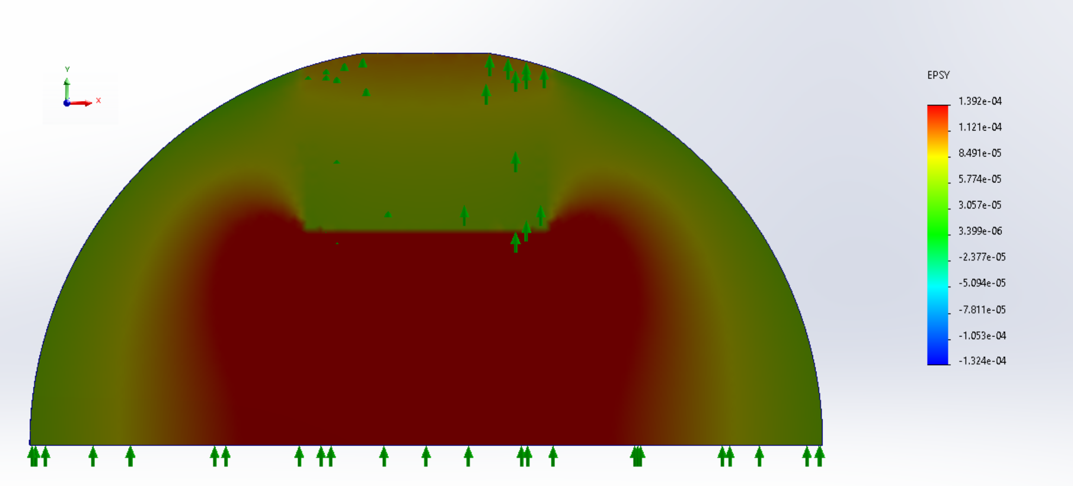

FIGURE 4.29: FEA Si wafer model with calculated ϵ_y distribution

4.3.7 Summary

The development and use of a THz ellipsometry system and fitting algorithm based on a frequency multiplied VNA was demonstrated. The system was calibrated by extracting the optical parameters of silicon, a well-investigated material in THz and showed excellent agreement with literature values. The system was further evaluated for the characterisation of low refractive index material (HDPE) and high-absorption composite materials (Tufnol and PDMS loaded with TiO_2), showing satisfactory results. An in situ measurement of the decreasing thickness of a silicon wafer being etched in KOH was demonstrated. Lastly, the system was used to extract the optically anisotropic complex refractive index of a split-ring metamaterial. Following was a simple and effective method for measuring sub-wavelength film thickness for materials transparent in THz. A constructed mirror delay line at grazing angles was demonstrated to measure SU8 films with sub-micrometer precision. Finally, using a reduced version of the ellipsometry system, the stress-optical and strain-optical coefficients of n-type monocrystalline Si at THz frequencies in the frequency domain were measured to our best knowledge for the first time. They showed good agreement with the values obtained from THz TDS measurements, resulting in $q_{11} = -16.933 \times 10^{-13}$, $q_{12} = 7.2068 \times 10^{-13}$ and $q_{44} = 18.075 \times 10^{-13}$. Consequently, the same measurement setup was extended to successfully extract a map of the stress and strain distributions of a Si wafer under extension. The maps clearly showed internal pressures within the wafer with feature resolution of 0.5

mm, restricted by the pixel size of the THz receiver. The experiments showed that THz frequency-domain spectroscopy is a viable method for non-contact stress / strain testing and can be used for the purposes of digital photoelasticity measurements.

Chapter 5

Waste Oil Characterisation Using THz TDS Spectroscopy

5.1 Introduction

The following chapter explores the application of THz TDS spectroscopy in conjunction with machine learning to create a reliable waste acceptance quality criteria for oil recycling. Current industry best practices for determining a waste oil sample's suitablility for treatment include a combination of laboratory tests. This can include water content measurements (such as Karl-Fischer titration), viscosity measurements, flash point measurements, colorimetric tests for the presence of polychlorinated biphenyls, ferrogprahy tests and measurements for quantifying contaminants using elemental analysis and/or Fourier-Transform Infrared Spectroscopy (FTIR). Due to the nature of waste oil generation and collection - usually in small batch sizes from car garages, individual testing on each waste oil batch is not practical and samples from mixed large batches are measured instead. It is then up to the laboratory technicians to determine if the waste oil is suitable for treatment. The complex composition of waste oil can make this a non-straightforward and time consuming task, where mistakes can lead to both economical and environmental risks. Here the suitability of THz TDS spectroscopy as a quick and reliable method for determining a waste oil sample's acceptance for treatment is investigated. A 1-D Convolutional Neural Network (CNN) is then trained on the data for a specific waste oil recycling plant and its prediction accuracy is presented.

5.2 Waste Oils and Waste Oil Refining

Used lubricating oil, often referred to as waste oil, is any lubricating oil, which has been contaminated by physical or chemical impurities as a result of use [123]. Waste oils represent the largest amount of liquid, non-aqueous hazardous waste in the world [124]. As lubricants operate in hostile, high-temperature environments, they are exposed to chemically reactive by-products such as partially burned hydrocarbons, soot, water, wear debris and products of combustion, nitric acid (HNO3) and sulfuric acid (H2SO4) [125]. Once they reach a level of degradation, such that they no longer serve their purpose, used lubricants need to be disposed of and enter the hazardous waste stream. Waste oils can be generated from engine oils, hydraulic working fluids and lubricants, compressor oils, gearbox oils and various types of mineral and synthetic industrial lubricating oils, with engine oils being by far the largest waste generator. Generally, lubricating oils are a complex mixture of isoalkanes, monocycloalkanes and monoaromatics [126]. The chemical structure of the lubricating oil differs considerably depending on additives in the lubricant blend. Additives differ with lubricating applications [127]. Most impurities in the oils are generated during oxidation, especially during internal combustion engine applications. Contaminants include unsaturated hydrocarbons, phenolic compounds, aldehyde, acidic compounds, additives, metals, varnish, gums and other asphaltic compounds originating from the overlay of bearing surfaces and degradation of the base oil components [123]. Despite the presence of impurities, most of the base oil part in the waste oil is not exhausted. The chemical composition of the lubricating oil is usually preserved to a large amount because of the high stability of the heavy compounds contained in the base oil [125]. Fresh base oil can be recovered from waste oils with an efficiency as high as 95%. By comparison, crude oil lubricant refining yields an efficiency of around 67% [123]. Waste oils are classified as hazardous waste, as they are toxic to the environment and particularly dangerous to aquatic life, as one litre of oil can contaminate 1 million litres of water [128]. Various lubricant additives are also labelled as potentially carcinogenic and burning waste oil can release toxic substances in the air. Due to the necessity to dispose of nearly 3 million tonnes of waste oil in Europe per year alone [124], as well as its high recovery gain, various methods for the treatment and recovery of waste oils are being developed. The simplest treatments, such as selective solvent extraction and pyrolysis are used to extract light fuels such as diesel and gasoline, as well as heavy fuel oils, which then can be applied in fuel mixtures in burners and marine fuels. A more complicated process is necessary for the re-refining of waste oils into lubricant base stocks. This usually includes removal of mechanical impurities, water separation, vacuum distillation, hydrogenation and/or bleaching. Regardless of the recycling process employed, quality control of the waste oil feed stock is crucial before any kind of treatment.

5.2.1 Quality Criteria and Composition

The importance of quality control of waste oil feedstock in re-refining and waste treatment facilities is two-fold. On the one hand it ensures that the feedstock is economically viable – it needs to give a high enough yield, to be compatible to the treatment processes that it is about to undergo, it has to prevent causing damage to the equipment or cause delays and setbacks due to process parameter changes and unscheduled cleaning. On the other hand, quality control is paramount as a waste acceptance benchmark and a health and safety procedure. Waste acceptance is a practically and legally required procedure.

Fresh Oil Composition

Used oil is treated with the end goal of refining it into fresh lubricant oils. The composition of fresh lubricants themselves however, is quite complex. They are mainly mixtures of straight and branched chain hydrocarbons (alkanes), cycloalkanes, and aromatic hydrocarbons. Polynuclear aromatic hydrocarbons (and the corresponding alkylated derivatives) and metal-containing constituents are components of motor oils and crankcase oils, with the used oils typically having higher concentrations of these substances than the new unused oils. A low concentration of aromatics is desired, as they are good solvents and are too reactive in comparison to the base oil. Oxidation of aromatics can start a chain reaction that can dramatically shorten the useful life of base oil. The viscosity of aromatic components is also undesirably susceptible to changes in temperature [123]. The main functions of lubricating oil include reducing friction, heat transfer, rust and wear protection and removing contaminants, which are achieved through the introduction of additives [129]. Common additives include: antifoaming agents, antioxidants, antiwear additives, corrosion and rust inhibitors, viscosity and pour point modifiers, detergents and dispersants. The typical fresh oil composition is given in Table 5.1

Component	% w/w
Base oil	71.5 - 96.2
Metallic detergents	2.0 - 10.2
Dispersants	1.0 - 9.0
Zinc dithiophosphate	0.5 - 3.0
Antioxidant/antiwear	0.1 - 2.0
Friction modifier	0.1 - 3.0
Pour point depressant	0.1 - 1.5
Antifoam	2 - 15 ppm

TABLE 5.1: Typical composition of lubricating oil. Sources from [123], [130]

.

Used Oil Composition

Used lubricating oil is a complex mixture of paraffinic, naphthenic, aromatic petroleum hydrocarbons and contaminants. Typical contaminants can be carbon deposits, sludge, aromatic and non-aromatic solvents, water (as a water-in-oil emulsion), glycols, wear metals and metallic salts, silicon based antifoaming compounds, fuels, polynuclear aromatic hydrocarbons, and miscellaneous lubricating oil additives. The contaminants in used oil can be classified as extraneous contaminants and products of oil deterioration. Extraneous contaminants are introduced from the surrounding air and by metallic particles (such as from the engine in motor oils). Air-borne contaminants can be dust, dirt, and moisture, whereas contaminants from the engine can be (1) metallic particles resulting from wear of the engine, (2) carbonaceous particles due to incomplete fuel combustion, (3) metallic oxides present as corrosion products of metals, (4) water from leakage of the cooling system, (5) water as a product of fuel combustion, and (6) fuel or fuel additives or their by-products, which might enter the crankcase of engines.

Contaminants from oil deterioration tend to be more prevalent. Some of the important by-products of oil deterioration are (1) sludge: a mixture of oil, water, dust, dirt, and carbon particles that results from the incomplete combustion of the fuels; (2) lacquer: a hard or gummy substance that gets deposited on engine parts as a result of subjecting sludge in the oil to high temperature operation; and (3) oil-soluble products: the result of oil oxidation products that remain in the oil and cannot be filtered out and are thus deposited on the engine parts. The quantity and distribution of engine deposits vary widely depending on its operation [123]. A comparison between the physical and chemical properties of fresh lubricant oils and waste oils is shown in Table 5.2

Properties	Fresh lubricating oil	Used lubricating oil
Physical properties		
Specific gravity	0.882	0.910
Dynamic viscosity SUS at 40°C	-	324.0
Bottom sediment and water, % v/v	0	12.3
Carbon residue, % w/w	0.82	3.00
Ash yield, % w/w	0.94	1.30
Flash point,°C	-	175.56
Pour point,°C	-37.7	-37.7
Chemical properties		
Saponification number	3.94	12.7
Total acid number	2.20	4.40
Total base number	4.70	1.70
Nitrogen, % w/w	0.05	0.08
Sulphur, % w/w	0.32	0.42
Lead, ppm	0	7535
Calcium, ppm	1210	4468
Zinc, ppm	1664	1097
Phosphorus, ppm	1397	931
Magnesium, ppm	675	1097
Barium, ppm	37	297
Iron, ppm	3	205
Sodium, ppm	4	118
Potassium, ppm	<1	31
Copper, ppm	0	29

TABLE 5.2: Comparison between fresh and used lubricant oil physical and chemical properties. Sources from [123], [130]

.

5.3 Preliminary THz TDS measurements

All oil samples were provided by Polihim-SS Ltd waste oil refinery and subsequent neural network training was done on the data from the company's specific treatment system. For initial testing of THz TDS spectroscopy on oils, three kinds of samples were measured - a waste oil sample which has been previously accepted, a SN100 (API standard) base stock oil (one that has already undergone treatment) and a rejected waste oil sample. The SN100 base stock was found to have a kinematic viscosity of 4.2 cSt at 100° C and a specific gravity of 0.875 at 15° C. The waste oil samples had similar parameters, with a kinematic viscosity of 4.3 cSt at 100° C and a specific gravity of 0.8744 at 15° C for the accepted waste oil and 0.875 for the rejected oil sample. The rejected oil sample was suspected to contain low-boiling point solvents, but the exact composition of the contaminants was unknown.

The THz transmission spectra were taken with the aid of polypropylene cuvettes of 5 mm pathlength. The accepted waste oil and base stock sample measurements were provided by Manchester University THz group. These measurements were taken with a time-domain spectrometer which used the 20 fs laser pulses generated by a 80 MHz Ti:Sapphire oscillator. The generated terahertz radiation was aligned through a series of off-axis parabolic mirrors and detected using standard electro-optic detection techniques. A 1 mm-thick (110)-cut zinc telluride (ZnTe) crystal and a 100 µm-thick (110)-cut ZnTe crystal were used for generation and detection respectively. A clear difference between the two can be seen, with this particular blend of waste oil having a feature at 0.45 THz, a frequency shift and an amplitude difference as high as 40%. As can be expected, the base stock transparency is higher than the used oil, due to the presence of fewer contaminants. Despite the differences in their transmission spectra, the base stock and accepted waste oil overall show a similar envelope. The rejected waste oil sample, however, shows a very different spectral shape. As seen in Figure 5.1 it doesn't exhibit any of the similar features present in the other two samples. This is a promising result, as a strong difference between the acceptable and contaminated waste oil increases the accuracy of the machine learning predictions. Preliminary measurements therefore showed promise for the applicability of THz spectroscopy for waste oil quality control. The rejected waste oil sample and all subsequent measurements were taken with the Durham University Engineering Department's THz TDS system, as described in Chapter 2. Measurements of the base oil and accepted waste oil from the Durham TDS system were compared to results from the Manchester system, in order to assess repeatability of the experiments and avoid any errors due to differences in the two measurements systems. Figures 5.2 and 5.3 show three measurements of SN100 base oil samples and three measurements of accepted waste oil samples respectively. In both figures, Sample 1 has been measured with the TDS provided by Manchester University and Samples 2 and 3 have been measured with the Durham system. Samples 2 and 3 were individual samples from the same oil, whereas Sample 1 was taken from a different oil of the same type. As expected, the strongest similarities are between individual measurements of the same oil, having a correlation coefficient of 0.9995 for the base oil (between Sample 2 and 3) and 0.9976 for the accepted waste oil (also between Sample 2 and 3). The correlation between different batches is weaker but still very satisfactory, with correlation coefficients [0.9812, 0.9827] between Sample 1 and Samples 2 and 3 respectively for the the base oil traces and [0.8968,0.9032] for the accepted waste oil samples. The accepted waste oil is expected to have a larger difference between batches in comparison to the base oil samples, which are more similar in terms of composition. The largest deviations in measurements between samples were expected in the rejected waste oils, where there could be little chemical similarity between individual samples. This is clear in Figure 5.4, where again Sample 1 was taken from a different rejected oil sample and Samples 2 and 3 are individual measurements of the same oil type. All measurements are done with the Durham TDS system. The correlation between Sample 1 and Samples 2, 3 is significantly lower, with the correlation coefficients calculated to be 0.4881 and 0.4830 respectively. Samples 2 and 3 were taken from the top and bottom of the rejected oil container, which are expected to have differences in composition due to sedimentation, as the samples weren't homogenised prior to measuring. This is reflected in the lower fit between Sample 2 and Sample 3, with a correlation coefficient of 0.9959. There is a promising repeatability between experiments with the oil samples provided and between the measurements taken with the two TDS systems.

Figure 5.5 shows the reference transmission spectrums of the University of Manchester TDS measurements and Durham University TDS measurements respectively, both of which have a low spectral uncertainty within the frequency range shown in the oil measurements (0-2.5 THz).

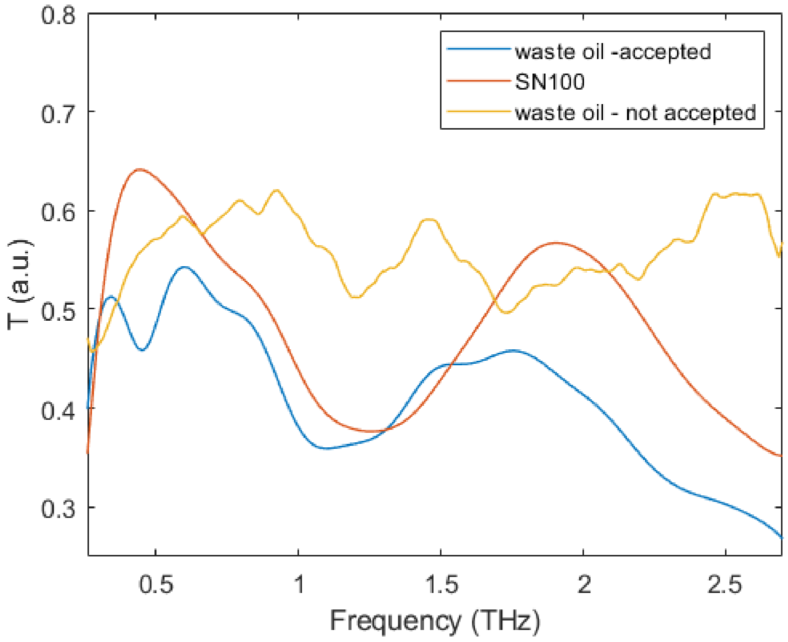

FIGURE 5.1: THz TDS measurements of the transmission spectrum of base stock oil, waste oil suitable for treatment and waste oil rejected for treatment

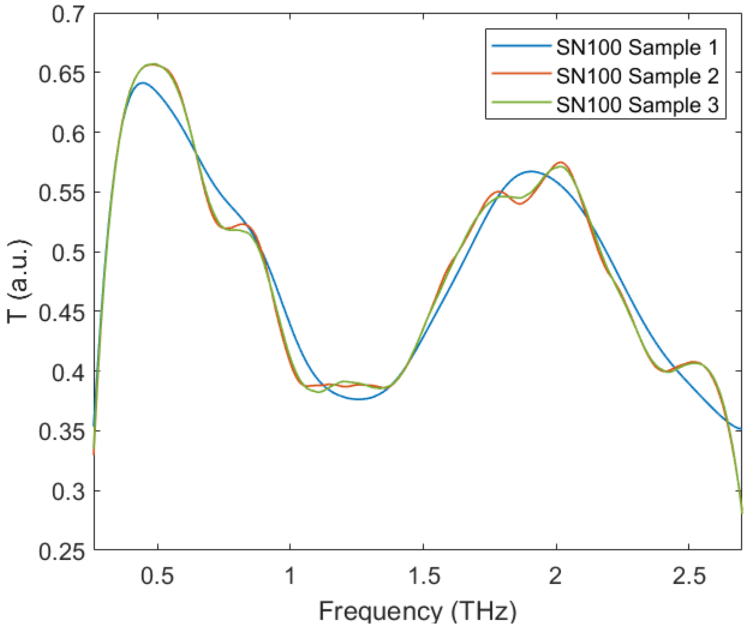

FIGURE 5.2: Comparison between the transmission spectrum of base oil samples

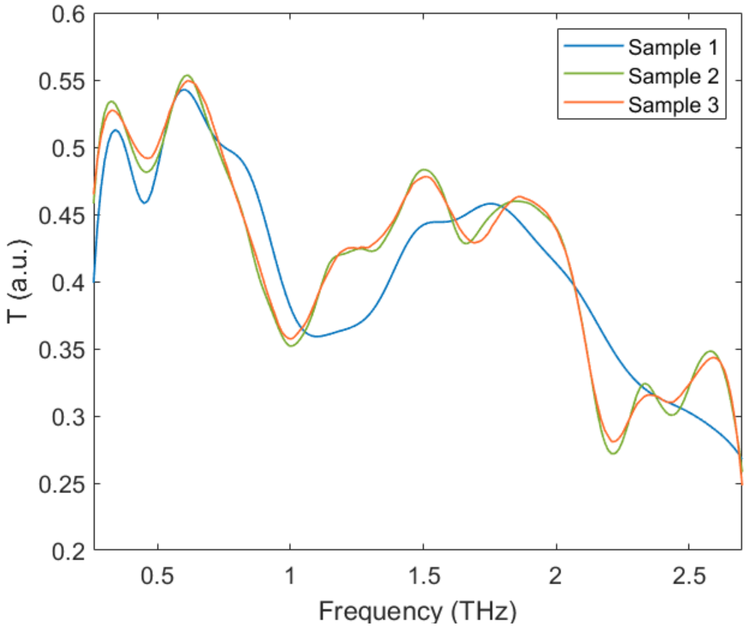

FIGURE 5.3: Comparison between the transmission spectrum of accepted waste oil samples

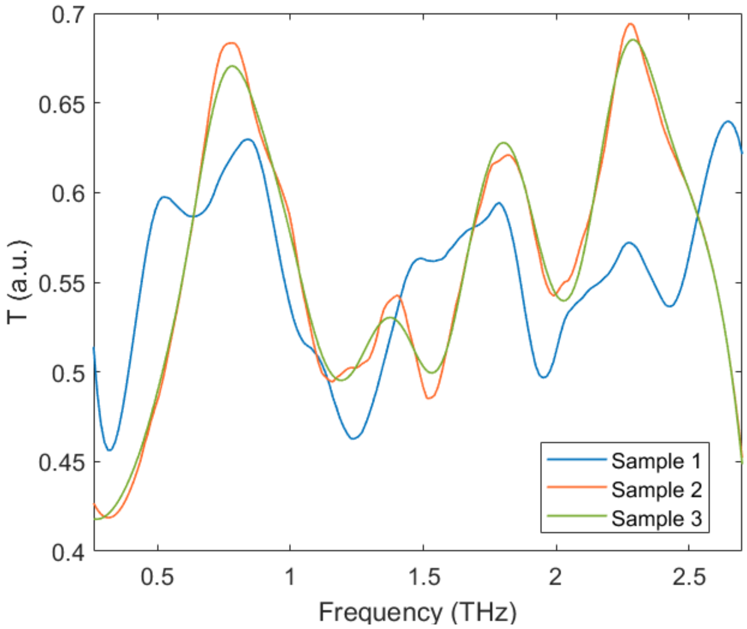

FIGURE 5.4: Comparison between the transmission spectrum of rejected waste oil samples

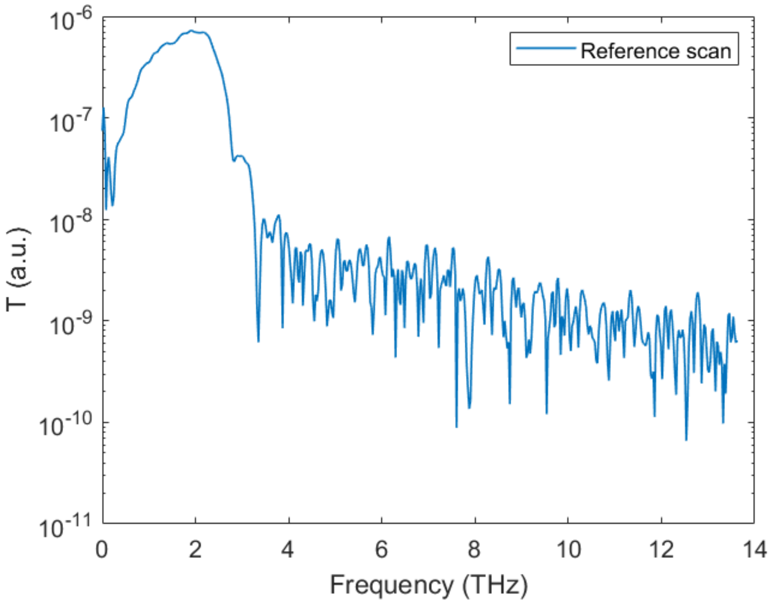

(A) University of Manchester TDS

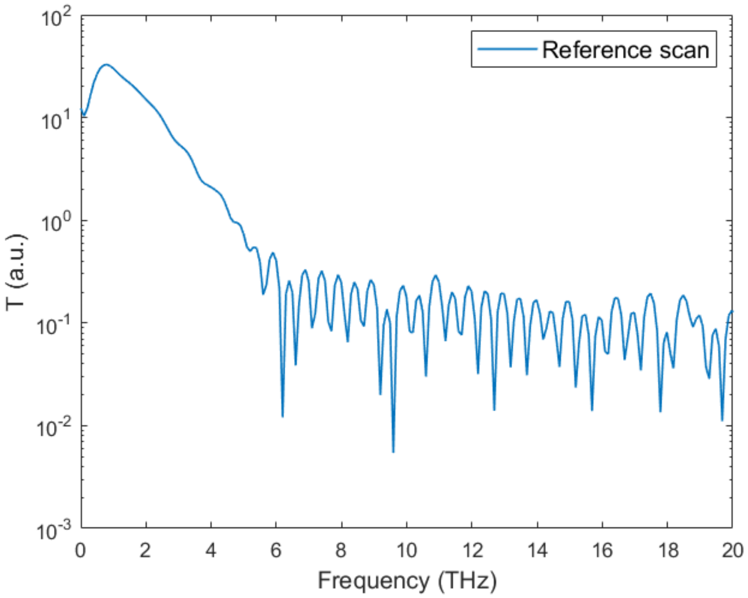

(B) Durham University TDS

FIGURE 5.5: Reference scans for both TDS systems used

5.3.1 Introduction to Artificial Neural Networks

Artificial neural networks (ANNs) are a computational method, based on an abstraction of the operation of biological neural networks. Although the first ANN architecture was introduced back in 1943 by neurophysiologist Warren McCulloch and the mathematician Walter Pitts [131], widespread interest and application surged mainly since the beginning of the 2010s. Today ANNs are the state-of-the art technology for complex pattern recognition and decision making. The advances in related fields brought upon the practical applicability of ANNs. Most notably these are the ability to collect, store, and operate over large amounts of data, the ability to generate labeled training data via crowd-sourcing services (such as Amazon Mechanical Turk), vast improvements in computational power via Graphical Processor Units (GPUs) and advances in both theory and software implementation of automatic differentiation (e.g. Theano) [132]. The applications for ANNs are too numerous to list, but perhaps most famously they are known for their powerful use in chess engines, image and voice recognition and high-frequency stock market trading. Several terms, such as "deep learning" and "artificial intelligence (AI)" are used sometimes interchangeably with ANNs, but they are in fact subsets of the methodology. Their relationship from top to bottom is as follows: Artificial Intelligence → Machine Learning → Neural Networks → Deep Learning (DL). The underlying concept behind DL algorithms is to supply vast amounts of input training data (either labeled but in more flexible algorithms also raw unlabeled data), and by an iterative process to update the relationship between inputs and outputs, so that the outputs are susceptible to features of interest in the input. The algorithm essentially learns from past experiences and can be constantly evolving to better recognise patterns and predict outcomes [133].

The basic unit of the ANNs, analogous to biological neural networks is the neuron (sometimes also just referred to as "unit"). The neuron is a function that has several characteristics. Firstly, it takes in an input vector $x \in \mathbb{R}^n$ and outputs a scalar. It is parameterised by a weight vector $w \in \mathbb{R}^n$ and a bias term b. The output of the unit can be described as

$$f(\sum_{i=1}^{n} w_i.x_i + b) \tag{5.1}$$

, where $f : \mathbb{R} \rightarrow \mathbb{R}$ is referred to as activation function [132]. Various activation functions can be used depending on the application, but generally they are non-linear. This is commonly referred to as a feed forward network, and the process of the unit neural network is visually represented in Figure 5.6.

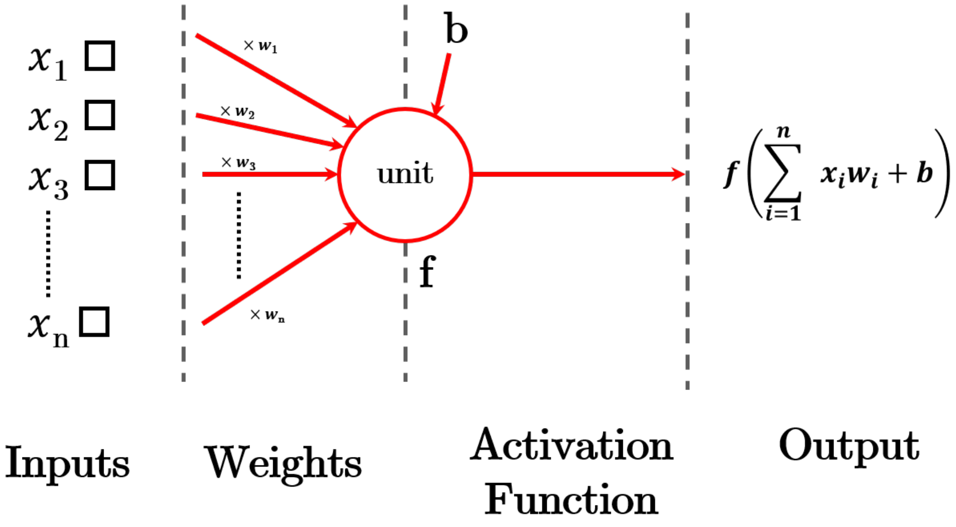

FIGURE 5.6: Graphical representation of single neural network unit [134]

Neural Network Structure

Using the unit as a basic building block, neural networks are organised in layers, with each layer containing one or mode units. The number of units in a layer is denoted as the width of the layer and the overall number of layers is referred to as the depth of the network (hence the concept of "deep learning") [132]. The first layer, called the "input layer" takes the input data for the network, whereas all subsequent layer inputs are the outputs of the previous layer, as displayed in Figure 5.7. The final layer computes the overall output of the network, hence its name "output layer". The width of each layer can be individually assigned and doesn't need to be the same. All layers between the input and output layers are also called hidden layers. The collection of all weights w and bias terms b in the network is denoted by $\theta \in \mathbb{R}$ and the output of the network by $\hat{y}$. The choice of network width and depth is a crucial part of neural network design [134].

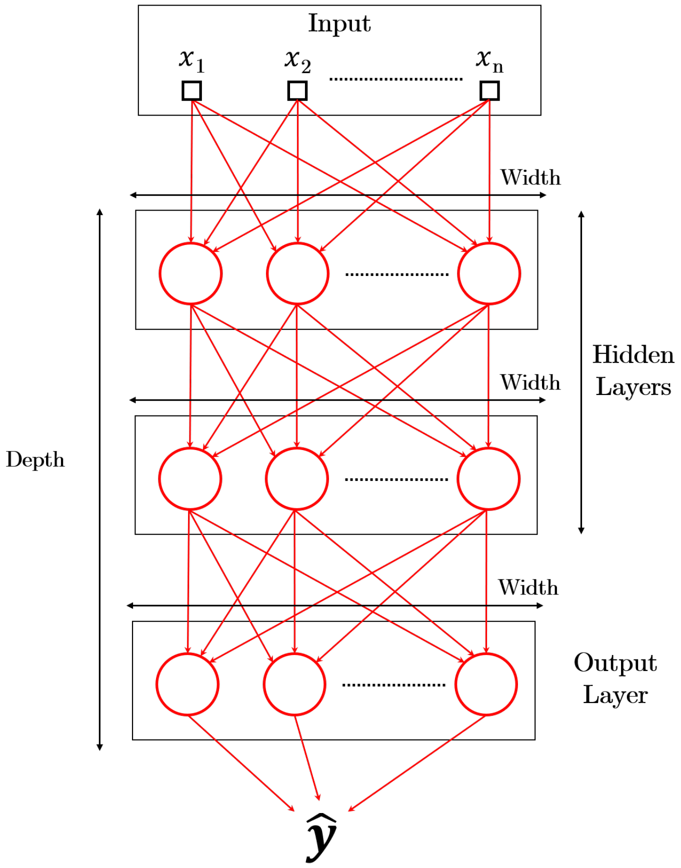

FIGURE 5.7: Graphical representation of general neural network structure [134]

Neural Network Training

Initially random values are assigned to the weights and bias terms θ. If the function describing the whole network is denoted as f_{NN}, the error between the target output and the output of the network is called the loss function and is defined as $l(f_{NN}(x, \theta), y)$, where x is the input vector and y is the target output. The values in θ are then updated, such as the loss function is minimised using gradient descent. The step-by-step update is given by

$$\theta_s = \theta_{s-1} - \alpha . \nabla l(f_{NN}(x, \theta), y), \tag{5.2}$$

where s is the step number [132]. The computation of the gradient of the loss function is executed using automatic differentiation. The optimisation of the loss function is done through stochastic gradient descent methods. For our current application the Adam optimiser was used [135]. It is an algorithm for first-order gradient-based optimization of stochastic objective functions, based on adaptive estimates of lower-order moments. The method is straightforward to implement, and computationally efficient.

Binary Cross Entropy Loss Function

In the case of waste oil quality control, the output of the neural network needs to be binary - the feed stock is either accepted or rejected. This is a popular classification problem, described by a special case of the multi-class classification. The loss function employed is called a binary cross entropy loss function. For the input/target output data $D = [x_1, y_1, x_2, y_2, ...x_n, y_n]$ and network parameters θ, the probability that the target output is acquired is denoted as $P(D|\theta)$. The network training aims to update θ such that it maximises $P(D|\theta)$. Assuming that each pair of variables x_i, y_i is independent and the probability is given by a Bernoulli distribution (for binary classification such as the toss of a coin), the probability is given by

$$P(D|\theta) = \prod_{i=1}^{n} f(x_i, \theta)^{y_i} (1 - f(x_i, \theta))^{(1-y_i)} \tag{5.3}$$

The binary cross entropy loss function $l(f_{NN}(x, \theta), y)$ is then given by taking the negative logarithm of the probability, making the optimisation a minimisation problem.

$$\begin{aligned} l(f_{NN}(x, \theta), y) &= -\log P(D|\theta) \\ &= -log \prod_{i=1}^{n} f(x_i, \theta)^{y_i} (1 - f(x_i, \theta))^{(1-y_i)} \\ &= -\sum_{i=1}^{n} y_i \log f(x_i, \theta) + (1 - y_i) \log (1 - f(x_i, \theta)) \end{aligned} \tag{5.4}$$

5.3.2 Activation Functions

Activation functions, as previously shown in Figure 5.6 dictate what function a unit applies to its input to produce the output. Depending on the activation function of their units, layers can have different behaviours and applications within the network structure. In general, best results are achieved when the activation function is non-linear and continuously differentiable, so that gradient descent loss function optimisations can be applied. A commonly used hidden layer unit is the Rectified Linear Unit (ReLU). Its activation function is defined as $f(x) = max(0, wx + b)$, which applies a linear function to positive values of x and rectifies negative values. Empirical results have shown that ReLU units lead to large and consistent gradients, which helps gradient-based learning [136]. For binary and multi-class classification problems, the cross entropy loss function is used in conjunction with the Softmax output layer. This layer provides normalisation of the output values, so that the sum of outputs from each class adds up to 1. This way the output for each class represents the probability of the input data belonging to said class. The unit activation function for an input x_i is formulated as $f(x_i) = \frac{e^{x_i}}{\sum_{m=1}^{n} e^{x_m}}$, where $x = [x_1, x_2, x_3 ... x_n]$ is the input vector of the Softmax layer.

Convolutional Layer

Convolutional layers as the name suggests, perform convolution as their activation function. This type of layer, and by extension the neural networks that employ them - convolutional neural networks have proven to be extremely successful in applications involving 1-D data, such as time / spectrum traces and 2-D image data [136]. Recently proposed 1D CNNs have achieved state-of-the-art results in early health diagnosis, structural health monitoring, anomaly detection and identification in power electronics and electrical motor fault detection [137]. A major advantage of these types of networks is that their implementation requires simple and fast 1D convolution operations (only scalar multiplication and addition), leading to low-cost hardware requirements and real-time performance. In addition, unlike higher dimension CNNs and other DL architectures, they can be trained on small data sets and do not require any feature engineering. This makes 1D CNNs an ideal choice for our application. Convolution and cross-correlation in the context of 1D convolutional layers is used interchangeably. For an input $I(t)$ and a kernel $K(a)$, the cross-correlation is given by

$$s(t) = \sum_a I(t+a)K(a) \tag{5.5}$$

For discrete inputs the operation can be visualised in Figure 5.8. The kernel is essentially slided over the input and the output shows how similar the kernel is with this portion of the input. The convolution operation produces the highest value where the kernel is most similar with a portion of the input, equivalent to a feature being discovered [136]. To achieve this through a layer in the CNN, instead of a fully connected layer, as displayed in Figure 5.9a, a partially connected layer is used, Figure 5.9b. The weights between each pair of neurons in a fully connected layer are unique, whereas in the convolution layer the weights are repeated and essentially represent the kernel. The choice of kernel size is an important part of fine-tuning the neural network.

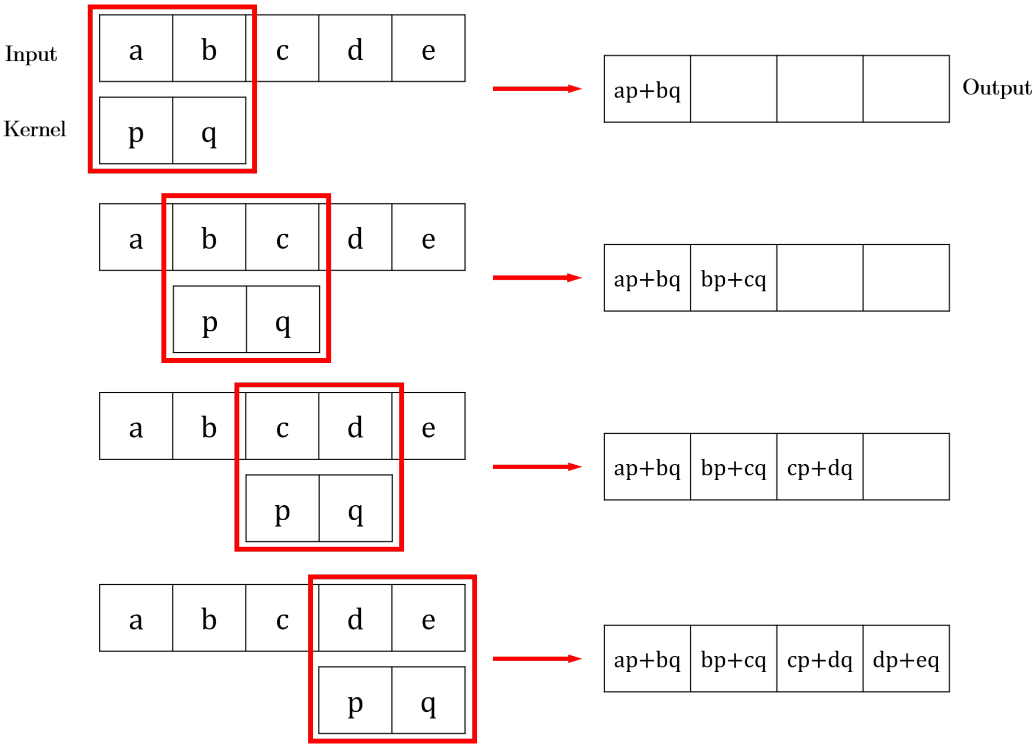

FIGURE 5.8: Discrete convolution

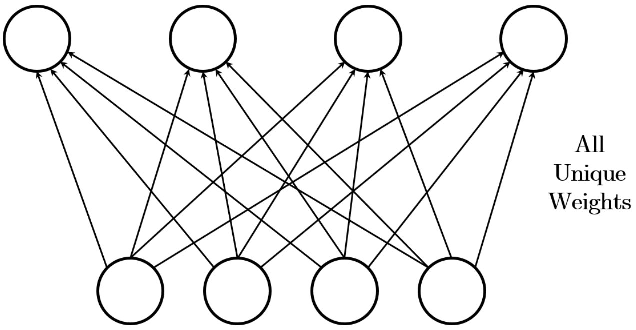

(A) Fully connected layer

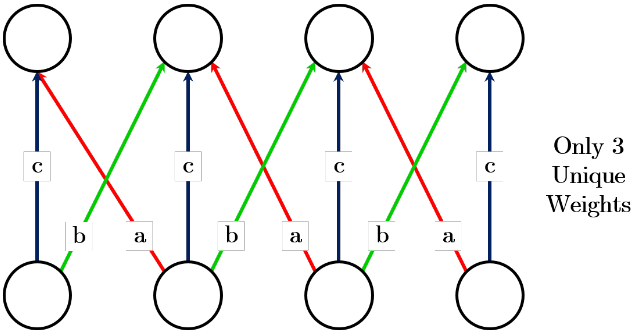

(B) Partially connected convolution layer with a kernel size of 3. The kernel is represented by the weights [a b c]

FIGURE 5.9: Comparison between layers [136]

Pooling Layer

A pooling layer is almost always used in conjuction with convolutional layers. When a feature has been discovered by the convolutional layer, the exact location of the feature is not of importance. The pooling layer provides this translational invariance. It is most intuitive in image processing applications. Assuming that the task at hand is to learn to detect faces in photographs but the faces on the input are tilted: the convolutional layer can learn to detect the eyes and the pooling layer abstracts the location of the eyes in the photograph from their orientation. This is most often achieved through a simple max() function, applied through a separate pooling kernel, as shown in Figure 5.10. The output of the pooling layer is therefore much smaller than the input [136].

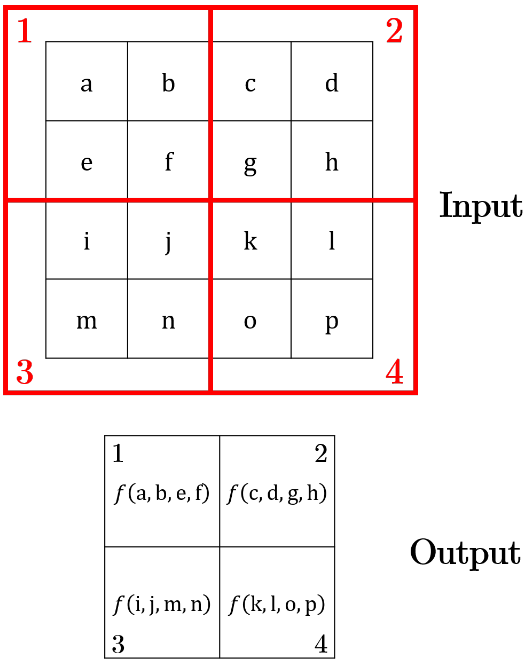

FIGURE 5.10: Pooling layer operation

Dropout Layer

The dropout layer is used to prevent overfitting of the training data. Overfitting is linked to the complexity, or capacity of the fitting model. For a given data, which can be fitted with a 2-degree polynomial, the same can be done with a 5 - degree polynomial with 3 zero-value terms. In this case using the latter would be considered overfitting. The logical extreme of this situation is that for a N-valued input vector, an N-valued polynomial can give perfect fit, in which case no real learning has taken place. The dropout layer therefore randomly sets input units to 0 at a given rate at each step during training time. Inputs not set to 0 are scaled up by 1/(1 - rate) such that the sum over all inputs is unchanged [138]. Preventing overfitting is important when the network is trained on small datasets.

5.3.3 Training and Test Data Formatting

An overall of 30 oil samples were obtained for spectroscopy measurements - 10 samples of base oil, 10 accepted waste oil and 10 rejected waste oil. The data necessary for training a CNN is however in the order of thousands of observations, much larger than the sample sizes and spectroscopy measurements obtainable in practice.

To mitigate this, derivatives of the available data were made. Firstly, the average spectral variance (the difference in transmission amplitude response at the same frequency) between different oil samples of the same type was measured and was found to be rounded to 0.2. For the training data for accepted waste oil, 5 of each unique sample measurements of base oil and accepted waste oil were given a confidence interval of 0.2 and derivative data was generated by adding a randomised bias, constant over the whole spectrum, within the confidence interval. This is illustrated in the top two plots in Figure 5.11. Then for each combination between an accepted waste oil measurement and a base oil measurement (with 5 samples of each, accounting for an overall of 25 combinations), a confidence interval was calculated and the data was randomly generated within the interval limits (as seen in Figure 5.11 bottom). A sample measurement similar to the derived data is expected to be treated as acceptable waste oil. The same procedure was applied to the other 10 base and accepted waste oil samples to generate the test data. This was the data against which the model was tested and was therefore generated separately to the training data, to ensure it is as independent as possible.

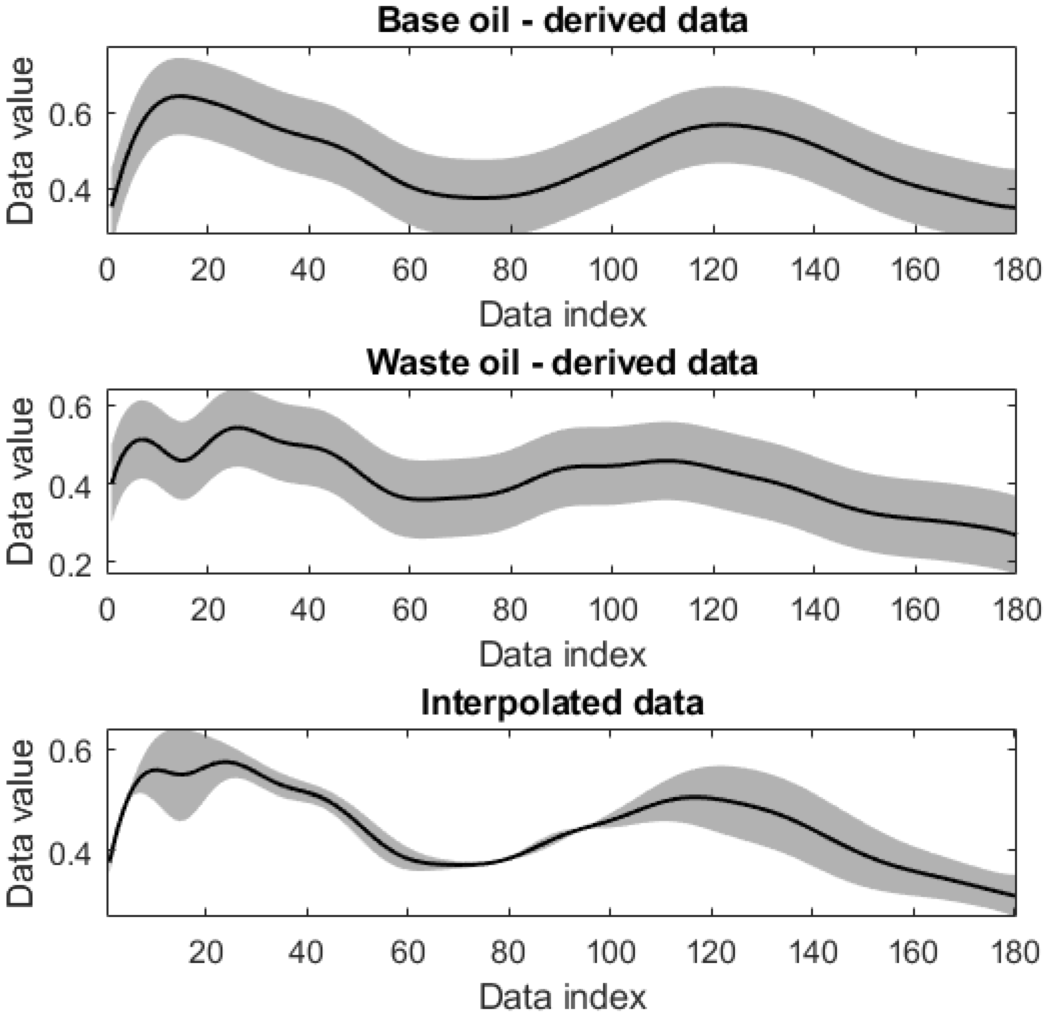

FIGURE 5.11: Accepted waste oil training data

Similarly derived data was generated for the rejected oil training and testing data. The first type of derived data was again a simple bias applied to the rejected oil spectroscopy measurements within the confidence interval. Since it is desirable for the model to be able to reject data coming from a non-oil or noise sample (such as pure solvent, water etc), randomly generated spectral shapes within the confidence interval 0.2-0.7 were also added to the rejected data training set and testing set (seen in Figure 5.12). The data value (y-axis) in Figure 5.12) represent the transmission spectra amplitude and the data index (x-axis) the frequency points.

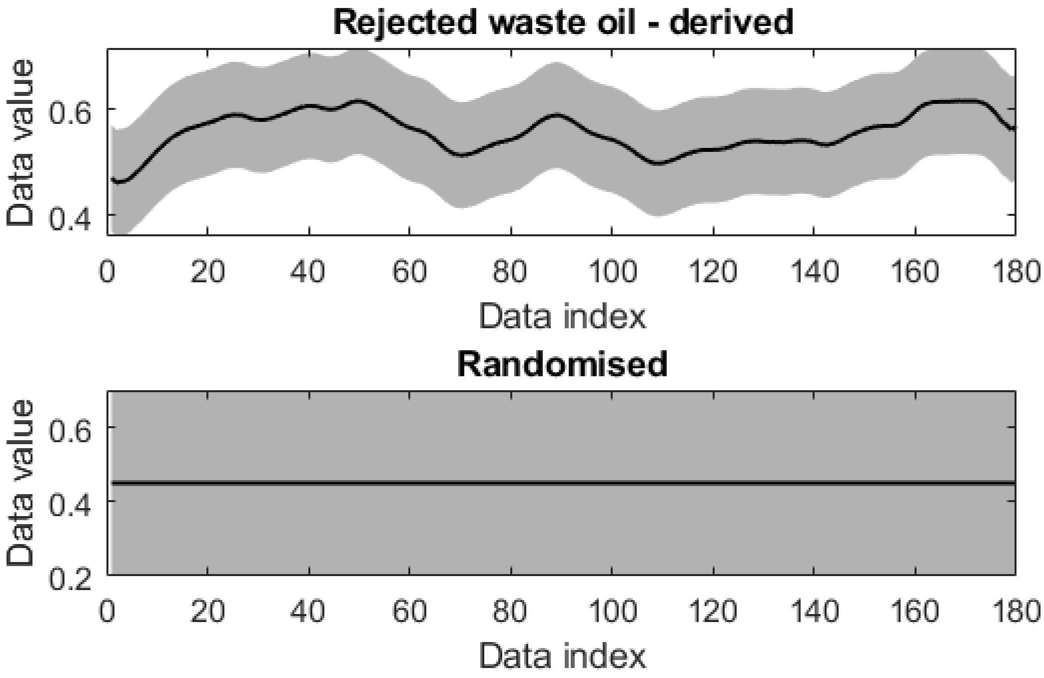

FIGURE 5.12: Rejected waste oil training data. The gray regions show the limits within which randomised data is generated.

5.4 Results

The implemented 1-D CNN structure is shown in Figure 5.13. The sequential Keras model was used, provided by the Tensorflow library for Python [139]. Two convolution layers were used, which is a standard implementation providing better feature recognition. The convolution layers were both set to a kernel size of 3 and 64 parallel feature maps. The number of feature maps determines the number of times the input is processed, producing parallel outputs. A dropout layer was then introduced to avoid overfitting, as CNNs tend to learn very quickly. This slows down the learning speed. The pooling layer then reduced the number of discovered features to 25%, so that the learning is concentrated on only the most notable features. A flattening layer formatted all outputs into one array, which was then fed into a fully connected ReLU layer, before returned to a Softmax layer. The output showed the test input's probability to be classified as "accepted oil" or "rejected oil". The Adam algorithm for stochastic gradient descent was used, applying the cross entropy loss function to optimise the network. The network was trained for 10 epochs and an input data batch size of 32. The batch size determines how many observations of the input data are used before the weights in the network are updated.

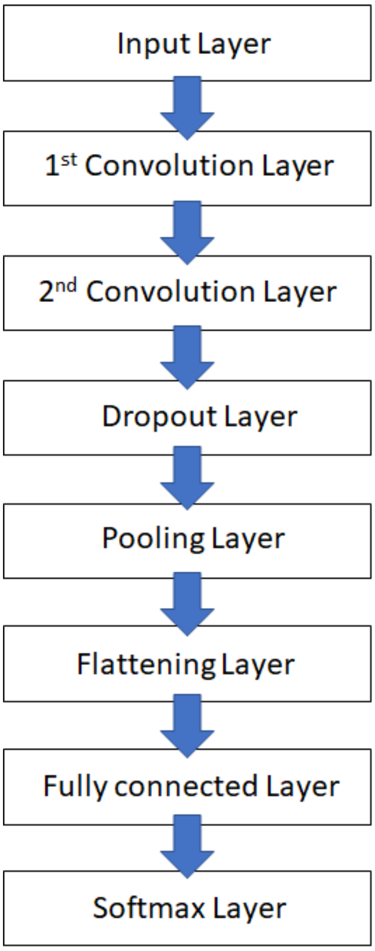

FIGURE 5.13: Implemented 1-D CNN structure

Once the model was fit, it was evaluated on the test dataset and the accuracy of the fit was returned. Neural networks are stochastic in nature, therefore each time they are retrained they have the potential to return different results. Therefore, in order to evaluate the model, the network was re-trained 20 times and the accuracy recorded and summarised. The network was found to be successful into identifying the waste oil classification with a 100 % accuracy every time. Table 5.3 shows the probability values for a randomly selected test data, the certainty being often close to 99%, which explains the perfect accuracy results. The computation times were also in the order of seconds per evaluation on an Intel i5-8600K overclocked at 4.8 GHz. This shows great promise for the identification of waste oil through THz spectroscopy, as the resulting transmission spectrum shows sufficiently different features that can be easily classified by a 1-D CNN. Still, larger and more varied training and testing data is necessary in order to fully verify the reliability of the system in a practical context.

Probability data belongs to	
Class 1	Class 2
9.99950409e-01	4.96469329e-05
9.99973774e-01	2.62026588e-05
9.99961257e-01	3.87437794e-05
6.81794609e-06	9.99993205e-01
9.99921203e-01	7.87922618e-05
9.99988079e-01	1.18864755e-05
9.99991298e-01	8.67326798e-06
2.60719971e-05	9.99973893e-01
5.72572526e-06	9.99994278e-01
9.99997616e-01	2.40383429e-06
9.99949336e-01	5.07126715e-05
5.69226177e-05	9.99943018e-01
1.47010669e-05	9.99985337e-01
9.99949694e-01	5.03201009e-05

TABLE 5.3: Output layer probabilities sample

.

5.5 Summary

THz TDS spectroscopy was evaluated for waste oil quality control. The transmission spectrum of oil samples was used to train a 1-D CNN, which successfully performed binary classification with 100 % accuracy. The technique showed great promise and can be further developed through more training and testing data. Further work includes the extension of binary to multi-class classification. By introducing labeled data - both the THz tranmission spectrum and an elemental /physical analysis of the composition / properties of the oil samples, a more detailed prediction could be evaluated. Classifications can include flash point, elemental contaminants, water content and other properties of interest, as introduced in Table 5.2. This can potentially reduce the need for an extensive laboratory setup to only one measurement tool.

Chapter 6

Conclusions

In the last two decades the field of THz science has experienced an exponential growth, with advances that pushed it tentatively from the realm of academic research into real-life applications. Progress in THz sources, detectors, auxillary components and materials have achieved the introduction of new systems. By being more compact, cheaper and with improved performance, these systems can be made suitable for a large range of applications in security, biomedicine, quality control and communications. Despite these developments, the THz field still has a long way to go before it catches up with the rest of the electromagnetic spectrum, with its devices and materials performing orders of magnitude worse than their microwave or optical counterparts. In this thesis a new design for the enhancement of THz resonant metamaterials was proposed, as well as new measurement techniques and industrial applications of THz spectroscopy and imaging.

Chapter 2 presented the measurement, fabrication and computational methods used throughout the thesis. Durham University's THz-VNA and THz-TDS systems were introduced, as well as the microfabrication methods used for sample preparation. A light-weight 1-D and 2-D FDTD engine was developed as a validation step for more complex and computationally expensive FDTD simulations using Ansys Lumerical. An analytical method for the calculation of the scattering parameters of stratified dielectric media was also introduced, followed by a numerical method for the extraction of optical material parameters from transmission and reflection spectra. The presented computational methods were compared through the analysis of a THz Bragg reflector.

Chapter 3 demonstrated the use of metamaterial structures on Si as optically actuated THz modulators. Sharp resonances above the fundamental frequency of the metamaterial resonators were discovered and investigated. The phenomena was found to be caused by photonic crystal resonant modes, excited through the interaction between the metamaterial lattice and the substrate thickness. Tuning these properties showed a larger than three-fold improvement in the metamaterial resonance. The newly designed metamaterials were microfabricated and tested, showing good agreement with theoretical expectations. The fabricated metamaterials were tested as optically controlled THz modulators, achieving high modulation depth and transmission, on par with other state of the art THz modulators. Modulation was achieved using a white light LED array, rather than a laser source. An application of the metamaterials as optically actuated spatial modulators was also demonstrated.

Chapter 4 introduced the development of a THz ellipsometer and several measurement techniques for material characterisation based on it. The ellipsometer was fully automated to take measurements at a sweep of incidence angles for the frequency band between 0.75 - 1.1 THz with a high angular and spectral resolution. The method was used for the extraction of optical parameters of a range of materials - a high refractive index material, low refractive index material, high absorption material, composite material and optically anisotropic material. The method was also tested in an in situ measurement of the decreasing thickness of a Si wafer, etched in KOH.

A THz grazing angle material characterisation technique was subsequently introduced, which achieved sub-wavelength resolution for thickness measurements of thin films. The method was used for the measurement of SU-8 layers, resulting in nanometer resolution of layers tens of micrometers thick.

The ellipsometry system was then used to extract the photoelastic coefficients of Si at THz frequencies, where little data is available in literature and values differ by two orders of magnitude. The system was then extended to image the internal stresses and strains of a Si wafer under mechanical stress. The results showed good agreement with FEA numerical computations, demonstrating a wide range of possible applications for the system.

Chapter 5 investigated the use of THz-TDS for quality control of waste oils due for re-refining. A large spectral difference was observed between accepted waste oils and rejected waste oils in THz frequencies. A 1-D convolutional neural network was developed to perform binary characterisation between accepted and rejected oil spectra. Despite the small sample size, a 100% correct classification was achieved, showing great promise for the application of THz spectroscopy for waste oil characterisation.

Further Work

In Chapter 3, several tuning approaches of the metamaterial lattice to substrate thickness were suggested - coupling the photonic crystal slab band gap to the metallic resonators' fundamental resonance, coupling the resonant modes to the same, or making use of the excited resonant modes above the fundamental resonance. Out of the three proposed mechanisms only the last one was tested in practice. Further work can focus on implementing the other tuning mechanisms and comparing their performance, as well as their dependence on the resonator structure design and material properties of the substrate. Effects of substrate materials, where the thickness can be more easily manipulated, such as spin-on polymers can be investigated.

Waste oil binary quality control using THz-TDS and a 1-D convolutional neural network was demonstrated as a proof of concept. A larger data set needs to be collected to further validate the applicability of the method to a wide range of waste chemical compositions. A data set with labeled data, showing the elemental analysis of every sample would provide a benchmark to test THz-TDS as a method of not only binary quality control, but also chemical composition.

Appendix A

Appendix

S1813 Photolithography Recipe for 2 µm Layer

1. Clean wafer - with solvents (Acetone followed by IPA), sonic bath, (Piranha solution for Si wafers), dry with N_2.
2. Spin coat photoresist - ramp to 500 rpm with acceleration 100 rpm/s and hold for 5 s, spin at 1950 rpm.
3. Soft bake on hot plate 60s at 115°C.
4. Expose with EVG620 for 90mJ/cm2 (soft contact).
5. Develop in MF319 for 60s
6. Hardbake for 90s at 90°C.

SU-8 2000 Photolithography Recipe

1. Clean wafer - with solvents (Acetone followed by IPA), sonic bath, (Piranha solution for Si wafers), dry with N_2.
2. Spin coat photoresist - ramp up to 500 rpm with acceleration 100 rpm/s and hold for 5 s, spin between 1500 and 3000 rpm depending on film thickness.
3. Edge bead removal - wait 1 min for edge beads to even out. Keep spinner hood closed.
4. Soft bake on hot plate 6 min at 65°C, then 30 min at 95°C.
5. Expose with EVG620 450 mJ/cm2 (soft contact).

6. Hard bake for 1 min at 65°C and 6 min at 95°C, allow to cool

7. Develop in EC solvent for 10 min or until clear. Dry with N2.

THz Modulator Review References

Data point	Reference	Data point	Reference
1	[44]	22	[140]
2	[48]	23	[141]
3	[142]	24	[141]
4	[49]	25	[143]
5	[50]	26	[144]
6	[53]	27	[57]
7	[54]	28	[145]
8	[55]	29	[146]
9	[56]	30	[147]
10	[51]	31	[147]
11	[148]	32	[149]
12	[150]	33	[151]
13	[152]	34	[153]
14	[60]	35	[154]
15	[52]	36	[155]
16	[46]	37	[156]
17	[46]	38	[156]
18	[157]	39	[158]
19	[47]	40	[60]
20	[45]	41	[159]
21	[160]	42	[161]
		43	[58]

TABLE A.1: Data points and their corresponding references according to Figure 3.2

Orthotropic Stiffness Matrix for Silicon

$$\begin{bmatrix} 165.7 & 63.9 & 63.9 & 0 & 0 & 0 \\ 63.9 & 165.7 & 63.9 & 0 & 0 & 0 \\ 63.9 & 63.9 & 165.7 & 0 & 0 & 0 \\ 0 & 0 & 0 & 79.6 & 0 & 0 \\ 0 & 0 & 0 & 0 & 79.6 & 0 \\ 0 & 0 & 0 & 0 & 0 & 79.6 \end{bmatrix}$$

FIGURE A.1: Stiffness matrix of Si according to [119] in GPa

FEA Strain Results

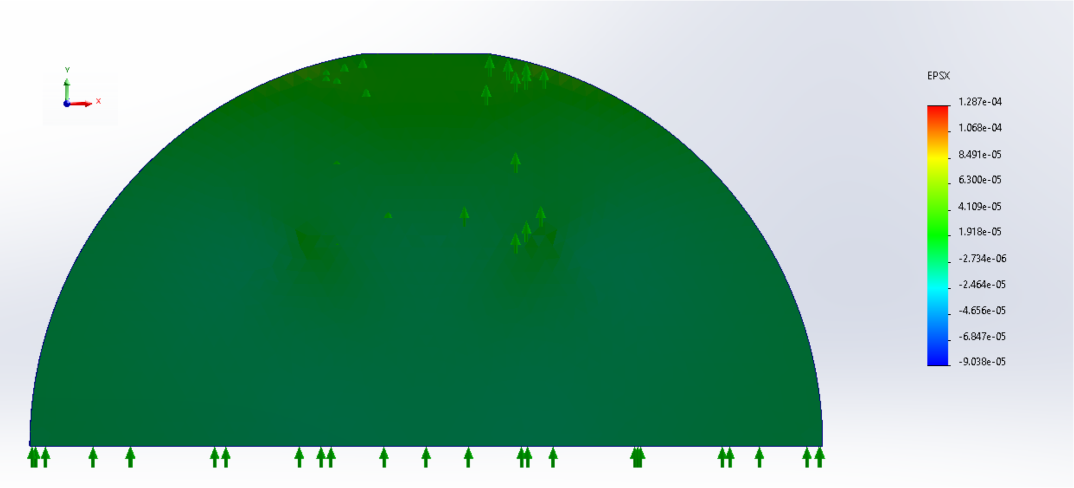

(A) ϵ_x

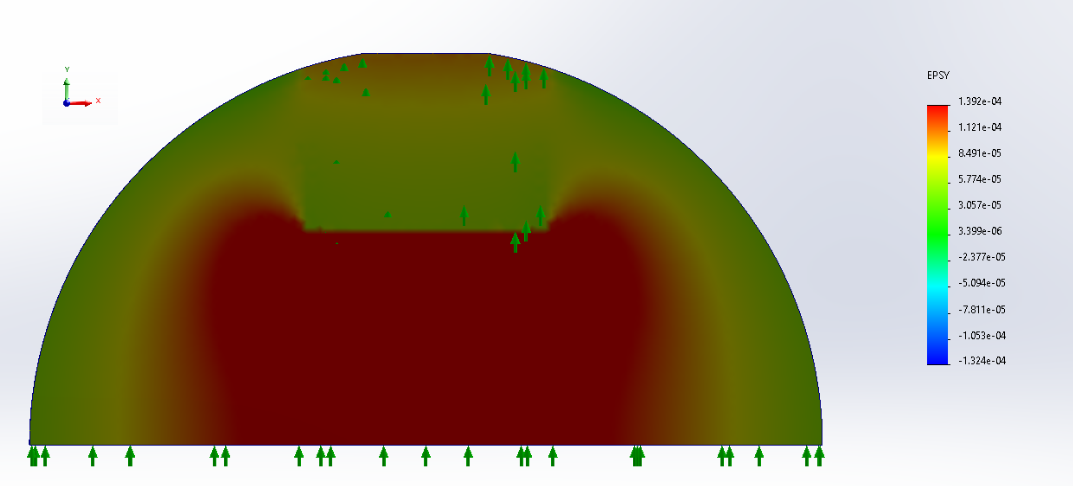

(B) ϵ_y

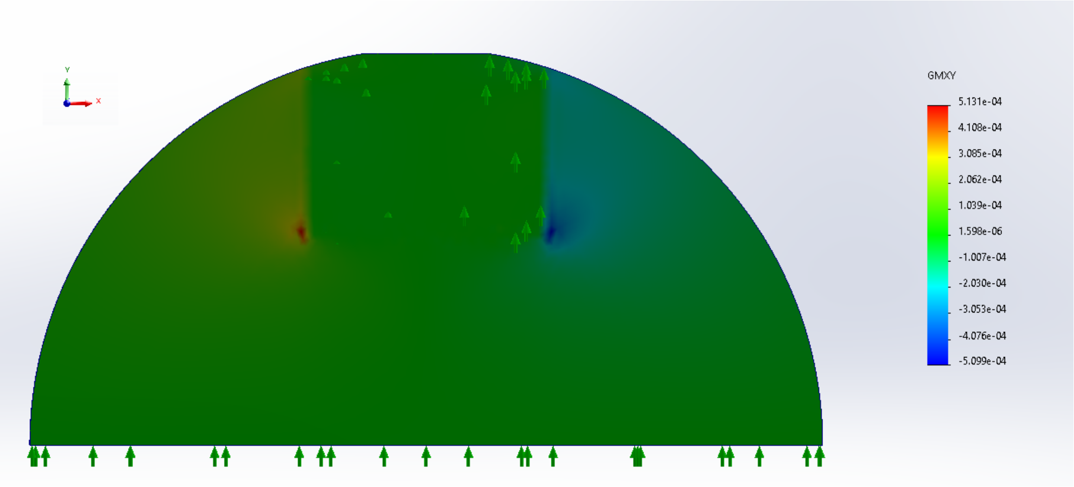

(C) ϵ_{xy}

FIGURE A.2: Calculated strain distributions for <100> Si wafer using FEA

FEA Stress results

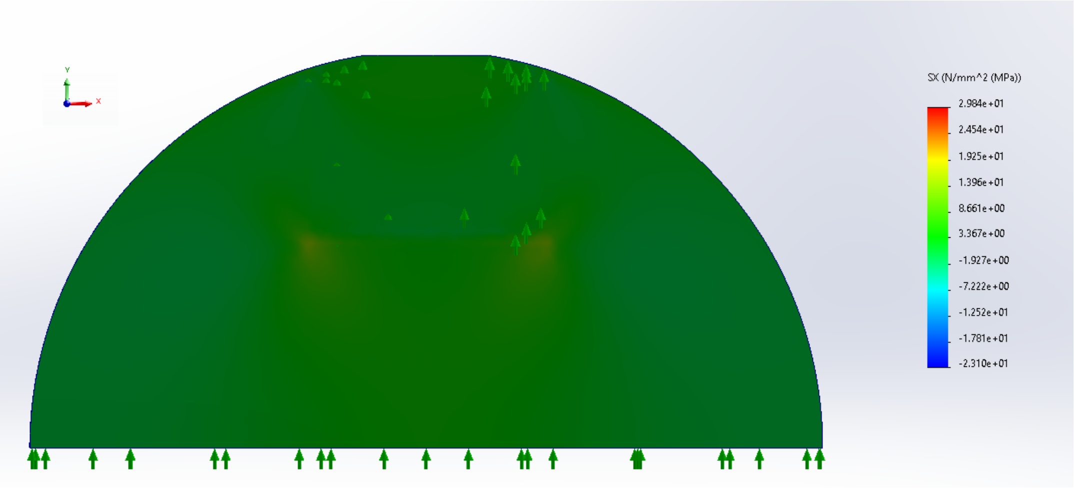

(A) σ_x

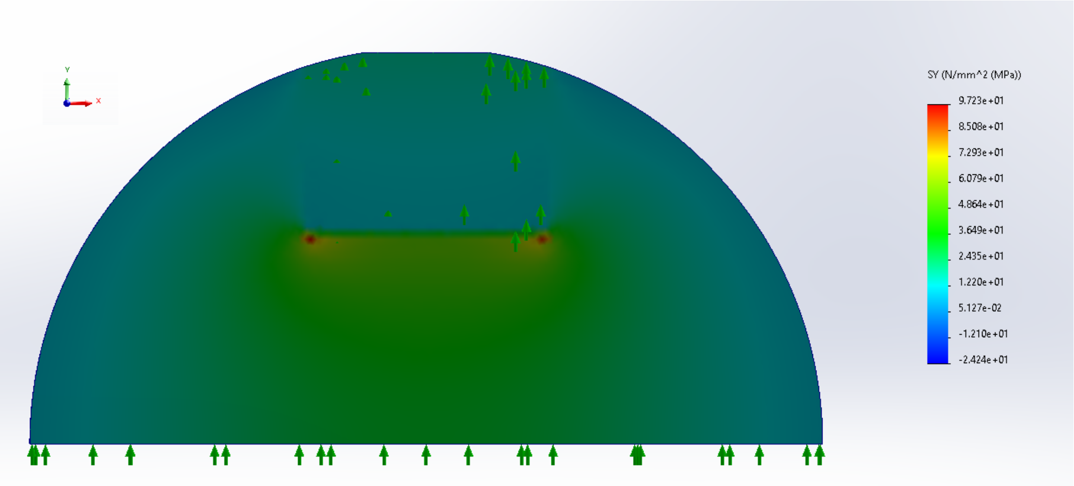

(B) σ_y

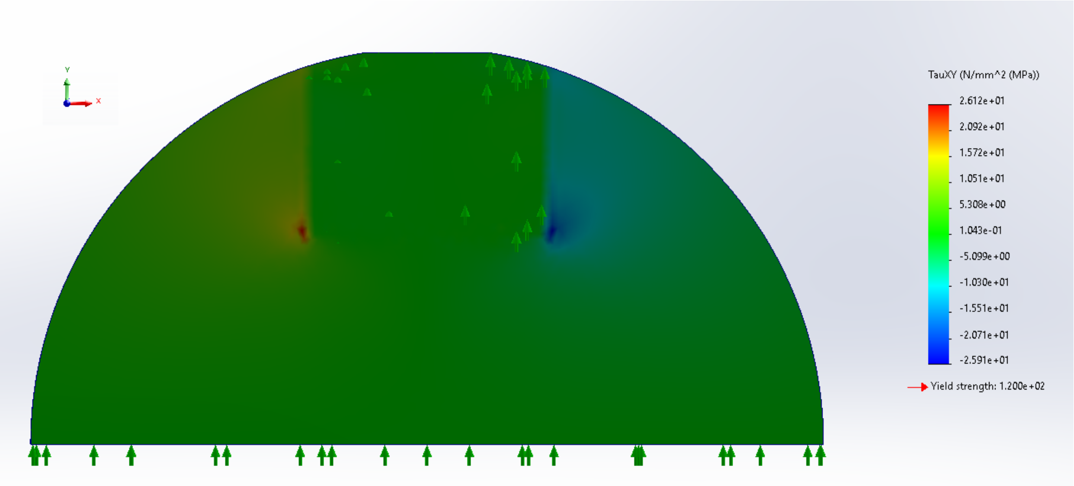

(C) σ_{xy}

FIGURE A.3: Calculated stress distributions for <100> Si wafer using FEA

Bibliography

[1] H. Song and N. J., *Handbook of Terahertz Technologies: Devices and Applications*, 1st ed. Jenny Stanford Publishing, 2015. DOI: https://doi.org/10.1201/b18381.

[2] Y. Takida, K. Nawata, and H. Minamide, "Security screening system based on terahertz-wave spectroscopic gas detection," *Opt. Express*, vol. 29, no. 2, pp. 2529–2537, 2021. DOI: 10.1364/OE.413201.

[3] Z. Geng, X. Zhang, Z. Fan, X. Lv, and H. Chen, "A route to terahertz metamaterial biosensor integrated with microfluidics for liver cancer biomarker testing in early stage," *Scientific Reports*, vol. 7, no. 1, p. 16 378, 2017, ISSN: 2045-2322. DOI: 10.1038/s41598-017-16762-y.

[4] P. E and V. P. Wallace, "Biomedical applications of terahertz technology," *Journal of Physics D: Applied Physics*, vol. 39, no. 17, R301, 2006. DOI: 10.1088/0022-3727/39/17/R01.

[5] C. Yi, D. Kim, S. Solanki, J Kwon, M. Kim, S. Jeon, Y.-C. Ko, and I. Lee, "Design and performance analysis of THz wireless communication systems for chip-to-chip and personal area networks applications," *IEEE Journal on Selected Areas in Communications*, vol. 39, no. 6, pp. 1785–1796, 2021. DOI: 10.1109/JSAC.2021.3071849.

[6] E. Castro-Camus, M. Koch, T. Kleine-Ostmann, and A. Steiger, "On the reliability of power measurements in the terahertz band," *Communications Physics*, vol. 5, no. 1, p. 42, 2022, ISSN: 2399-3650. DOI: 10.1038/s42005-022-00817-2.

[7] P. Siegel, "Terahertz technology," *IEEE Transactions on Microwave Theory and Techniques*, vol. 50, pp. 910 –928, Apr. 2002. DOI: 10.1109/22.989974.

[8] B. S. Williams, "Terahertz quantum-cascade lasers," *Nature Photonics*, vol. 1, no. 9, pp. 517–525, 2007, ISSN: 1749-4893. DOI: 10.1038/nphoton.2007.166.

[9] R. Köhler, A. Tredicucci, F. Beltram, H. E. Beere, E. H. Linfield, A. G. Davies, D. A. Ritchie, R. C. Iotti, and F. Rossi, "Terahertz semiconductor-heterostructure laser," *Nature*, vol. 417, no. 6885, pp. 156–159, 2002, ISSN: 1476-4687. DOI: `10.1038/417156a`.

[10] B. Wen and D. Ban, "High-temperature terahertz quantum cascade lasers," *Progress in Quantum Electronics*, vol. 80, p. 100 363, 2021, ISSN: 0079-6727. DOI: `https://doi.org/10.1016/j.pquantelec.2021.100363`.

[11] R. A. Lewis, "A review of terahertz detectors," *Journal of Physics D: Applied Physics*, vol. 52, no. 43, p. 433 001, 2019. DOI: `10.1088/1361-6463/ab31d5`.

[12] TYDEX. (2022). "THz materials," [Online]. Available: `https://www.tydexoptics.com/products/thz_optics/thz_materials/` (visited on 12/05/2022).

[13] J. Dai, J. Zhang, W. Zhang, and D. Grischkowsky, "Terahertz time-domain spectroscopy characterization of the far-infrared absorption and index of refraction of high-resistivity, float-zone silicon," *J. Opt. Soc. Am. B*, vol. 21, no. 7, pp. 1379–1386, 2004. DOI: `10.1364/JOSAB.21.001379`.

[14] M. N. Afsar and H. Chi, "Millimeter wave complex refractive index, complex dielectric permittivity and loss tangent of extra high purity and compensated silicon," *International Journal of Infrared and Millimeter Waves*, vol. 15, no. 7, pp. 1181–1188, 1994, ISSN: 1572-9559. DOI: `10.1007/BF02096073`.

[15] W. R. Runyan, *Silicon Semiconductor Technology*. New York: McGraw-Hill, 1965.

[16] R. Kshetrimayum, "A brief intro to metamaterials," *IEEE Potentials*, vol. 23, no. 5, pp. 44–46, 2005. DOI: `10.1109/MP.2005.1368916`.

[17] J. Hesler, Y. Duan, B. Foley, and T. Crowe, "THz vector network analyzer measurements and calibration," pp. 23–25, Jan. 2010.

[18] Keysight. (2022). "N5224a PNA microwave network analyzer, 43.5 GHz," [Online]. Available: `https://www.keysight.com/us/en/product/N5224A/pna-microwave-network-analyzer-435-ghz.html`. (visited on 08/12/2022).

[19] Virginia Diodes. (2022). "Vector network analyzer extenders," [Online]. Available: `https://www.vadiodes.com/index.php/en/component/content/article?id=274`. (visited on 08/12/2022).

[20] Y. Cai, I. Brener, J. Lopata, J. Wynn, L. Pfeiffer, and J. Federici, "Design and performance of singular electric field terahertz photoconducting antennas," *Applied Physics Letters*, vol. 71, no. 15, pp. 2076–2078, 1997. DOI: `10.1063/1.119346`.

[21] T. S. Narasimhamurty, "Pockels' phenomenological theory of photoelasticity of crystals," in *Photoelastic and Electro-Optic Properties of Crystals*. Boston, MA: Springer US, 1981, pp. 47–133. DOI: `10.1007/978-1-4757-0025-1_3`.

[22] C. Winnewisser, P. U. Jepsen, M. Schall, V. Schyja, and H. Helm, "Electro-optic detection of THz radiation in LiTaO3, LiNbO3 and ZnTe," *Applied Physics Letters*, vol. 70, no. 23, pp. 3069–3071, 1997. DOI: `10.1063/1.119093`.

[23] I. Maeng, J. Kim, and H. Choi, "Ultrabroadband terahertz spectroscopy," *Convergence of Terahertz Sciences in Biomedical Systems. ISBN 978-94-007-3964-2. Springer Science+Business Media Dordrecht, 2012, p. 219*, pp. 219–, Oct. 2012. DOI: `10.1007/978-94-007-3965-9_12`.

[24] U. van Rienen, *Numerical Methods in Computational Electrodynamics–Linear Systems in Practical Applications*. Jan. 2001, vol. 12, ISBN: 978-3-540-67629-4. DOI: `10.1007/978-3-642-56802-2`.

[25] K. Yee, "Numerical solution of initial boundary value problems involving maxwell's equations in isotropic media," *IEEE Transactions on Antennas and Propagation*, vol. 14, no. 3, pp. 302–307, 1966. DOI: `10.1109/TAP.1966.1138693`.

[26] N. J. Higham, *Accuracy and Stability of Numerical Algorithms*. 2002, ISBN: 978-0-89871-521-7. DOI: `https://doi.org/10.1137/1.9780898718027`.

[27] C. Shannon, "Communication in the presence of noise," *Proceedings of the IRE*, vol. 37, no. 1, pp. 10–21, 1949. DOI: `10.1109/jrproc.1949.232969`.

[28] S. Wang and F. Teixeira, "Grid-dispersion error reduction for broadband FDTD electromagnetic simulations," *IEEE Transactions on Magnetics*, vol. 40, no. 2, pp. 1440–1443, 2004. DOI: `10.1109/TMAG.2004.824904`.

[29] A. F. J. Levi, "The lorentz oscillator model," in *Essential Classical Mechanics for Device Physics*, ser. 2053-2571, Morgan Claypool Publishers, 2016, 5–1 to 5–21, ISBN: 978-1-6817-4413-1. DOI: 10.1088/978-1-6817-4413-1ch5.

[30] X. Chen, T. M. Grzegorczyk, B.-I. Wu, J. Pacheco, and J. A. Kong, "Robust method to retrieve the constitutive effective parameters of metamaterials," *Phys. Rev. E*, vol. 70, p. 016 608, 1 2004. DOI: 10.1103/PhysRevE.70.016608.

[31] Z. Szabo, G.-H. Park, R. Hedge, and E.-P. Li, "A unique extraction of metamaterial parameters based on Kramers-Kronig relationship," Undetermined, *IEEE Transactions on Microwave Theory and Techniques*, vol. 58, no. 10, pp. 2646 –2653, 2010. DOI: 10.1109/TMTT.2010.2065310.

[32] D. R. Smith, S. Schultz, and C. M. Soukoulis, "Determination of effective permittivity and permeability of metamaterials from reflection and transmission coefficients," *Phys. Rev. B*, vol. 65, p. 195 104, 19 2002. DOI: 10.1103/PhysRevB.65.195104.

[33] P. Markoš and C. M. Soukoulis, "Transmission properties and effective electromagnetic parameters of double negative metamaterials," *Opt. Express*, vol. 11, no. 7, pp. 649–661, 19 2003. DOI: 10.1364/OE.11.000649.

[34] Y. T. Aladadi and M. A. S. Alkanhal, "Extraction of metamaterial constitutive parameters based on data-driven discontinuity detection," *Opt. Mater. Express*, vol. 9, no. 9, pp. 3765–3780, 19 2019. DOI: 10.1364/OME.9.003765.

[35] R. de L. Kronig, "On the theory of dispersion of X-Rays," *J. Opt. Soc. Am.*, vol. 12, no. 6, pp. 547–557, 19 1926. DOI: 10.1364/JOSA.12.000547.

[36] Ansys Lumerical. (2022). "Lumerical STACK," [Online]. Available: https://optics.ansys.com/hc/en-us/articles/360034914653-STACK-Optical-Solver-Overview. (visited on 08/12/2022).

[37] Microchem. (2002). "SU-8 2000 permanent epoxy photoresist," [Online]. Available: https://kayakuam.com/wp-content/uploads/2019/09/SU-82000DataSheet2000_5thru2015Ver4.pdf. (visited on 08/12/2022).

[38] Shipley. (2002). "Micoposit S1800 series photoresists," [Online]. Available: `https://amolf.nl/wp-content/uploads/2016/09/datasheets_S1800.pdf`. (visited on 08/12/2022).

[39] N. Duangrit, B. Hong, A. D. Burnett, P. Akkaraekthalin, I. D. Robertson, and N. Somjit, "Terahertz dielectric property characterization of photopolymers for additive manufacturing," *IEEE Access*, vol. 7, pp. 12 339–12 347, 19 2019. DOI: `10.1109/ACCESS.2019.2893196`.

[40] Z. T. Ma, Z. X. Geng, Z. Y. Fan, J. Liu, and H. D. Chen, "Modulators for terahertz communication: The current state of the art," *Research*, vol. 2019, p. 6 482 975, 19 2019. DOI: `10.34133/2019/6482975`.

[41] E. Herrmann, H. Gao, Z. Huang, S. R. Sitaram, K. Ma, and X. Wang, "Modulators for mid-infrared and terahertz light," *Journal of Applied Physics*, vol. 128, no. 14, p. 140 903, 19 2020. DOI: `10.1063/5.0025032`.

[42] M. Rahm, J.-S. Li, and W. J. Padilla, "THz wave modulators: A brief review on different modulation techniques," *Journal of Infrared, Millimeter, and Terahertz Waves*, vol. 34, no. 1, pp. 1–27, 19 2013, ISSN: 1866-6906. DOI: `10.1007/s10762-012-9946-2`.

[43] R. Degl'Innocenti, H. Lin, and M. Navarro-Cía, "Recent progress in terahertz metamaterial modulators," *Nanophotonics*, vol. 11, no. 8, pp. 1485–1514, 19 2022. DOI: `doi:10.1515/nanoph-2021-0803`.

[44] E. Hendry, M. J. Lockyear, J. Gomez Rivas, L. Kuipers, and M. Bonn, "Ultrafast optical switching of the THz transmission through metallic subwavelength hole arrays," *Phys. Rev. B*, vol. 75, p. 195 104, 19 2007. DOI: `10.1103/PhysRevB.75.235305`.

[45] Y. K. Srivastava, A. Chaturvedi, M. Manjappa, A. Kumar, G. Dayal, C. Kloc, and R. Singh, "MoS2 for ultrafast all-optical switching and modulation of THz Fano metaphotonic devices," *Advanced Optical Materials*, vol. 5, no. 23, p. 1 700 762, 19 2017. DOI: `https://doi.org/10.1002/adom.201700762`.

[46] A. C. Tasolamprou, A. D. Koulouklidis, C. Daskalaki, C. P. Mavidis, G. Kenanakis, G. Deligeorgis, Z. Viskadourakis, P. Kuzhir, S. Tzortzakis, M. Kafesaki, E. N. Economou, and C. M. Soukoulis, "Experimental demonstration of ultrafast THz modulation in a graphene-based thin film absorber through negative photoinduced conductivity," *ACS Photonics*, vol. 6, no. 3, pp. 720–727, 19 2019. DOI: `10.1021/acsphotonics.8b01595`.

[47] P. Weis, J. L. Garcia-Pomar, M. Höh, B. Reinhard, A. Brodyanski, and M. Rahm, "Spectrally wide-band terahertz wave modulator based on optically tuned graphene," *ACS Nano*, vol. 6, no. 10, pp. 9118–9124, 19 2012, ISSN: 1936-0851. DOI: `10.1021/nn303392s`.

[48] W. J. Padilla, A. J. Taylor, C. Highstrete, L. Mark, and R. D. Averitt, "Dynamical electric and magnetic metamaterial response at terahertz frequencies," *Phys, Rev. Lett.*, vol. 96, p. 195 104, 19 2006. DOI: `10.1103/PhysRevLett.96.107401`.

[49] D. R. Chowdhury, R. Singh, J. F. O'Hara, H.-T. Chen, A. J. Taylor, and A. K. Azad, "Dynamically reconfigurable terahertz metamaterial through photo-doped semiconductor," *Appl. Phys. Lett.*, vol. 99, p. 195 104, 19 2011. DOI: `10.1063/1.3667197`.

[50] T. Kleine-Ostmann, P. Dawson, K. Pierz, G. Hein, and M. Koch, "Room-temperature operation of an electrically driven terahertz modulator," *Appl. Phys. Lett.*, vol. 84, p. 195 104, 19 2004. DOI: `10.1063/1.1723689`.

[51] D. Shrekenhamer, A. C. Strikwerda, C. Bingham, R. D. Averitt, S. Sonkusale, and W. J. Padilla, "High speed terahertz modulation from metamaterials with embedded high electron mobility transistors," *Opt. Express*, vol. 19, p. 195 104, 19 2011. DOI: `10.1103/PhysRevB.65.195104`.

[52] S. Savo, D. Shrekenhamer, and W. J. Padilla, "Liquid crystal metamaterial absorber spatial light modulator for THz applications," *Advanced Optical Materials*, vol. 2, no. 3, pp. 275–279, 19 2014. DOI: `https://doi.org/10.1002/adom.201300384`.

[53] H.-. T. Chen, W. J. Padilla, J. M. O. Zide, A. C. Gossard, A. J. Taylor, and R. D. Averitt, “Active terahertz metamaterial devices,” *Nature*, vol. 444, p. 195 104, 19 2006. DOI: 10.1038/nature05343.

[54] H.-. T. Chen, L. Hong, A. K. Azad, R. D. Averitt, A. C. Gossard, S. A. Trugman, J. F. O’Hara, and A. J. Taylor, “Electronic control of extraordinary terahertz transmission through subwavelength metal hole arrays,” *Opt. Express*, vol. 16, p. 195 104, 19 2008. DOI: 10.1364/OE.16.007641.

[55] O. Paul, C. Imhof, B. Lagel, S. Wolff, J. Heinrich, S. Hofling, A. Forchel, R. Zengerle, R. Beigang, and M. Rahm, “Polarization-independent active metamaterial for high-frequency terahertz modulation,” *Opt. Express*, vol. 17, p. 195 104, 19 2009. DOI: 10.1103/PhysRevB.65.195104.

[56] H.-. T. Chen, S. Palit, T. Tyler, C. M. Bingham, J. M. O. Zide, J. F. O’Hara, D. R. Smith, A. C. Gossard, R. D. Averitt, W. J. Padilla, N. M. Jokerst, and A. J. Taylor, “Hybrid metamaterials enable fast electrical modulation of freely propagating terahertz waves,” *Appl. Phys. Lett.*, vol. 93, p. 195 104, 19 2008. DOI: 10.1063/1.2978071.

[57] F. Hu, W. Guo, Q. Rong, L. Zhang, W. Zhang, J. Han, H. Dong, and Y. Zhou, “Electrically controlled terahertz binary coder based on hysteresis of vanadium dioxide embedded modulator,” *Journal of Lightwave Technology*, vol. 39, no. 8, pp. 2476–2481, 19 2021. DOI: 10.1109/JLT.2021.3051077.

[58] A. Kumar, A. Solanki, M. Manjappa, S. Ramesh, Y. K. Srivastava, P. Agarwal, T. C. Sum, and R. Singh, “Excitons in 2D perovskites for ultrafast terahertz photonic devices,” *Science Advances*, vol. 6, no. 8, eaax8821, 19 2020. DOI: 10.1126/sciadv.aax8821.

[59] M Sotoodeh, A. Khalid, and A. Rezazadeh, “Empirical low-field mobility model for III-V compounds applicable in device simulation codes,” *Journal of Applied Physics*, vol. 87, pp. 2890–2900, 19 Mar. 2000. DOI: 10.1063/1.372274.

[60] H.-. T. Chen, H. Yang, R. Singh, J. F. O’Hara, A. K. Azad, S. A. Trugman, Q. X. Jia, and A. J. Taylor, “Tuning the resonance in high-temperature superconducting terahertz metamaterials,” *Phys. Rev. Lett.*, vol. 105, p. 195 104, 19 2010. DOI: 10.1103/PhysRevLett.105.247402.

[61] D Schroder, “Carrier lifetimes in silicon,” *IEEE Transactions on Electron Devices*, vol. 44, no. 1, p. 195 104, 19 1997. DOI: `10.1103/PhysRevB.65.195104`.

[62] A. Krotkus, R. Viselga, K. Bertulis, V. Jasutis, S. Marcinkevičius, and U. Olin, “Subpicosecond carrier lifetimes in GaAs grown by molecular beam epitaxy at low substrate temperature,” *Applied Physics Letters*, vol. 66, no. 15, pp. 1939–1941, 19 1995. DOI: `10.1063/1.113283`.

[63] Cree. (2022). “Xlamp CXB3070 LED,” [Online]. Available: `https://assets.cree-led.com/a/ds/x/XLamp-CXB3070.pdf`. (visited on 08/12/2022).

[64] Z. Shi, X. Cao, Q.-Y. Wen, T. Wen, Q. Yang, Z. Chen, W. Shi, and H. Zhang, “Terahertz modulators based on silicon nanotip array,” *Advanced Optical Materials*, vol. 6, p. 195 104, 19 Dec. 2017. DOI: `10.1002/adom.201700620`.

[65] J. Pendry, A. Holden, D. Robbins, and W. Stewart, “Magnetism from conductors and enhanced nonlinear phenomena,” *IEEE Transactions on Microwave Theory and Techniques*, vol. 47, no. 11, pp. 2075–2084, 19 1999. DOI: `10.1109/22.798002`.

[66] J. Naqui, *Symmetry Properties in Transmission Lines Loaded with Electrically Small Resonators, Circuit Modeling and Applications*. American Physical Society, 2016, vol. 65, p. 210, ISBN: 978-3-319-24566-9. DOI: `10.1103/PhysRevB.65.195104`.

[67] Ansys Lumerical. (2022). “Plane wave and beam source simulation object,” [Online]. Available: `https://optics.ansys.com/hc/en-us/articles/360034382854-Plane-wave-and-beam-source-Simulation-object`. (visited on 08/12/2022).

[68] I. Al-Naib, E. Hebestreit, C. Rockstuhl, F. Lederer, D. Christodoulides, T. Ozaki, and R. Morandotti, “Conductive coupling of split ring resonators: A path to THz metamaterials with ultrasharp resonances,” *Phys. Rev. Lett.*, vol. 112, p. 183 903, 18 2014. DOI: `10.1103/PhysRevLett.112.183903`.

[69] J. Dai, J. Zhang, W. Zhang, and D. Grischkowsky, “Terahertz time-domain spectroscopy characterization of the far-infrared absorption and index of refraction of high-resistivity, float-zone silicon,” *J. Opt. Soc. Am. B*, vol. 21, no. 7, pp. 1379–1386, 19 2004. DOI: `10.1364/JOSAB.21.001379`.

[70] I. Bahl and P Bhartia, *Microwave Solid State Circuit Design*. New York: Wiley-Interscience, 2003, vol. 65, p. 195 104. DOI: 10.1103/PhysRevB.65.195104.

[71] S. Noda, F. Mahi, and H. Zappe, "Photonic crystals," in *Reference Module in Materials Science and Materials Engineering*, vol. 65, Elsevier, 2016, p. 195 104, ISBN: 978-0-12-803581-8. DOI: https://doi.org/10.1016/B978-0-12-803581-8.00555-5.

[72] S. Romano, S. Cabrini, I. Rendina, and V. Mocella, "Guided resonance in negative index photonic crystals: A new approach," *Light: Science & Applications*, vol. 3, no. 1, e120–e120, 19 2014, ISSN: 2047-7538. DOI: 10.1038/lsa.2014.1.

[73] M. F. Limonov, M. V. Rybin, A. N. Poddubny, and Y. S. Kivshar, "Fano resonances in photonics," *Nature Photonics*, vol. 11, no. 9, pp. 543–554, 19 2017, ISSN: 1749-4893. DOI: 10.1038/nphoton.2017.142.

[74] S. Fan and J. D. Joannopoulos, "Analysis of guided resonances in photonic crystal slabs," *Phys. Rev. B*, vol. 65, p. 235 112, 23 2002. DOI: 10.1103/PhysRevB.65.235112.

[75] S. Johnson, S. Fan, P. Villeneuve, J. Joannopoulos, and L. Kolodziejski, "Guide modes in photonic crystal slabs," *Phys. Rev. B*, vol. 60, pp. 5751–5758, 19 Aug. 1999. DOI: 10.1103/PhysRevB.60.5751.

[76] A. K. Azad, J. Dai, and W. Zhang, "Transmission properties of terahertz pulses through subwavelength double split-ring resonators," *Opt. Lett.*, vol. 31, no. 5, pp. 634–636, 19 2006. DOI: 10.1364/OL.31.000634.

[77] S. Busch, B. Scherger, M. Scheller, and M. Koch, "Optically controlled terahertz beam steering and imaging," *Opt. Lett.*, vol. 37, no. 8, pp. 1391–1393, 19 2012. DOI: 10.1364/OL.37.001391.

[78] D. Brunet, E. R. Vrscay, and Z. Wang, "On the mathematical properties of the structural similarity index," *IEEE Trans Image Process*, vol. 21, no. 4, pp. 1488–1499, 19 2012. DOI: 10.1103/PhysRevB.65.195104.

[79] T. Nagashima and M. Hangyo, "Measurement of complex optical constants of a highly doped Si wafer using terahertz ellipsometry," *Applied Physics Letters*, vol. 79, pp. 3917–3919, 19 Dec. 2001. DOI: 10.1063/1.1426258.

[80] M Hangyo, T Nagashima, and S Nashima, “Spectroscopy by pulsed terahertz radiation,” *Measurement Science and Technology*, vol. 13, no. 11, p. 1727, 19 2002. DOI: 10.1088/0957-0233/13/11/309.

[81] T. Hofmann, C. M. Herzinger, A. Boosalis, T. E. Tiwald, J. A. Woollam, and M. Schubert, “Variable-wavelength frequency-domain terahertz ellipsometry,” *Review of Scientific Instruments*, vol. 81, no. 2, p. 023 101, 19 2010. DOI: 10.1063/1.3297902.

[82] M. Neshat and N. P. Armitage, “Terahertz time-domain spectroscopic ellipsometry: Instrumentation and calibration,” *Opt. Express*, vol. 20, no. 27, pp. 29 063–29 075, 19 2012. DOI: 10.1364/OE.20.029063.

[83] R. Espinosa-Luna, D. Rodríguez-Carrera, E. Bernabeu, and S. Hinojosa-Ruíz, “Transformation matrices for the Mueller–Jones formalism,” *Optik*, vol. 119, no. 16, pp. 757–765, 19 2008, ISSN: 0030-4026. DOI: https://doi.org/10.1016/j.ijleo.2007.03.008.

[84] D. R. Smith, S. Schultz, and C. M. Soukoulis, “Principles of spectroscopic ellipsometry,” in *Spectroscopic Ellipsometry*. John Wiley & Sons, Ltd, 2007, vol. 65, ch. 4, pp. 81–146, ISBN: 9780470060193. DOI: https://doi.org/10.1002/9780470060193.ch4.

[85] F. Ferrieu, “Infrared spectroscopic ellipsometry using a fourier transform infrared spectrometer: Some applications in thin-film characterization,” *Review of Scientific Instruments*, vol. 60, no. 10, pp. 3212–3216, 19 1989. DOI: 10.1063/1.1140554.

[86] N. Ismail, C. C. Kores, D. Geskus, and M. Pollnau, “Fabry-Pérot resonator: Spectral line shapes, generic and related airy distributions, linewidths, finesses, and performance at low or frequency-dependent reflectivity,” *Opt. Express*, vol. 24, no. 15, pp. 16 366–16 389, 19 2016. DOI: 10.1364/OE.24.016366.

[87] A. R. Forouhi and I. Bloomer, “Optical dispersion relations for amorphous semiconductors and amorphous dielectrics,” *Phys. Rev. B*, vol. 34, pp. 7018–7026, 10 1986. DOI: 10.1103/PhysRevB.34.7018.

[88] ——, “Optical properties of crystalline semiconductors and dielectrics,” *Phys. Rev. B*, vol. 38, pp. 1865–1874, 3 1988. DOI: `10.1103/PhysRevB.38.1865`.

[89] D. R. Smith, S. Schultz, and C. M. Soukoulis, “Optical parameters for the materials in HOC I, HOC II, and HOC III,” in *Handbook of Optical Constants of Solids*. Academic Press, 1998, vol. 3, ch. 7, pp. 187–227, ISBN: 0125444230. DOI: `https://doi.org/10.1002/9780470060193.ch4`.

[90] J. Johansson and N. Whyborn, “The diagonal horn as a sub-millimeter wave antenna,” *IEEE Transactions on Microwave Theory and Techniques*, vol. 40, no. 5, pp. 795–800, 19 1992. DOI: `10.1109/22.137380`.

[91] A. K. Klein, “Controlling terahertz radiation, novel fabrication methods and materials for terahertz components,” Ph.D. dissertation, 2019, ch. 7, pp. 187–227, ISBN: 0125444230. DOI: `https://doi.org/10.1002/9780470060193.ch4`.

[92] Y.-L. Liao and Y. Zhao, “Design of wire-grid polarizer with effective medium theory,” *Optical and Quantum Electronics*, vol. 46, no. 5, pp. 641–647, 19 2014, ISSN: 1572-817X. DOI: `10.1007/s11082-013-9768-z`.

[93] A. K. Klein, P. S. Stefanova, A. Gallant, and C. Balocco, “Material characterization with frequency domain THz ellipsometry,” in *2018 43rd International Conference on Infrared, Millimeter, and Terahertz Waves (IRMMW-THz)*, vol. 3, Academic Press, 2018, ch. 7, pp. 1–2, ISBN: 0125444230. DOI: `10.1109/IRMMW-THz.2018.8510238`.

[94] Z. Wang, A. Bovik, H. Sheikh, and E. Simoncelli, “Image quality assessment: From error visibility to structural similarity,” *IEEE Transactions on Image Processing*, vol. 13, no. 4, pp. 600–612, 19 2004. DOI: `10.1109/TIP.2003.819861`.

[95] A. Rehman, “Ssim-inspired quality assessment, compression, and processing for visual communications,” Ph.D. dissertation, Aug. 2013, ch. 7, pp. 187–227, ISBN: 0125444230. DOI: `https://doi.org/10.1002/9780470060193.ch4`.

[96] J. Dai, J. Zhang, W. Zhang, and D. Grischkowsky, “Terahertz time-domain spectroscopy characterization of the far-infrared absorption and index of refraction of high-resistivity, float-zone silicon,” *J. Opt. Soc. Am. B*, vol. 21, no. 7, pp. 1379–1386, 19 2004. DOI: `10.1364/JOSAB.21.001379`.

[97] M. Naftaly, “An international intercomparison of THz time-domain spectrometers,” in *Handbook of Optical Constants of Solids*, vol. 3, Academic Press, Sep. 2016, ch. 7, pp. 1–2, ISBN: 0125444230. DOI: `10.1109/IRMMW-THz.2016.7758763`.

[98] C. Ronne, L. Thrane, P.-O. Åstrand, A. Wallqvist, K. V. Mikkelsen, and S. R. Keiding, “Investigation of the temperature dependence of dielectric relaxation in liquid water by THz reflection spectroscopy and molecular dynamics simulation,” *The Journal of Chemical Physics*, vol. 107, no. 14, pp. 5319–5331, 19 1997. DOI: `10.1063/1.474242`.

[99] S. Wen-Feng, W. Xin-Ke, and Z. Yan, “Measurement of refractive index for high reflectance materials with terahertz time domain reflection spectroscopy,” *Chinese Physics Letters*, vol. 26, no. 11, p. 114 210, 19 2009. DOI: `10.1088/0256-307X/26/11/114210`.

[100] Tydex Optics. (2022). “Thz materials,” [Online]. Available: `https://www.tydexoptics.com/products/thz_optics/thz_materials/`. (visited on 08/12/2022).

[101] P. D. Cunningham, N. N. Valdes, F. A. Vallejo, L. M. Hayden, B. Polishak, X.-H. Zhou, J. Luo, A. K.-Y. Jen, J. C. Williams, and R. J. Twieg, “Broadband terahertz characterization of the refractive index and absorption of some important polymeric and organic electro-optic materials,” *Journal of Applied Physics*, vol. 109, no. 4, pp. 043 505–043505–5, 19 2011. DOI: `10.1063/1.3549120`.

[102] R. Piesiewicz, C. Jansen, S. Wietzke, D. M. Mittleman, M. Koch, and T. Kürner, “Properties of building and plastic materials in the THz range,” *International Journal of Infrared and Millimeter Waves*, vol. 28, pp. 363–371, 19 2007. DOI: `https://doi.org/10.1002/9780470060193.ch4`.

[103] A. Sengupta, A. Bandyopadhyay, B. F. Bowden, J. A. Harrington, and J. F. Federici, “Characterisation of olefin copolymers using terahertz spectroscopy,” *Electronics Letters*, vol. 42, pp. 1477–1479, 19 2006. DOI: `https://doi.org/10.1002/9780470060193.ch4`.

[104] Y.-S. Jin, G. J. Kim, and S. G. Jeon, "Terahertz dielectric properties of polymers," *Journal of the Korean Physical Society*, vol. 49, pp. 513–517, 19 2006. DOI: `https://doi.org/10.1002/9780470060193.ch4`.

[105] M. L. Hamilton, B. B. Perston, P. W. Harland, B. E. Williamson, M. A. Thomson, and P. J. Melling, "Grazing-angle fiber-optic irras for in situ cleaning validation," *Organic Process Research & Development*, vol. 9, no. 3, pp. 337–343, 19 2005, ISSN: 1083-6160. DOI: `10.1021/op040213z`.

[106] N. Ghalichechian and K. Sertel, "Permittivity and loss characterization of SU-8 films for mmW and terahertz applications," *IEEE Antennas and Wireless Propagation Letters*, vol. 14, pp. 723–726, 19 2015. DOI: `10.1109/LAWP.2014.2380813`.

[107] T. S. Narasimhamurty, "Photoelasticity of crystals. Introduction," in *Photoelastic and Electro-Optic Properties of Crystals*. Boston, MA: Springer US, 1981, vol. 3, ch. 7, pp. 1–8, ISBN: 978-1-4757-0025-1. DOI: `10.1007/978-1-4757-0025-1_1`.

[108] S. S. K. Ramesh, "Digital photoelasticity: Recent developments and diverse applications," *Optics and Lasers in Engineering*, vol. 135, pp. 187–227, 19 2020. DOI: `https://doi.org/10.1002/9780470060193.ch4`.

[109] R. D. Nishimura, K. T. Ochiai, A. A. Caputo, and C. M. Jeong, "Photoelastic stress analysis of load transfer to implants and natural teeth comparing rigid and semirigid connectors," *J Prosthet Dent*, vol. 81, no. 6, pp. 696–703, 19 Jun. 1999. DOI: `https://doi.org/10.1002/9780470060193.ch4`.

[110] M. Coelho Goiato, A. A. Pesqueira, D. M. D. Santos, M. F. Haddad, and A. Moreno, "Photoelastic stress analysis in prosthetic implants of different diameters: Mini, narrow, standard or wide," *J Clin Diagn Res*, vol. 8, no. 9, ZC86–90, 19 Sep. 2014. DOI: `https://doi.org/10.1002/9780470060193.ch4`.

[111] C. Herráez-Galindo, D. Torres-Lagares, J. Martínez, A. Pérez-Velasco, E. Torres-Carranza, M.-A. Serrera-Figallo, and J.-L. Gutiérrez-Pérez, "A comparison of photoelastic and finite elements analysis in internal connection and bone level dental implants," *Metals*, vol. 10, p. 648, 19 May 2020. DOI: `10.3390/met10050648`.

[112] K. Ramesh, “Fusion of digital photoelasticity, rapid prototyping and rapid tooling technologies,” in *Digital Photoelasticity: Advanced Techniques and Applications*, K. Ramesh, Ed. Berlin, Heidelberg: Springer Berlin Heidelberg, 2000, vol. 3, ch. 7, pp. 347–367, ISBN: 978-3-642-59723-7. DOI: `10.1007/978-3-642-59723-7_10`.

[113] Y. Ju, Z. Ren, L. Mao, and F.-P. Chiang, “Quantitative visualisation of the continuous whole-field stress evolution in complex pore structures using photoelastic testing and 3D printing methods,” *Opt. Express*, vol. 26, no. 5, pp. 6182–6201, 19 2018. DOI: `10.1364/OE.26.006182`.

[114] K. Ramesh and S. Sasikumar, “Digital photoelasticity: Recent developments and diverse applications,” *Optics and Lasers in Engineering*, vol. 135, p. 106 186, 19 2020, ISSN: 0143-8166. DOI: `https://doi.org/10.1016/j.optlaseng.2020.106186`.

[115] M. Stoehr, G. Gerlach, T. Härtling, and S. Schoenfelder, “Analysis of photoelastic properties of monocrystalline silicon,” *Journal of Sensors and Sensor Systems*, vol. 9, no. 2, pp. 209–217, 19 2020. DOI: `10.5194/jsss-9-209-2020`.

[116] D. K. Biegelsen, “Photoelastic tensor of silicon and the volume dependence of the average gap,” *Phys. Rev. Lett.*, vol. 32, pp. 1196–1199, 21 1974. DOI: `10.1103/PhysRevLett.32.1196`.

[117] Tokyo Measuring Instrument Lab. (2022). “F series foil strain guage,” [Online]. Available: `https://www.tml.jp/e/node/154` (visited on 11/09/2022).

[118] P. S. Stefanova, T. Hehne, A. K. Klein, A. J. Gallant, and C. Balocco, “Tensile stress measurements with photoelastic scattering at THz frequencies,” in *2020 45th International Conference on Infrared, Millimeter, and Terahertz Waves (IRMMW-THz)*, vol. 3, Academic Press, 2020, ch. 7, pp. 1–2, ISBN: 0125444230. DOI: `10.1109/IRMMW-THz46771.2020.9370726`.

[119] W. P. Mason, *Physical acoustics and the properties of solids*. van Nostrand, 1958, vol. 3, ch. 7, pp. 187–227, ISBN: 0125444230. DOI: `https://doi.org/10.1002/9780470060193.ch4`.

[120] J. F. Nye *et al.*, *Physical properties of crystals: their representation by tensors and matrices*. Oxford university press, 1985, vol. 3, ch. 7, pp. 187–227, ISBN: 0125444230. DOI: https://doi.org/10.1002/9780470060193.ch4.

[121] J. J. Hall, "Electronic effects in the elastic constants of n-type silicon," *Physical Review*, vol. 161, no. 3, p. 756, 19 1967. DOI: https://doi.org/10.1002/9780470060193.ch4.

[122] K. Kang, S. Wang, L. an Li, Z. Wang, and C. Li, "Terahertz-elasticity for single crystal silicon," *Optics and Lasers in Engineering*, vol. 137, p. 106 396, 19 2021, ISSN: 0143-8166. DOI: https://doi.org/10.1016/j.optlaseng.2020.106396.

[123] D. I. E. James Speight, "Used lubricating oils," in *Refining Used Lubricating Oils*, vol. 3, CRC Press, 2021, ch. 3, pp. 73–88, ISBN: 0125444230. DOI: https://doi.org/10.1002/9780470060193.ch4.

[124] Groupement Européen de l'Industrie de la Régénération. (2022). "Geir vision," [Online]. Available: https://www.geir-rerefining.org/about-us/ (visited on 11/09/2022).

[125] D. Wooton, R. Thomas, and S. Barry. (2022). "Using infrared spectroscopy in used engine oils - estimating base number," [Online]. Available: https://www.machinerylubrication.com/Read/808/infrared-spectroscopy-oil (visited on 11/09/2022).

[126] E. T. Cutler, "Conserve lube oil: Re-refine. (propane-vacuum-hydrogen process)," *Hydrocarbon Process.; (United States)*, vol. 55:5, pp. 187–227, 19 May 1976. DOI: https://doi.org/10.1002/9780470060193.ch4.

[127] J. Cerny, Z. Strnad, and G. Sebor, "Composition and oxidation stability of SAE 15W-40 engine oils," *Tribology International*, vol. 34, no. 2, pp. 127–134, 19 2001, ISSN: 0301-679X. DOI: https://doi.org/10.1016/S0301-679X(00)00150-X.

[128] P. Nowak, K. Kucharska, and M. Kamiński, "Ecological and health effects of lubricant oils emitted into the environment," *Int J Environ Res Public Health*,

vol. 16, no. 16, pp. 187–227, 19 Aug. 2019. DOI: https://doi.org/10.1002/9780470060193.ch4.

[129] L. R. Rudnick, "Additives for crankcase lubricant applications," in *Lubricant Additives*, vol. 3, CRC Press, 2009, ch. 19, p. 462, ISBN: 9780429137334. DOI: https://doi.org/10.1002/9780470060193.ch4.

[130] W. Gergel, *Lubricant Additive Chemistry*. Lubrizol Additive Company, Lubrizol Corporation, 1992, vol. 3, ch. 7, pp. 187–227, ISBN: 0125444230. DOI: https://doi.org/10.1002/9780470060193.ch4.

[131] W. S. McCulloch and W. Pitts, "A logical calculus of the ideas immanent in nervous activity," *The bulletin of mathematical biophysics*, vol. 5, no. 4, pp. 115–133, 19 1943, ISSN: 1522-9602. DOI: 10.1007/BF02478259.

[132] N. Ketkar, "Introduction to deep learning," in *Deep Learning with Python: A Hands-on Introduction*. Berkeley, CA: Apress, 2017, vol. 3, ch. 7, pp. 1–5, ISBN: 978-1-4842-2766-4. DOI: 10.1007/978-1-4842-2766-4_1.

[133] ——, "Machine learning fundamentals," in *Deep Learning with Python: A Hands-on Introduction*. Berkeley, CA: Apress, 2017, vol. 3, ch. 7, pp. 7–16, ISBN: 978-1-4842-2766-4. DOI: 10.1007/978-1-4842-2766-4_2.

[134] ——, "Feed forward neural networks," in *Deep Learning with Python: A Hands-on Introduction*. Berkeley, CA: Apress, 2017, vol. 3, ch. 7, pp. 17–33, ISBN: 978-1-4842-2766-4. DOI: 10.1007/978-1-4842-2766-4_3.

[135] D. Kingma and J. Ba, "Adam: A method for stochastic optimization," *International Conference on Learning Representations*, vol. 3, pp. 187–227, 19 Dec. 2014. DOI: https://doi.org/10.1002/9780470060193.ch4.

[136] N. Ketkar, "Convolutional neural networks," in *Deep Learning with Python: A Hands-on Introduction*. Berkeley, CA: Apress, 2017, vol. 3, ch. 7, pp. 63–78, ISBN: 978-1-4842-2766-4. DOI: 10.1007/978-1-4842-2766-4_5.

[137] S. Kiranyaz, O. Avci, O. Abdeljaber, T. Ince, M. Gabbouj, and D. J. Inman, "1D convolutional neural networks and applications: A survey," *Mechanical Systems and Signal Processing*, vol. 151, p. 107 398, 19 2021, ISSN: 0888-3270. DOI: https://doi.org/10.1016/j.ymssp.2020.107398.

[138] Google Inc. (2022). "Keras API reference," [Online]. Available: `https://keras.io/api/layers/regularization_layers/dropout/` (visited on 11/14/2022).

[139] TensorFlow. (2022). "Tensorflow," [Online]. Available: `https://www.tensorflow.org/` (visited on 11/14/2022).

[140] H. Jung, J. Koo, E. Heo, B. Cho, C. In, W. Lee, H. Jo, J. H. Cho, H. Choi, M. S. Kang, and H. Lee, "Electrically controllable molecularization of terahertz meta-atoms," *Advanced Materials*, vol. 30, no. 31, p. 1 802 760, 19 2018. DOI: `https://doi.org/10.1002/adma.201802760`.

[141] M. Liu, H. Y. Hwang, H. Tao, A. C. Strikwerda, K. Fan, G. R. Keiser, A. J. Sternbach, K. G. West, S. Kittiwatanakul, J. Lu, S. A. Wolf, F. G. Omenetto, X. Zhang, K. A. Nelson, and R. D. Averitt, "Terahertz-field-induced insulator-to-metal transition in vanadium dioxide metamaterial," *Nature*, vol. 487, no. 7407, pp. 345–348, 19 2012, ISSN: 1476-4687. DOI: `10.1038/nature11231`.

[142] H.-. T. Chen, W. J. Padilla, J. M. O. Zide, S. R. Bank, A. C. Gossard, A. J. Taylor, and R. D. Averitt, "Ultrafast optical switching of terahertz metamaterials fabricated on ErAs/GaAs nanoisland superlattices," *Opt. Lett.*, vol. 32, pp. 187–227, 19 2007. DOI: `10.1364/OL.32.001620`.

[143] Y. Zhang, S. Qiao, L. Sun, Q. W. Shi, W. Huang, L. Li, and Z. Yang, "Photoinduced active terahertz metamaterials with nanostructured vanadium dioxide film deposited by sol-gel method," *Opt. Express*, vol. 22, no. 9, pp. 11 070–11 078, 19 2014. DOI: `10.1364/OE.22.011070`.

[144] Q.-Y. Wen, H.-W. Zhang, Q.-H. Yang, Y.-S. Xie, K. Chen, and Y.-L. Liu, "Terahertz metamaterials with VO2 cut-wires for thermal tunability," *Applied Physics Letters*, vol. 97, no. 2, p. 021 111, 19 2010. DOI: `10.1063/1.3463466`.

[145] M. Jiang, F. Hu, L. Zhang, B. Quan, W. Xu, H. Du, D. Xie, and Y. Chen, "Electrically triggered VO2 reconfigurable metasurface for amplitude and phase modulation of terahertz wave," *Journal of Lightwave Technology*, vol. 39, no. 11, pp. 3488–3494, 19 2021. DOI: `10.1109/JLT.2021.3068395`.

[146] P. Pitchappa, A. Kumar, S. Prakash, H. Jani, R. Medwal, M. Mishra, R. S. Rawat, T. Venkatesan, N. Wang, and R. Singh, "Volatile ultrafast switching at

multilevel nonvolatile states of phase change material for active flexible terahertz metadevices," *Advanced Functional Materials*, vol. 31, no. 17, p. 2 100 200, 19 2021. DOI: `https://doi.org/10.1002/adfm.202100200`.

[147] H. Sun, Y. Hu, Y. Tang, J. You, J. Zhou, H. Liu, and X. Zheng, "Ultrafast polarization-dependent all-optical switching of germanium-based metaphotonic devices," *Photon. Res.*, vol. 8, no. 3, pp. 263–270, 19 2020. DOI: `10.1364/PRJ.380446`.

[148] B. Sensale-Rodriguez, R. Yan, M. M. Kelly, T. Fang, K. Tahy, W. S. Hwang, D. Jena, L. Liu, and H. G. Xing, "Broadband graphene terahertz modulators enabled by intraband transitions," *Nature Communications*, vol. 3, pp. 187–227, 19 2012. DOI: `10.1038/ncomms1787`.

[149] W. He, M. Tong, Z. Xu, Y. Hu, X. Cheng, and T. Jiang, "Ultrafast all-optical terahertz modulation based on an inverse-designed metasurface," *Photon. Res.*, vol. 9, no. 6, pp. 1099–1108, 19 2021. DOI: `10.1364/PRJ.423119`.

[150] S. H. Lee, M. Choi, T.-T. Kim, S. Lee, M. Liu, X. Yin, H. K. Choi, S. S. Lee, C.-G. Choi, S.-Y. Choi, X. Zhang, and B. Min, "Switching teraherz waves with gate-controlled active graphene metamaterials," *Nature Mat.*, vol. 11, pp. 936–941, 19 2012. DOI: `doi:10.1038/nmat3433`.

[151] W. X. Lim, M. Manjappa, Y. K. Srivastava, L. Cong, A. Kumar, K. F. MacDonald, and R. Singh, "Ultrafast all-optical switching of germanium-based flexible metaphotonic devices," *Advanced Materials*, vol. 30, no. 9, p. 1 705 331, 19 2018. DOI: `https://doi.org/10.1002/adma.201705331`.

[152] T. Driscoll, H. T. Kim, B. G. Chae, B. J. Kim, Y. W. Lee, N. M. Jokerst, S. Palit, D. R. Smith, M. D. Ventra, and D. N. Basov, "Memory metamaterials," *Science*, vol. 325, pp. 187–227, 19 2009. DOI: `10.1126/science.1176580`.

[153] X. Chen, Z. Tian, Y. Lu, Y. Xu, X. Zhang, C. Ouyang, J. Gu, J. Han, and W. Zhang, "Electrically tunable perfect terahertz absorber based on a graphene salisbury screen hybrid metasurface," *Advanced Optical Materials*, vol. 8, no. 3, p. 1 900 660, 19 2020. DOI: `https://doi.org/10.1002/adom.201900660`.

[154] K. Fan, J. Zhang, X. Liu, G.-F. Zhang, R. D. Averitt, and W. J. Padilla, "Phototunable dielectric huygens' metasurfaces," *Advanced Materials*, vol. 30, no. 22, p. 1 800 278, 19 2018. DOI: `https://doi.org/10.1002/adma.201800278`.

[155] J. Kappa, D. Sokoluk, S. Klingel, C. Shemelya, E. Oesterschulze, and M. Rahm, "Electrically reconfigurable micromirror array for direct spatial light modulation of terahertz waves over a bandwidth wider than 1 THz," *Scientific Reports*, vol. 9, no. 1, p. 2597, 19 2019, ISSN: 2045-2322. DOI: `10.1038/s41598-019-39152-y`.

[156] R. Xu, X. Xu, B.-R. Yang, X. Gui, Z. Qin, and Y.-S. Lin, "Actively logical modulation of MEMS-based terahertz metamaterial," *Photon. Res.*, vol. 9, no. 7, pp. 1409–1415, 19 2021. DOI: `10.1364/PRJ.420876`.

[157] W. Gao, J. Shu, K. Reichel, D. V. Nickel, X. He, G. Shi, R. Vajtai, P. M. Ajayan, J. Kono, D. M. Mittleman, and Q. Xu, "High-contrast terahertz wave modulation by gated graphene enhanced by extraordinary transmission through ring apertures," *Nano Letters*, vol. 14, no. 3, pp. 1242–1248, 19 2014, ISSN: 1530-6984. DOI: `10.1021/nl4041274`.

[158] S. Kalhor, M. Ghanaatshoar, T. Kashiwagi, K. Kadowaki, M. J. Kelly, and K. Delfanazari, "Thermal tuning of high-T_c Superconducting $Bi_2Sr\ _2CaCu_2\ O_{8+\delta}$ terahertz metamaterial," *IEEE Photonics Journal*, vol. 9, no. 5, pp. 1–8, 19 2017. DOI: `10.1109/JPHOT.2017.2754465`.

[159] C. Zhang, J. Wu, B. Jin, X. Jia, L. Kang, W. Xu, H. Wang, J. Chen, M. Tonouchi, and P. Wu, "Tunable electromagnetically induced transparency from a superconducting terahertz metamaterial," *Applied Physics Letters*, vol. 110, no. 24, p. 241 105, 19 2017. DOI: `10.1063/1.4985618`.

[160] Y. Zhao, L. Wang, Y. Zhang, S. Qiao, S. Liang, T. Zhou, X. Zhang, X. Guo, Z. Feng, F. Lan, Z. Chen, X. Yang, and Z. Yang, "High-speed efficient terahertz modulation based on tunable collective-individual state conversion within an active 3 nm two-dimensional electron gas metasurface," *Nano Letters*, vol. 19, no. 11, pp. 7588–7597, 19 2019, ISSN: 1530-6984. DOI: `10.1021/acs.nanolett.9b01273`.

[161] Y. K. Srivastava, M. Manjappa, L. Cong, H. N. S. Krishnamoorthy, V. Savinov, P. Pitchappa, and R. Singh, “A superconducting dual-channel photonic switch,” *Advanced Materials*, vol. 30, no. 29, p. 1 801 257, 19 2018. DOI: `https://doi.org/10.1002/adma.201801257`.